博士論文

Spectroscopic measurement of geoneutrinos from uranium and thorium with KamLAND

カムランドによるウラン・トリウムに由来する地球ニュートリノの分離測定

川田 七海

令和4年

Doctoral Dissertation

Spectroscopic measurement of geoneutrinos from uranium and thorium with KamLAND

by Nanami Kawada

Tohoku University

A dissertation submitted for the degree of

Doctor of Philosophy (Science)

2022

Abstract

The decays of radioactive isotopes, uranium, thorium and potassium, inside the Earth generate a significant amount of radiogenic heat and contribute to the Earth's heat budget. The abundance of these elements is a key parameter to reveal the planet's geophysical activities. Geoneutrinos originated from these isotopes are unique probe to the composition, and thus, the radiogenic heat amount in the Earth. KamLAND has observed geoneutrinos from ^{238}U and ^{232}Th with 1 kt liquid scintillator for more than 18 years. The low-reactor period since 2011 enabled a spectroscopic measurement of geoneutrinos from uranium and thorium by reducing the most significant reactor neutrino background. The number of geoneutrino signal is estimated to be $116.6^{+41.0}_{-38.5}$, $57.5^{+24.5}_{-24.1}$ and $173.7^{+29.2}_{-27.7}$ from ^{238}U, ^{232}Th and ^{238}U $+^{232}$ Th, respectively. These correspond to geoneutrino flux of $14.7^{+5.2}_{-4.8}$, $23.9^{+10.2}_{-10.0}$ and $32.1^{+5.8}_{-5.3}$ $\times 10^5$ cm^{-2}s^{-1}, respectively. The null-signal hypothesis is disfavored at 8.3σ confidence level. This study yields the first constraint on the radiogenic heat contribution from ^{238}U and ^{232}Th, which is consistent to geochemical predictions based on the compositional analysis of chondrite meteorites.

Contents

List of Figures

List of Tables

Chapter 1

Introduction

Neutrino observations are an indispensable part of the history of particle physics. The first observation of supernova neutrinos by Dr. Masatoshi Koshiba established neutrino astronomy. The proof of neutrino oscillation by Dr. Takaaki Kajita solved the solar neutrino problem. Neutrinos are powerful probes of the Sun and other objects that cannot be observed optically because of their high penetrating power.

In 2005, the KamLAND detector successfully observed geoneutrinos for the first time in the world and established neutrino geoscience. Geoneutrinos is unique probes of the chemical composition and heat budget of the Earth. Complementary studies with seismic wave observations and geochemistry provide the key to revealing the history and dynamics of the Earth.

This study summarizes the results of observations of reactor neutrinos and geoneutrinos by the KamLAND antielectron neutrino detector, and the findings on neutrino oscillation parameters and the thermal and chemical properties of the earth obtained from these observations.

Chapter 1 summarized the background of this study and the motivation for the research. Chapter 2 introduce geoscientific approach using geoneutrinos. The structure and calibration of the KamLAND detector and event reconstruction are summarized in Chapter 3 and Chapter 4. The selection criteria and systematic uncertainties of the antielectron neutrinos in KamLAND are discussed in Chapter 5, and Chapter 6 describes the estimation of background events. Finally, reactor neutrino observations and neutrino oscillation analysis results are discussed in Chapter 7, and the geoneutrino observations are discussed in Chapter 8.

Chapter 2

Neutrino Geoscience

2.1 Open Questions in Geoscience

The Earth is composed of three layers: crust, mantle and core. This fact was revealed by seismic wave observations beginning in the 20th century. Not only that, precise observations of the non-uniformity of seismic wave propagation velocities have suggested that the mantle is convective. Although seismic wave observations have greatly contributed to the construction of the Earth's structural model, the chemical composition, which is indispensable for the formation and evolutionary history of the Earth, cannot be determined by seismic wave observations.

The chemical composition of the Earth has been revealed by geochemistry based on petrology and the compositional analysis of meteorite. In particular, the BSE model based on the composition of CI carbonaceous chondrite meteorites (McDonough and Sun 1995) is the basis of today's geoscience. However, geochemical composition models based on meteorite compositional analysis are indirect estimates, and no direct verification of the Earth's interior exists. In addition, the type of meteorite that formed the Earth has not been identified, and the geochemical composition based on meteorite compositional analysis bears intrinsic uncertainties.

To reveal the history of Earth's evolution and the geophysical activities, understanding the Earth's heat budget is also essential. Earth's history is essentially a cooling process, and geophysical activities such as plate tectonics, earthquakes, volcanism, and geomagnetism are driven by heat in the Earth's interior. The heat flow at the Earth's surface is estimated to be about 47 ± 2 TW based on multi-point borehole measurements Davies and Davies (2010). The heat sources include remnants of primordial heat, latent heat from the inner core growth, and radiogenic heat from heat producing elements. Radiogenic heat, in particular, is a heat source necessary for the Earth to remain an active planet for billions of years, and the distribution of radiogenic heat sources is also important in addition to its quantity.

However, the fraction of radiogenic heat has not been solved. There are some competing estimates for the radiogenic heat abundance. HighQ model (Turcotte and Schubert 2002) predicts radiogenic heat of more than 25 TW based on seismology and realistic mantle convection models. MiddleQ (McDonough and Sun 1995) and

LowQ (Javoy et al. 2010) model predict 17–22 TW and 10–15 TW, respectively, based on the compositional analysis of CI carbonaceous chondrites and enstatite chondrites with terrestrial samples and consideration of elemental enrichment during the planetary differentiation.

Neutrinos originating from radioactive elements, such as uranium, thorium and potassium, in earth, or "geoneutrinos", are key of revealing the Earth's chemical composition and heat budget. Because neutrinos have very small reaction cross sections, they reach the Earth's surface almost unimpeded by the Earth itself. Geoneutrinos provide direct information on the abundances of radioactive isotopes, and therefore, radiogenic heat in the Earth. Besides, since the energy of geoneutrino depends on the source elements, the spectrum is useful to measure the abundances of each heat producing element, and thus the chemical composition is directly measured. Neutrino observation is the only way to directly verify the chemical composition and the abundance of radiogenic heat in the Earth's interior.

In this chapter, motivation and strategy of "neutrino geoscience" are introduced.

2.2 Geoscientific Approaches and Earth Models

2.2.1 Boring

The simplest approach to study the Earth's interior is to bore the ground, take samples and analyze it. The deepest borehole ever made by humans is the Kola Superdeep Borehole (KSDB-3) in Russia, reaching a final depth of 12262 m (Trčková et al. 2002). This is an important achievement in geoscience, but at this depth it cannot even penetrate the continental crust, which is thought to be 20–70 km thick. It is technically impossible to drill a hole any deeper than this because geothermal heat prevents the drilling rig from operating. Therefore, this method is not suitable for the study of the Earth's deep interior, including the mantle and core.

2.2.2 Structural Model

Global Structure

The structure of the Earth has been revealed by seismology. When seismic waves, or earthquake, propagates through the earth, they are reflected or bent at the boundaries of layers with different elastic properties. By observing these reflected or bent seismic waves at many points on the earth, the propagation velocity and other elastic properties in the earth is measured as shown in Figure 2.1.

Dziewonski and Anderson (1981) proposed the Preliminary Reference Earth Model (PREM), describing the seismic wave velocity, density distribution and other elastic parameters as a function of radius (Figure 2.2). As shown in the figure, the multi-layered structure of the earth, crust, mantle, liquid outer core and solid inner core, is clearly demonstrated by seismology. The mass of each reservoir in earth given by PREM is summarized in Table 2.1

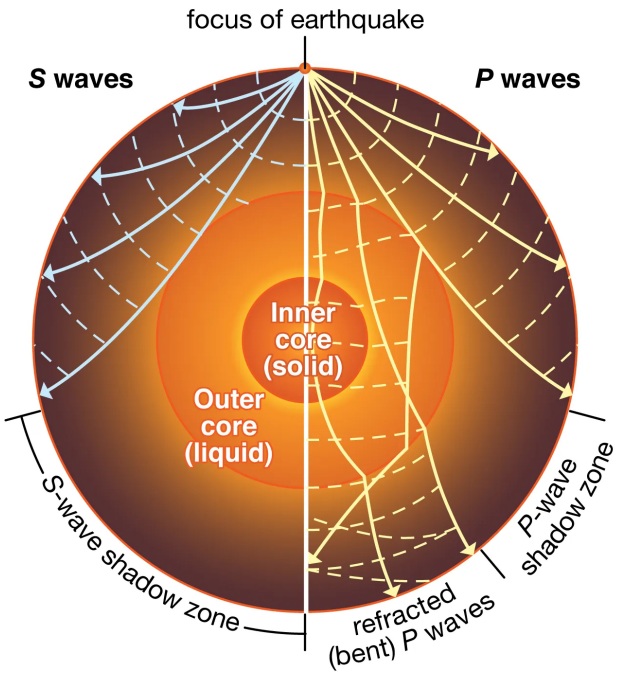

Figure 2.1: Earth structural modeling based on seismic wave observation (Britannica)

Table 2.1: The mass of each layer of the Earth (Dziewonski and Anderson 1981)

reservoir	mass [kg]
– sediment –	
continental	9.238×10^{20}
oceanic	4.114×10^{20}
– crust –	
upper continental	6.613×10^{21}
middle continental	7.325×10^{21}
bottom continental	7.084×10^{21}
oceanic	4.229×10^{21}
– mantle –	
upper	1.068×10^{24}
lower	2.937×10^{24}
– core –	
outer	1.840×10^{24}
inner	9.841×10^{22}

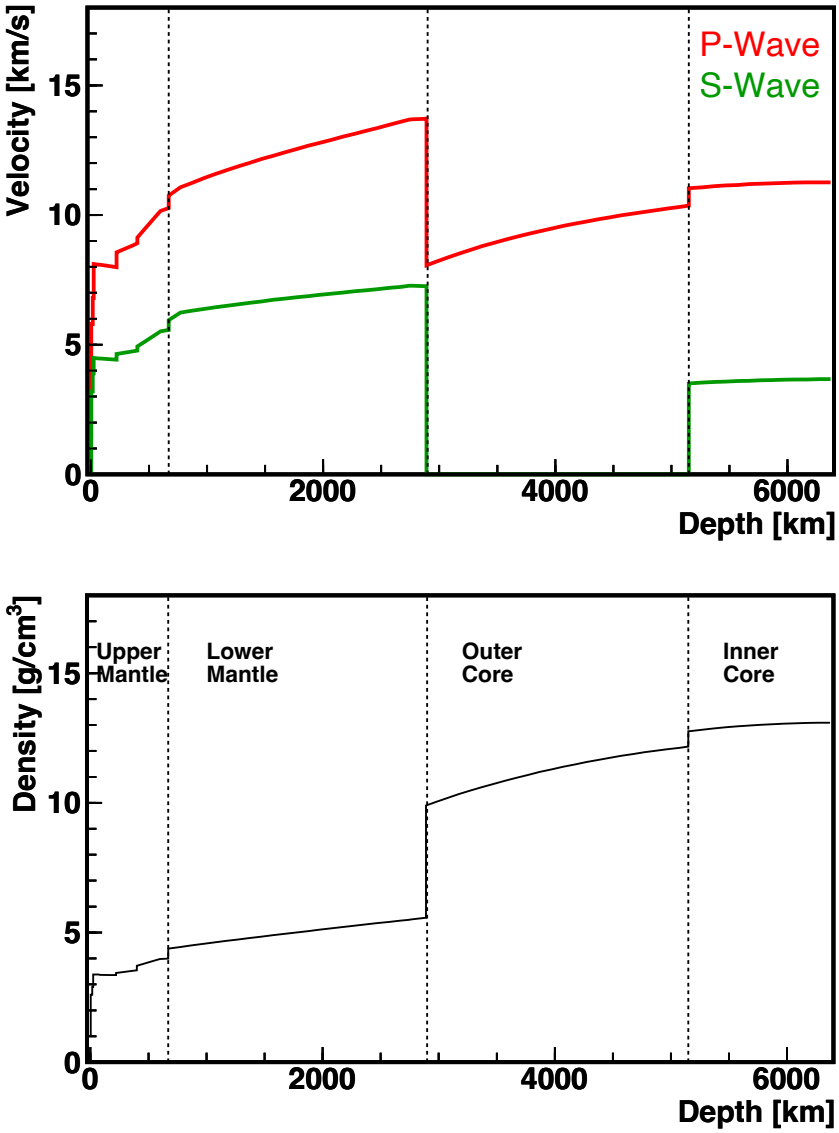

Figure 2.2: The Preliminary Reference Earth Model, describing the seismic wave velocity (top) and density (bottom) profiles as a function of radius. The figure is cited from Enomoto (2005). The original data is provided from Dziewonski and Anderson (1981).

Crust

Not only the global structure, but also the properties of each reservoir are studied by seismology. Bassin et al. (2000) compiled a $2^\circ \times 2^\circ$ grid crustal thickness map from seismic wave measurement, describing the thickness and density of soft sediment, hard sediment, upper crust, middle crust and lower crust. The map is distributed as CRUST 2.0 data set (Laske et al. 2001). Figure 2.3 shows a crustal thickness map given by CRUST 2.0. This data set was improved to a $1^\circ \times 1^\circ$ resolution and distributed as CRUST 1.0 (Laske et al. 2011), incorporating a sediment thickness map Laske and Masters (1997).

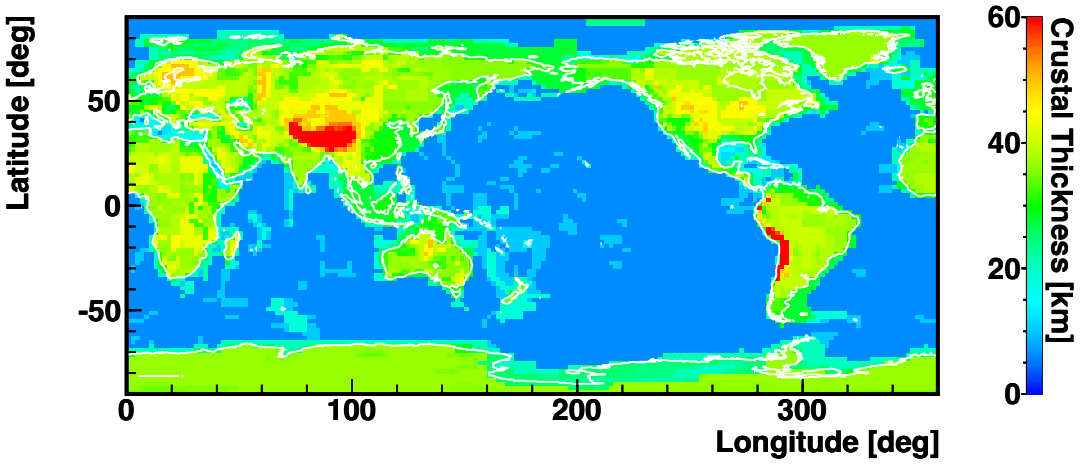

Figure 2.3: Crustal thickness map given by CRUST 2.0 dataset (Laske et al. 2001)

As is clearly seen in Figure 2.3, the oceanic crust is quite different from the continental crust. The oceanic crust is constantly created at ocean ridges with typical thickness of 6–8 km and subducted at trenches. The oceanic crust is relatively young ($\sim$ 80 million years old) and uniformly composed mainly of basalt. On the other hand, the continental crust is relatively old ($\sim$ 2 billion years old on average) and the thickness varies from 20 to 70 km. The continental crust has seismological boundary called "Conrad discontinuity". The lower part consist mainly of basalt, whereas the upper part is typically composed of granite.

Mantle

For the mantle, non-uniform seismic wave velocity is studied by Bull et al. (2009). Figure 2.4 shows seismic wave velocity heterogeneity in the mantle. This anomaly implies the temperature inhomogeneity in the mantle, i.e. fast seismic wave in dense therefore cold mantle, slow wave in sparse therefore hot mantle. The temperature inhomogeneity may represents mantle convection structure. In Figure 2.4, there are two up-going hot plume, or super plume, beneath South Pacific and Africa, and a down-going plume, or cold plume, beneath Asia.

Besides, the mantle tomography analysis predicts a whole-layer convection of the mantle, whereas the geochemical studies (Sec.2.2.3) support a two-layer convection

in which the upper layer is highly depleted of refractory and lithophile elements, e.g. uranium and thorium, as shown in Figure 2.5.

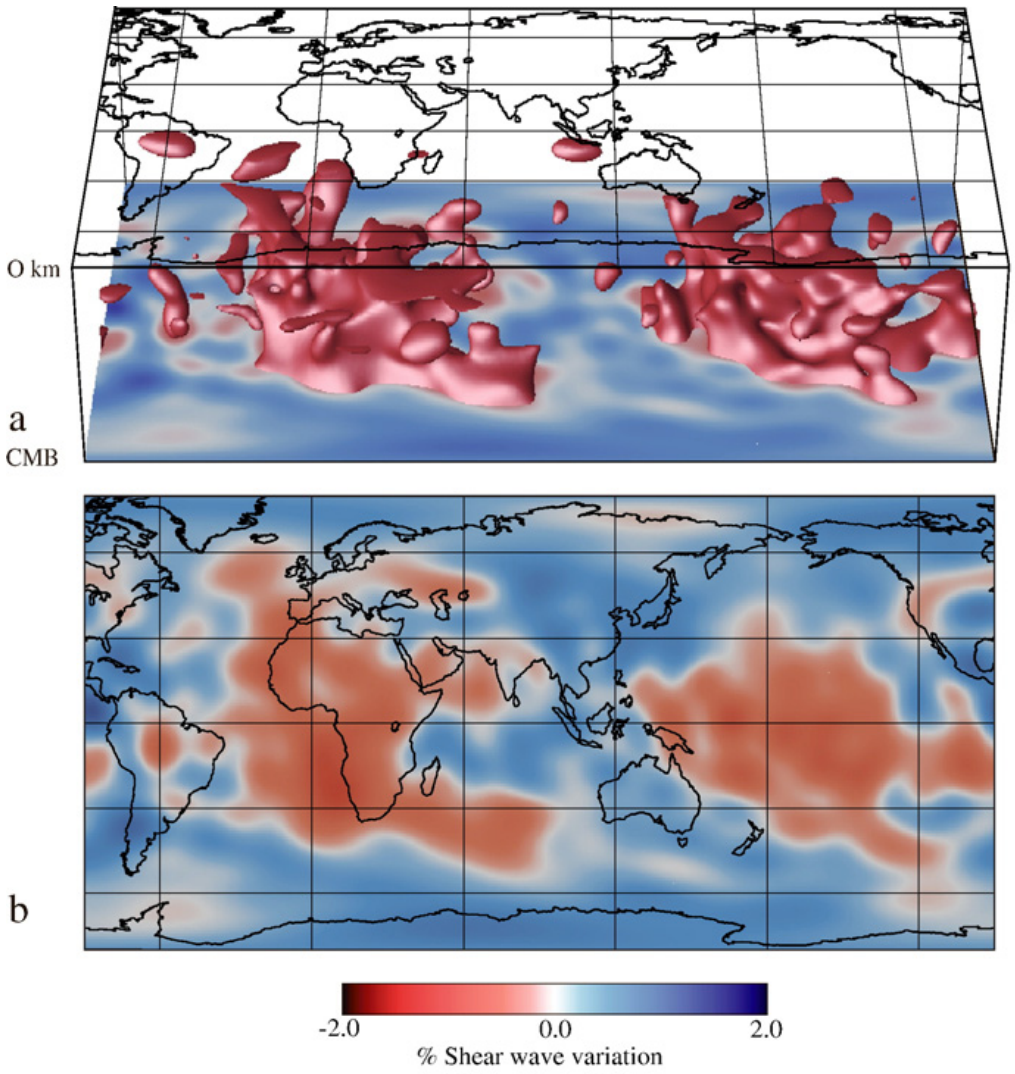

Figure 2.4: Mantle tomography by seismic wave analysis (Bull et al. 2009). CMB in this figure is an acronym for "Core Mantle Boundary". (a) an isosurface in cross-sectional view through the mantle (b) a map view at a depth of 2750 km.

2.2.3 Geochemical Model

Rationale of Geochemistry

The chemical properties of the Earth are discussed based on compositional analysis of rocks and meteorites collected from the Earth's surface. Our planet was formed by repeated collisions and fusions of meteorites within the primordial solar system. Therefore, the meteorites preserve the chemical composition of the primitive Earth.

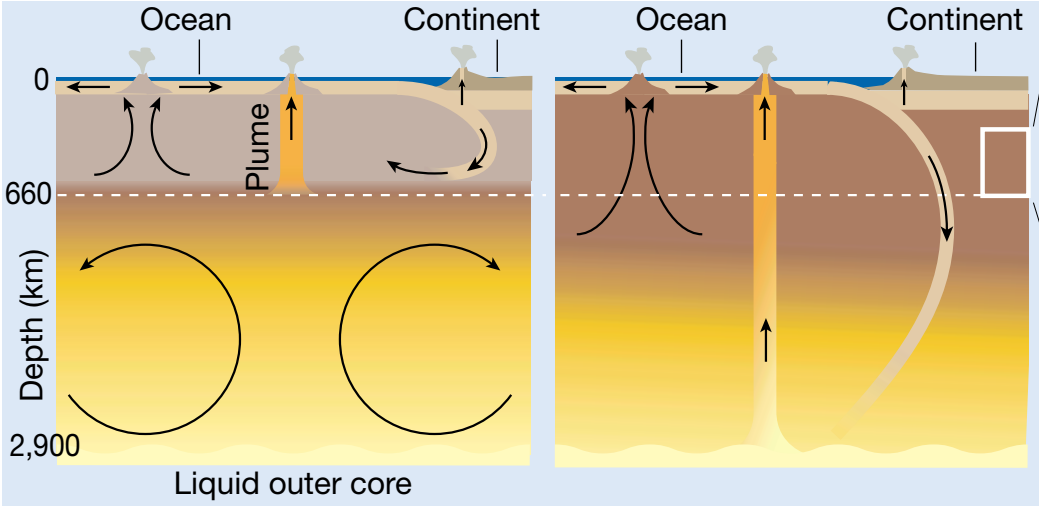

Figure 2.5: Models of mantle convection. (Left) Two-layer model supported by geochemistry, in which the upper layer of mantle is depleted in incompatible elements and separated from the lower mantle. (Right) Whole-layer model supported by seismology. (Hofmann 2003)

During the cooling process, the Earth was differentiated into the core, mantle and crust. The presence of a geomagnetic field indirectly indicates that the core is made of metal, and its size is also estimated from seismic wave observations. It is known experimentally that refractory lithophile elements do not exist under the high temperatures and pressures of the core, whereas they accumulated in the primitive mantle, which was composed of silicates. The composition of the crust is analyzed from rocks sampled at the surface. Therefore, the composition of the mantle can also be estimated by subtracting elemental inventories in the crust from the total elemental abundances in the silicate earth (crust + mantle).

There are multiple candidates for the type of meteorite that formed the Earth. CI carbonaceous chondrite meteorite is one of candidates because of its inclusion of volatile elements and similarity to the solar atmosphere (McDonough and Sun 1995). Enstatite chondrite is another candidate meteorites because of its similarity to the Earth in oxygen isotopic ratio and iron abundance (Javoy et al. 2010). By examining the isotopic abundance ratios of several elements, Warren (2011) suggests that our planet was formed from a mixture of several types of meteorites.

While these approaches are essential to geoscience, there are intrinsic uncertainties due to absence of the direct test of the Earth's interior.

Crust

The crust is the layer between the Mohorovičić discontinuity and the Earth's surface. As described in Sec.2.2.2, the crust is classified into the continental crust and the oceanic crust. Both the crustal and oceanic crust float on the mantle since their less dense than the mantle.

There are various approaches to study the chemical composition of the continental

crust, e.g. tectonic models (Taylor and McLennan 1995), geologic models (Condie 1993) and seismic models (Wedepohl 1995, Rudnick and Fountain 1995). Table. 2.2 summarizes the uranium and thorium concentration from these approaches.

Table 2.2: Uranium and thorium concentration in the continental crust. Condie (1993) estimated the composition of the upper crust with and without a correction of crust lost by erosion. Rudnick and Fountain (1995) employed Taylor and McLennan (1995) for the upper continental crust. Rudnick and Gao (2014) cited Rudnick and Fountain (1995) for the lower continental crust.

	element	concentration [ppm]		
		upper	middle	lower
Taylor and McLennan (1995)	U	2.8	-	0.53
	Th	10.7	-	2.0
Condie (1993)	U	2.4/2.2	-	-
	Th	9.1/8.6	-	-
Wedepohl (1995)	U	2.5	1.93	
	Th	10.3	6.6	
Rudnick and Fountain (1995)	U	(2.8)	1.6	0.2
	Th	(10.7)	6.1	1.2
Rudnick and Gao (2014)	U	2.7	1.4	(0.2)
	Th	10.5	6.5	(1.2)

In the planetary differentiate process, the Large Ion Lithophile (LIL) elements such as uranium, thorium and potassium are extracted from the mantle materials by the repeated melting and accumulated to the crust due to their high incompatibility to the mantle and core. Thus, through the continental crust total up to only 0.4% of the Earth's mass, it contains about half of uranium and thorium in the Earth.

The uranium and thorium concentration in the oceanic crust is reported by Taylor and McLennan (1985) to be ∼0.10 ppm and ∼0.22 ppm, respectively. These values are smaller than that of the continental crust (Table. 2.2) but larger than of the mantle (∼0.01 ppm and ∼0.05 ppm). Since the oceanic crust is constantly created at mid-ocean ridge or at intra-plate volcanos, relatively young and homogeneous in the thickness and composition compared to the continental crust.

Mantle

As is mentioned in the crust part above, the incompatible elements are extracted to the crust by the repeated melting and depleted in the upper mantle. Though this extraction take place near the crust–mantle boundary, the global convection of the mantle results in the global depletion of these elements.

The direct sampling of the mantle is essentially impossible, especially of the lower

mantle. Rather, the composition of the mantle is estimated by cosmochemical methods and laboratory methods such as high-temperature and high-pressure lithology.

As for the upper mantle, there are some samples available as ultramafic massifs, which were transported from the Earth's deep interior by ascending magmas. However, such samples are transported to the surface by special tectonics, and it is not clear whether they represent the composition of the entire mantle.

Hence, the chemical composition of the mantle in the reference model (Sec.2.4) is determined by subtracting the crustal element abundances from the composition of the whole Earth expected from the meteorite analysis.

Core

As with the mantle, the direct core sampling is impossible. The compositional analysis of chondrite meteorites and iron meteorites help understand the composition of the core, as well as the seismological and terrestrial magnetism studies.

The core is a Fe-Ni alloy whose density is 10–12 g/cm^3. It is demonstrated by laboratory compression experiments that only low-atomic-weight elements such as hydrogen, carbon, nitrogen, oxygen, magnesium, silicon and sulfur can be contained in such high density alloy (McDonough 1999). Besides, Murthy et al. (2003) reported that potassium is a substantial radiogenic heat source in the core by high-pressure and high-temperature experimental data.

Bulk-Silicate Earth Model

The Bulk-Silicate Earth (BSE), or the primitive mantle, refers to the intermediate stage between the core-mantle differentiation and mantle-crust separation (Lyubetskaya and Korenaga 2007). The BSE composition is supposed to give the average elemental abundances in the silicate earth (mantle + crust), which is studied based on analysis of chondrite meteorites with considering the core separation and escape of volatile elements.

McDonough and Sun (1995) constructed a BSE model based on CI carbonaceous chondrite composition with taking account for lithological and geological measurement on the earth. This model is a part of fundamental basis of today's geoscience. There are some BSE models with different chondrite for rationale, and they have different predictions of elemental abundances as summarized in Table. 2.3. Most of them are based on CI carbonaceous chondrite, whereas Javoy (1999) is based on enstatite chondrite.

2.2.4 Earth's Surface Heat Flux

The history of the Earth is a process of global cooling. The geodynamics, e.g. tectonics, volcanism and magnetism, are powered by heat inside earth. Therefore, it is important to understand the Earth's heat budget for revealing the geophysical activity.

Table 2.3: Abundances of heat producing elements in BSE models

	U [ppb]	Th [ppb]	K [ppb]	Th/U
Taylor and McLennan (1985)	18	65	180	3.6
Hart and Zindler (1986)	21	79	264	3.8
Hofmann (1988)	20	80	254	4.0
McDonough and Sun (1995)	20.3 ± 4.1	79.5 ± 11.9	240 ± 48	3.9
Javoy (1999)	20	69	270	3.5
Palme and O'Neill (2007)	21.8 ± 3.3	83.9 ± 12.5	261 ± 39	3.8
Lyubetskaya and Korenaga (2007)	17.3 ± 3.0	62.6 ± 10.7	190	3.6

The total heat flow at the surface is measured in a number of bore holes by several researches as summarized in Table. 2.4. Except Hofmeister and Criss (2005), the total heat flow from earth is estimated to be around 46 TW.

Table 2.4: Total heat flow from earth

	total heat flow [TW]
Williams and Von Herzen (1974)	43
Davies (1980)	41
Sclater et al. (1980)	42
Pollack et al. (1993)	44 ± 1
Hofmeister and Criss (2005)	31 ± 1
Jaupart et al. (2007)	46 ± 3
Davies and Davies (2010)	47 ± 2

There are several different heat sources in the Earth's interior, including remnants of primordial heat, radiogenic heat from heat producing elements such as uranium, thorium, and potassium, gravitational energy release from accretion and metal core separation, and latent heat from inner core growth.

The radiogenic heat sources have heated the Earth and allowed it to exist as a geophysically active planet for much longer than expected from Lord Kelvin's heat conduction calculations. Therefore, radiogenic heat plays a decisive role in the thermal evolution of the Earth.

However, the heat flow measurement at the surface, and also the seismological approach, does not provide any information about the fraction of radiogenic heat to the Earth's total heat flow. Geochemical approaches give predictions via the abundance of the heat producing elements but there are intrinsic uncertainties as is also mentioned in Sec.2.2.3.

Hence, geoneutrino observation is the only way to directly verify the amount of radiogenic heat sources in the Earth's interior.

2.3 Geoneutrino

2.3.1 Properties of Geoneutrino

Electron antineutrinos produced in beta decays in the decay process of radioactive elements in earth, or "geoneutrino", provide important information of the Earth's interior. Using a linear relationship between the geoneutrino luminosity and the amount of radiogenic heat, earth's thermal property is uniquely verified.

Radioactive elements which is abundant in the present earth are classified into three groups: ^{238}U ($\tau_{1/2} = 4.47 \times 10^9$ year) series, ^{232}Th ($\tau_{1/2} = 14.0 \times 10^9$ year) series and ^{40}K ($\tau_{1/2} = 1.25 \times 10^9$ year) as shown in Eq. 2.1–2.4.

$$^{238}\mathrm{U} \xrightarrow[100\%]{} {}^{206}\mathrm{Pb} + 8\,{}^{4}\mathrm{He} + 6e^- + 6\overline{\nu}_\mathrm{e} + 61.7\ [\mathrm{MeV}] \tag{2.1}$$

$$^{232}\mathrm{Th} \xrightarrow[100\%]{} {}^{208}\mathrm{Pb} + 6\,{}^{4}\mathrm{He} + 4e^- + 4\overline{\nu}_\mathrm{e} + 42.7\ [\mathrm{MeV}] \tag{2.2}$$

$$^{40}\mathrm{K} \xrightarrow[89.28\%]{} {}^{40}\mathrm{Ca} + e^- + \overline{\nu}_\mathrm{e} + 1.311\ [\mathrm{MeV}] \tag{2.3}$$

$$^{40}\mathrm{K} + e^- \xrightarrow[10.72\%]{} {}^{40}\mathrm{Ar} + \nu_\mathrm{e} + 1.505\ [\mathrm{MeV}] \tag{2.4}$$

In the ancient earth, ^{235}U and ^{237}Np contributed to significant geoneutrino luminosity and radiogenic heat, but have already decayed away due to short half lives ($\tau_{1/2} = 0.71 \times 10^9$ year and $\tau_{1/2} = 0.002 \times 10^9$ year, respectively). On the other hand, ^{87}Rb ($\tau_{1/2} = 49.7 \times 10^9$ year), ^{138}La ($\tau_{1/2} = 110.0 \times 10^9$ year) and ^{176}Lu ($\tau_{1/2} = 21.0 \times 10^9$ year) still remains in earth but their radiogenic heat production and geoneutrino emission are negligible due to small Q-value of decays less than 0.5 MeV.

Figure 2.6 shows radiogenic heat flux through time from each element calculated by Arevalo et al. (2009). ^{40}K acted as the dominant and ^{235}U acted as the second dominant radiogenic heat source in the past, whereas ^{238}U and ^{232}Th total up to 80% of the present radiogenic heat production.

Energy spectrum of electron antineutrino from beta decay with maximum electron energy E_max is given by a well-established formula as

$$\mathrm{d}N(E_\mathrm{e}) = \frac{G_\mathrm{F}^2 |M|^2}{2\pi^3 \hbar^7 c^5} F(Z, E_\mathrm{e})(E_\mathrm{max} - E_\mathrm{e})^2 \sqrt{E_\mathrm{e}^2 - m_\mathrm{e}^2 c^4} E_\mathrm{e}\, \mathrm{d}E_\mathrm{e} \tag{2.5}$$

$$E_{\overline{\nu}_\mathrm{e}} = E_\mathrm{max} - E_\mathrm{e} \tag{2.6}$$

where $F(Z, E_\mathrm{e})$ is the Fermi function representing the electric field effect of nuclei given by

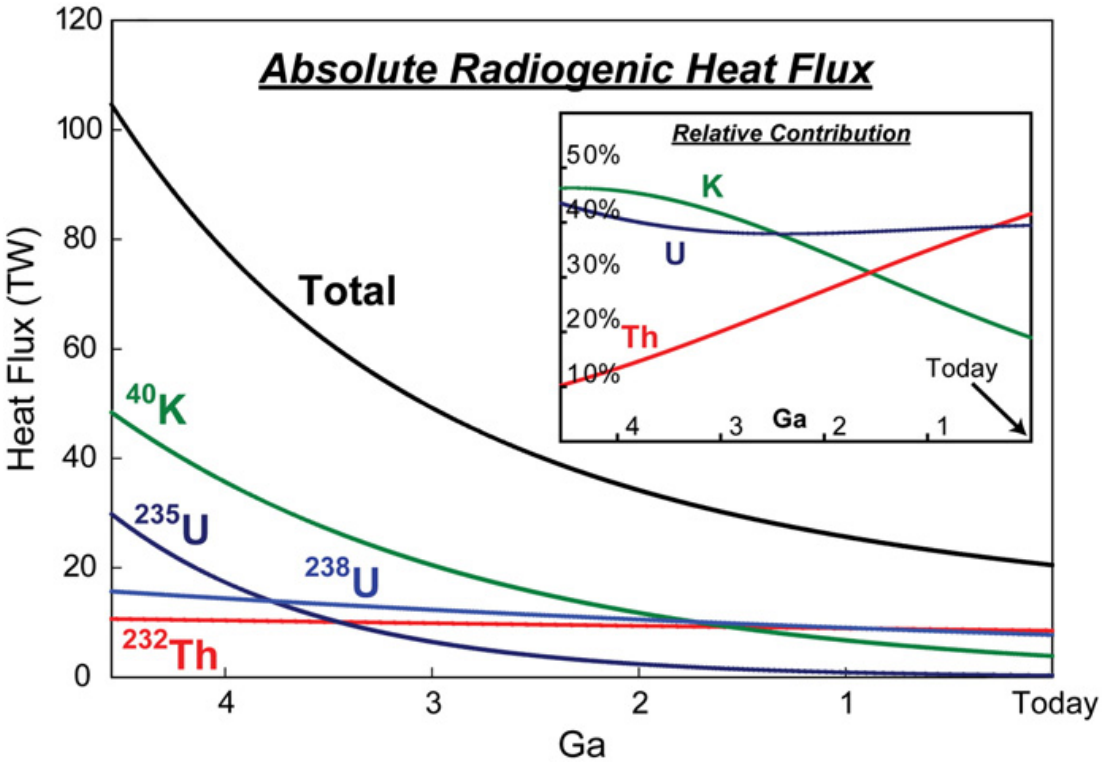

Figure 2.6: Earth's radiogenic heat production from the decay of radioactive elements through time (Arevalo et al. 2009)

$$F(Z, E_{\mathrm{e}}) = 2(1+\gamma)(2\sqrt{W^2-1}R)^{2(\gamma-1)}e^{xy}\frac{|\Gamma(\gamma+iy)^2|}{|\Gamma(2\gamma+1)^2|} \tag{2.7}$$

$$\gamma = \sqrt{1-(\alpha Z)^2} \tag{2.8}$$

$$W = \frac{E_{\mathrm{e}}}{mc^2} \tag{2.9}$$

$$y = \alpha Z\frac{W}{\sqrt{W^2-1}} \tag{2.10}$$

$$R = 0.426\alpha A^{\frac{1}{3}} \tag{2.11}$$

$$\alpha = \frac{e^2}{\hbar c} = \frac{1}{137.0355989} \tag{2.12}$$

Geoneutrino spectrum from ^{238}U decay series and ^{232}Th decay series are calculated by summing up normalized spectra of each isotope over the series assuming radioactive equilibrium. Using R_{isotope} as a production ratio and $R_{\beta-\mathrm{branch}}$ as a branching ratio to beta decay, the normalized spectra of an isotope is given by

$$\frac{\mathrm{d}N}{\mathrm{d}E_\nu} = \sum_{\mathrm{isotope}}\sum_{\beta\text{-branch}} R_{\mathrm{isotope}}R_{\beta\text{-branch}}\left(\frac{1}{N}\frac{\mathrm{d}N}{\mathrm{d}E_\nu}\right)_{\mathrm{isotope},\beta\text{-branch}} \tag{2.13}$$

$$R_{\mathrm{isotope}} = \begin{cases} 1 & (\text{decay series head}) \\ \sum_{\mathrm{parent}}\sum_{\mathrm{branch}} R_{\mathrm{parent}}R_{\mathrm{branch}} & (\text{daughter isotopes}) \end{cases} \tag{2.14}$$

where R_{parent} is the production rate of a parent isotope. Enomoto (2005) calculated antineutrino spectra from ^{238}U series including 82 beta decays, ^{232}Th series including 70 beta decays and ^{40}K beta decay as shown in Figure 2.7.

2.3.2 Radiogenic Heat Estimate

The corresponding radiogenic heat production is calculated by subtracting the neutrino energy from the decay Q value as

$$Q_{\mathrm{heat}} = Q - Q_\nu = Q - \int_0^{E_{\max}} E_\nu\frac{\mathrm{d}N}{\mathrm{d}E_\nu}\,\mathrm{d}E_\nu \tag{2.15}$$

where $\frac{\mathrm{d}N}{\mathrm{d}E_\nu}$ is the differential neutrino spectrum (Eq. 2.13) and Q is shown in Eq. 2.1–2.4. The calculated radiogenic heat is summarized in Table. 2.5.

Using natural abundance, atomic weight, half life, calculated radiogenic heat production and calculated neutrino luminosity summarized in Table. 2.6, the conversion factors between radiogenic heat, mass and neutrino luminosity are given as

$$\text{Uranium}: L_{\overline{\nu}_{\mathrm{e}}}\ [\mathrm{s}^{-1}] = 7.84\times10^{11}\cdot Q_{\mathrm{heat}}\ [\mathrm{W}] = 7.41\times10^{7}\cdot M\ [\mathrm{kg}] \tag{2.16}$$

$$\text{Thorium}: L_{\overline{\nu}_{\mathrm{e}}}\ [\mathrm{s}^{-1}] = 6.18\times10^{11}\cdot Q_{\mathrm{heat}}\ [\mathrm{W}] = 1.62\times10^{7}\cdot M\ [\mathrm{kg}] \tag{2.17}$$

$$\text{Potassium}: L_{\overline{\nu}_{\mathrm{e}}}\ [\mathrm{s}^{-1}] = 7.98\times10^{12}\cdot Q_{\mathrm{heat}}\ [\mathrm{W}] = 2.70\times10^{4}\cdot M\ [\mathrm{kg}] \tag{2.18}$$

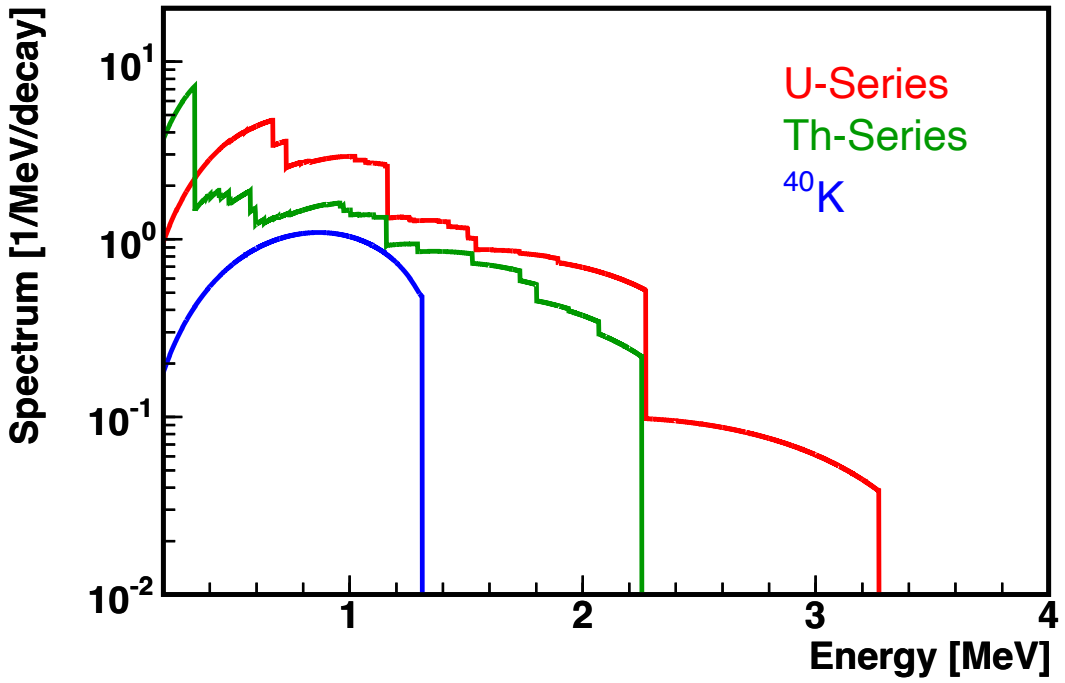

Figure 2.7: Spectra of geoneutrinos produced by radioactive decays of ^{238}U, ^{232}Th and ^{40}K (Enomoto 2005). Neutrinos from ^{40}K electron capture is not shown.

Table 2.5: Radiogenic heat generation per decay (Enomoto 2005)

	^{238}U series	^{232}Th series	^{40}K	
			β^- (89.28%)	EC (10.72%)
Q [MeV/decay]	51.7	42.7	1.311	1.505
Q_ν [MeV/decay]	3.96	2.23	0.724	0.044
Q_{heat} [MeV/decay]	47.7	40.4	0.587	1.461

Table 2.6: Radiogenic heat production and neutrino luminosity (Enomoto 2005)

– isotope –			
	^{238}U	^{232}Th	^{40}K
natural abundance [%]	99.27	100	0.01167
N_{atom}/M [kg^{-1}]	2.530×10^{24}	2.596×10^{24}	1.506×10^{25}
lifetime [s]	2.034×10^{17}	6.397×10^{17}	5.814×10^{16}
N_{decay}/M [s^{-1}kg^{-1}]	1.244×10^{7}	4.058×10^{6}	2.590×10^{8}
$N_{\bar{\nu}_e}/N_{\mathrm{decay}}$	6	4	0.8927
$L_{\bar{\nu}_e}/M$ [s^{-1}kg^{-1}]	7.464×10^{7}	1.623×10^{7}	2.312×10^{8}
Q_{heat}/M [W $\cdot$ kg^{-1}]	9.515×10^{-5}	2.628×10^{-5}	2.613×10^{-5}

– natural element –			
	Uranium	Thorium	Potassium
$L_{\bar{\nu}_e}/M$ [s^{-1}kg^{-1}]	7.410×10^{7}	1.623×10^{7}	2.698×10^{4}
Q_{heat}/M [W $\cdot$ kg^{-1}]	9.446×10^{-5}	2.628×10^{-5}	3.049×10^{-5}

2.4 Reference Earth Model

Based on the structural model (Sec.2.2.2) and geochemical model (Sec.2.2.3), Enomoto et al. (2007) constructed a reference earth model for geoneutrino flux model calculation. The Earth is divided to 10 reservoirs, and uranium and thorium concentration in each reservoir is assigned as Table 2.7. The values for sedimentary part, crustal part and core are imported from the reference articles. Each reservoir is assumed to be uniform in composition. The intrinsic uncertainty by this assumption is discussed later in Sec. 2.6. Though the oceanic crust consists of three layers as of the continental crust, they are treated as one united layer because oceanic contribution to the total geoneutrino flux at the KamLAND site is negligible and such treatment effectively reduces unnecessary complication. The mantle values are decided by Enomoto (2005) by subtracting the crustal abundances from a BSE composition by McDonough and Sun (1995). Henceforth, contribution from potassium is ignored since the energy of ^{40}K geoneutrinos are lower than the IBD reaction threshold and not relevant to geoneutrino observation at KamLAND.

2.5 Geoneutrino Flux Estimate

The differential geoneutrino flux at a point, $\vec{r}$, is given by Eq. 2.19.

$$\frac{\mathrm{d}\Phi(E_\nu, \vec{r})}{\mathrm{d}E_\nu} = \sum_{i \in \mathrm{U,Th}} A_i \cdot \frac{\mathrm{d}N_i}{\mathrm{d}E_\nu} \int_{\mathrm{earth}} \mathrm{d}^3\vec{r'} \, \frac{a_i(\vec{r'})\rho(\vec{r'})}{4\pi|\vec{r} - \vec{r'}|^2} P(E_\nu, |\vec{r} - \vec{r'}|) \tag{2.19}$$

Table 2.7: Uranium and thorium concentration in a reference geochemical model. The values for the continental sediment are the same as those for the upper continental crust because the continental sediment origins from the upper continental crust and usually its composition is similar to the continental crust.

reservoir	U [ppm]	Th [ppm]	reference
– sediment –			
continental	(2.7)	(10.5)	Rudnick and Gao (2014)
oceanic	1.68	6.91	Plank and Langmuir (1998)
– crust –			
upper continental	2.7	10.5	Rudnick and Gao (2014)
middle continental	1.4	6.5	Rudnick and Gao (2014)
lower continental	0.2	1.2	Rudnick and Fountain (1995)
oceanic	0.10	0.22	Taylor and McLennan (1985)
– mantle –			
upper	0.012	0.048	Enomoto (2005)
lower	0.012	0.048	Enomoto (2005)
– core –			
outer	0.0	0.0	McDonough (1999)
inner	0.0	0.0	McDonough (1999)

where A_i is the number of $\overline{\nu}_e$ per decay (given in Eq. 2.1 and Eq. 2.2), $\frac{dN_i}{dE_\nu}$ is the $\overline{\nu}_e$ spectra at the source, $a_i(\vec{r'})$ and $\rho(\vec{r'})$ are the concentration and the density at position $\vec{r'}$, and $P(E_\nu, |\vec{r} - \vec{r'}|)$ is the $\overline{\nu}_e$ survival probability. Given the spacial integration within a much larger scale than the ν_1-ν_2 oscillation length, the oscillation effect is well averaged out for distance. Similarly for the energy, the effect is well averaged due to a large propagation length and finite energy resolution of KamLAND detector. Therefore, an average survival probability, $P_{ee} = 0.554^{+0.012}_{-0.009}$, was used.

Hence, the geoneutrino flux is calculated by integrating the differential flux over energy as

$$\begin{aligned}\Phi(E_\nu) &= \int dE_\nu \frac{d\Phi_i}{dE_\nu} \\ &= \sum_{i\in \mathrm{U,Th}} A_i \cdot N_i \int_{\mathrm{earth}} d^3\vec{r'} \frac{a_i(\vec{r'})\rho(\vec{r'})}{4\pi|\vec{r} - \vec{r'}|^2} P(|\vec{r} - \vec{r'}|)\end{aligned} \tag{2.20}$$

The result is summarized in Table. 2.8. The flux are also represented in Terrestrial Neutrino Unit (TNU). 1 TNU corresponds to one IBD reaction by geoneutrino in 1-year live time on 10^{32} target protons assuming 100% detection efficiency. The conversion factor from $[\mathrm{cm}^{-2}\mathrm{s}^{-1}]$ to [TNU] is unique for each isotope due to different neutrino energy spectrum and energy-dependent IBD reaction cross section. The

conversion factor is given as following.

$$\text{Uranium} : 1\ [\text{TNU}] = 7.674 \times 10^4\ [1/\text{cm}^2/\text{sec}] \tag{2.21}$$
$$\text{Thorium} : 1\ [\text{TNU}] = 2.477 \times 10^5\ [1/\text{cm}^2/\text{sec}] \tag{2.22}$$

Table 2.8: Reference geoneutrino flux at KamLAND (Enomoto et al. 2007)

reservoir	U geoneutrino		Th geoneutrino	
	$[1/\text{cm}^2/\text{sec}]$	[TNU]	$[1/\text{cm}^2/\text{sec}]$	[TNU]
– sediment –				
continental	0.75×10^5	0.80	0.63×10^5	0.20
oceanic	0.14×10^5	0.18	0.12×10^5	0.05
– crust –				
upper continental	11.5×10^5	15.01	9.5×10^5	3.86
middle continental	4.31×10^5	5.61	3.57×10^5	1.44
lower continental	0.53×10^5	0.68	0.69×10^5	0.28
oceanic	0.09×10^5	0.12	0.04×10^5	0.02
– mantle –				
upper	2.20×10^5	2.87	1.91×10^5	0.77
lower	4.03×10^5	5.25	3.51×10^5	1.42
– core –				
outer	0	0	0	0
inner	0	0	0	0

Figure 2.8 shows the cumulative geoneutrino flux as a function of distance calculated as

$$\frac{\mathrm{d}\Phi}{\mathrm{d}R} = \sum_{i \in \mathrm{U,Th}} A_i \cdot N_i \int_{\text{earth}} \mathrm{d}^3\vec{r'}\, \frac{a_i(\vec{r'})\rho(\vec{r'})}{4\pi|\vec{r} - \vec{r'}|^2} P(|\vec{r} - \vec{r'}|) \cdot \delta(|\vec{r} - \vec{r'}| - R) \tag{2.23}$$

The crustal contribution total up to about 75% of total geoneutrino flux. Especially, about half of the total geoneutrino flux is originated from the crust within 500 km.

2.6 Model-Related Uncertainties for Crustal Estimates

The reference earth model Enomoto et al. (2007) is constructed under an assumption that each reservoir is uniform in composition and any local geological effects are averaged. Enomoto (2005) evaluated possible biases by local geology in Japan. As is discussed in later this section, they are smaller than the U/Th concentration measurement uncertainties, which accompany the values in reference articles mentioned in Table. 2.7.

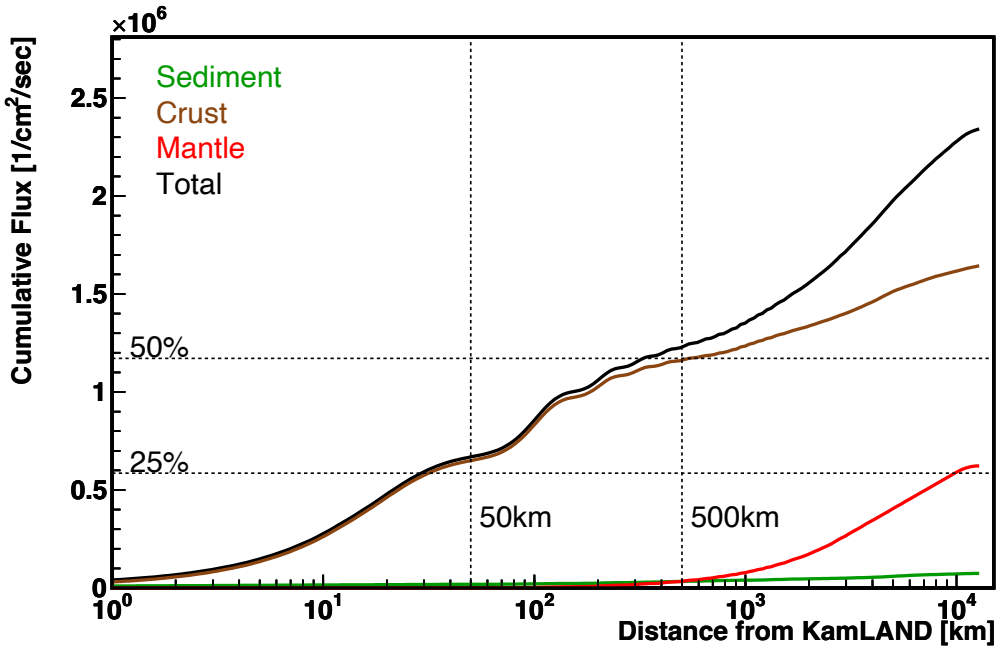

Figure 2.8: Cumulative geoneutrino from against distance (Enomoto 2005)

2.6.1 Global U/Th Concentration Measurement Uncertainties

Uncertainties of uranium and thorium abundances in each layer of continental crust and continental sediment are summarized in Table. 2.9. The oceanic crust uncertainty is ignored since the contribution of oceanic crust to total estimated geoneutrino flux is much smaller than the continental crust. By taking flux-weighted average of each layer, the flux estimate uncertainties originating from U/Th abundances in the crust and sediment is evaluated to be 24% for uranium and 11% for thorium. These values are larger than other possible biases described in this section, and assigned as the crustal uncertainties in the Earth model discussion introduced in Sec.2.7.

Table 2.9: Uncertainties of uranium and thorium abundances in the continental crust

reservoir	U [%]	Th [%]	reference
– sediment –			
continental	21%	10%	Rudnick and Gao (2014)
– crust –			
upper continental	21%	10%	Rudnick and Gao (2014)
middle continental	31%	8%	Rudnick and Gao (2014)
lower continental	40%	40%	Šrámek et al. (2016)

2.6.2 Continental Crust Non-Uniformity

The continental crust formation began when the first plate tectonics took place about 4 billion years (Ga) ago. While oceanic crust is recycled in a time scale of 0.1 Ga, continental crust has grown on the surface over billions of years. The growth of the continental crust is not constant; 50–60% of present continental crust was formed during the latest Archean, 2.8–2.6 Ga, whereas there also exist recently formed crust. Continental crust formed in different era is thought to be different in composition because relatively higher temperature of the primitive Earth melted not only the mantle but also the subducting slub. In general, the Archean crust is less enriched in incompatible elements than the newer crust. Therefore, the present continental crust is not uniform in composition.

While reference studies employed in Table. 2.7 give global average, Togashi et al. (2000) conducted a geochemical survey over Japan Island Arc and reported the uranium and thorium concentrations in the Japanese upper continental crust are 2.32 ppm and 8.3 ppm, respectively. This result indicates local depletion of incompatible elements in Japan Island Arc compared to the global average. Since the Japan Island Arc accounts for about 75% of the expected geoneutrino flux from upper continental crust and the upper continental crust accounts for about half of the total expected flux, this local depletion of uranium and thorium can reduce the geoneutrino flux about 6.4% and 8.4%, respectively.

2.6.3 Oceanic Crust beneath Sea of Japan

Crust beneath Sea of Japan is classified as oceanic crust. However, it should differ from typical oceanic crust formed at mid-ocean ridges; rather it be similar to continental crust in composition since it was formed by stretching the continental crust at eastern edge of Eurasia. Besides the sediment under Sea of Japan is much thicker than typical oceanic sediment and might be different in composition due tue different geomorphological settings.

This effect is evaluated by assigning the composition of continental crust to the crust beneath Sea of Japan. Even in this extreme case, the total expected geoneutrino flux at KamLAND site is increased by only 2% considering oceanic crust within 1,200 km account for 46% of total oceanic crust contribution and assuming half of them come from Sea of Japan.

2.6.4 Local Geology

The effect of local geology in Japan was studied based on a geological map compiled by Geological Survey of Japan (GSJ), classifying Japan Island Arc into 165 geological groups. Togashi et al. (2000) re-classified GSJ's 165 groups into 37 groups and collected rock samples representing each group. The uranium and thorium concentrations in Japan mentioned in Sec. 2.6.2 were calculated by taking the surface-exposure-weighted average of these groups.

To understand how local geological variation affects the geoneutrino flux estimates at the KamLAND site, three different uranium and thorium concentration map were constructed and compared to each other. In the first method, Homogeneous Japan Arc model, the exposure-average concentrations are assigned over the Japan Island Arc. The second method, Heterogeneous Japan Arc model, assigns concentration of each group to corresponding group in the geological map. In these two methods, the concentration of each group is determined by taking average of all samples belonging to each group. The third method, Kamioka-Area Represented Heterogeneous Japan Arc model, is basically identical to the second method except that the concentration of a few group surrounding the KamLAND site is determined by taking average of samples collected around the KamLAND site.

Comparing these three concentration maps with assumption that the surface geology extends to 5 km in depth, the variation of the geoneutrino flux estimates from nearby upper continental crust is 20% and 16%, respectively for uranium and thorium, which correspond to 3.2% and 2.6% in the total flux estimates.

2.7 Goal of Neutrino Geoscience

This section summarizes the motivation and strategy of "neutrino geoscience". The motivation of neutrino geoscience is to reveal the Earth's heat powering the geodynamics and the Earth's history with geoneutrino as a probe of deep earth.

Great efforts have been made in conventional geoscience to understand how our planet was formed and how it has evolved. Seismology provided the structural modeling of the Earth, i.e. well-known "core-mantle-crust" layers. Cosmochemistry and geochemistry gave compositional estimates of the Earth based on rock samples and chondrite meteorites. Besides, there also be geothermal approach such as heat flux measurement at the surface to verify the geothermal activities of our planet. In spite of various approaches, there still be some open questions such as which type of meteorite formed the Earth, what powers the geodynamics and how many layers the mantle has, since there were no direct test of chemical or thermal properties inside the Earth. Geophysics, geochemistry and cosmochemistry predict different amount of heat producing elements and radiogenic heat based on different rationale, and there are no consensus in conventional geoscience.

Geoneutrino is a key of these questions. Geoneutrino flux is proportional to the abundances of heat producing elements, e.g. uranium, thorium and potassium, in the Earth. The abundance of heat producing elements can be converted to the amount of radiogenic heat in deep earth. Thus, geoneutrino measurement provides a direct test of the radiogenic heat powering the planetary activities. Moreover, geoneutrino measurement also provides an insight into the planet's history. Each heat producing element has different geoneutrino spectrum. Therefore, measuring the abundance of each heat producing element by geoneutrino spectroscopy allows us to test multiple competing compositional models and reveal the raw materials of our planet.

There are three groups of competing estimates for the BSE composition as categorized by Šrámek et al. (2013). The High-Q model (Turcotte and Schubert 2002)

is a geophysical model based on seismological data and geodynamical modeling of realistic mantle convection, requiring relatively large amount of radiogenic heat to drive whole-layer mantle convection; 30–35 TW. The Middle-Q model (McDonough and Sun 1995) is a geochemical model based on compositional analysis of CI carbonaceous chondrite and terrestrial earth samples with consideration of elemental enrichment during planetary differentiation, predicting 17–22 TW of radiogenic heat. The Low-Q model (Javoy et al. 2010) is a cosmochemical estimate based on enstatite chondrite, resulting low radiogenic heat amount of 10–15 TW.

The current targets of neutrino geoscience are summarized as twofold. One is to validate the High-Q model and provide implications for mantle convection structure; the HighQ model requires mantle whole-layer convection, whereas the other two models based on compositional estimates allow mantle multi-layer convection. The other is the identification of the Earth's primordial materials by distinguishing between Middle-Q and Low-Q models.

Chapter 3

KamLAND Experiment

Kamioka **L**iquid-scintillator **A**nti-**N**eutrino **D**etector (KamLAND) is a large-volume neutrino detector located in Kamioka, Japan. KamLAND has better sensitivity for low-energy (sub-MeV) neutrinos compared to water-cherenkov detector as a scintillation detector. This chapter describes the details of the KamLAND detector(Sec.3.2) and neutrino detection method (Sec3.4). Besides, KamLAND-Zen experiment is briefly described in Sec.3.5.

3.1 KamLAND Detector

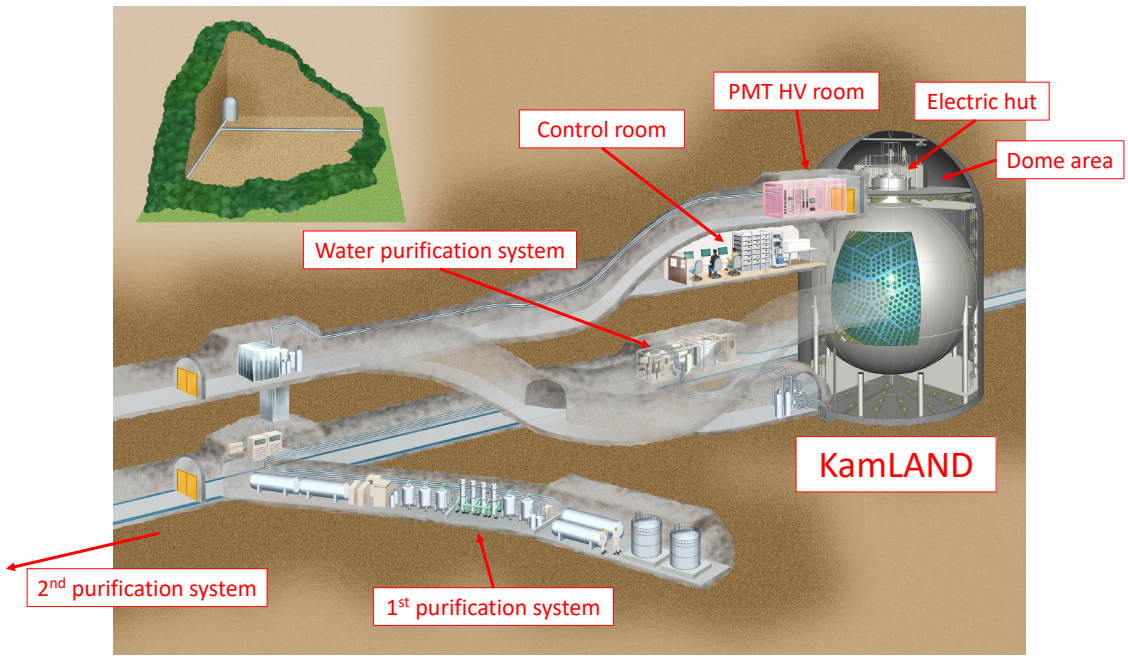

Figure 3.1: KamLAND site overview

The KamLAND detector is located in the Kamioka mine under Mount Ikenoyama at a depth of 2,700 m water-equivalent, where the former detector KamiokaNDE

was placed. The rock overburden effectively suppress the cosmic-ray muon flux by a factor of roughly 10^{-5} with respect to the surface flux. The cosmic-ray muon flux is about 0.34 Hz in the inner detector.

As is shown in Figure 3.1, not only KamLAND and the equipments essential for its operation, i.e. Electric hut and PMT HV/control room, but also the purification equipments necessary to keep the detector in a low-radioactivity environment, i.e. the water purification system and 1st/2nd LS purification system, are located in the same tunnel.

3.2 Detector Design

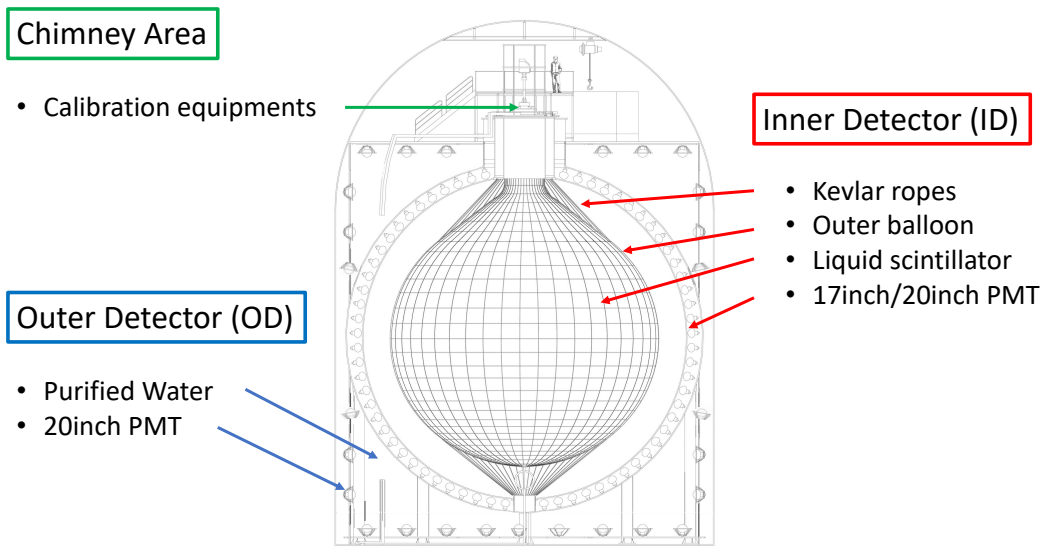

Figure 3.2: Schematic view of the KamLAND Detector

Figure 3.2 show a schematic view of the KamLAND detector. The detector consist of two major layers, the outer detector (OD) and the inner detector (ID), separated by a spherical stainless steel tank of 18.0m diameter.

The outer detector is a 3.2 kt water-cherenkov detector, which provides shielding from external γ-ray backgrounds and an active veto counter.

The inner detector is a 1 kt liquid scintillator detector designed for the detection of anti-electron neutrinos, $\overline{\nu_e}$.

Light produced in the ID (Sec.3.2.2) and OD (Sec.3.2.1) is viewed by the photo-multiplier tubes (PMT, Sec.3.3.1), which concert photons that hit their photo-cathode to electric signals. The PMT signals are sent to read-out electronics and data selected by the trigger system are recorded (Sec.3.3.5).

The KamLAND liquid scintillator (Sec.3.3.2) is purified in 1st/2nd purification system (Sec.3.3.6) to keep a low-radioactivity environment.

The detector calibration (Sec.3.3.7) is performed periodically to suppress the reconstructed vertex and energy biases.

3.2.1 Outer Detector (OD)

The outer detector is a 10 m radium $\times$ 20m hight cylindrical rock cavity with 225 photomultiplier tubes before a refurbishment in 2016 and 140 tubes after the refurbishment(Ozaki and Shirai 2016). It contains about 3.2 kt purified water to provide shielding against γ-rays coming from surrounding rocks. It also provides active muon-veto counter by detecting Cherenkov emission produced by muons going through the OD. The water in the OD is circulated constantly to remove excess heat produced by PMTs in the ID and OD.

3.2.2 Inner Detector (ID)

The inner detector is a 9 m radius spherical stainless steel tank with 1325 17inch PMTs and 554 20inch PMTs mounted on the inner surface. The main volume of the ID is a 1 kt liquid scintillator held by a 6.5 m radius nylon/EVOH balloon installed in the stainless steel tank. Liquid scintillator emits isotropic scintillation light for α, β and γ-rays, which are detected by ID PMTs. The balloon holding the liquid scintillator is called "outer balloon" and described in Sec.3.3.3. Outside the outer balloon is filled with non-scintillating mineral oil called "buffer oil". Another nylon balloon for the KamLAND-Zen experiment is installed at the center of the detector as described in Sec.3.5.

3.3 Detector Components

3.3.1 Photomultiplier Tube (PMT)

PMT is a high time-resolution optical sensor capable of detecting weak optical signals equivalent to one photon.

Figure 3.3 shows the detection process of photons by PMT. When a photon enters the photocathode, electrons (called photoelectrons) are emitted due to the photoelectric effect. The photoelectrons are guided to the dynode by the focusing electrodes, and are amplified in multiple steps among multiple dynode. The amplified electrons are collected at the anode and sent as an electrical signal to the subsequent stage after the low-frequency component is removed by a capacitor. KamLAND uses various types of PMTs to detect scintillation light and Cherenkov light as described below.

ID PMT

The ID has 1325 17inch PMT and 554 20inch PMTs mounted on the inner surface of the stainless steel tank.

The 20inch PMTs (R3600) were originally used in the KamiokaNDE detector and re-used in the KamLAND after the refurbishment for the oil resistant.

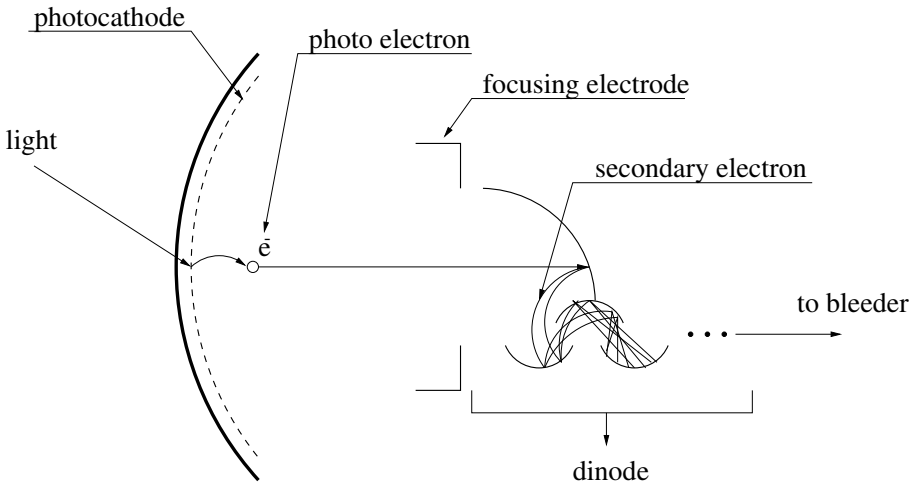

Figure 3.3: Detection process of photons by PMT, A Box&Line type dynode structure is shown.(Tagashira 2000)

The 17inch PMTs (R7250) were developed based on the 20inch PMTs, aiming at considerably improve the charge and time resolution. The biggest difference between the 20inch and 17inch PMT are the dynode structure. The 17inch PMT adopted Box&Line structure (Figure 3.4) for better charge and time resolution, while the 20inch PMTs adopted Venetian-Blind structure (Figure 3.5), which is suitable for large diameter photocathode. Another difference is the area of photocathode. The outer fringe of the 17inch PMT's cathode is masked to obtain better time resolution. The total photo coverage is 34% by 1879 PMTs, 22% by only 17inch PMTs.

The dynode of 17inch PMTs have a 10-step (1-step box and 9-step line) structure, and the low-frequency component is removed (cutoff frequency is ∼2.13 kHz) by a low-frequency cutoff circuit consisting of C7 and R14 in the Figure 3.6.

The quantum efficiency as a function of incident wavelength is shown in Fig3.7. It depends on the material of the photocathode, bialkali, although individual differences exist due to the variation in the thickness of the material. The quantum

The performance of these PMTs are summarized in Table 3.1.

Table 3.1: Summary of the 17inch and 20inch PMT performance(Ozaki 2016)

parameter	17inch PMT	20inch PMT
Photocathode area (ϕ [mm])	430	460
Dynode structure	Box&Line (10 step)	Venetian-Blind (13 step)
Quantum efficiency at 390 nm	22%	23%
transit time [ns]	110	90
transit time spread (FWHM) [ns]	3.5	7.7
Peek-to-Vally ratio	3	1.5
Dark rate [kHz]	22	40

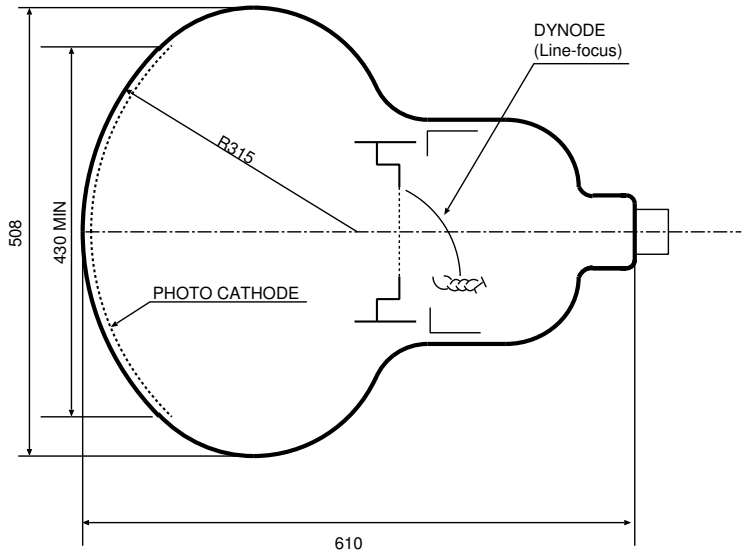

Figure 3.4: Schematic view of 17inch PMT (R7250)

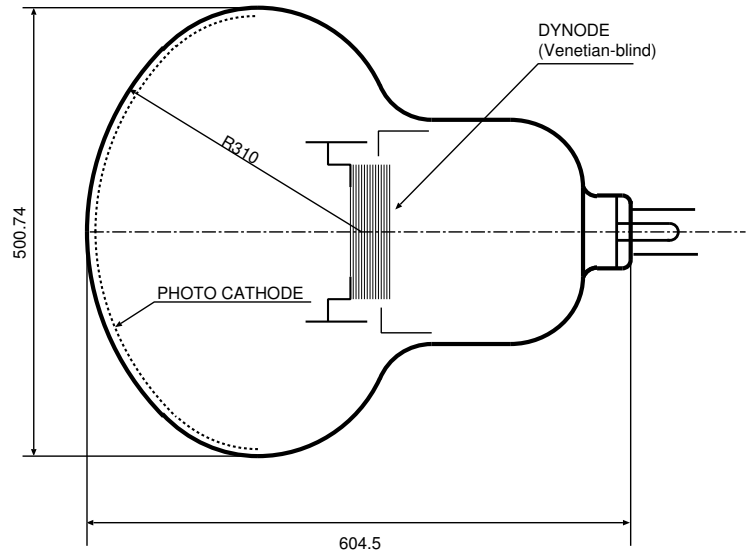

Figure 3.5: Schematic view of 20inch PMT (R3600)

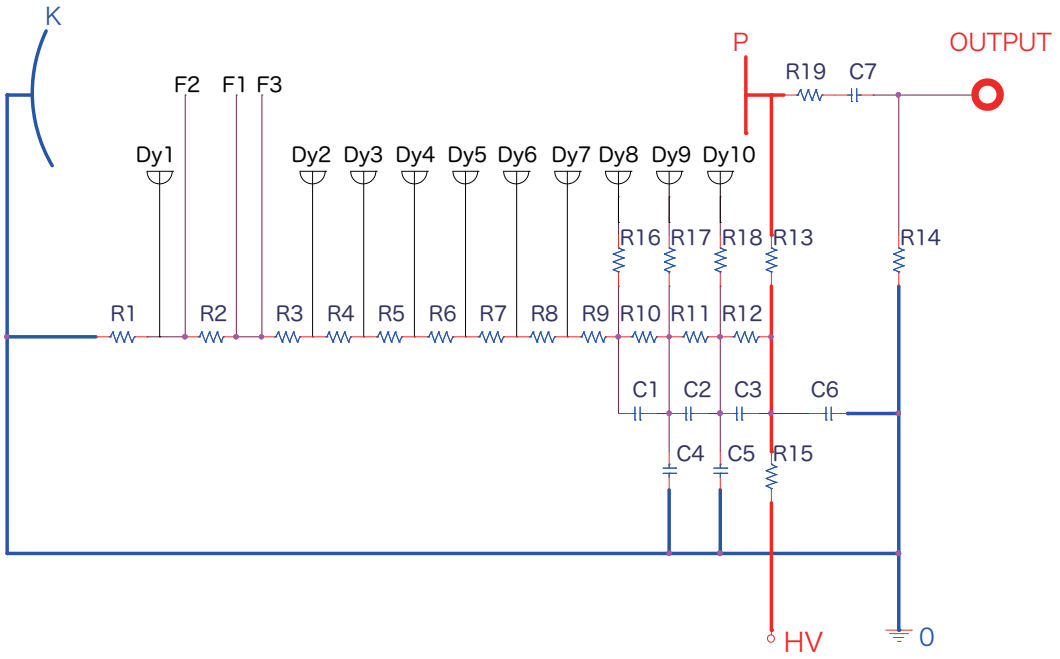

Figure 3.6: Breeder circuit for ID 17inch PMT (R7250) (Takemoto 2009)

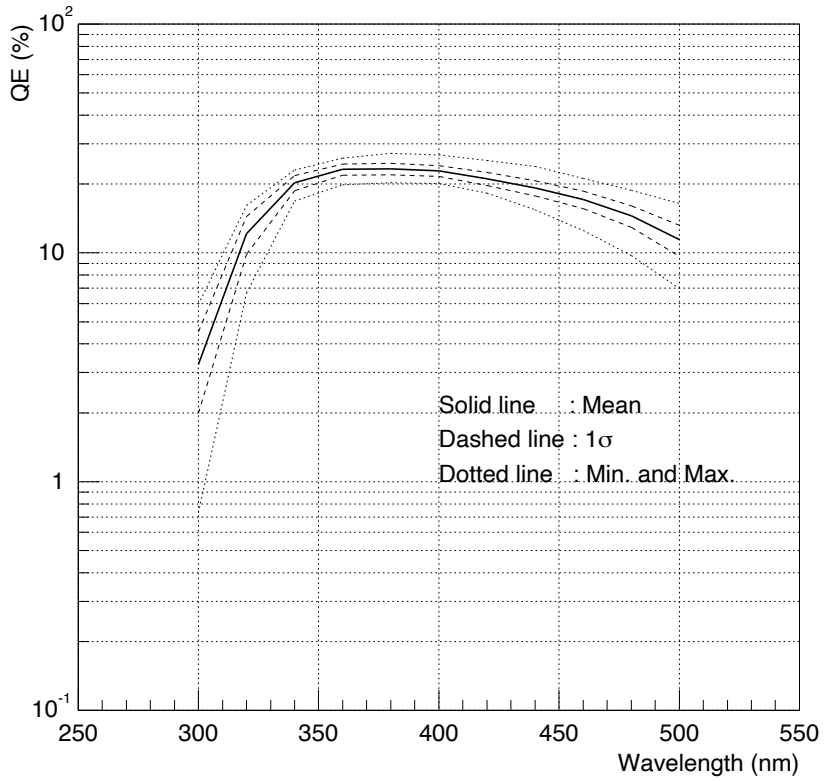

Figure 3.7: Quantum efficiency (QE) of the 17inch PMT as a function of incident wavelength(Tagashira 2000)

OD PMT

In the construction of the detector, 225 OD PMTs (R3600) was inherited from the KamiokaNDE detector. In 2016, the OD was refurbished and 225 OD PMTs were replaced with 140 new OD PMTs.

The new OD PMTs, R3600-06MOD, is the same model as used in the Super-Kamiokande detector but with higher quantum efficiency.

The schematic view of PMT and the diagram of breeder circuit are shown in Figure 3.8 and Figure 3.9, respectively. The performance of OD PMTs and OD HQE PMTs are summarized in Figure 3.2.

Table 3.2: Summary of the OD 20inch PMT performance(Ozaki 2016)

parameter	OD PMT	OD HQE PMT
Photocathode area (ϕ [mm])	460	
Dynode structure	Venetian-Blind (11 step)	
Quantum efficiency at 390 nm	20–21%	32%
transit time [ns] (representative)	95	
transit time spread (FWHM) [ns] (average)	5.9	
Peek-to-Vally ratio	1.6	
Dark rate [kHz]	17	25

3.3.2 Liquid Scintillator (LS)

A scintillator is a material that emits light upon radiation and is widely used as an important component of radiation detectors. When radiation deposits energy to the scintillator and excites it, it emits light in an isotropic direction when it is de-excited. The radiation can be detected by capturing this light with an optical sensor. The light emitted by the scintillator is called "scintillation light". Scintillation light is brighter than the Cherenkov light emitted when charged particles exceed the speed of light in water due to radiation. Therefore, compared to detectors such as Super-Kamiokande that use Cherenkov light, KamLAND, which uses scintillation light, is sensitive to lower energies.

Liquid scintillators, as the name implies, are liquids that perform as scintillators. They are used in numerous experiments that involve radiation detection. Liquid scintillators were also used in the experiment of F. Reines and C.L. Cowan Jr, which was the first ever to successfully detect neutrinos(Reines and Jr. 1956, Cowan et al. 1956). Compared to solid scintillators, liquid scintillators are superior in that they can be purified by liquid-liquid extraction or distillation, which makes it possible to achieve an extremely low-radioactivity environment.

The ID is filled with about 1200 m^3 of liquid scintillator. The KamLAND liquid scintillator is basically a mixture of long chain and aromatic ring hydrocarbons with an H:C proportion of ~ 2 where hydrogen is the target of $\overline{\nu_e}$ detection. Table3.3 shows the composition of the KamLAND liquid scintillator. The solvent of the KamlAND liquid

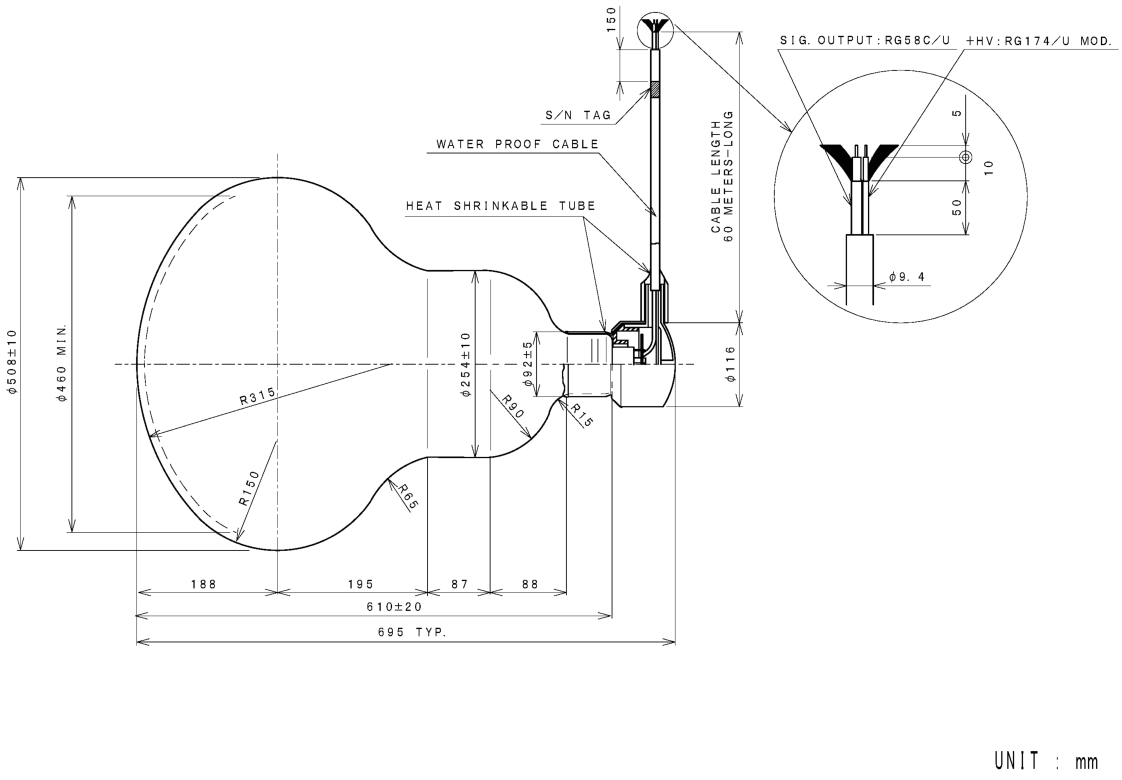

Figure 3.8: Schematic view of OD HQE PMT (R3600-06MOD). Figure is brought from Ozaki (2016). The original data is provided from Hamamatsu Photonics K.K.

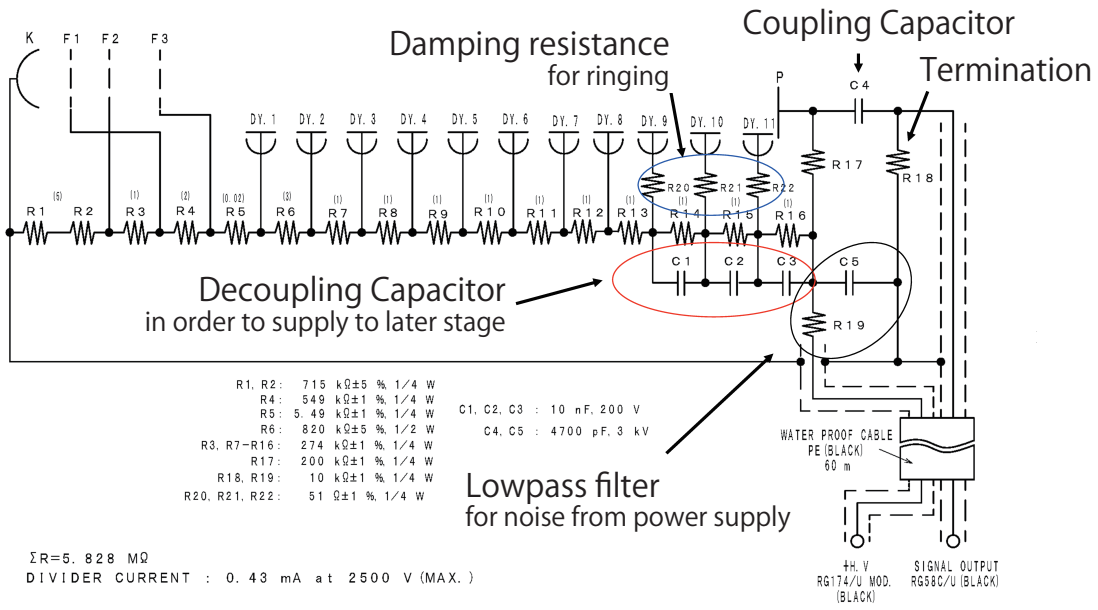

Figure 3.9: Breeder circuit for OD HQE PMT (R3600-06MOD). Figure is brought from Obara (2018). The original data is provided from Hamamatsu Photonics K.K.

scintillator is Pseudocumene, and PPO is added as a luminescent agent Dodecane plays a role in preventing a decrease in the transmittance and in adjusting the density. Though the mixture of Pseudocumene and PPS can work as liquid scintillator, the transmittance becomes so low that scintillation light cannot effectively reach the PMTs, which makes it unsuitable for use in KamLAND.

Table 3.3: Composition of the KamLAND liquid scintillator(Obara 2018)

Material	Chemical formula	Density	Volume ratio
Dodecane (N-12)	$C_{12}H_{26}$	0.749 g/cm^3	80%
Pseudocumene (1,2,4-Trimethylbenzen)	C_9H_{12}	0.875 g/cm^3	20%
PPO (2,5-Diphenyloxazole)	$C_{15}H_{11}NO$	-	1.36 g/l
Liquid scintillator		0.77721 g/cm^3	-

The KamLAND liquid scintillator is purified by liquid-liquid extraction and distillation to remove radioactive impurities. Assuming radiative equilibrium of ^{214}Bi-^{214}Po in the U series and ^{212}Bi-^{212}Po in the Th series, the concentration of ^{238}U is evaluated to be less than $(5.2 \pm 0.2) \times 10^{-18}$g/g and that of 232Th is less than $(1.3 \pm 0.1) \times 10^{-17}$g/g(Gando et al. 2015).

Figure 3.10 shows the transmittance and emission spectrum of the KamLAND liquid scintillator. The peak wavelength of the emission is around 375 nm, and the KamLAND liquid scintillator has high transmittance in that region.

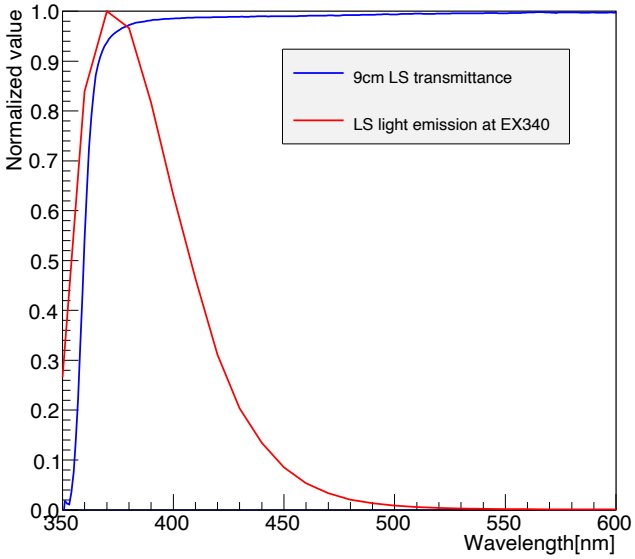

Figure 3.10: KamLAND LS transmittance (blue) and emission (red) spectrum

3.3.3 Outer Balloon and Kevlar Ropes

The KamLAND liquid scintillator is supported by a 13 m diameter spherical balloon called "outer balloon". This balloon is the key component of the detector which isolates the liquid scintillator from the external buffer oil (Sec.3.3.4). Thus, the outer balloon need to have high transparency to light with wavelength 350–500 nm, chemical compatibility with both the liquid scintillator and buffer oil, low radioactivity, impermeability to Rn and mechanical strength to maintain the spherical shape of liquid scintillator. The outer balloon is made of 5-layer composite film of EVOH(25 μm)/Nylon(15 μm)/Nylon/Nylon/EVOH, where the total thickness is 135 μm. Nylon is adopted because of its excellent strength, and EVOH is added since it can effectively precent the permeation of radon and oxygen. The outer balloon consists of 44 gores welded with each other, and the light transparency is more than 90%.

The outer balloon is hanged by 44 Kevlar ropes to stabilize its position. The Kevlar is made of para-aramid fiber, whose excellent strength is suitable for KamLAND.

The radioactivity in the outer balloon film and Kevlar ropes are summarized in Table 3.4.

Table 3.4: Radioactivity in the outer balloon film and Kevlar ropes(Watanabe 2012)

	U	Th	^{40}K
– Outer balloon film –			
concentration [ppb]	0.018	0.014	0.27
radioactivity [Bq]	0.02	0.006	7.2
– Kevlar rope –			
concentration [ppb]	0.08	0.08	1.2
radioactivity [Bq]	0.1	0.33	31

3.3.4 Buffer Oil

The space between the PMT array and the liquid scintillator is filled with mineral oil. This layer is called "buffer oil". The composition of the KamLAND buffer oil is shown in Table 3.5. Buffer oil is supporting the outer balloon and the liquid scintillator. In addition, the buffer oil is preventing the liquid scintillator from emitting light due to radiation derived from radioactive impurities in the ID stainless steel tank and PMTs.

The buffer oil is divided into two layers by a 3 mm thick acrylic panel, i.e. the inner layer in contact with the nylon balloon and the outer layer in contact with the PMT. This is to prevent radioactive impurities derived from the PMT glass from diffusing into the detector. The acrylic panel also serves to prevent the spread of damage by scattering debris around the PMT in the event of its implosion in the ID.

Table 3.5: Composition of the KamlAND buffer oil(Obara 2018)

Material	Chemical formula	Density	Volume ratio
Dodecane (N-12)	$C_{12}H_{26}$	0.749 g/cm^3	53%
Isoparaffin (Paraol 250)	C_nH_{2n+2}	0.795 g/cm^3	48%
Buffer oil		0.7769 g/cm^3	-

3.3.5 Electronics and Data-acquisition System

The analog signal output from the PMT is digitized and recorded in an electric hat on top of the detector. In KamLAND, the two data acquisition systems are operated quasi-independently by two electronic circuits, KamFEE and MoGURA, as shown in Figure 3.11. The KamFEE data acquisition system (KamDAQ) has been in operation since the construction of the KamLAND detector, and the analysis of the antineutrino observation is mainly based on the data acquired by this system. The MoGURA data acquisition system (MogDAQ) was added to compensate for the weakness of KamFEE when the KamLAND-Zen experiment was started, and is used to detect neutron capture events immediately after a muon event, taking advantage of its dead-time-free circuit with a 1 GHz flash ADC.

Since MoGURA does not cover the full dataset of this study, the this study is based on the data only from KamDAQ. MoGURA electronics was well studied in Takemoto (2009). Kawada (2020) also describes the details of MogDAQ.

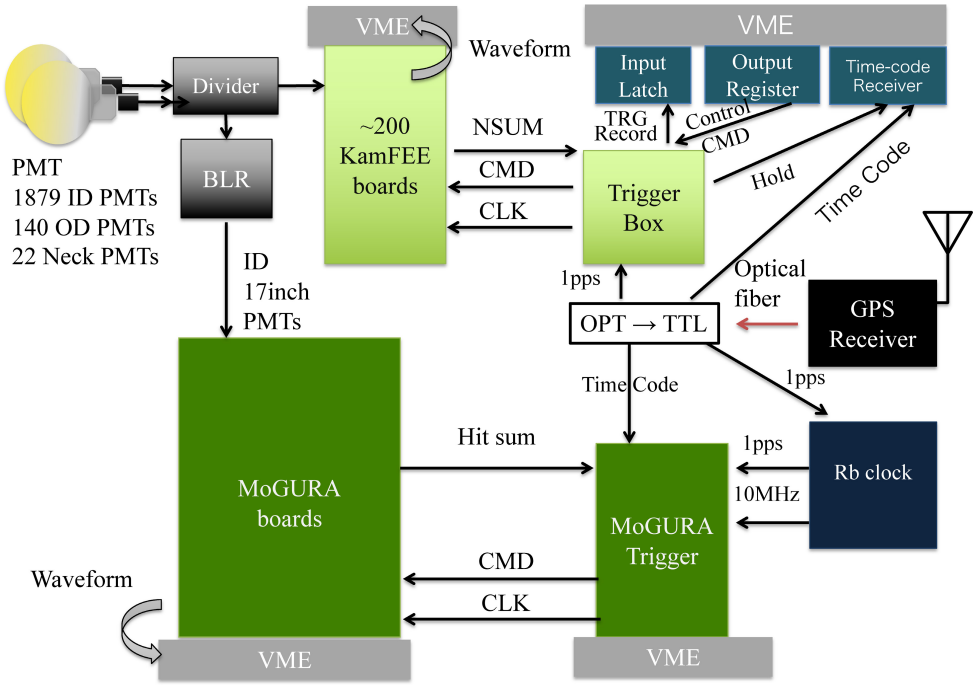

Figure 3.11: Configuration of KamLAND DAQ system (Ozaki 2020)

KamDAQ is the primary data acquisition system of the KamLAND detector, which consists of KamFEE ATWD board and KamFEE Trigger module.

These component is described below.

KamFEE ATWD board (KamFEE)

KamLAND **F**ront-**E**nd **E**lectronics ATWD (KamFEE) board is a data acquisition circuit originally developed for the KamLAND detector.

All PMT signals of KamLAND are connected to KamFEE board as shown in Figure 3.12, which is operated as the primary read-out circuit of KamLAND as described above. Each KamFEE board has 12 input channels, and about 200 KamFEE boards are in operation in KamLAND(Enomoto 2005).

Figure 3.13 shows the analog signal path in the KamFEE board. The incoming analog signal is divided into two parts, one of which is sent to the discriminator for hit detection. The other goes through a delay and is amplified by various gains before being sent to an ADC chip called "Analog Transient Waveform Digitizer (ATWD)", where it is stored as an analog signal in a capacitor array inside the ATWD.

The PMTs output a wide range of signals from single photoelectron signal to more than 10^5 photoelectrons signal. In order to record all of these signals with high resolution, the PMT signal is divided into three parts and sent to amplifiers with different amplification gains. These amplification gains are set to x20, x4, and x0.5. If the signal passing through the amplifier with the higher amplification gain reaches the upper limit of ATWD's dynamic range, the signal passing through the amplifier with the lower amplification gain is digitized.

The hit information determined by each channel's discriminator is sent to the KamFEE Trigger module. The KamFEE Trigger module issues data acquisition commands to the KamFEE boards based on the delivered hit information. The KamFEE boards that received the data acquisition command digitize the analog signals stored in the capacitor array in the ATWD, and record them in a on-board memory.

Data recorded in the on-board memory is sequentially transferred to an external computer via VME. The VME can also be used to set various parameters and send commands related to DAQ control.

KamFEE Trigger module

Hit information sent from the KamFEE boards is aggregated in the the KamFEE Trigger module. Based on the number of hits across KamLAND within a certain time window, the data acquisition command is issued to the KamFEE boards to record the signals. In normal operation, digitization and data recording are performed only on channels for which the discriminator detects a hit, but force acquisition triggers that force digitization on all channels for calibration, etc., and PPS triggers used for baseline analysis, etc., are also issued as needed.

The KamLAND Trigger system has various types of triggers. The details are described in Enomoto (2005). Here, four trigger types which is related to this study

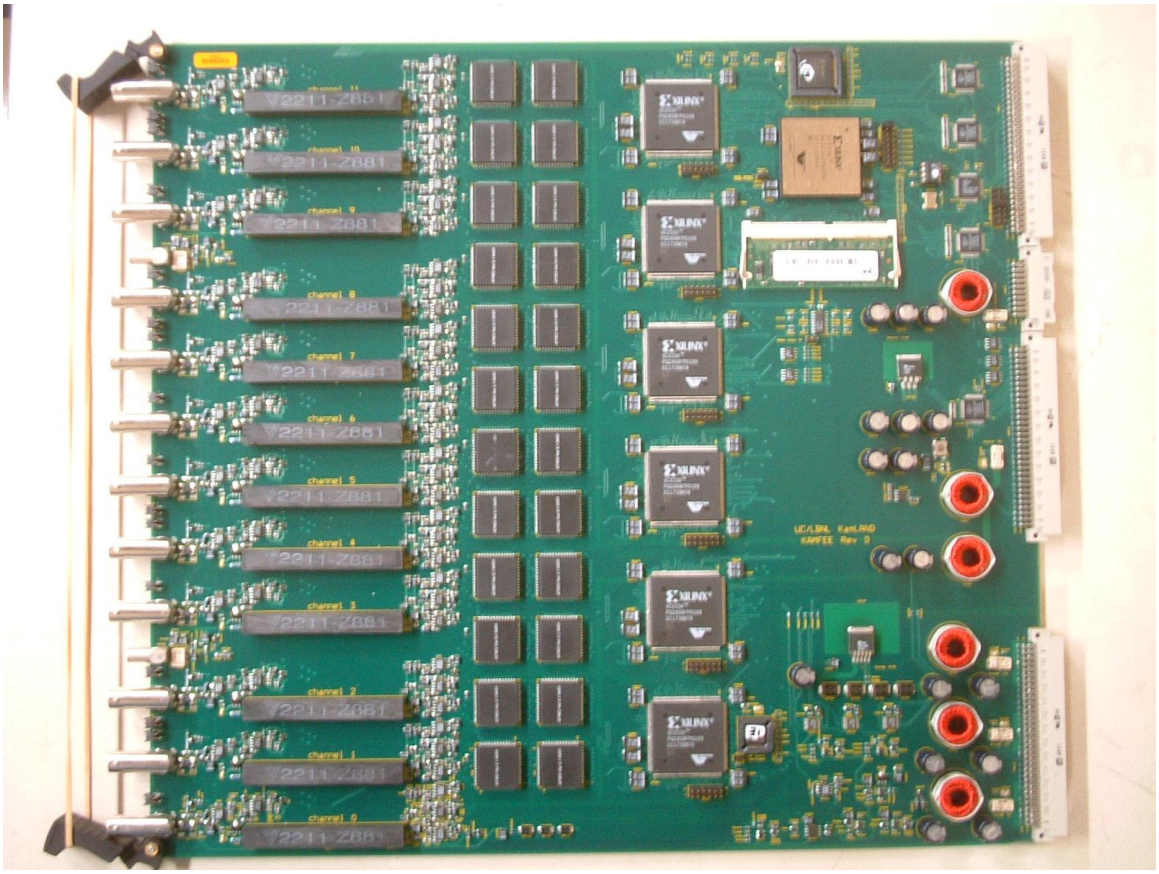

Figure 3.12: Shematic view of KamFEE ATWD board (Enomoto 2005)

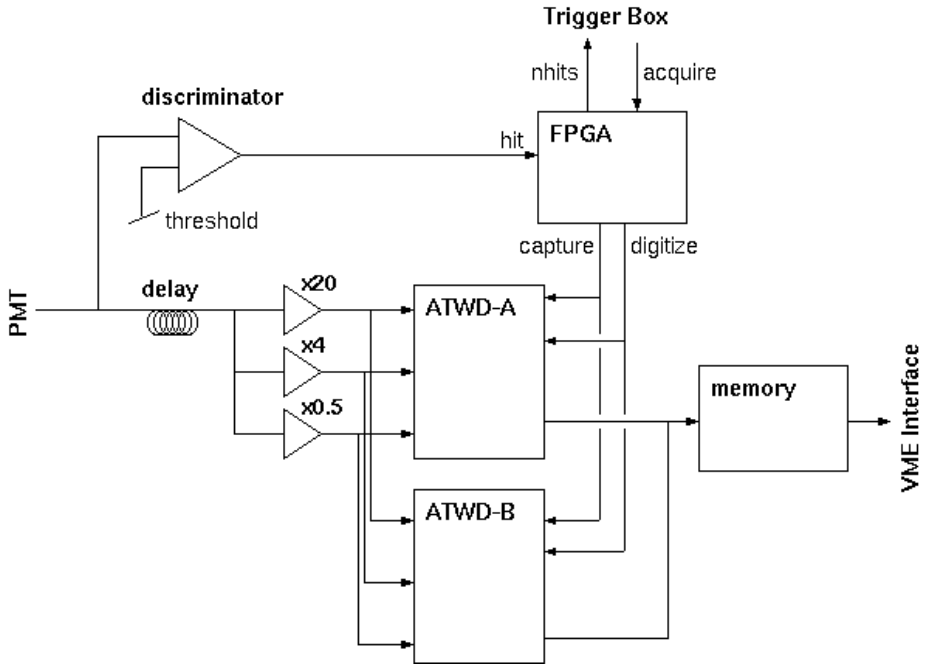

Figure 3.13: Analog signal path in the KamFEE ATWD board (Enomoto 2005)

is mentioned.

The most important trigger in normal physics run is prompt trigger. This trigger is issued when NSum excesses a preset "prompt trigger threshold", where Nsum refers to the number of ID 17inch PMT hit in a 125 ns time window. Following evergy prompt trigger, another trigger "delayed trigger" is activated for 1ms and issued when Nsum excesses a preset "delayed trigger threshold". These two triggers are implemented to efficiently detect time correlated events. Therefore, the delayed trigger threshold is set lower than the prompt trigger threshold for the study of low-energy background such as ^{214}Po, ^{212}Po and ^{85}Kr.

Prescale trigger is another important trigger. This trigger is a thinning trigger with a lower threshold than delayed trigger threshold, and used for low-energy (high rate) event studies, e.g. source calibration and solar neutrino. Prescale trigger is also used to estimate the trigger efficiencies of delayed trigger.

The threshold values of above three triggers are set and changed considering the status of the detector, e.g. the purifications, mini balloon installation and other on-site activities, and background studies. Figure 3.14 show the time variation of trigger thresholds. The efficiencies and their uncertainties are discussed later in Sec.5.6.2.

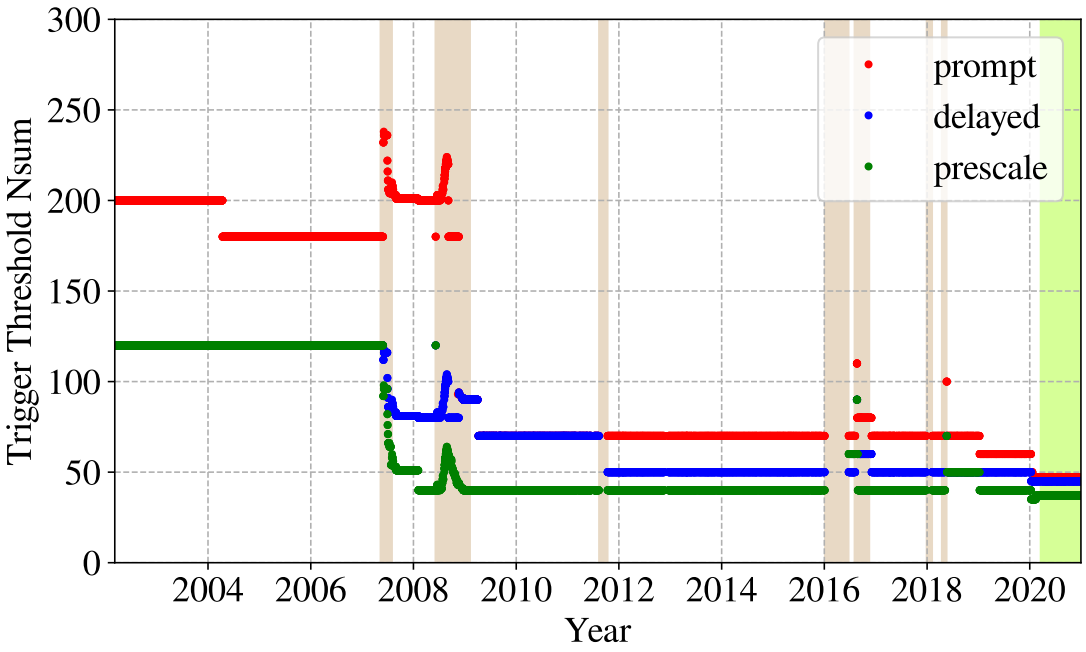

Figure 3.14: Time variation of Nsum threshold for various trigger types.

Not only ID hit but also OD hit contribute the trigger decision. OD-to-ID trigger is issued when the number of OD hit excesses presets threshold, regardless of Nsum in ID. This trigger is useful for studying OD-correlated event such as fast neutron.

Besides, the Trigger module contains a 40 MHz system clock synchronized with GPS, which is distributed to all the KamFEE boards to add time information to

the data packets. This time information to reconstruct events is used in the offline analysis, i.e. the event reconstruction and physics discussion.

3.3.6 Purification System

Low-radioactivity of the detector components is an essential requirement for the KamLAND experiment. Aiming at detecting anti-neutrino signal, whose detection rate is expected to be about 1 event/day, the background rate need to be suppressed to < 0.1 event/day. To achieved this target, concentration of ^{238}U, ^{232}Th, ^{40}K in the liquid scintillator have to be $< 10^{-14}$ g/g, $< 10^{-14}$ g/g, $< 10^{-15}$ g/g, respectively.

During the construction of the KamLAND detector, the liquid scintillator and the buffer oil were purified by the liquid-liquid extraction method and the nitrogen purge method as shown in Figure 3.15 in the "1st purification system".

However, further purification were needed for low-energy solar neutrino studies. Although ^{85}Kr and ^{210}Pb are not effectively removed by the 1st purification system, they make serious backgrounds for solar neutrino observations and also for the anti neutrino observations called $^{13}\mathrm{C}(\alpha, n)^{16*}\mathrm{O}$ reaction. To remove these radioactive impurities in the liquid scintillator, the "2nd purification system" was built and further purification by the distillation was performed twice, from 2007 March to 2007 August (1st purification campaign) and from 2008 July to 2009 February (2nd purification campaign).

This section briefly describes the purification systems for KamLAND. The details are described in Nakajima (2009).

The 1st Purification System

The schematic view of the 1st purification system is shown in Figure 3.15. The 1st purification systems consists of the liquid-liquid extraction tower, or "Water extraction" in Figure 3.15, and the nitrogen purge tower.

The liquid-liquid extraction traps heavy metal element, e.g. uranium, thorium, potassium and radium dissolved in the LS materials with purified water. These elements dissolve better in the water, i.e. polar molecules, than in the LS materials, i.e. non-polar molecule.

After passing liquid-liquid extraction tower, the materials are sent to the nitrogen purge tower. This stage is implemented to remove remnant water from the liquid-liquid extraction tower, which decrease the transparency and light yield of the liquid scintillator. Oxygen, which cause a decrease of the light yield by quenching, is also removed in this stage. In addition, some noble gas elements, radon, argon and krypton, are purged to reduce the background for the anti neutrino detection.

The radioactivity measurement result before and after the 1st purification is summarized in Table 3.6. The raw LS material are measured by the ICP-MS, whereas the mixture, i.e. the KamLAND liquid scintillator, was measured by the KamLAND itself. The radioactive impurities were reduced by a factor of $\mathcal{O}(10^{-5})$.

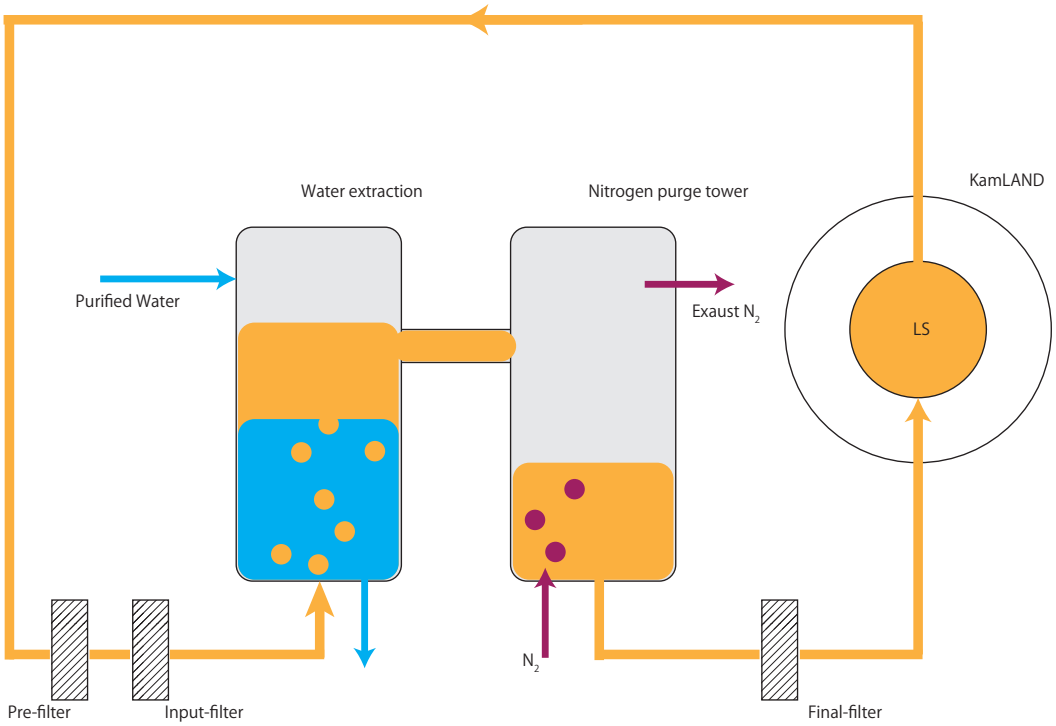

Figure 3.15: Schematic view of the liquid-liquid extraction system for KamLAND. The liquid-liquid extraction is shown as "water extraction"(Obara 2018)

Table 3.6: Radioactivity measurement result before and after the 1st purification(Nakajima 2009)

Material	^{238}U [g/g]	^{232}Th [g/g]	^{40}K [g/g]
– before 1st purification –			
Pseudocumene (1,2,4-Trimethylbenzen)	$\leq 10^{-13}$	-	-
Dodecane (N-12)	$\leq 10^{-13}$	$\leq 6 \times 10^{-12}$	$\leq 1.2 \times 10^{-12}$
Isoparaffin (Paraol 250)	3×10^{-13}	$\leq 6 \times 10^{-12}$	-
PPO (2,5-Diphenyloxazole)	1.2×10^{-13}	$\leq 5 \times 10^{-11}$	$\leq 5.3 \times 10^{-11}$
– after 1st purification –			
mixture (LS)	$(3.4 \pm 0.4) \times 10^{-18}$	$(5.7 \pm 0.8) \times 10^{-17}$	$\leq 2.7 \times 10^{-16}$
target level	$\leq 10^{-14}$	$\leq 10^{-14}$	$\leq 10^{-15}$

The 2nd Purification System

Figure 3.16 shows the schematic view of the 2nd purification system. The distillation is a powerful method to remove radioactive isotopes, which cannot be extracted in the 1st purification system, e.g. ^{85}Kr and ^{210}Pb. Reduction of ^{210}Pb is especially important for the anti neutrino observation because it feed ^{210}Po in its decay series. The $^{13}\mathrm{C}(\alpha, n)^{16*}\mathrm{O}$ reaction caused by α-particle from ^{210}Po was one of the most major backgrounds for the geo-neutrino observation. The purification campaigns were performed totally over 9 months from 2007 to 2009. The total amount of distilled LS was more than 5000 [m^3], corresponding to three full-volume exchange of the KamLAND liquid scintillator.

The distillation procedure in the 2nd purification system is as follows.

1. The liquid scintillator is drawn from the detector and sent to the buffer tank with 1.5 [m$^3/h$].

2. The liquid scintillator is distilled into three distillation towers, whose pressure and temperature are well controlled. The radioactive impurities are removed in this stage.

3. The distilled materials are sent to the mixing tank and mixed to adjust a density with the accuracy of 10^{-3} [g/cm^3].

4. The mixed liquid scintillator is sent to the nitrogen purge tower, where the noble gas contamination is purged by nitrogen supplied by 30 [m$^3/h$]

5. The purified liquid scintillator is filled into the detector after checking the PPT concentration, the ^{222}Rn/^{85}Kr concentration, and the transparency.

3.3.7 Calibration Equipment

The KamLAND data is corrected and verified using various kind of sealed radiation sources as shown in Table 3.7. The source calibration has been performed periodically before the start of the KamLAND-Zen experiments (Sec.3.5). Instead of the periodical source calibrations, the muon-spallation products and neutron capture events after the muon events are used to confirm the detecter stability.

For precise measurement of the fiducial volume uncertainties, a full-volume calibration called "4-π calibration" is performed. Calibration sources attached to a segmented pole (Figure 3.17) is installed in the detector so that the source can go elsewhere in the detector as shown in Figure 3.18. The details of 4-π calibration is summarized in Berger et al. (2009).

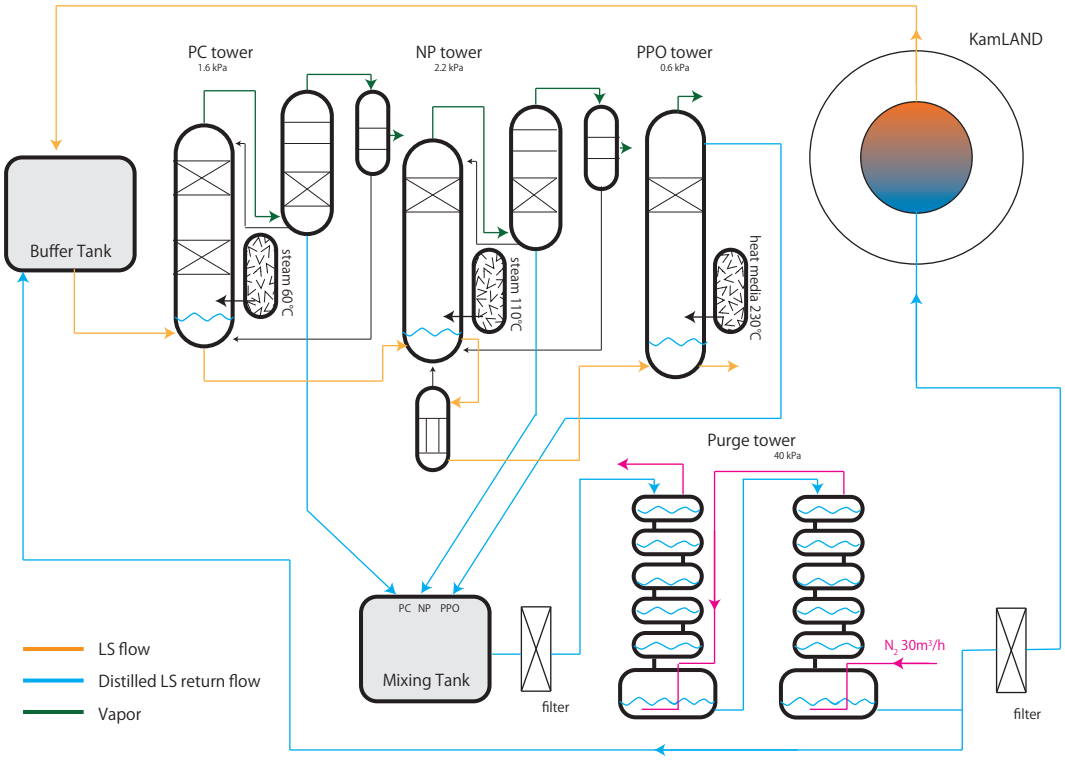

Figure 3.16: Schematic view of the distillation system for KamLAND(Obara 2018)

Table 3.7: KamLAND calibration sources with their primary decay type and its corresponding real energy(Watanabe 2012)

source	particle type	energy [MeV]	half life
^{208}Hg	γ	0.2792	46.612 d
^{137}Cs	γ	0.6616	30.07 y
^{65}Zn	γ	1.1116	244.3 d
^{68}Ge	2γ	0.551×2	270.8 d
^{60}Co	γ	1.732, 1.3325	5.271 y
^{241}Am^{9}Be	γ,n	γ:4.4,n:$<$ 10	432 y
^{210}Po^{13}C	γ,n	γ:6.13,n:$<$ 7.5	22 y

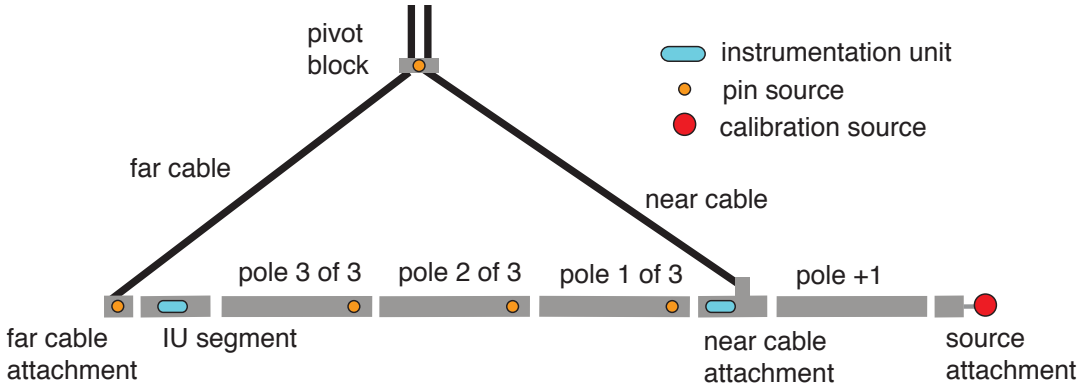

Figure 3.17: Schematic diagram of the main component of the 4-π calibration(Berger et al. 2009)

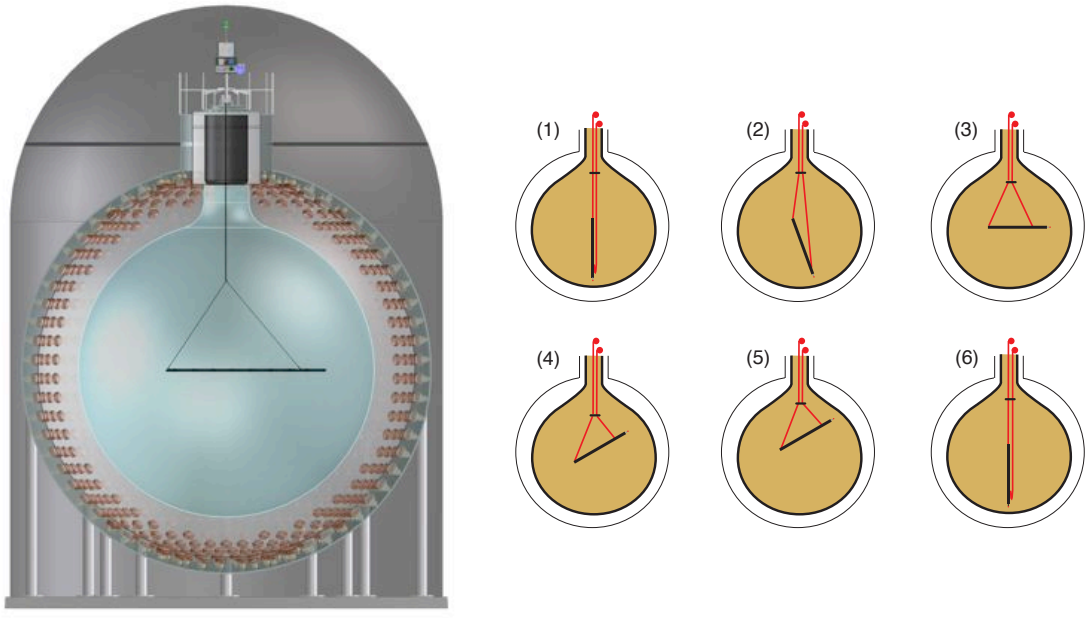

Figure 3.18: Illustration of the 4-π calibration(Berger et al. 2009)

3.4 Neutrino Detection Channel

3.4.1 Inverse-Beta Decay

Anti-electron neutrinos can be detected via the inverse-beta decay as shown in Eq.3.1.

$$p + \bar{\nu_e} \rightarrow n + e^+ \tag{3.1}$$

The positron generated in this reaction annihilates an electron as in Eq.3.2, and emits two annihilation γ-rays. The liquid scintillator emits scintillation light due to the energy deposit by e^+ and the two γ-rays, which is the prompt signal shown in Figure 3.19.

$$e^+ + e^- \rightarrow 2\gamma \tag{3.2}$$

On the other hand, neutrons are captured by protons (hydrogen nuclei in the liquid scintillator) and emit 2.2 MeV γ-ray as shown in Eq.3.3 with a lifetime of 210 μs. The scintillation light emission of the liquid scintillator by this "capture γ-ray" is the delayed signal shown in Figure 3.19.

$$n + p \rightarrow d + \gamma \tag{3.3}$$

Exploiting the time-spacial correlation between the prompt and delayed signal, we can observe anti-electron neutrinos in an almost background-free condition.

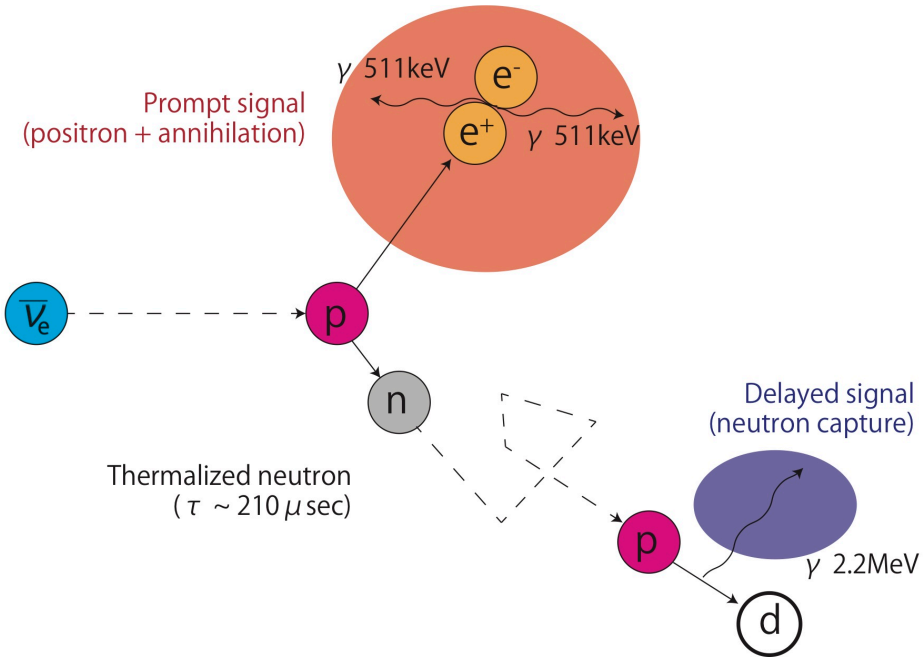

Figure 3.19: Anti-electron neutrino detection via the inverse-beta decay

Another advantage of this reaction channel is the ability to reconstruct the energy of the incident anti-electron neutrino from the observed prompt energy. With the energy of incident neutrino, E_ν, and the kinetic energy of generated positron (neutron),

$T_e(T_n)$, the conservation of energy low for Eq.3.1 can be written as

$$E_\nu + m_p = T_e + m_e + T_n + m_n \tag{3.4}$$

where m_e, m_n and m_p are the mass of electron, neutron and proton, respectively. Then, the observed energy from the prompt signal, E_{prompt} is written as

$$\begin{aligned} E_{prompt} &= T_e + 2m_e \\ &= E_\nu + m_p + m_e - T_n - m_n \\ &= E_\nu - T_n - 0.783 \text{ [MeV]} \end{aligned} \tag{3.5}$$

and this gives the relation between the prompt energy and the incident neutrino energy as

$$E_\nu = E_{prompt} + T_n + 0.783 \text{ [MeV]}. \tag{3.6}$$

The kinetic energy of neutron (T_n), i.e. the thermalization of the neutron, is quenched and ignorable in the observation of sub-MeV energy neutrinos as shown in Figure 3.20.

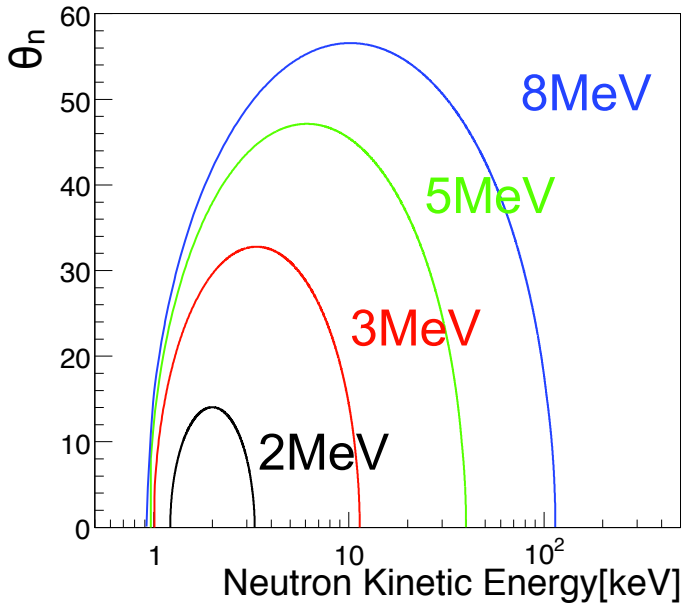

Figure 3.20: The correlation between the neutron kinetic energy and the scattering angle, θ_n, for various incident neutrino energies (different colors)(Watanabe 2012)

In spite of the advantages described above, there is a reaction threshold for inverse beta decay, and neutrinos with energies below the threshold cannot be detected by this channel.

Denoting the lowest anti-electron neutrino energy at which inverse beta decay occurs as $E_\nu^{threshold}$, the conservation of invariant mass in Eq.3.1 can be written as

$$(m_p + E_\nu^{threshold})^2 - (E_\nu^{threshold})^2 = (m_n + m_e)^2 \tag{3.7}$$

and it gives

$$E_\nu^{threshold} = \frac{(m_n + m_e)^2 - m_p^2}{2m_p} \approx 1.806 \text{ [MeV]} \tag{3.8}$$

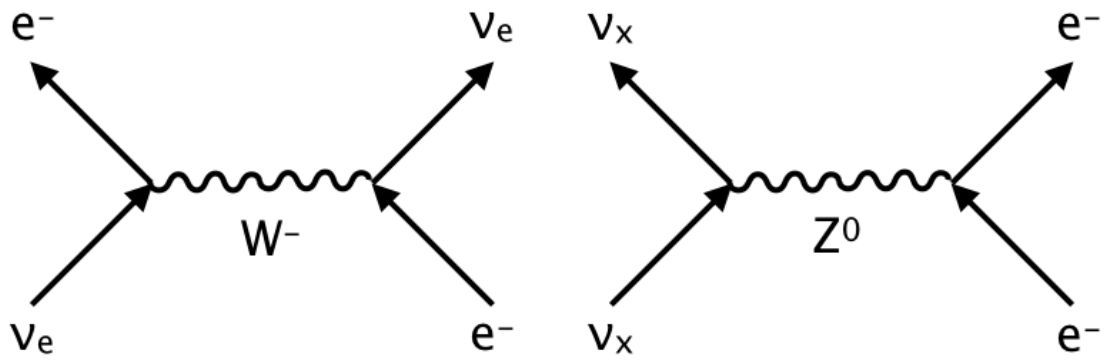

Figure 3.21: Feynman diagram of Charged-Current (left) and Neutral-Current (right) interaction(Kawada 2020)

3.4.2 Electron Scattering

Another neutrino detection channel used in KamLAND is the electron scattering. Electron scattered by neutrino like Eq.3.9 deposit energy to the liquid scintillator, and make a scintillation light emission, whereas the prompt scintillation of inverse beta decay channel is accompanied by a delayed scintillation.

$$\nu_x + e^- \rightarrow \nu_x + e^- \qquad (x = e, \mu, \tau) \tag{3.9}$$

Since electron scattering makes only one scintillation, background rejection by the delayed coincidence strategy cannot be applied. Therefore, the signal is verified by removing the background event from the obtained energy spectrum and the spectrum fitting.

It is advantage of this channel to have sensitivity to neutrinos of all flavors. It is also advantageous that there are no reaction threshold. In KamLAND, this reaction channel is used in the studies mainly of astrophysical neutrinos, e.g. ^{7}Be solar neutrino(Gando et al. 2015), ^{8}B solar neutrino(Abe et al. 2011b), solar flare neutrino(Abe et al. 2022).

Electron scattering can be classified into two categories, i.e. Charged-Currect (CC) and Neutral-Currecnt (NC) reactions as shown in Figure 3.21. Muon and tau neutrinos can occur only neutral-current reactions, while electron neutrinos also interact by charged-current reactions. Therefore, the reaction cross section is largest for electron neutrinos.

3.5 KamLAND-Zen experiment

KamLAND-Zen (KamLAND Zero-neutrino double-beta decay search) is an experiment to search for neutrinoless double beta decays ($0\nu\beta\beta$) by introducing ^{136}Xe, a double beta decay nucleus, into KamLAND.

The first phase of the experiment using about 380 kg of xenon (KamLAND-Zen400) gave the world's most stringent limit on the effective Majorana mass of

neutrinos(Gando et al. 2013b, 2016). In 2018, the KamLAND-Zen experiment was upgraded to kamLAND-Zen800 by doubling the amount of xenon, and it is still in operation(Takeuchi 2022).

During the KamLAND-Zen periods described below, the region with ^{136}Xe double-beta decay source is excluded from the effective volume of anti-neutrino observation to prevent backgrounds from the decay source itself and supporting structures.

This section briefly describes the KamLAND-Zen experiment.

3.5.1 Motivation of $0\nu\beta\beta$ Search

Majorana Neutrino

Observations of neutrino oscillations have shown that neutrinos have non-zero mass. Since the Dirac particle acquires its mass through the coupling of a right-handed particle and a left-handed particle, the Dirac mass of neutrino must be extremely small compared to other elementary particles for which only left-handed neutrinos and right-handed antineutrinos have been experimentally confirmed(Goldhaber et al. 1958).

A theoretical interpretation that naturally explains the extremely small mass of neutrino is that neutrino is Majorana particle that acquire mass by a different mechanism than the Dirac particle. The Majorana particle is a subatomic particle formulated by E. Majorana, which acquires mass by the coupling of a left(right)-handed particle and a right(left)-handed antiparticle. It also has the property that the particle and the antiparticle are identical (Majorana neutrino). If neutrino is Majorana particle, the seesaw mechanism may explain why neutrinos have extremely small mass compared to other elementary particles.

$0\nu\beta\beta$ search

The most realistic and most effective way of verifying the Mayorana nature of neutrinos is thought to be the detection of $0\nu\beta\beta$.

Beta decay is the decay of a neutron to a proton in a nucleus, emitting an electron and a neutrino, and is described by Eq.3.10.

$$(Z, A) \rightarrow (Z + 1, A) + e^- + \bar{\nu}_e \tag{3.10}$$

Beta decay does not occur unless the energy level of the nucleus after decay is lower than that of the original nucleus, so not all nuclei undergo beta decay. However, some nuclei for which beta decay is prohibited can transition to a lower energy level by undergoing two simultaneous beta decays (Eq.3.11), which is called double beta decay ($2\nu\beta\beta$). So far, $2\nu\beta\beta$ has been directly observed in 10 different nuclei. The Feynman diagram of $2\nu\beta\beta$ is shown in Figure 3.22.

$$(Z, A) \rightarrow (Z + 2, A) + 2e^- + 2\bar{\nu}_e \tag{3.11}$$

If the neutrino is a Majorana particle, then double beta decay without neutrinos is allowed, as in Eq.3.12. Since this decay does not conserve lepton number and

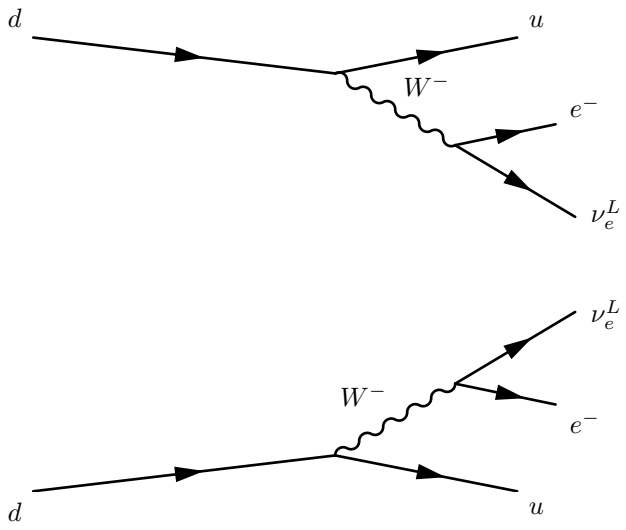

Figure 3.22: Feynman diagram of double-beta decay

only occurs if the neutrino is a Majorana particle, the observation of $0\nu\beta\beta$ is a proof of the Majorana nature of neutrinos. The Feynman diagram of $0\nu\beta\beta$ is shown in Figure 3.23.

$$(Z, A) \rightarrow (Z + 2, A) + 2e^- \tag{3.12}$$

If we can prove that neutrinos are Majorana particles by observing $0\nu\beta\beta$, we can explain why neutrinos have extremely small masses compared to other elementary particles. In addition, if it is found that neutrinos violate the law of lepton number conservation, it is expected that the leptogenesis theory can reveal the process by which the matter-dominated universe was formed(Fukugita and Yanagida 1986). Furthermore, it is possible to obtain a limit on the effective Majorana mass of the neutrino from its decay rate, i.e. the rate of $0\nu\beta\beta$, $(T^{0\nu}_{1/2})^{-1}$, can be written as

$$(T^{0\nu}_{1/2})^{-1} = G^{0\nu} \left|M^{0\nu}\right|^2 \langle m_{\beta\beta}\rangle^2 \tag{3.13}$$

$$\langle m_{\beta\beta}\rangle \equiv \left||U^L_{e1}|^2 m_1 + |U^L_{e2}|^2 m_2 \mathrm{e}^{i\phi_2} + |U^L_{e3}|^2 m_3 \mathrm{e}^{i\phi_3}\right| \tag{3.14}$$

where $G^{0\nu}$ is the phase space factor, $M^{0\nu}$ is the nuclear matrix elements, $\langle m_{\beta\beta}\rangle$ is the effective Majorana mass of neutrino, $\mathrm{e}^{i\phi_2}$ and $\mathrm{e}^{i\phi_3}$ are the Majorana CP phase, and $U^L_{ej}(j = 1, 2, 3)$ are the mixing matrix elements. Besides, since each neutrino mass hierarchy has a different range of acceptable neutrino effective Majorana masses, it may be possible to determine the mass hierarchy from measurements of neutrino effective Majorana masses.

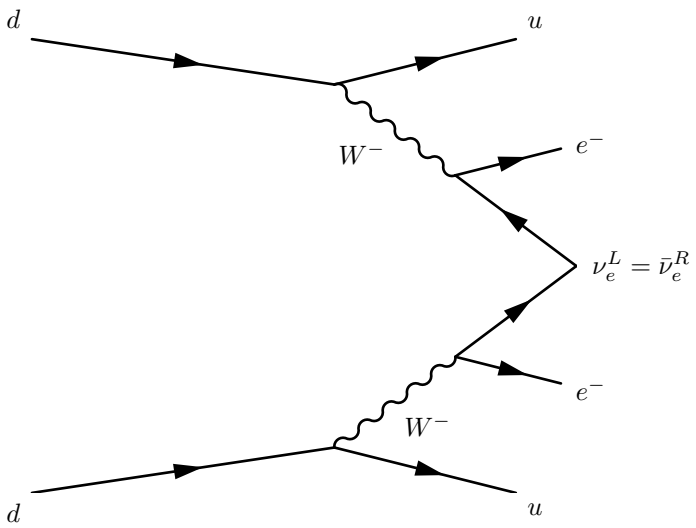

Figure 3.23: Feynman diagram of neutrinoless double-beta decay

3.5.2 KamLAND-Zen

$0\nu\beta\beta$ is an extremely rare phenomenon, and an extremely low radioactivity environment with few background events is essential for its observation. In addition, it is desirable to use as many double beta decay nuclei as possible to achieve high sensitivity. From these points of view, KamLAND, which is a large detector that has originally realized an extremely low radiation environment, is a suitable detector for $0\nu\beta\beta$ search.

A schematic diagram of the KamLAND-Zen experiment is shown in Figure 3.24. The double beta decay nucleus, ^{136}Xe, is dissolved in a liquid scintillator and held at the center of the detector by a nylon balloon called "mini balloon".

Xenon-loaded liquid scintillator

Examples of nuclide that undergo double beta decay with Q-values above 2 MeV are listed in Table 3.8. Among these, ^{136}Xe is superior in the points described below and has been adopted as a double beta decay nucleus for use in KamLAND-Zen.

- chemical stability and ease to handle
- solubility into liquid scintillator and transparency after dissolution
- relatively high natural abundance and established enrichment method by centrifugation
- purifiability by distillation
- possibility of extraction from liquid scintillator

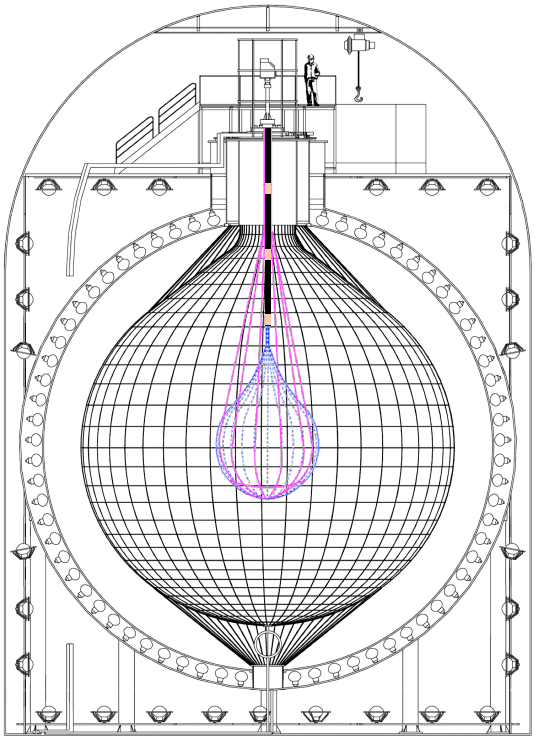

Figure 3.24: Schematic diagram of KamLAND-Zen experiment, The mini balloon shown in this figure is that for KamLAND-Zen800

- relatively long half life of $2\nu\beta\beta$

Table 3.8: Examples of nuclide that undergo double beta decay(Zuber 2004, Olive 2014)

nuclide	Q-value [keV]	natural abundance (%)	$2\nu\beta\beta$ half life $T^{2\nu}_{1/2}(\times 10^{21}\mathrm{yr})$
^{48}Ca	4274 ± 4	0.187	$(4.4^{+5}_{-4} \pm 0.4) \times 10^{-2}$
^{76}Ge	2039.04 ± 0.16	7.8	$(1.84^{+0.14}_{-0.10})$
^{82}Se	2995.5 ± 1.3	9.2	$(9.6 \pm 0.3 \pm 1.0) \times 10^{-2}$
^{96}Zr	3347.7 ± 2.2	2.8	$(2.35 \pm 0.14 \pm 0.16) \times 10^{-2}$
^{100}Mo	3034.40 ± 0.17	9.6	$(7.11 \pm 0.22 \pm 0.54) \times 10^{-3}$
^{116}Cd	2809 ± 4	7.5	$(2.8 \pm 0.1 \pm 0.3) \times 10^{-3}$
^{130}Te	2527.01 ± 0.32	34.5	$(0.7 \pm 0.09 \pm 0.11)$
^{136}Xe	2457.83 ± 0.37	8.9	$(2.165 \pm 0.016 \pm 0.059)$
^{150}Nd	3367.7 ± 2.2	5.6	$(9.11^{+0.25}_{-0.22} \pm 0.63) \times 10^{-3}$

Xenon is concentrated by centrifugation to a ^{136}Xe isotope enrichment of $90.77 \pm 0.08\%$, dissolved in liquid scintillator and introduced into KamLAND. The liquid scintillator containing enriched xenon is called "xenon-loaded liquid scintillators (XeLS)", whereas the liquid scintillators that have been originally filled in KamLAND are called "KamLAND liquid scintillators (KamLS)" to distinguish them.

The composition of XeLS is shown in Table 3.9. The quenching effect of dissolved xenon reduces the light yield of the liquid scintillator, and it is compensated for by adding more PPO, the luminescent agent, in the XeLS than in the KamLS. In addition, the density of XeLS and KamLS should be adjusted to be equivalent to reduce the load on the mini-balloon, which will be described later. Therefore, instead of dodecane used in KamLS, decane with a lower density is used.

Table 3.9: Composition of the xenon-loaded liquid scintillator. The density is without xenon. The values are for KamLAND-Zen800(Takeuchi 2022)

Material	Chemical formula	Density	Volume ratio
Decane (N-12)	$C_{10}H_{22}$	0.735 g/cm^3	82.4%
Pseudocumene (1,2,4-Trimethylbenzen)	C_9H_{12}	0.875 g/cm^3	17.6%
PPO (2,5-Diphenyloxazole)	$C_{15}H_{11}NO$	-	2.38 g/l
xenon	Xe	-	3.13 wt%

Mini balloon

Since the main background events of KamLAND-Zen, such as those originating from spallation products and ^{8}B solar neutrinos, are proportional to the volume of the liquid scintillator, it is effective to maintain a high concentration of xenon, which

emits the signal, in order to increase the signal-to-noise ratio. In addition, xenon nuclei should be kept near the center of the detector to avoid background events due to γ-rays from the rock outside the detector.

For these reasons, the XeLS is held at the center of the detector by a 25 μm thick nylon balloon (mini balloon). The diameter of the mini balloon is 3.08 m for KamLAND-Zen 400 and 3.84 m for KamLAND-Zen 800 with increased xenon. To prevent contamination of KamLAND with radioactive impurities, the mini balloon was hand-made by heat-welding nylon film. The shape of the mini balloon is shown in Figure 3.25.

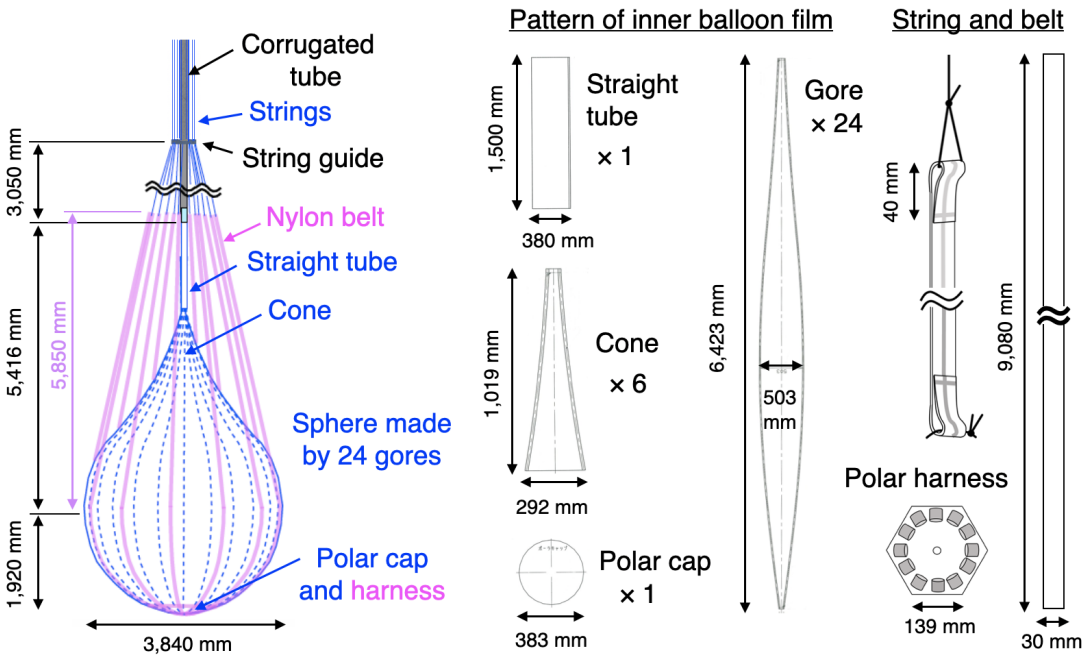

Figure 3.25: Schematic view of the mini balloon for KamLAND-Zen800(Gando et al. 2021)

KamLAND-Zen 400

The first phase of KamLAND-Zen experiment with approximately 380 kg of xenon, KamLAND-Zen 400, was performed from October 2011 to December 2015. At the beginning of the experiment, it was found that ^{110m}Ag, which creates background events in the $0\nu\beta\beta$ energy region, was unexpectedly contaminated. From June 2012 to November 2013, the XeLS was purified through liquid-liquid extraction and distillation. The observation period of KamLAND-Zen 400 was divided into 1st and 2nd period before and after this purification work. Figure 3.26 and Figure 3.27 show the observed energy spectrum in KamLAND-Zen 400.

The combined 1st and 2nd period analysis of the KamLAND-Zen 400 yields a limit of $(T^{0\nu}_{1/2})^{-1} > 1.07\times10^{26}$ yr (90% C.L.) for the half-life of the $0\nu\beta\beta$ of ^{136}Xe. From this,

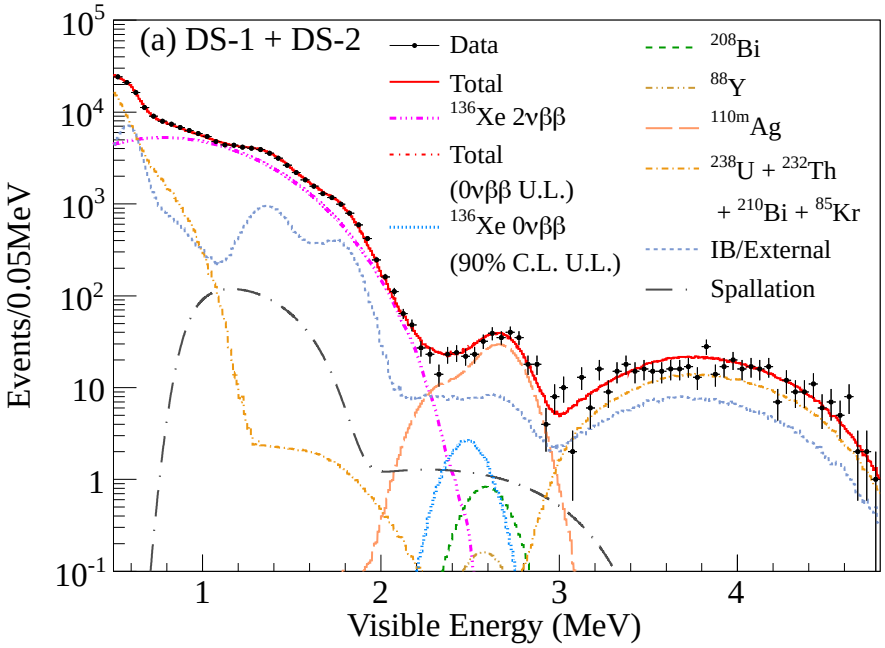

Figure 3.26: Observed energy spectrum in KamLAND-Zen400 1st period

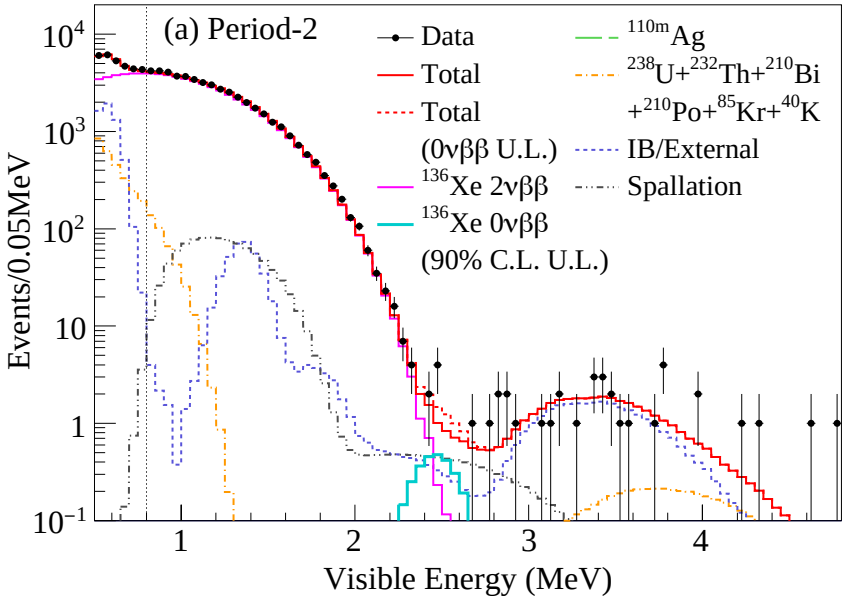

Figure 3.27: Observed energy spectrum in KamLAND-Zen400 2nd period

the limit of the neutrino effective Majorana mass was given to be $\langle m_{\beta\beta} \rangle < (61 - 165)$ meV (Gando et al. 2016).

KamLAND-Zen 800

The second phase of KamLAND-Zen experiment with approximately 745 kg of xenon, KamLAND-Zen 800, started in January 2019. For increasing the amount of xenon, a new mini-balloon larger than the one used for KamLAND-Zen 400 was created.

In August of 2016, a new mini-balloon was introduced into KamLAND, but it was found to be leaking and was removed without xenon installation. After retrieval, multiple holes were found on the weld line of the mini-balloon. The welding method was reviewed and the mini balloon was re-created by a renewed method (Gando et al. 2021). The installation process was performed again in May 2018. No leakage was confirmed on this installation, and over the next six months, the detector was purified by distillation circulation and the xenon was installed. The preparation of KamLAND-Zen 800 was completed on the first day of 2019.

Figure 3.28 shows the observed energy spectrum in KamlAND-Zen 800. This observation gives the upper limit of $(T^{0\nu}_{1/2})^{-1} > 1.98 \times 10^{26}$ yr (90% C.L.) for the half-life of the $0\nu\beta\beta$ of ^{136}Xe. The combined analysis of KamLAND-Zen 400 2nd period and KamLAND-Zen 800 improve the upper limit to $(T^{0\nu}_{1/2})^{-1} > 2.25 \times 10^{26}$ yr (90% C.L.) as shown in Figure 3.29. The 90% C.L. upper limit on the effective Majorana mass obtained from this combined result is $\langle m_{\beta\beta} \rangle < (36 - 156)$ meV as shown in Figure 3.30(Takeuchi 2022).

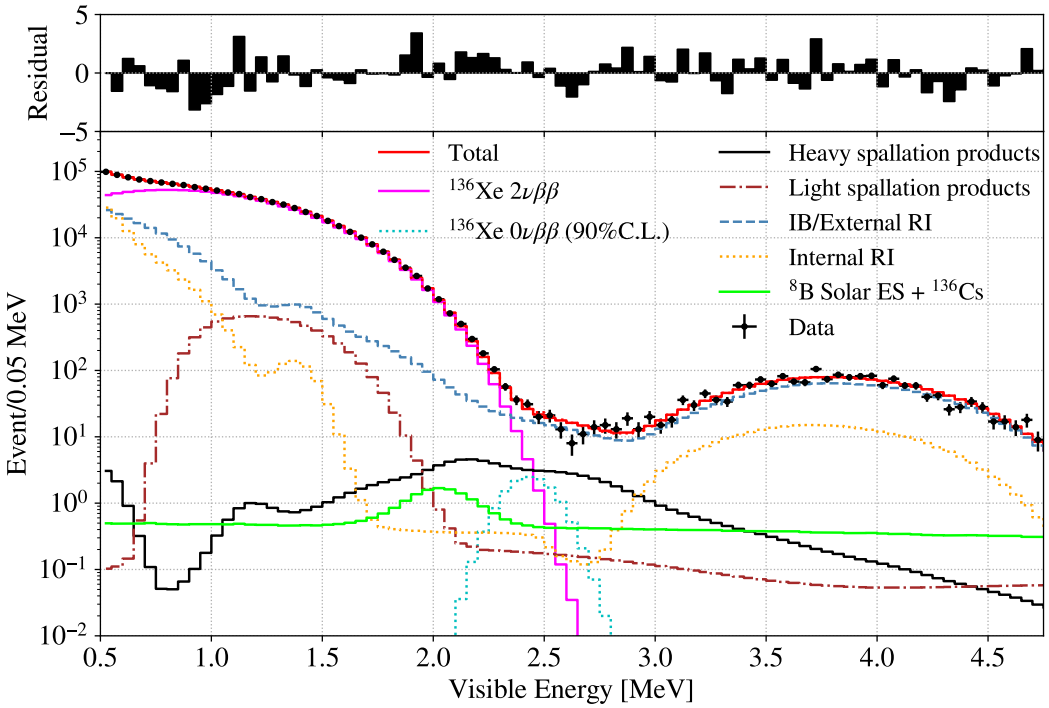

Figure 3.28: Observed energy spectrum in KamLAND-Zen 800 (Takeuchi 2022)

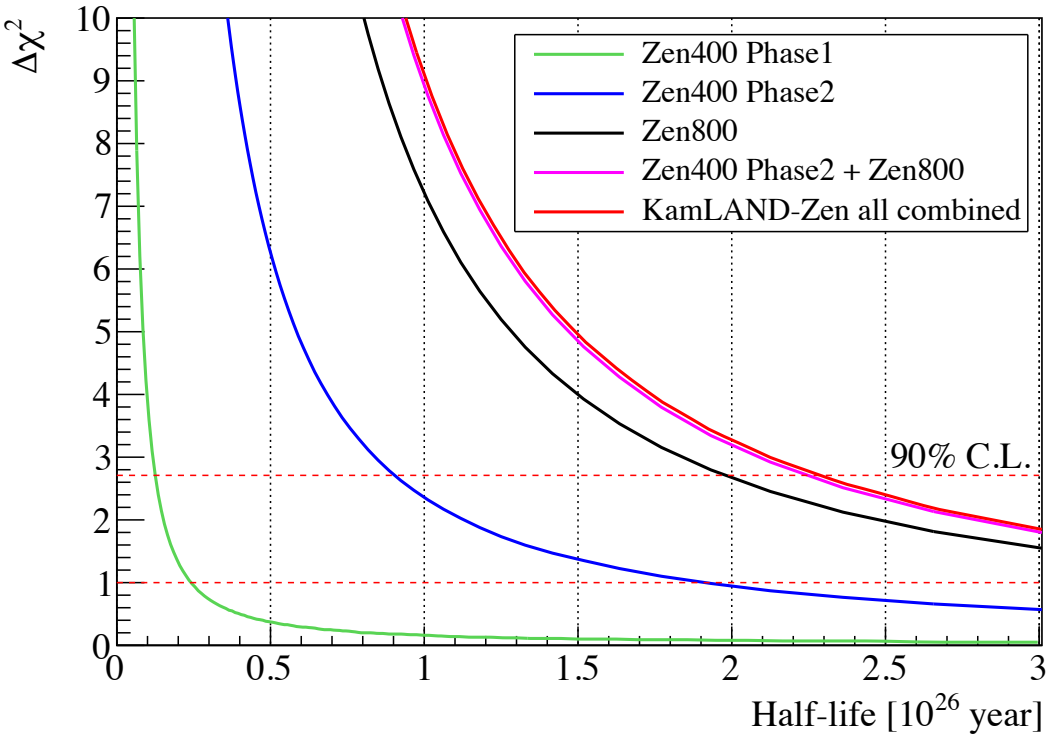

Figure 3.29: $\Delta\chi^2$ plot against the $0\nu\beta\beta$ half life(Takeuchi 2022)

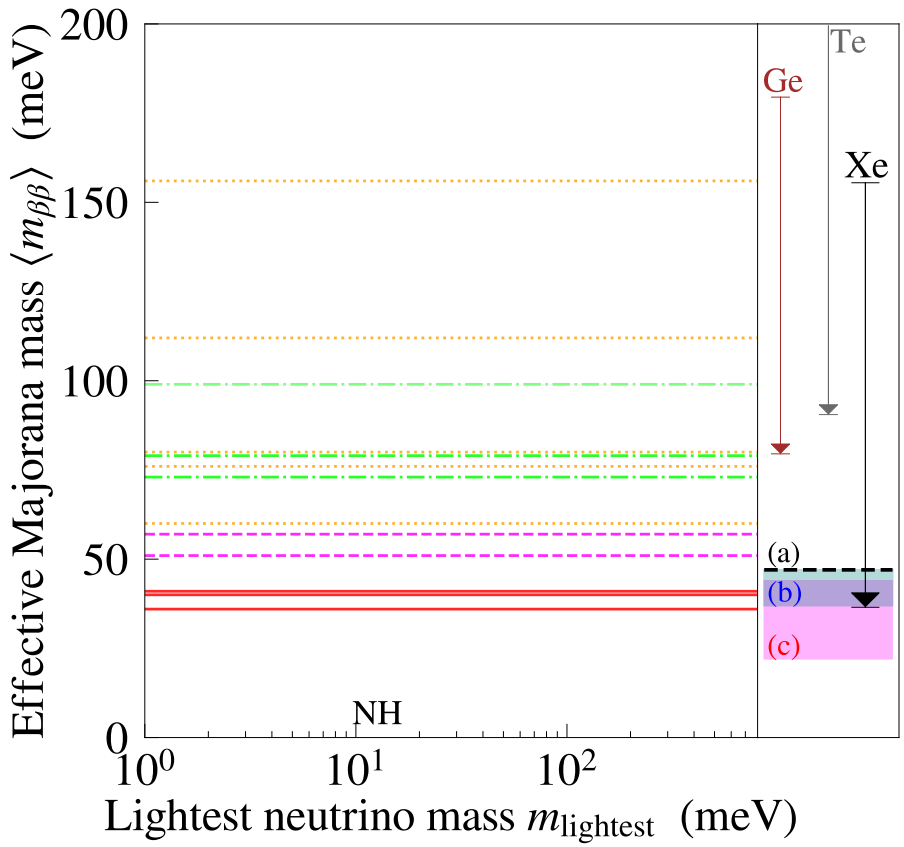

Figure 3.30: Allowed region of neutrino effective Majorana mass as a function of the lightest neutrino mass(Takeuchi 2022)

Chapter 4

Event Reconstruction and Detector Calibration

The KamLAND detector observe scintillation light by 1,879 PMTs mounted on the inner surface of the ID. Scintillation events are divided into two classification: track-like events and point-like events. Cosmic-ray muons with GeV-scale energies go through KamLAND with $\tilde{0}.3$ Hz. KamLAND detect those muon as $\mathcal{O}(10^3) <$ photo-electron large scintillation events called track-like scintillation. Tagging these large scintillation as muon and reconstructing the muon track are important to understand muon-related background correctly. On the other hand, reactor/geo neutrino interaction, radioactive impurities backgrounds, muon-spallation products and other miscellaneous backgrounds with typically MeV-scale energies are detected as isotropic light emission called point-like event. Non-physical event such as electrical noise can be contaminated in the physical scintillations. So it is necessary to identify physics events from the raw data. Energy and vertex information is a key of understanding backgrounds correctly and observe anti-neutrino signal precisely. So, it is also necessary to understand the reconstruction quality and their uncertainties correctly. The procedure and quality of event reconstruction are discussed in this chapter.

4.1 Overview of Event Reconstruction

The procedure of event reconstruction is as follows:

1. Waveform Analysis (Sec.4.2)
   PMT hit-timing and observed number of photoelectron (charge) is extracted from PMT waveform data.

2. Time and Charge Calibration and data-quality check of each PMTs (Sec.4.3 and Sec.4.4)
   The signal transit time and the size of waveform vary among PMTs, which need to be calibrated using a pulse dye-laser and observed charge distribution, respectively. To improve event reconstruction quality, bad-status and unstable PMTs are excluded from the event reconstruction.

3. Muon Identification and Track Reconstruction (Sec.4.6)
   Muon track is reconstructed from the first photon hit timing.
4. Point-like event reconstruction (Sec.4.7)
5. Vertex/Energy calibration and reconstruction quality check (Sec.4.8)

4.2 Waveform Analysis

The hit timing and charge information is extracted from PMT waveform. In KamLAND, A waveform consists of 128 ADC count samples of which the sampling frequency is about 1.49 ns, which is almost the same as the transit time spread (TTS) of the 170-inch PMTs.

The analog buffer of ATWD for each PMTs have different offset levels. It also varies for each waveform samples. To evaluate these offsets, the "pedestal" waveform are acquired at the beginning of each runs, and subtracted from PMT signal waveform so that the baseline of waveform are adjusted to be zero. Then, the waveforms are smoothed to reject high-frequency noise using an algorithm which calculates an average first derivative.

The procedure of extracting hit timing and charge from waveform data is shown in Figure 4.1. At first, the maximum ADC count point is searched for and defined as "peak" of the waveform. Then, the nearest zero coefficient before and after the peak are defined as "leading edge" and "trailing edge", respectively. The hit timing of the waveform refers to the absolute time of the leading edge. Finally, the waveform is integrated from the leading edge to the trailing edge, and the integral is defined as the charge of the waveform. If a waveform sample has multiple peaks, this procedure is applied for each peaks separately. In this case, the leading edge of the first pulse is assigned as the hit timing of waveform.

4.3 Time and Charge (TQ) Calibration

4.3.1 TQ Correction

Different PMTs have different cable lengths, different signal paths on the electronics and different signal latencies, therefore, it is necessary to evaluate the signal transition time of each PMTs.

Figure 4.2 shows the schematic view of the dye-laser calibration system to evaluate it. A dye-laser pulse (width $\sim$1.2 ns) is sent to the diffuser ball installed at the center of the detector via an optical fiber. The laser is also sent to a 2-inch PMT for monitoring and issuing the force trigger to KamFEE. The wavelength of the laser is chosen to be 500 nm to suppress inconvenient absorption and re-emission in the liquid scintillator. The laser intensities can be changed from a single photoelectron level to about 5000 photoelectron level.

The signal latencies are different among PMTs due to different PMT gains and FEE responses. It also varies by the charge of input signal. The correlations between

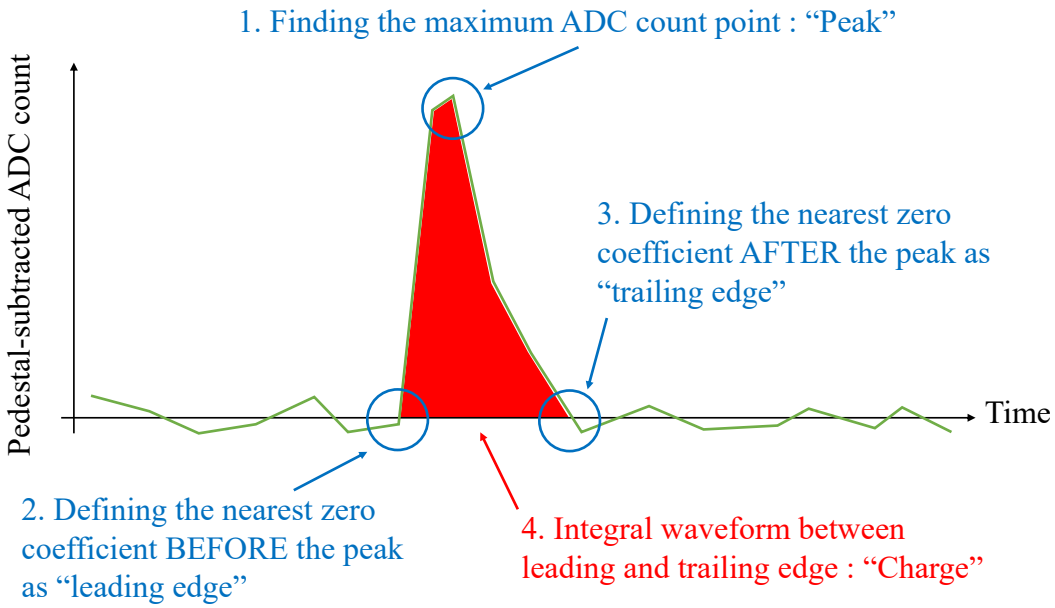

Figure 4.1: Overview of waveform analysis

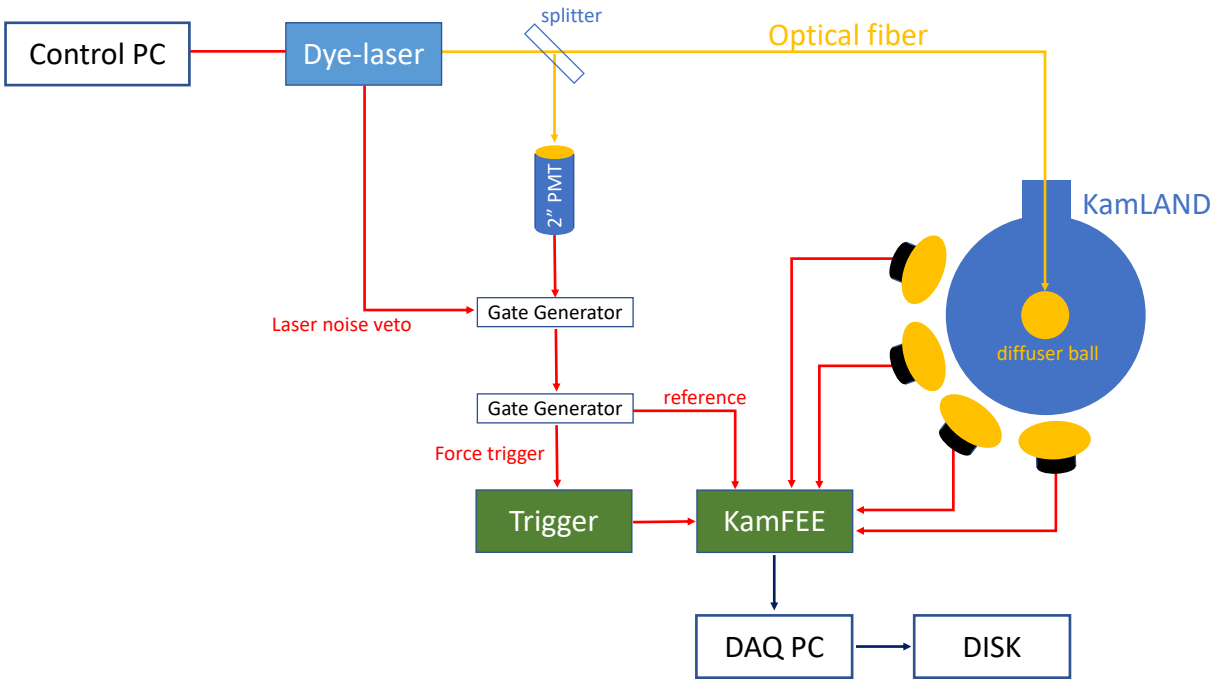

Figure 4.2: Schematic view of the dye-laser calibration system for the TQ correction

time and charge are verified PMT by PMT using the dye-laser calibration data. Figure 4.3 and Figure 4.4 show examples of the hit timing response as a function of charge. The TQ correction table is created by fitting these data with Eq.(4.1)

$$T(Q) = P_0 + P_1 \times \log_{10} Q + P_2 \times (\log_{10} Q)^2 \tag{4.1}$$

where P_0, P_1 and P_2 are the fitting parameters.

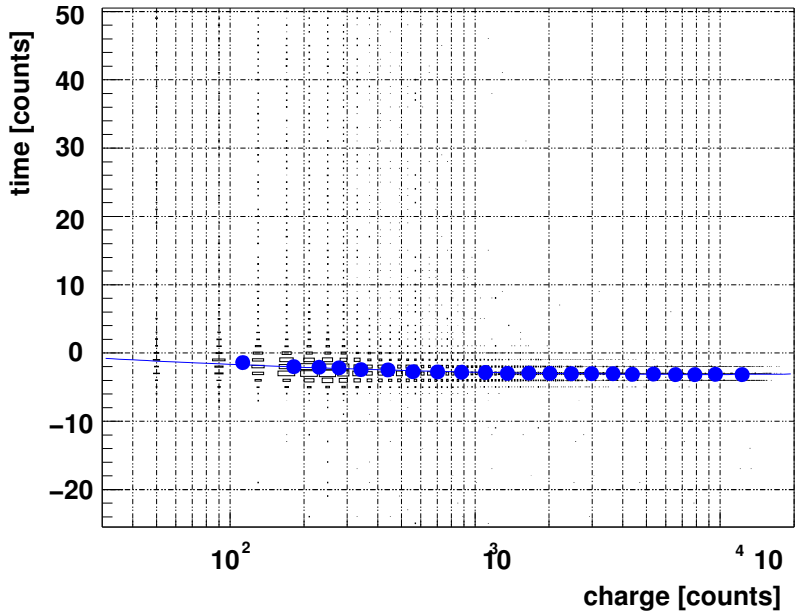

Figure 4.3: Timing-Charge calibration with a dye-laser data for a typical 17-inch PMT; In the horizontal axis, "charge" means the integrated ADCcount along time.(Shimizu 2005)

The comparison of timing distributions before and after the TQ correction is shown in Figure 4.5. After the correction, the deviation of the distributions were reduced, and almost consistent with the transit time spread (TTS) for the PMTs.

Due to change of liquid scintillator conditions and FEE status, the latencies of PMTs can have time variations. This time variation is verified using ^{60}Co source calibration installed at the center of the detector. ^{60}Co source emits isotropic 1173 keV and 1333 keV gamma-rays, and it can be expected that the photon-arrival times are the same for all PMTs. The ^{60}Co source calibration was performed periodically in each two weeks before the beginning of the KamLAND-Zen experiment.

After the beginning of the KamLAND-Zen experiments, the ^{60}Co source calibration was not performed because the inner ballon was installed at the center of the detector and installing a radioactive source for calibration might cause inconvenient contaminations. In place of ^{60}Co source, ^{40}K residue in the connection tube between the inner balloon and the corrugated tube was used as a calibration source. This connection tube is a Poly-Ether-Ether Ketone pipe (PEEK) and located at (z, ρ) = (4.3 m, 0 m).

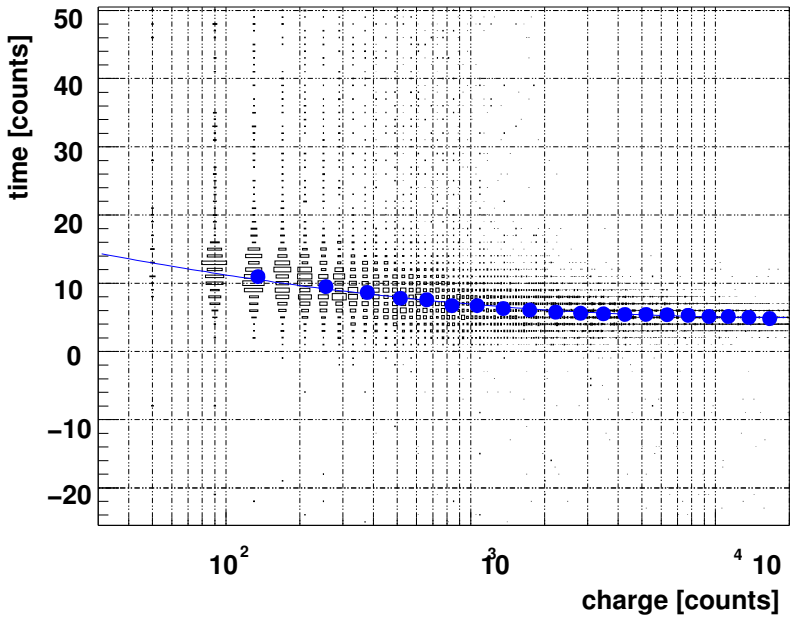

Figure 4.4: Timing-Charge calibration with a dye-laser data for a typical 20-inch PMT(Shimizu 2005)

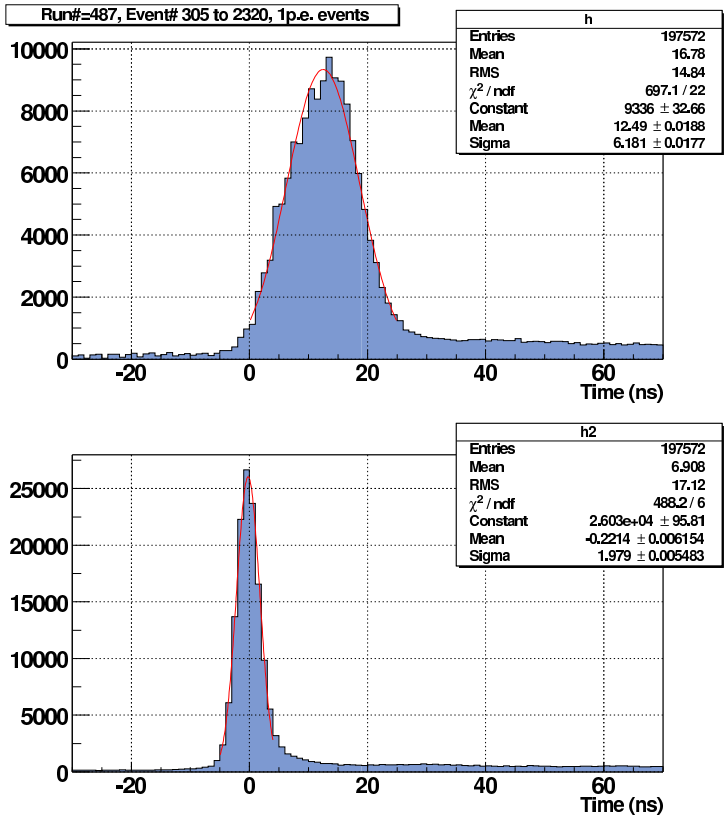

Figure 4.5: Hit timing distribution of all 17-inch PMTs in 1 photoelectron events before and after the TQ correction(Watanabe 2012)

4.3.2 PMT Gain Calibration

As is described in Sec.4.2, observed charge in KamLAND PMT is calculated by integrating the waveform. Then the charge is normalized by the average charge observed in single photoelectron (1 [p.e.]) input.

The selection of single photoelectron event is following,

1. not a muon event
   Since $\sim \mathcal{O}(10^3)$ photoelectron is expected in muon events, they should be excluded from the PMT Gain calibration.

2. not in 2 ms after the last muon event
   This selection is to avoid the effect of the overshoot and after pulse after muon events.

3. not in 100 μs after the last non-muon event
   This selection is to avoid missing-waveform effect due to the ATWD dead time.

4. The number of 17inch PMT which detected photoelectron is more than 120 and less than 230.
   This selection is determined considering Poisson distribution so that single photoelectron input is expected.

5. The distance between the rough-reconstructed light-emission vertex and the PMT is more than 33 cm.
   This selection is applied to select light emission in the liquid scintillator.

6. The number of peak in the waveform is 1.
   Multi-photon input might affect the area of single-photoelectron waveform.

and muon selection here is following,

1. The total observed charge in all 17inch PMTs are more than 20000 photoelectron.[1]

2. The number of OD PMT detecting photoelectron is more than a threshold[2].

Figure 4.6 is an example of observed charge distribution in "single photoelectron events", where the unit of charge is defined by "1[p.e.]=700[AdcSum]"[3]. The 1 p.e. charge distribution of 17inch PMTs have clear peak. This peak is fitted by Gaussian and the 1 p.e. charge is calibrated using the mean of the fitted Gaussian.

On the other hand, The 1 p.e. charge distribution in 20inch PMTs do not have clear peak (Figure 4.7) due to the different dynode type, and the same strategy as in 17inch cannot be applied. The gain of 20inch PMTs are calibrated using the charge

[1] 1[p.e.]=700[AdcSum] is used here.
[2] The threshold is defined considering the OD status. 9 is used in the latest data.
[3] [AdcSum] means the time integral of ADC counts

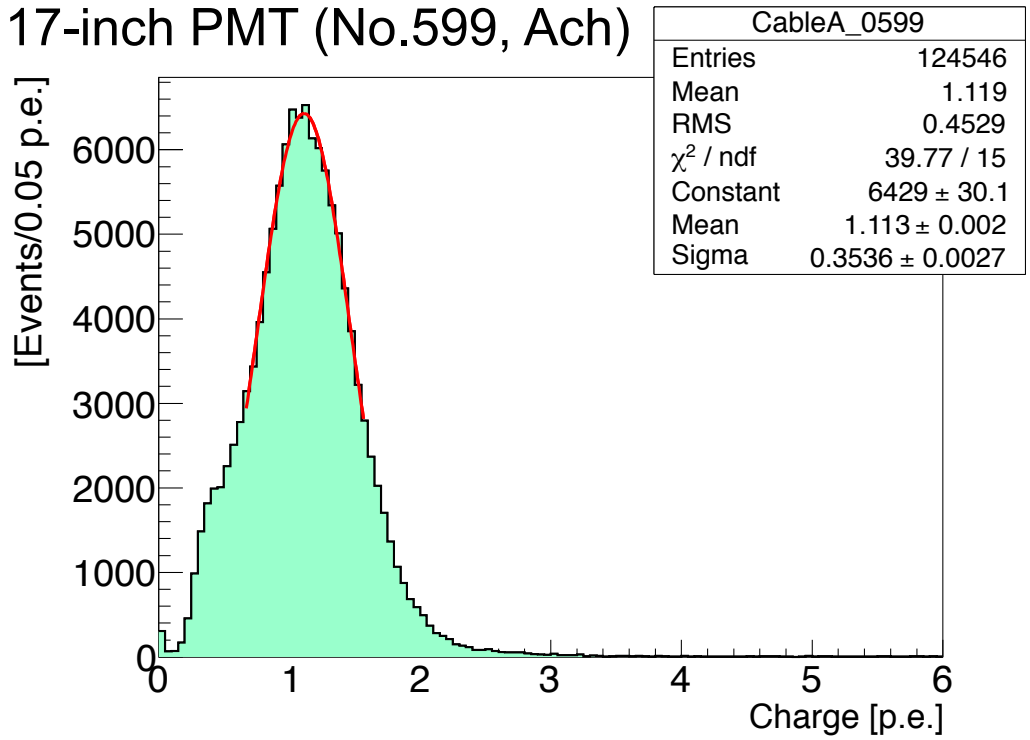

Figure 4.6: Single photoelectron charge distribution in a 17inch PMT(Watanabe 2012)

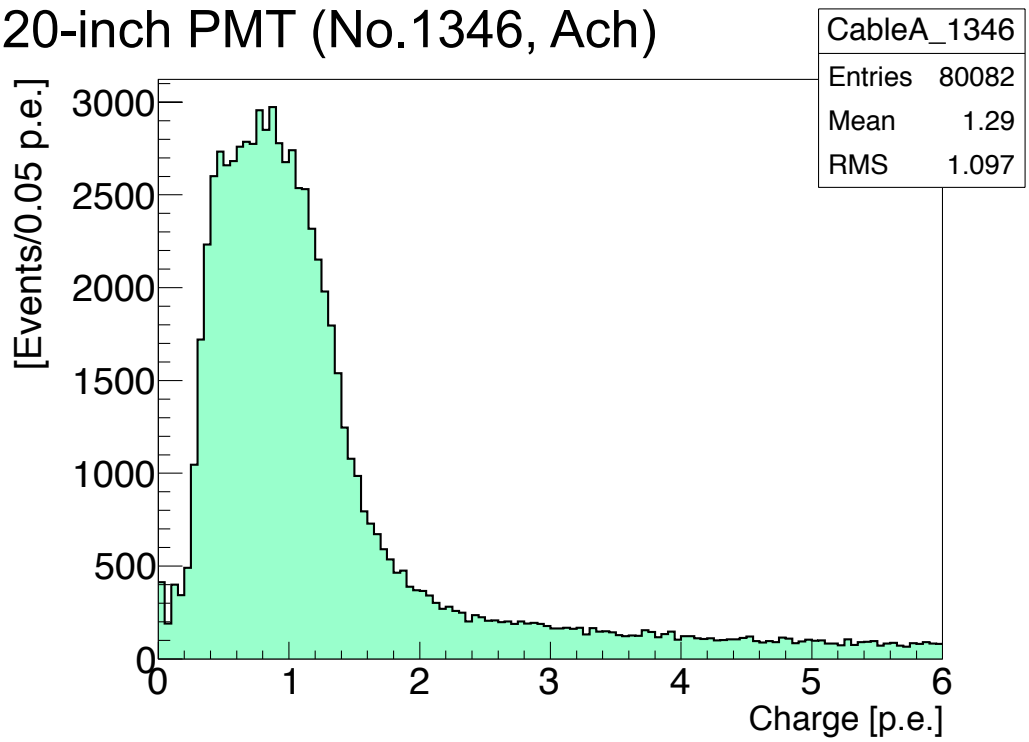

Figure 4.7: Single photoelectron charge distribution in a 20inch PMT(Watanabe 2012)

ratio from 17inch to 20inch PMTs as Eq.4.2 at a high-charge input (i.e. muon event).

$$\begin{aligned}&\text{(Charge Ratio) [AdcSum/p.e.]}\\&= \frac{\text{(Average waveform integral of 20inch PMT) [AdcSum]}}{\text{(Average observed charge in neighboring 8 17inch PMTs) [p.e.]}}\end{aligned} \tag{4.2}$$

Figure 4.8 shows an example of 20inch PMT gain calibration. The left column is a comparison of gain-calibrated 20inch PMT charge (horizontal) and average of observed charge in neighboring 8 17inch PMTs. The right column is the distribution of charge ratio calculated from left figures. Top and bottom panes correspond to ATWD A and B channel, respectively.

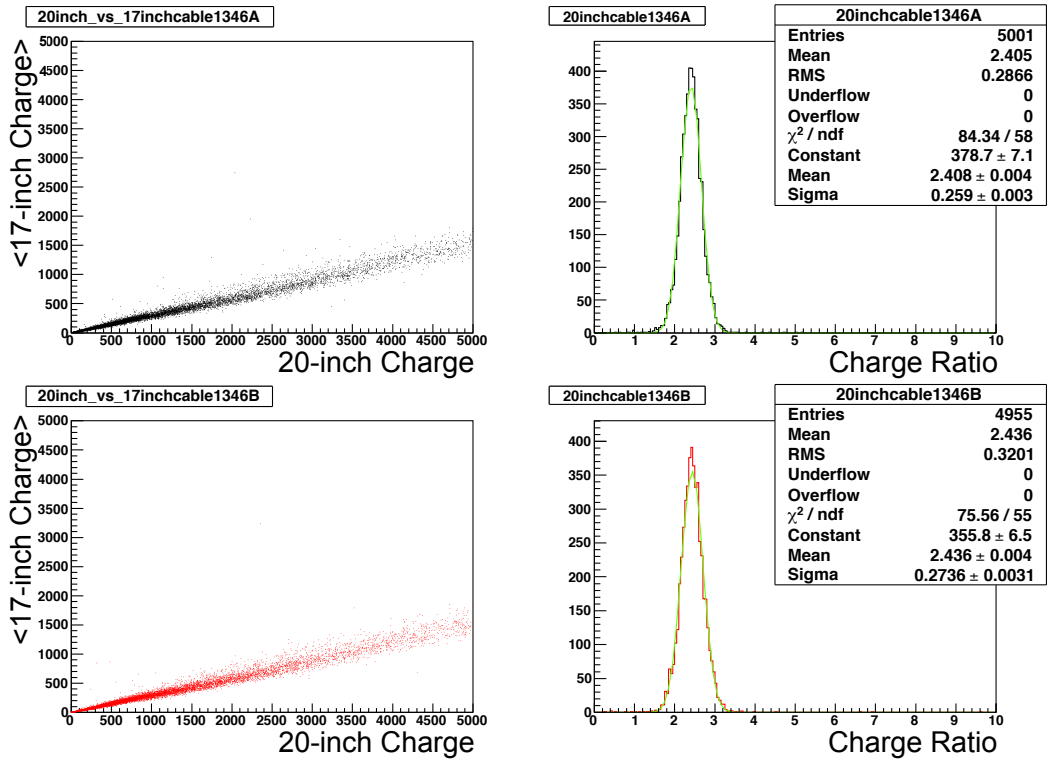

Figure 4.8: Gain calibration of a 20inch PMT(Watanabe 2012)

The PMT gain has time variation because it can varies due to PMT, electronics status and other hardware activities. It also depend on which ATWD channel is used. So, the gain calibration is performed run by run, and for each ATWD channel separately.

The time variations of the average gain in 17inch (20inch) PMTs are shown in Figure 4.9 (Figure 4.10). There are some gaps which are caused by hardware activities. The brown-shaded regions represent the 1st purification campaign, the 2nd purification campaign, KamlAND-Zen400 installation work, the OD refurbishment work, failed800 installation work, OD-off period in 2018 and KamLAND-Zen800 installation work, respectively from left. Since 2012, the average gain of 17inch PMTs

has been dropping. This is caused by the increase of the low-gain PMTs. The cause of low-gain PMTs is suspected to be an aging of PMTs, but under investigation. From 2020, signal amplifiers for low-gain PMTs have been installed, and the average gain of 17inch PMTs is increasing, which is shown as green-shaped region in Figure 4.9.

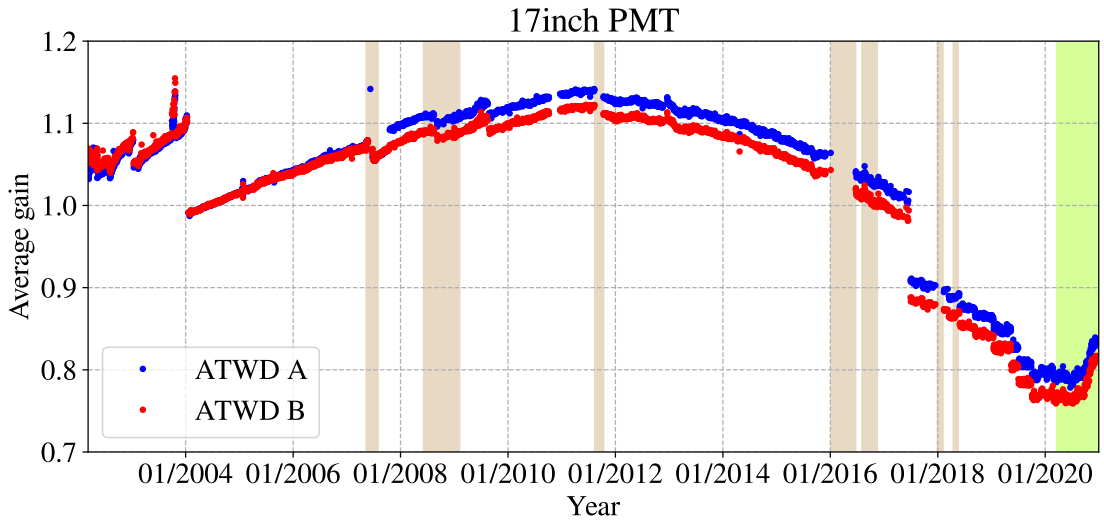

Figure 4.9: Time variation of average gain of 17inch PMTs

4.4 Bad-Channel Selection

KamLAND has a lot of PMTs. However, some of them may have strange behaver like unstable hit rate or abnormal charge distribution, which are caused by PMT malfunctions, unstable high voltage supplies or miss connections of signal cables. Even if a PMT works correctly, unstable behaver also can be caused by the failure of read-out electronics. These unstable PMTs are categorized as "bad channels" and masked in the event reconstructions to avoid inconvenient systematic biases. Since the status of the PMTs and electronics change run by run, bad channel selection is performed for each run independently.

The inner detector PMTs which meat all of following criteria are used in the event reconstruction. (All ID PMTs which does not meat any of following are categorized as bad channel.)

1. Normal and stable data acquisition
   In the first 10000 events in a run,
   - The PMT hits in more than 600 events.
   - Missing-waveform event is less than 1000 events.
   - The difference of hit between ATWD A and B channels is less than 20%.

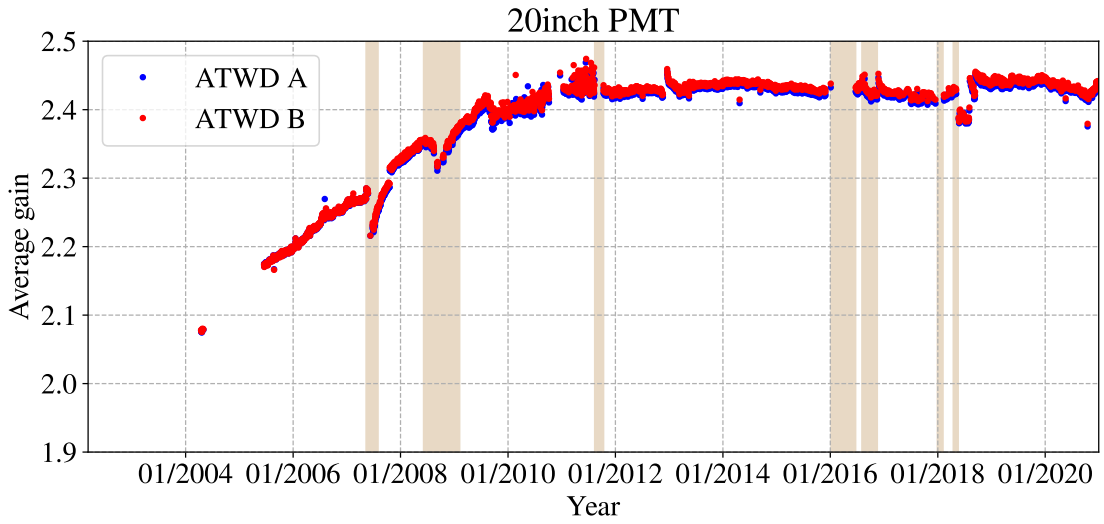

Figure 4.10: Time variation of average gain of 20inch PMTs

2. Stable response to low-energy events
   In the first 10000 events in which the number of OD hit is less than 5, and the total charge of ID 17inch PMTs is more than 500 p.e. and less than 10000 p.e.,

   - The PMT hits in more than 480 events.
   - The calibrated gain is more than 0.4 and less than 4.

3. Stable response to muon events
   In the first 100 events in which the number of OD hit is more than 4, and the total charge of ID 17inch PMTs is more than 316000 p.e.,

   - The PMT hits in more than 80 events.
   - The difference of observed charge from the neighbor PMTs meat Eq.4.3.

$$\frac{1}{\mathrm{N}}\sum_{i=1}^{N}\frac{(Q_i - Q_i^{\text{neighbor-average}})^2}{Q_i^{\text{neighbor-average}}} > 1000[\text{p.e.}] \tag{4.3}$$

     , where N is the number of event for selection (Here, N=100), Q_i is the observed charge in i-th event by the checked PMT and $Q_i^{\text{neighbor-average}}$ is the average of observed charge in i-th event among neighboring PMTs of the checked PMT. In the calculation of $Q_i^{\text{neighbor-average}}$, bad channels categorized by the above criteria are excluded.

The criterion for bad OD PMTs is simpler like following:

1. Stable response to muon events
   In the first 100 events in which the number of OD hit is more than 4, and the total charge of ID 17inch PMTs is more than 316000 p.e.,

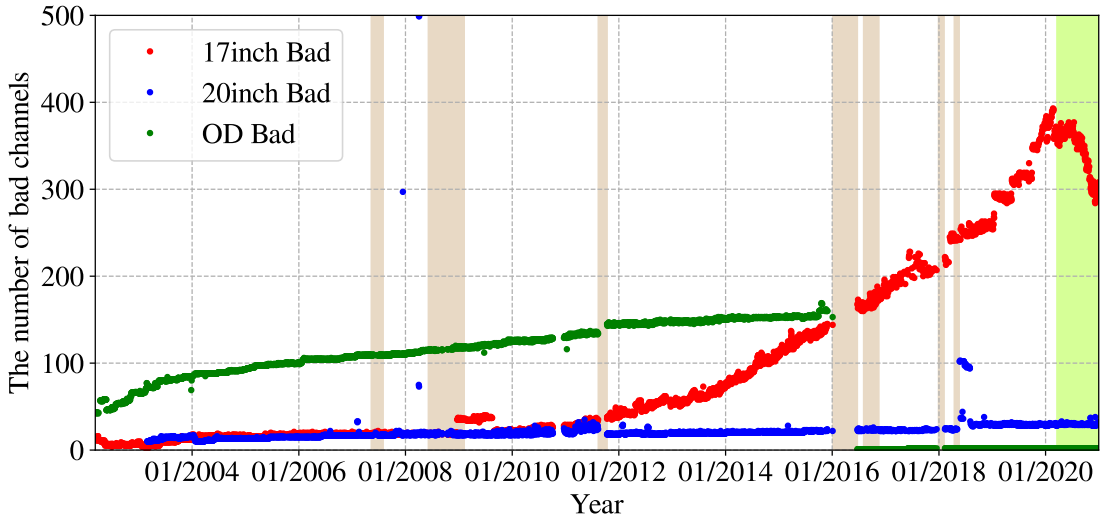

Figure 4.11: Time variations of the number of bad channels

- The PMT hits in less than 5 events.

Time variation of the number of bad channels are as shown in Figure 4.11. The number of bad 17inch PMTs has been increased since 2011 because of the same reason described in Sec.4.3.2. As is obviously shown in Figure 4.11, the amplifiers installation (shown as green band) is drastically decreasing the number of bad channels. The number of bad OD PMTs had been increased because they were going dead dut to failure of water-proof assemblies. After OD refurbishment work performed in 2016, the number of OD PMTs changed from 225 to 140 and all the OD PMTs were recovered.

4.5 Dark Charge Estimation

PMTs may detect "charge" event though no photoelectron incident on the PMT. Such "dark charge" detections are caused by thermal electron emissions from PMT photo-cathode or noises of electronics. Since dark charge detection has no correlations with the detections of scintillation photons, it can be estimated by counting detected charge in 50 ns off-time window while the vertex and energy reconstruction takes on-time window (Figure 4.12). Dark charge is calculated with Eq.4.4.

$$(\text{dark charge}) = \frac{(\text{charge sum of hit PMTs in off-time window})}{(\text{the number of hit PMTs in off-time windows})} \tag{4.4}$$

In the event reconstruction, the estimated dark charge is subtracted from the observed charge to suppress systematic effect by dark charge.

Since the dark charge depends on detector and other hardware conditions, this estimation is performed for each runs. Time variation of dark charge is shown in Figure 4.13.

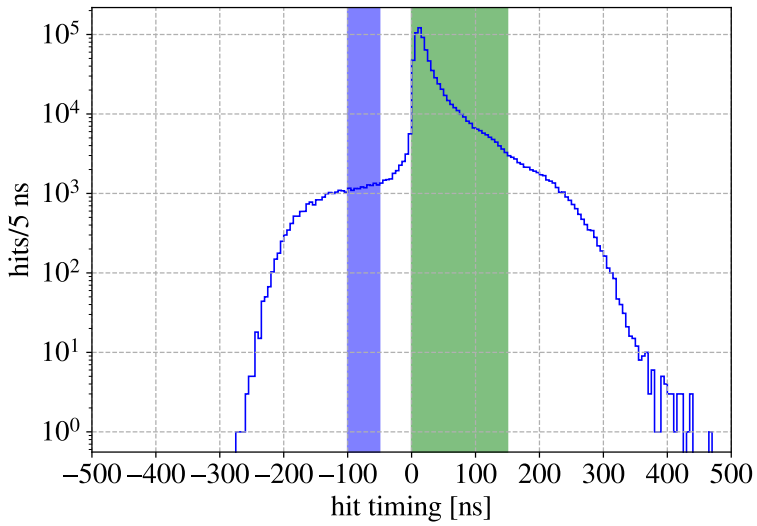

Figure 4.12: Hit time distribution of 17inch PMTs: blue(green) band represent off-(on-)time window.

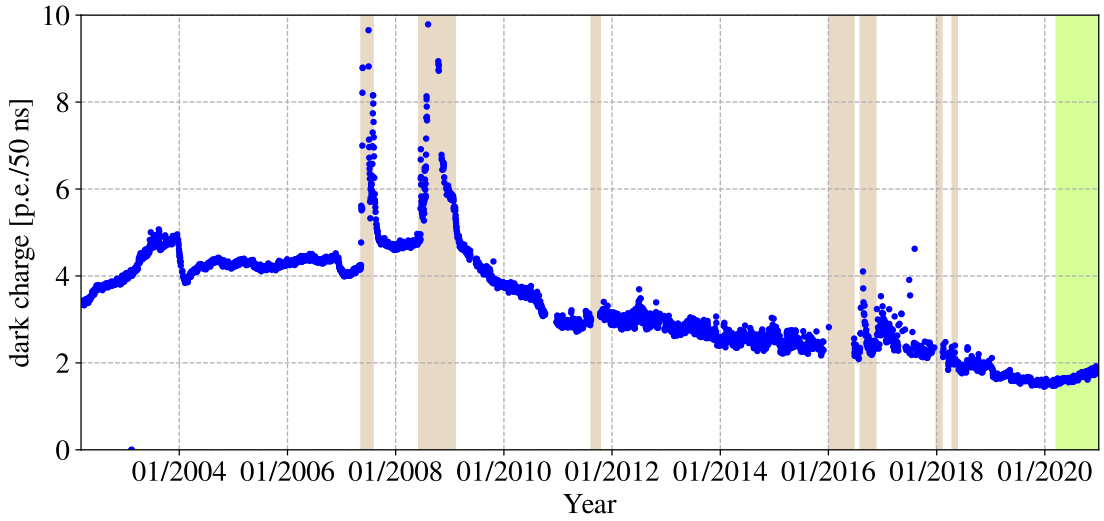

Figure 4.13: Time variation of dark charge

4.6 Muon Track Reconstruction

Although the 2700 w.e. overburden suppress the cosmic-ray muon flux by factor of $\sim 10^{-5}$ with respect to that on the surface, the cosmic-ray muons go through the inner detector on constant frequency, about 0.3 Hz.

These muons may react in the detector and generate various spallation products that can mimic the coincidence neutrino signals. On the other hands, some of spallation by-products can be used for the detector calibration and verification of the reconstruction qualities. For example, Thermal neutrons accompanying muons are captured on proton(^{12}C) and emit 2.2(4.9) MeV γ-rays, which are used for checking the stability of the reconstructed energies. One of spallation products, ^{12}B are used for the estimation of the fiducial volume uncertainties.

Therefore, identifying muon events, reconstructing their tracks and energy deposits, and verifying the reconstruction qualities are essential in the KamLAND experiment. In this section, muon event selection, tracking algorithm and its performance are described.

4.6.1 Muon Selection criteria

Muon can be easily identified by its large energy deposits in the liquid scintillator. In addition, muons going through OD make hits of multiple OD PMTs. So, simultaneous photoelectron detection in both ID and OD are useful to tag muons.

Selection criteria for muon events in KamLAND is as follows:

1. Through-going muon (scintillation muon): $Q_{17} \geq 10000$ [p.e.]
   Muons going through inside the liquid scintillator with both scintillation light and Cherenkov light emission

2. Clipping muon (Cherenkov muon): $Q_{17} \geq 500$ [p.e.] and $N_{200OD} \geq 5(9)$ hits
   Muons crossed the buffer oil with Cherenkov light emission

where Q_{17} is the total charge observed in the ID 17inch PMTs and N_{200OD} is the maximum number of hits in the OD within 200 ns time window. The N_{200OD} threshold was changed after the OD refurbishment work in 2016 because the number of OD PMTs, their quantum efficiencies and trigger scheme were upgraded. Figure 4.14 shows the distribution of the total charge in the ID 17inch PMTs and the number of hit OD PMTs in muon events, where the muon selection criteria are shown as red dotted line.

The through-going muons are further categorized into the following two types:

1. Showering muon ($\Delta(Q) > 10^6$ [p.e.])
   Energetic muons which often cause hadronic cascade showers and produce lots of radioactive isotopes

2. Non-showering muon ($\Delta(Q) \leq 10^6$ [p.e.])
   The less energetic muons

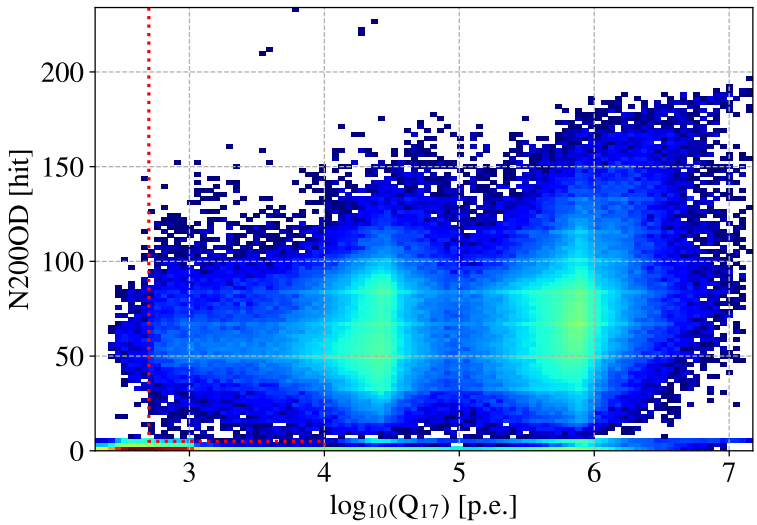

Figure 4.14: Muon selection criteria (red dotted line) drawn on 2D histogram of Q_{17} vs N_{200OD}

where ΔQ is the residual charge, which means the difference between the observed charge minus the charge that would be expected if the muon simply penetrated the detector (described in Sec.4.6.2). Non-showering muons account for 90% of all muon detected in KamLAND.

Figure 4.15 shows the observed charge distribution in muon events. The blue and green histogram correspond to the non-showering and showering muons, respectively. Two blue peaks around $\log_{10}(Q_{17}) \sim 4.5$ and $\log_{10}(Q_{17}) \sim 5.6$ correspond to the clipping muon (Cherenkov light emission) and through-going muon (scintillation light + Cherenkov light emission), respectively.

Muons whose observed charge are too small when considering the expected energy deposits per track length and reconstructed muon track described in Sec.4.6.2 are categorized "Miss-reconstructed muons" and shown as the orange histogram in Figure 4.15. The ratio of such muons in the through-going muon is about 0.2%.

The muon rate in KamLAND can be evaluated by studying the distribution of the time differences between muon events as Figure 4.16. The muon rate has been very stable since the beginning of the KamLAND experiment as shown in Figure 4.17.

4.6.2 Algorithm of Muon Track Reconstruction

Muons going through the detector produce a large amount of scintillation light in the liquid scintillator and Cherenkov light in both the liquid scintillator and the buffer oil. The Cherenkov light are emitted with the constant angle, θ_C (Cherenkov angle), against the muon track, whereas the scintillation light are emitted isotropically. The muon tracks are reconstructed with a maximum-likelihood method on the photon-arrival time distribution of both scintillation and Cherenkov photons.

With notations in Figure 4.18, the first photon-arrival time at a PMT, t, can be

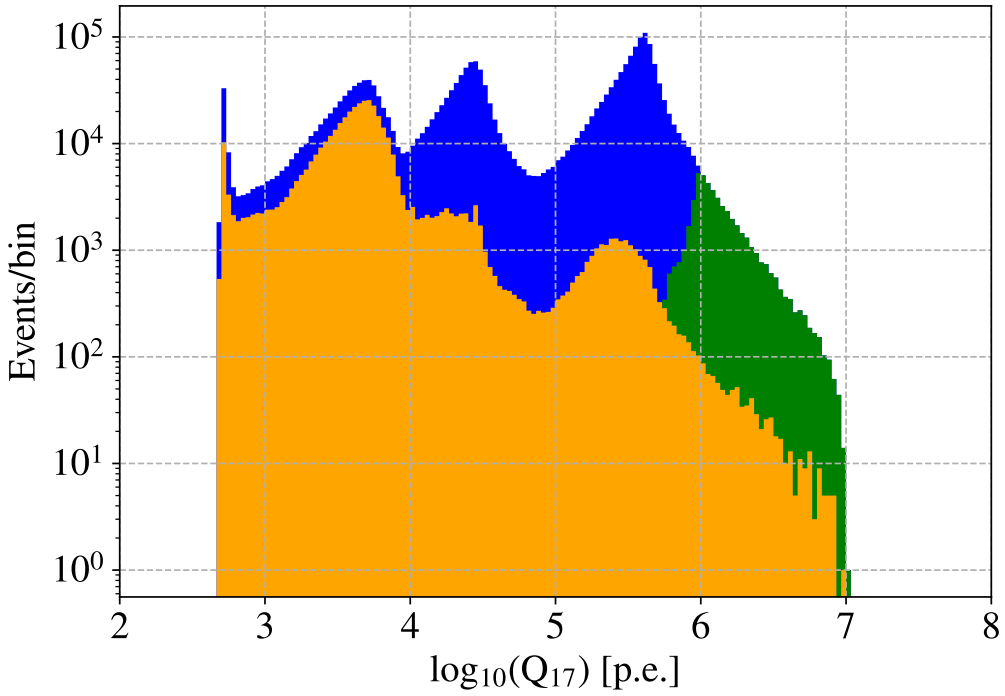

Figure 4.15: The distribution of charge observed by 17inch PMTs in muon events

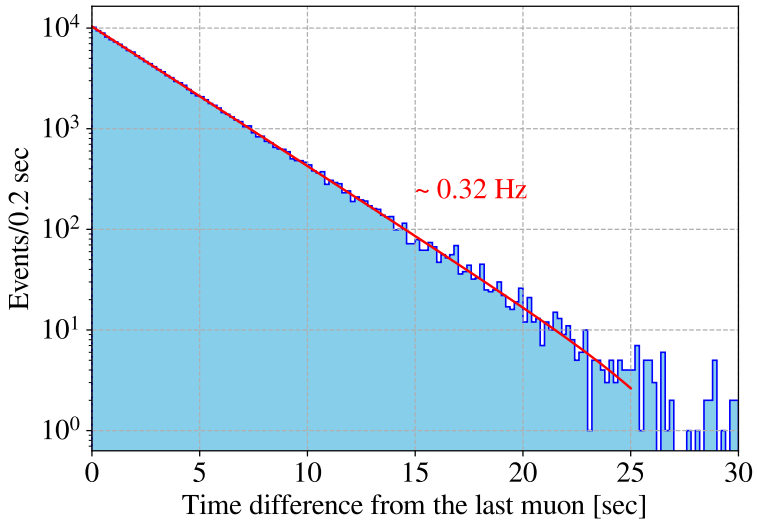

Figure 4.16: The distribution of time-difference between muon events.

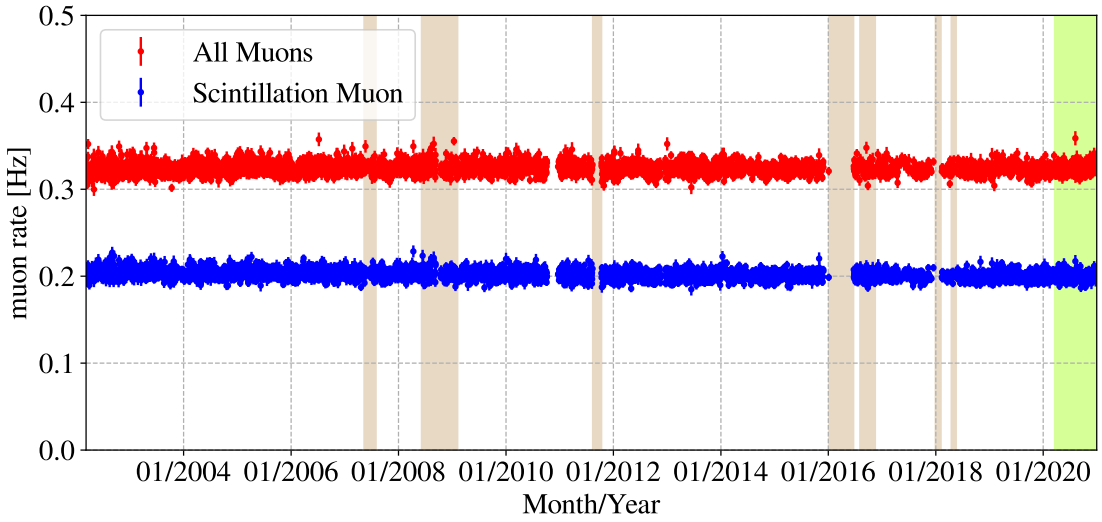

Figure 4.17: Time variation of muon rate

written as,

$$t = t_0 + \frac{l}{c} + \frac{(z-l)/\cos\theta}{c/n} \tag{4.5}$$

$$= t_0 + \frac{l}{c} + \frac{\sqrt{(z-l)^2+\rho^2}}{c/n} \tag{4.6}$$

where t_0 is the time a muon entered the detector, and n is the refraction index in the liquid scintillator. The refraction index is measured to be 1.44–1.47 in the various wavelength of the scintillation light. To consider any pass-length in both the liquid scintillator and the buffer oil, this parameter is tuned within the measured value in the reconstruction algorithm.

Assuming the velocity of muon is approximated to the velocity of light, the earliest photon arrival time in the detector should be given where $\theta = \theta_{\mathrm{C}}$, and,

$$\left.\frac{\partial(t-t_0)}{\partial\theta}\right|_{\theta_{\mathrm{C}}} = 0 \tag{4.7}$$

Once the expected distribution of the first photon-arrival time with respect to the entrance vertex and track direction are constructed, the muon track can be reconstructed by finding the most likely entrance vertex and track direction to reproduce the PMT hit times.

After the reconstruction of the tracks, the residual charge, $\Delta(Q)$, are calibrated as,

$$\Delta\mathrm{Q} \equiv \mathrm{Q}_{17} - (L_{\mathrm{LS}} + L_{\mathrm{BO}}) \left\langle \frac{\mathrm{d}Q}{\mathrm{d}X} \right\rangle_{\text{Cherenkov}} - L_{\mathrm{LS}} \left\langle \frac{\mathrm{d}Q}{\mathrm{d}X} \right\rangle_{\text{scintillation}} \tag{4.8}$$

where Q_{17} is the total charge observed in ID 17inch PMTs, $\mathrm{L}_{\mathrm{LS(OB)}}$ is the track length

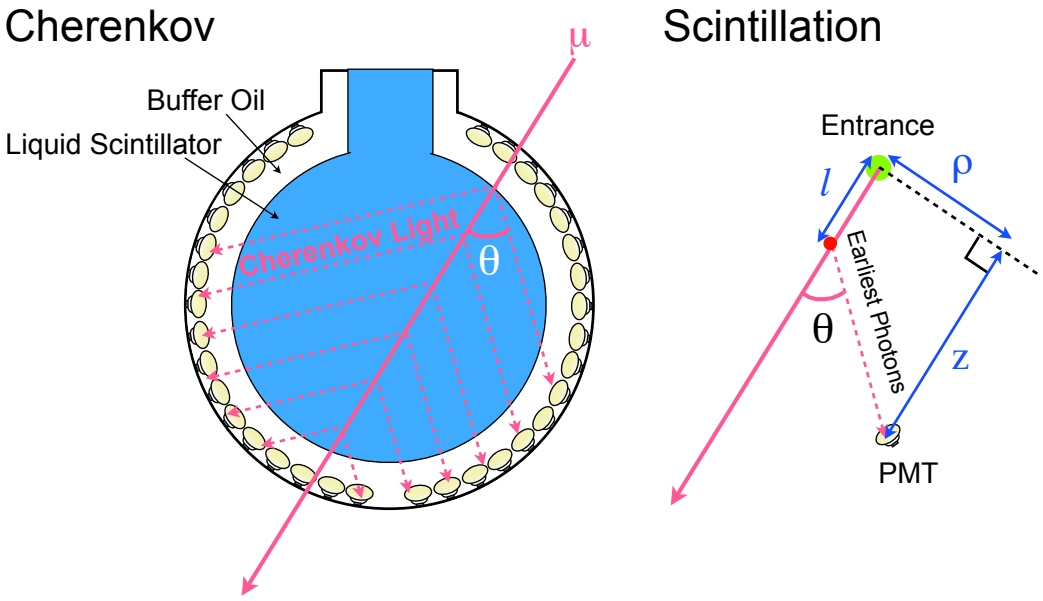

Figure 4.18: Schematic view of muon-track(Watanabe 2012)

in the liquid scintillator (the buffer oil) and the ideal light emissions per track length,

$$\left\langle \frac{\mathrm{d}Q}{\mathrm{d}X} \right\rangle_{\text{Cherenkov}} = 31.45 \text{ [p.e./cm]} \tag{4.9}$$

$$\left\langle \frac{\mathrm{d}Q}{\mathrm{d}X} \right\rangle_{\text{scintillation}} = 629.4 \text{ [p.e./cm]}. \tag{4.10}$$

These two values above were evaluated at the start of the KamLAND experiment by fitting the distributions of the following parameters.

For Cherenkov muons,

$$\left(\frac{\mathrm{d}Q}{\mathrm{d}X} \right)_{\text{Cherenkov}} = \frac{\mathrm{Q}_{17}}{L_{\mathrm{BO}}} \tag{4.11}$$

Besides, for scintillation muons,

$$\left(\frac{\mathrm{d}Q}{\mathrm{d}X} \right)_{\text{scintillation}} = \frac{\mathrm{Q}_{17} - L_{\mathrm{BO}} \left\langle \frac{\mathrm{d}Q}{\mathrm{d}X} \right\rangle_{\text{Cherenkov}}}{L_{\mathrm{LS}} + L_{\mathrm{BO}}} \tag{4.12}$$

The value of $\left(\frac{\mathrm{d}Q}{\mathrm{d}X}\right)_{\text{Cherenkov}}$ is monitored, and the muon reconstruction algorithm is calibrated by it to get stable charge calculation. Because the average amount of light emission in the buffer oil has been increasing while that in the liquid scintillator has been decreasing due to the purifications and other activities, the average charge reconstructed from through-going muons have been decreasing. Figure 4.19 and Figure 4.20 shows the time variation of $\left(\frac{\mathrm{d}Q}{\mathrm{d}X}\right)_{\text{Cherenkov}}$ and $\left(\frac{\mathrm{d}Q}{\mathrm{d}X}\right)_{\text{scintillation}}$. While $\left(\frac{\mathrm{d}Q}{\mathrm{d}X}\right)_{\text{Cherenkov}}$ seems stable —This is natural since it is corrected to be so— from the beginning of the KamLAND, $\left(\frac{\mathrm{d}Q}{\mathrm{d}X}\right)_{\text{scintillation}}$ has been decreasing. This "darker" effect is taken into account by a correction of the quenching factor in anti-neutrino analysis.

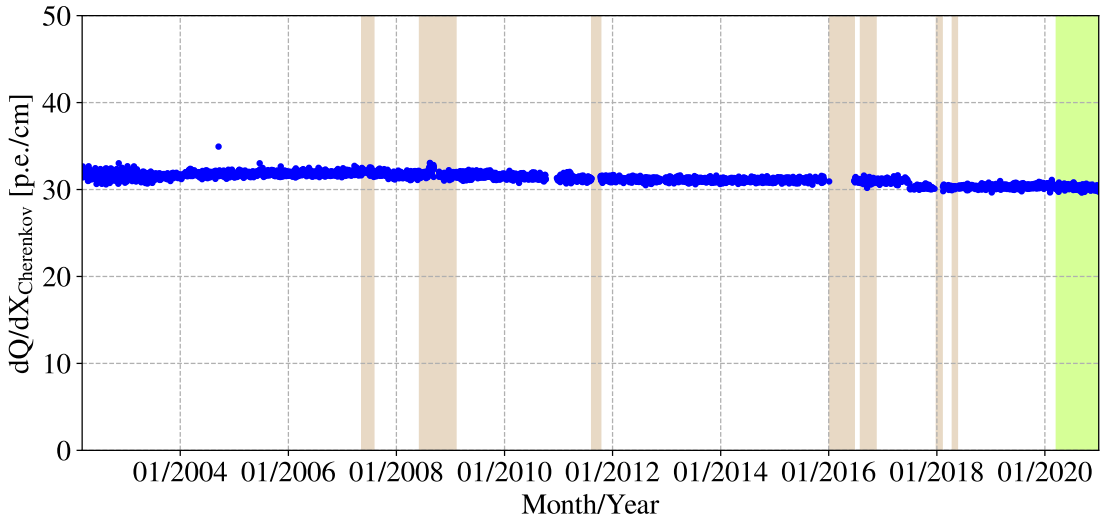

Figure 4.19: Time variation of the $\left(\frac{dQ}{dX}\right)_{\text{Cherenkov}}$

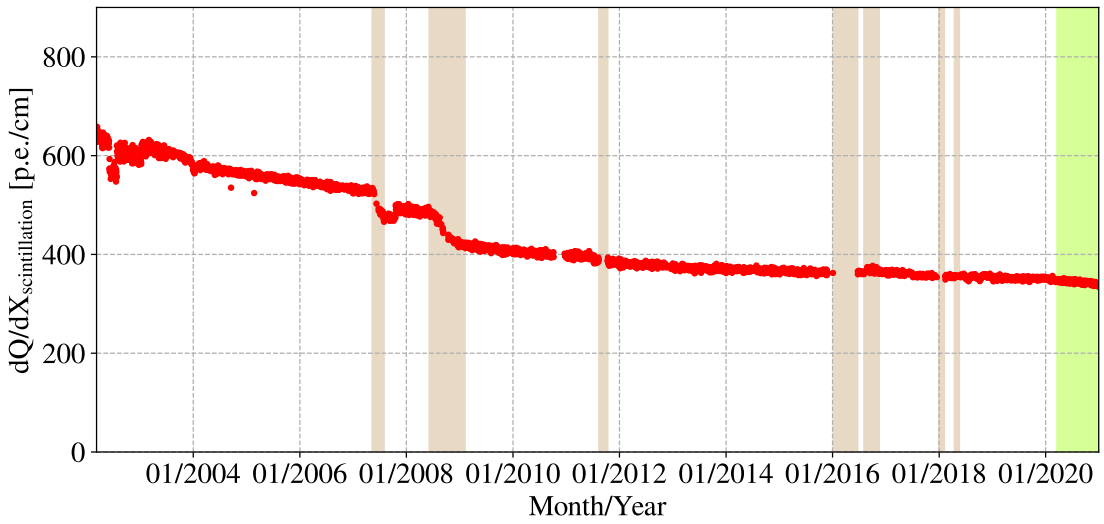

Figure 4.20: Time variation of the $\left(\frac{dQ}{dX}\right)_{\text{scintillation}}$

4.6.3 Tracking Performance

Figure 4.21 shows the correlation between the total observed charge in the ID 17inch PMTs (Q_{17}) and the distance of the muon track from the center of the detector (Impact Parameter). The Q_{17} gap at (Impact Parameter)=650 cm (red dotted line in the figure) corresponds to the boundary between the liquid scintillator and the buffer oil. The minimum-ionizing light emissions are greater inside (smaller outside) this boundary. The decreasing Q_{17} against the impact parameter agrees with that the farther the track is, the shorter the track is , and the fewer the light emission is. These are the evidence of the tracking performance.

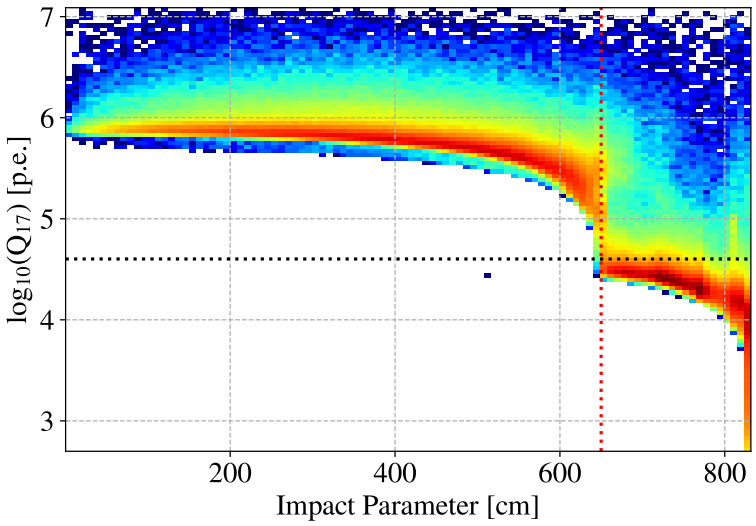

Figure 4.21: Correlation between the total observed charge in ID 17inch PMTs (Q_{17}) and the distance of the reconstructed muon track from the center of the detector (ImpactParameter)

4.7 Point-like Event Reconstruction

4.7.1 Vertex Reconstruction

Algorithm of Vertex Reconstruction

The vertex is reconstructed with a maximum-likelihood mehtod on the photon-arrival time distribution in the ID 17inch PMTs. Given a scintillation occurs on a vertex, (x, y, z), at a time, t, the photoelectron-detection time in i-th PMT, t_i, can be written as

$$t_i = t + \mathrm{ToF}_i(x, y, z) + \tau_i(t, x, y, z) \tag{4.13}$$

where $\mathrm{ToF}_i(x, y, z)$ is the calculated time of flight from the vertex (x, y, z) to the i-th PMT using the distance, refraction index, and other geometrical parameters. $\tau_i(t, x, y, z)$ represents the delay of signal detection timing for the i-th PMT compared

to the expected time from geometric calculation, which depends on the time spread of the photon emission (10 ns to a few fundred ns), absorption and re-emission process of the photons in the liquid scintillator. The distribution of τ_i, $\psi(\tau_i(t,x,y,z))$, was constructed by unsing source calibration data.

Once $\psi(\tau_i(t,x,y,z))$ is given, the likelihood function for the vertex, $L(x,y,z)$, can be defined as

$$L(t,x,y,z) = \prod_{i\in\text{hit}} \psi(\tau_i(x,y,z)) \tag{4.14}$$

The vertex and time is reconstructed by finding the set of (t, x, y, z) which maximize Eq.4.14.

The maximum of Eq.4.14 is searched for by solving

$$\frac{\partial(\log L)}{\partial t} = \sum_{i\in\text{hit}} \frac{\mathrm{d}(\log L)}{\mathrm{d}\tau_i}\frac{\partial\tau_i}{\partial t} = 0 \tag{4.15}$$

$$\frac{\partial(\log L)}{\partial x} = \sum_{i\in\text{hit}} \frac{\mathrm{d}(\log L)}{\mathrm{d}\tau_i}\frac{\partial\tau_i}{\partial x} = 0 \tag{4.16}$$

$$\frac{\partial(\log L)}{\partial y} = \sum_{i\in\text{hit}} \frac{\mathrm{d}(\log L)}{\mathrm{d}\tau_i}\frac{\partial\tau_i}{\partial y} = 0 \tag{4.17}$$

$$\frac{\partial(\log L)}{\partial z} = \sum_{i\in\text{hit}} \frac{\mathrm{d}(\log L)}{\mathrm{d}\tau_i}\frac{\partial\tau_i}{\partial z} = 0 \tag{4.18}$$

Vertex Reconstruction Quality

Vertex reconstruction quality is verified with various source calibration data including z-axis and off-axis calibration. This section referes to source calibration along z-axis, whereas off-axis calibration is used to study fiducial volume uncertainty as described in Sec. 4.8.2.

The reconstructed vertex bias is verified with z-axis calibrations. Figure 4.22 and Figure 4.23 show the reconstructed vertex (z) deviation from the true source deployed position. The vertex bias are comfirmed to be less than 3% and 5% for before and after the purifications, respectively.

Besides, vertex resolution is verified with source data. Figure 4.24 shows the comparison of distance distribution between the reconstructed vertex and the true source position in the calibration data and simulation by GEANT4(Agostinelli et al. 2003). Since the distribution of reconstructed vertex depends on not only the vertex resolution but also the particle dispersion, the simulated distribution is distorted assuming a vertex resolution before compared to calibration data. The vertex resolution is estimated by finding the most plausible vertex resolution to reproduce the calibration data.

The verified vertex resolution as a function of visible energy is shown in Figure 4.25. Since the purification campaigns changed the composition of the liquid scintillator and decreased the light yield, the vertex resolution after purifications is worse than that before the purification. On the other hand, the liquid scintillator is

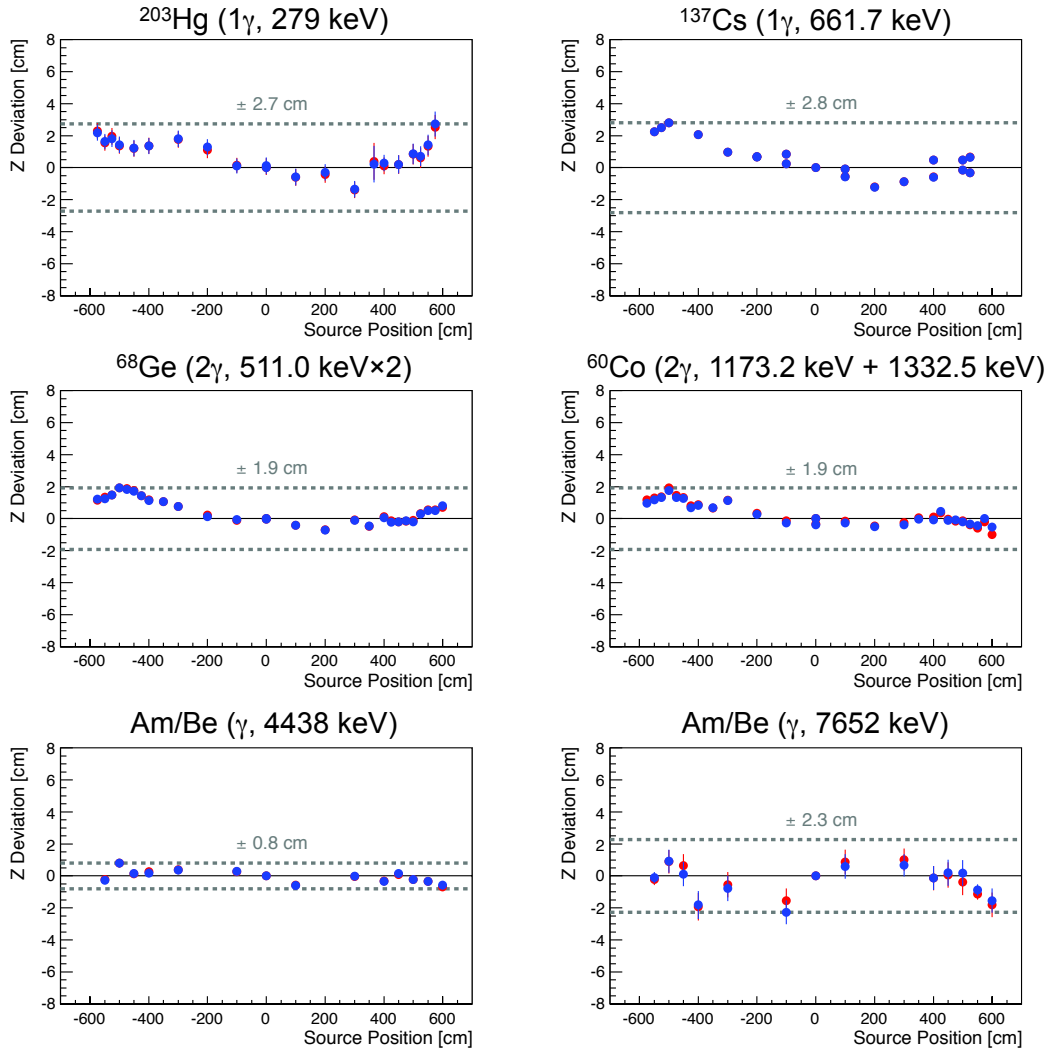

Figure 4.22: Vertex deviation between reconstructed vertical position and the deployed position before purifications (Watanabe 2012). The ^{203}Hg and ^{137}Cs calibration were performed in 2006 September. The ^{68}Ge, ^{60}Co and Am/Be calibration were performed in 2005 September.

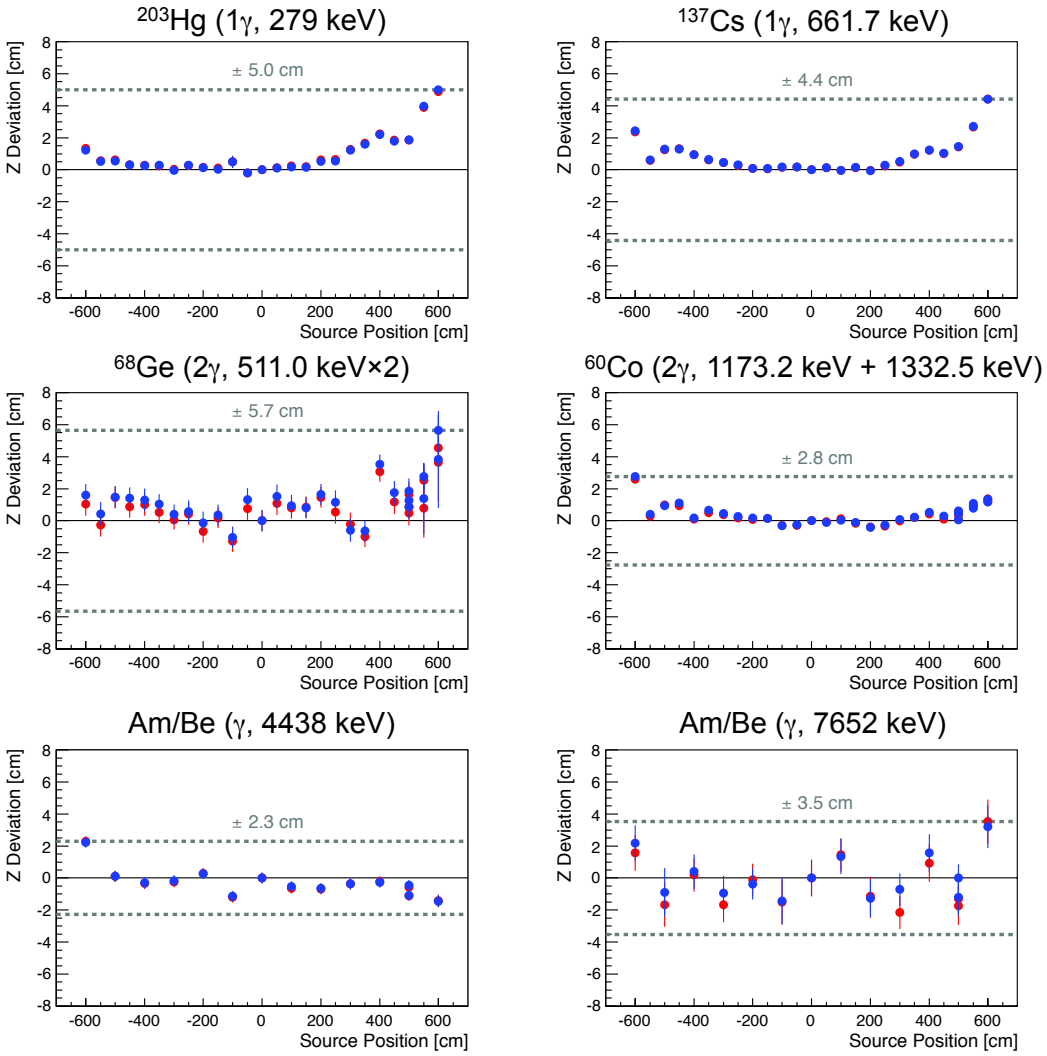

Figure 4.23: Vertex deviation between reconstructed vertical position and the deployed position after purifications (Watanabe 2012). These calibration data were taken in 2009 July.

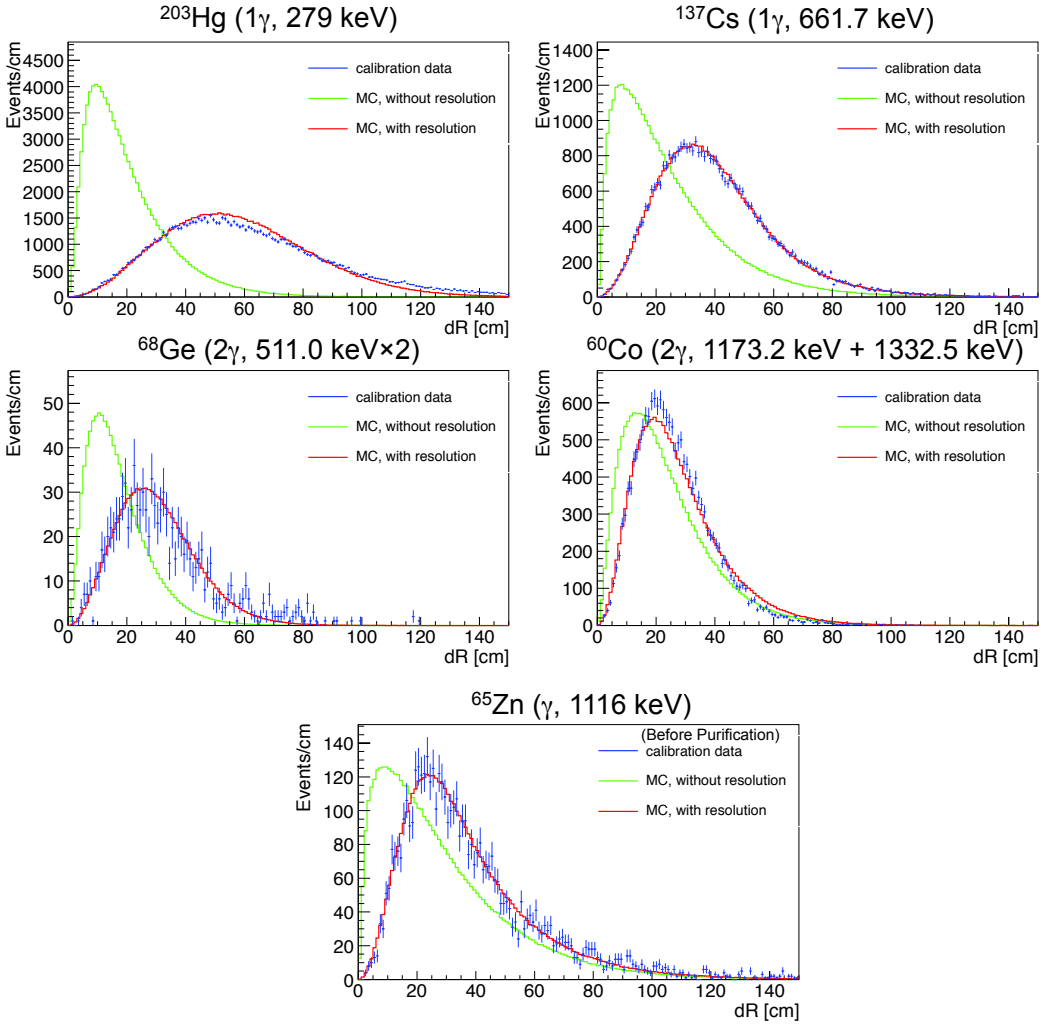

Figure 4.24: Comparison of distance between reconstructed vertex and the true source position in souce calibration data and simulation (Watanabe 2012). The top four figures show after-purification data whereas the bottom one before-purification data. The observed data is plotted with blue. The simulated data without(with) the vertex resolution is shown as green(red) stair plot.

identical in Period2 and Period3 and the vertex resolution verified after the purification is assumed to be valid for Period3. Though, actually, there are inceasing number of bad channels, which decrease the effective light yield and worse the resolution, the effect is corrected with the number of bad channel as described later.

4.7.2 Energy Reconstruction

The energy is defined by the deposited energy in the liquid scintillator. The deposited energy (or "real energy") is calculated from the visible energy, which corresponds to the scintillation light yield observed by ID PMTs. There is non-linear relationship between the real energy and visible energy. It is described in Sec.4.7.3.

The visible energy is estimated with a maximum-likelihood method on the PMT hit and charge profiles. To suppress the time variation of the detector response, the following corrections are applied to the PMT charge in advance.

Basic corrections

- PMT Gain calibration
  There are the small differences of single photoelectron charge between PMTs even if the high voltage are supplied correctly. The gain of a PMT might have time variation due to aging, high voltage tuning and changes in read-out electronics. Each PMT's charge is normalized channel by channel and run by run using the charge distribution by single photoelectron input as described in Sec.4.3.2.

- Bad channel selection
  PMTs which have abnormal behaver — too many hits, no hits or strange charge output — are selected as described in Sec.4.4 and masked in the energy reconstruction. The observed charge sum in ID PMTs are corrected to cancel the effect of absent charge from bad channels.

- Software discriminator threshold
  PMTs have noises which cause accidental dark hit. To reduce its effect, the software threshold is set at 0.3 p.e. for each PMT charge.

- Dark hit subtraction
  PMT charge always include dark charge contribution. As described in Sec.4.5, It can be estimated by counting charge in off-time window in the time spectra of the light emission run by run. The estimated charge charge contribution is subtracted from the total observed charge of each events.

Photon Yield Correction

The photon yield of the detector also depends on the property of the detector components. The following items are parameterized and set into the energy reconstruction algorithm.

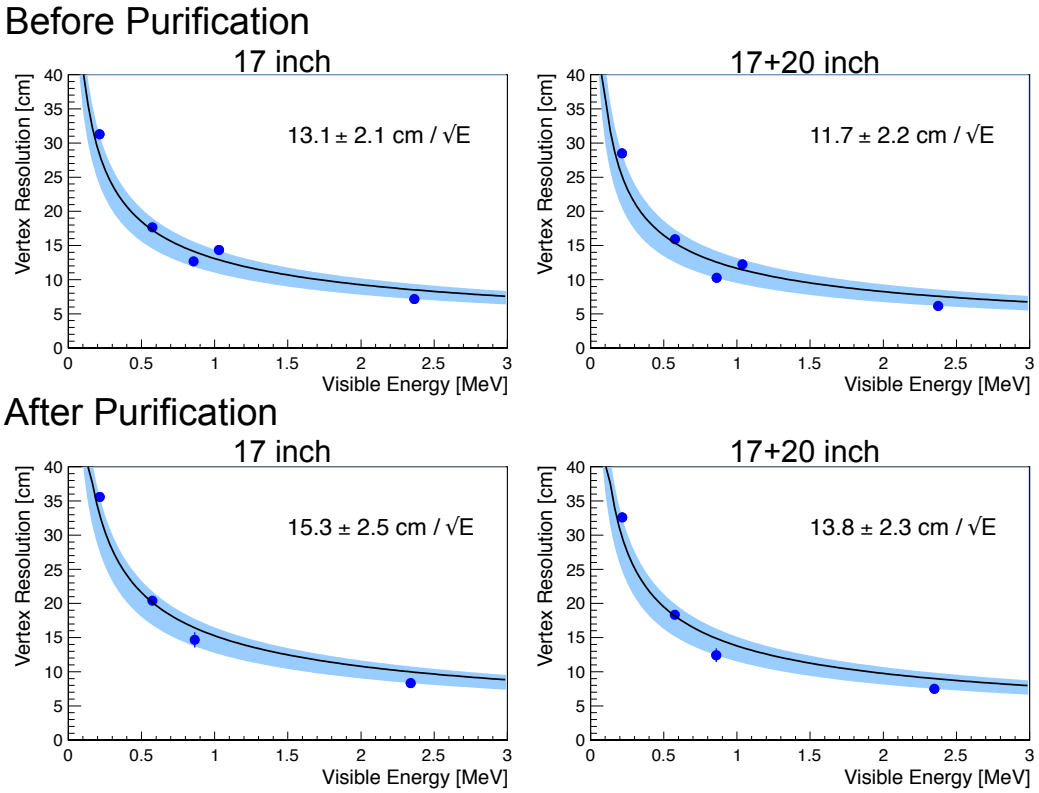

Figure 4.25: Vertex resolution verified with various calibration sources (Watanabe 2012). The black curve and blue shaded region present the best-fit vertex resolution as a function of visible energy and its uncertainty.

- Shadow effect
  The observed charge by the PMTs in the bottom and chimney regions are decreased because of the shadow effect for light traveling by the balloon film and supporting kevler ropes. This effect is studied using ^{60}C source calibration at the center of the detector. Figure 4.26 shows the effective charge as a function of PMT elevation angle before and after the correction. After the correction, the decrease of effective charge in the poles are suppressed.

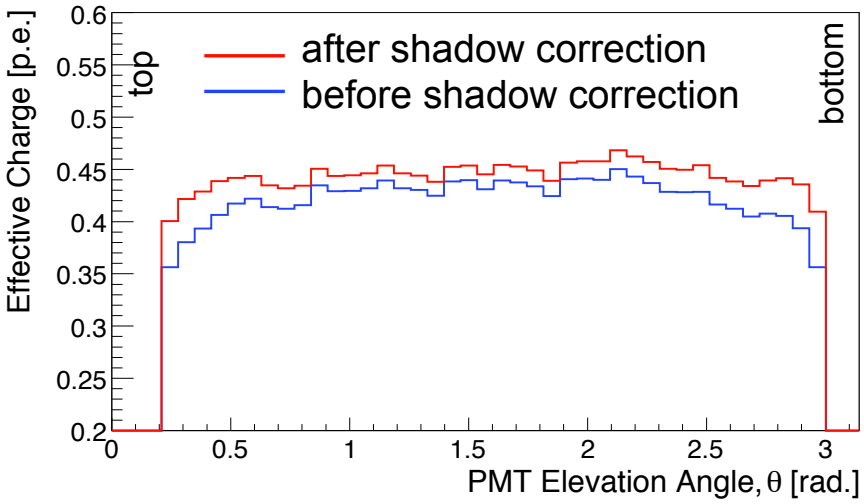

Figure 4.26: Shadow effect correction using the balloon and kevlar ropes(Watanabe 2012)

- Attenuation length
  A fraction of scintillation photon in the liquid scintillator is absorbed by the liquid scintillator itself. These photons absorption excites the liquid scintillator and cause another photon emission (re-emission). There effects need to be parameterized and called "effective attenuation length". Furthermore, the acrylic plate surrounding PMTs can reflect the scintillation or re-emission photons and affect the effective attenuation length. The effective attenuation length is estimated using neutron capture event (2.2 MeV γ-ray monochromatic spectrum) in the KamLAND dataset selected from the space perpendicular to exclude the solid angle effect for the charge, as described in Figure 4.27. This estimation are performed for each period: before 1st purification campaign, between 1st and 2nd purification campaigns and after the 2nd purification campaign because the different property of the liquid scintillator should expect different effective attenuation lengths. Figure 4.28 shows the mean corrected charge as a function of the distance from PMTs. By fitting these plots with exponential functions, the initial charge (Q_0) and the effective attenuation length (L_0) are extracted.

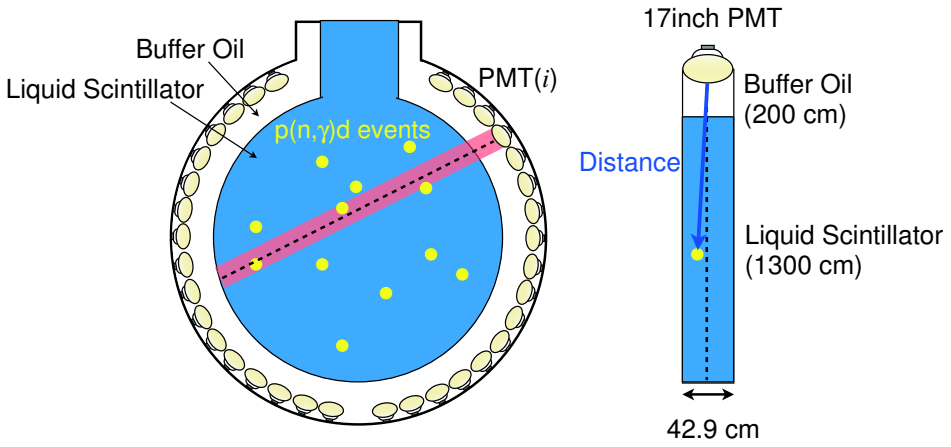

Figure 4.27: Schematic view of the attenuation length estimation(Watanabe 2012)

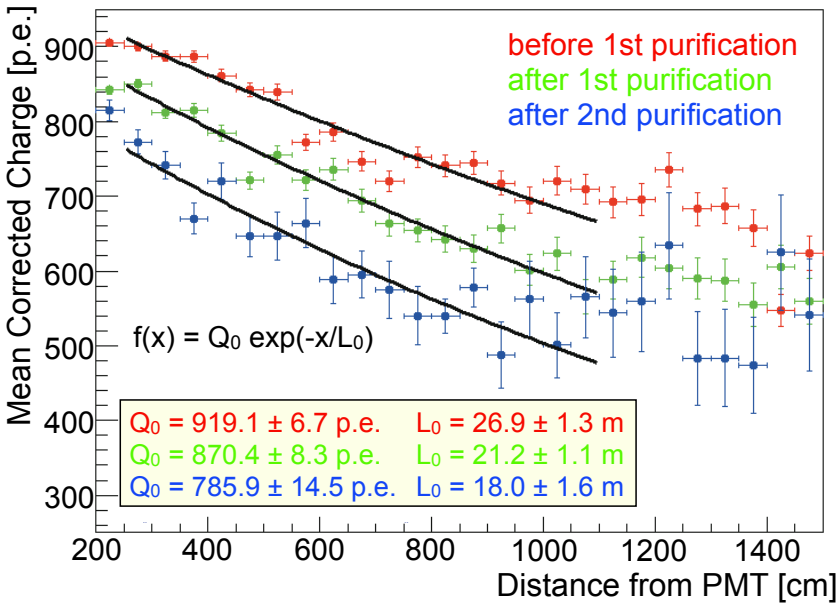

Figure 4.28: Estimation of effective attenuation length in the liquid scintillator. The slopes are fitted exponential function to extract the initial charge (Q_0) and the effective attenuation length (L_0). This estimation is performed separately for each period with different liquid scintillator status.(Watanabe 2012)

Photoelectron Detecting Efficiency

An photon detecting inefficiency comes from the 0.3 p.e. software threshold described above. Its non-linear effect on the total observed charge is parameterized and calibrated as below.

When a scintillation take a vertex, $\vec{X}$, and M photons are emitted, the average of the number of photoelectron coming out from the photo cathode of the i-th PMT, N_i, can be written as,

$$N_i = \mathrm{q} b_i(\vec{X}) M \tag{4.19}$$

where q is the quantum efficiency of the PMT and $b_i(\vec{X})$ is the fraction of photons arriving at i-th PMT, which account for the solid angle of the photocathode of the PMT viewed from the scintillation vertex, the shadow effect and the effective attenuation length described above. The normalization constant are omitted because it will be subdivided in the later calculation process.

The number of photoelectron detected in the i-th PMT, n, should follow a Poisson distribution whose mean is N_i, that is,

$$\mathrm{P}(n; N_i) = \frac{N_i^n \mathrm{e}^{-N_i}}{n!} \tag{4.20}$$

and the expected value of charge detected by i-th PMT, $Q_i^{\mathrm{expected-no-threshold}}$, is

$$Q_i^{\mathrm{expected-no-threshold}} \equiv q_1 N_i = \sum_{n \geq 1} q_n \mathrm{P}(n; N_i) \tag{4.21}$$

where q_n means the average value of the observed charge when the PMT detects n photoelectrons.

Using ϵ as the efficiency by the 0.3 p.e. software threshold, the effective distribution which n should follow, $P_{eff}(n; N_i)$, is

$$\begin{aligned} P_{eff}(0; N_i) &= P(0; N_i) + (1-\epsilon) P(1; N_i) \\ P_{eff}(1; N_i) &= \epsilon P(1; N_i) \\ P_{eff}(n; N_i) &\simeq P(1; N_i) \qquad\qquad (2 \leq n) \end{aligned} \tag{4.22}$$

Then, the expected value of charge detected by i-th PMT taking the software threshold effect, Q_i^{expected}, can be written using the average value of the observed charge in single photoelectron detection without the threshold effect, $q_{1,\mathrm{residual}}$, as

$$\begin{aligned} Q_i^{\mathrm{expected}} &= q_{1,\mathrm{residual}} \mathrm{P}_{eff}(1; N_i) + \sum_{n \geq 2} q_n \mathrm{P}_{eff}(n; N_i) \\ &= \sum_{n \geq 1} q_n \mathrm{P}(n; N_i) - q_1 \mathrm{P}(1; N_i) + q_{1,\mathrm{residual}} \mathrm{P}_{eff}(1; N_i) \\ &= Q_i^{\mathrm{expected-no-threshold}} - q_1 N_i \mathrm{e}^{-N_i} + \epsilon q_{1,\mathrm{residual}} N_i \mathrm{e}^{-N_i} \\ &= q_1 N_i - q_1 N_i \mathrm{e}^{-N_i} + \epsilon q_{1,\mathrm{residual}} N_i \mathrm{e}^{-N_i} \\ &= q_1 N_i \left(1 - \left(1 - \frac{q_{1,\mathrm{residual}}}{q_1} \epsilon \right) \mathrm{e}^{-N_i} \right) \\ &= Q_i^{\mathrm{expected-no-threshold}} (1 - \mathrm{e}^{-N_i} \delta) \end{aligned} \tag{4.23}$$

Here δ present the effect of the software threshold and defined as

$$\delta \equiv 1 - \frac{q_{1,\mathrm{residual}}}{q_1}\epsilon \tag{4.24}$$

The parameter δ is measured to be 0.03 using the source calibraiton data of ^{60}Co (2γ, 1.173 MeV + 1.333 MeV) and ^{65}Zn (γ, 1.116 MeV).

The expected number of detected photoelectrons in the i-th PMT, μ_i^{signal}, can be calculated by allocating the total observed charge to each PMT as

$$\mu_i^{\mathrm{signal}} = \sum_{j\in\mathrm{GoodPMT}} Q_i^{\mathrm{observed}} \times \frac{Q_i^{\mathrm{expected}}/q_i}{\sum_{j\in\mathrm{GoodPMT}} Q_j^{\mathrm{expected}}} \tag{4.25}$$

where "Good PMT" is a set of non-bad PMTs. This "μ_i^{signal}" as a function of M, i.e. as a function of visible energy, is one of the fundamental components of the likelihood function to estimate the visible energy.

Algorithm of The Energy Reconstruction

The likelihood function for the energy reconstruction, $\mathcal{L}$, is defined as

$$\mathcal{L} \equiv \prod_{i\in\text{no-hit}} \mathrm{P}^{\mathrm{hit}}(0|\mu_i) \times \prod_{i\in\mathrm{hit}} \left\{ \sum_{j=1}^{\infty} \mathrm{P}^{\mathrm{hit}}(j|\mu_i)\mathrm{PDF}^{\mathrm{charge}}(q_i, j|\mu_i) \right\} \mathrm{PDF}^{\mathrm{time}}(t_i|\mu_i) \tag{4.26}$$

where "no-hit" and "hit" present the set of PMTs which did not hit and hit, respectively. j, q_i and t_i is the number of detected photoelectron, the detected charge and the hit timing of the first photon detection. μ_i the expected number of detected photoelectron calculated from μ_i^{signal} (described above) and μ_i^{dark} (estimated in Sec.4.5) as

$$\mu_i = \mu_i^{\mathrm{signal}} + \mu_i^{\mathrm{dark}} \tag{4.27}$$

$\mathrm{P}^{\mathrm{hit}}(0|\mu_i)$ and $\mathrm{P}^{\mathrm{hit}}(1 \le |\mu_i)$ are non-hit and hit probability, respectively, under the expected number of detected photoelectron μ_i. Since the number of detected photoelectron follows a Poisson distribution, they can be written down as,

$$\begin{aligned} \mathrm{P}^{\mathrm{hit}}(0|\mu_i) &= \mathrm{e}^{-\mu_i} + (1-\epsilon)\mu_i\mathrm{e}^{-\mu_i} \\ \mathrm{P}^{\mathrm{hit}}(1 \le |\mu_i) &= 1 - \mathrm{P}^{\mathrm{hit}}(0|\mu_i) \end{aligned} \tag{4.28}$$

$\mathrm{PDF}^{\mathrm{charge}}(q_i, j|\mu_i)$ is the Probability-Density-Function (PDF) of charge and modeled by a combination of Poisson and Gaussian distribution as

$$\sum_{j=1}^{\infty} \mathrm{P}^{\mathrm{hit}}(j|\mu_i)\mathrm{PDF}^{\mathrm{charge}}(q_i, j|\mu_i) = \sum_{j=1}^{\infty} \left\{ \frac{\mu_i^j}{j!}\mathrm{e}^{-\mu_i} \times \frac{1}{\sqrt{2\pi j\sigma^2}}\mathrm{e}^{-\frac{(q_i-j)^2}{2j\sigma^2}} \right\} \tag{4.29}$$

where σ is the standard deviation of the 1 p.e. charge distribution from source calibration data.

The PDF of time, $\mathrm{PDF}^{\mathrm{time}}(t_i|\mu_i)$, consist of the hit timing distribution, $\phi_i(t_i)$, created from the source calibration data and dark hit rate, d_i, as

$$\mathrm{PDF}^{\mathrm{time}}(t_i|\mu_i) = \frac{(a_i\mu_i^{\mathrm{signal}})\phi_i(t_i) + d_i}{\mu_i} \tag{4.30}$$

with a set of normalization factors "a_i".

The visible energy is reconstructed by searching for the maximum likelihood point of $\mathcal{L}$, that is, finding the visible energy, E_{vis} that leads to

$$\frac{\partial \log \mathcal{L}}{\partial E_{\mathrm{vis}}} = 0 \tag{4.31}$$

with the Newton-Raphson method (Garrett 2015).

Combination of 17inch and 20inch PMTs

20inch PMTs have been used from Feb. 2003. Since they have no clear single photoelectron peak and their charge-energy linearity is different from that of 17inch PMTs, the energy reconstruction procedure described above is implemented in 17inch PMTs and 20inch PMTs, independently. Then, the visible energy is calculated with combining factor, α, as

$$E_{\mathrm{vis}} = (1-\alpha)E_{\mathrm{vis}}^{\mathrm{17inch}} + \alpha E_{\mathrm{vis}}^{\mathrm{20inch}} \tag{4.32}$$

Here, α is determined to give the best energy resolution using the various calibration data as Figure 4.29, and $\alpha = 0.3$ is used.

The deviation of the combined visible energy from "17inch-only" visible energy is also evaluated with the source calibration (low energy region) and the spallation products (high energy region) as Figure 4.30. The deviation of the combined energy is less than 0.6%.

4.7.3 Detector Energy Scale Model

The non-linear relation between the visible energy and the actual energy deposit, i.e. real energy, is modeled using Geant4 simulation tool kit(Agostinelli et al. 2003) and following sources of various particle types.

- γ-ray source : ^{203}Hg, ^{137}Cs, ^{68}Ge, ^{60}Co, spallation neutron capture on proton, spallation neutron capture on ^{12}C
- Positron source : ^{10}C, ^{11}C
- Electron source : spallation ^{12}B

Figure 4.31 and Figure 4.32 show the verified detector energy scale model (relationship between the visible energy and the real energy) before and after the purifications, respectively.

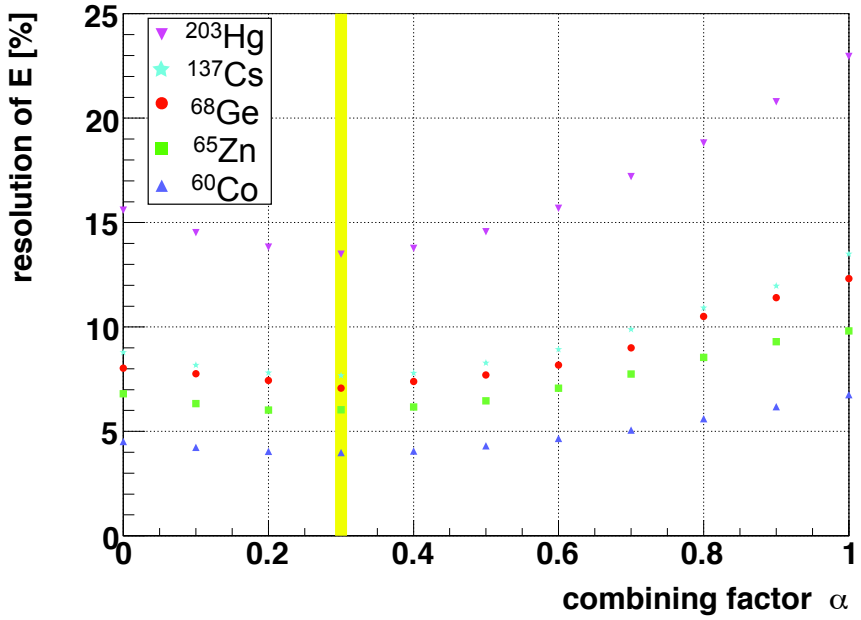

Figure 4.29: The combined energy resolution as a function of the combining factor, α, in various type of source calibration. The best α is found at 0.3 (yellow line) (Watanabe 2012)

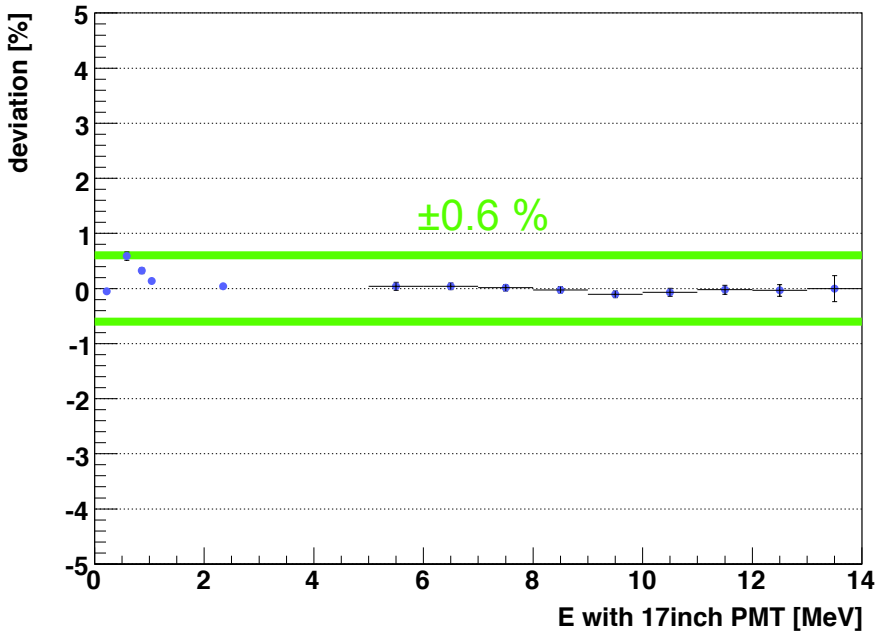

Figure 4.30: Combined visible energy deviation as a function of the "17inch-only" visible energy(Watanabe 2012)

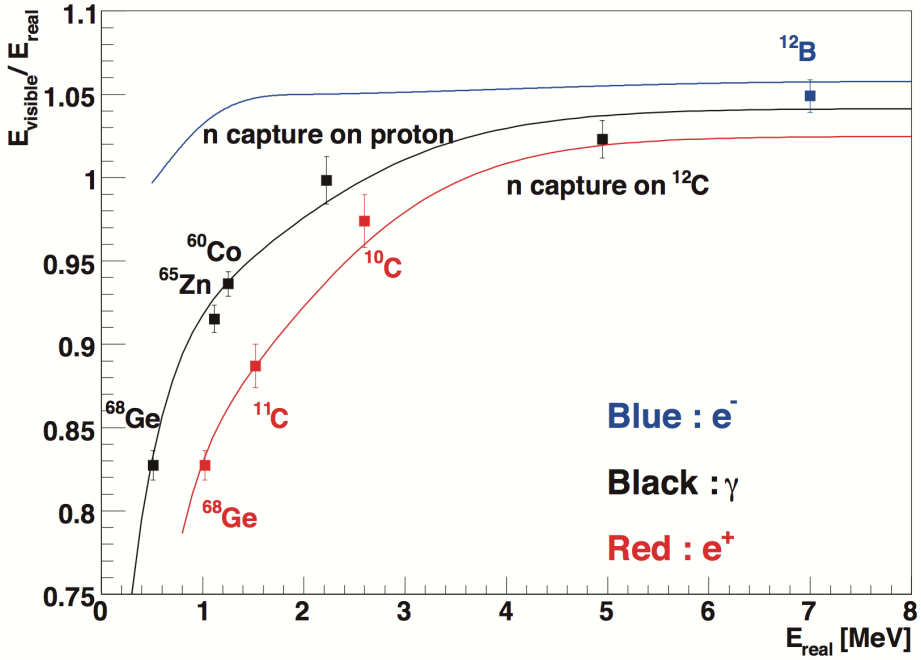

Figure 4.31: Detector energy scale model to various particle types before purifications(Ichimura 2008)

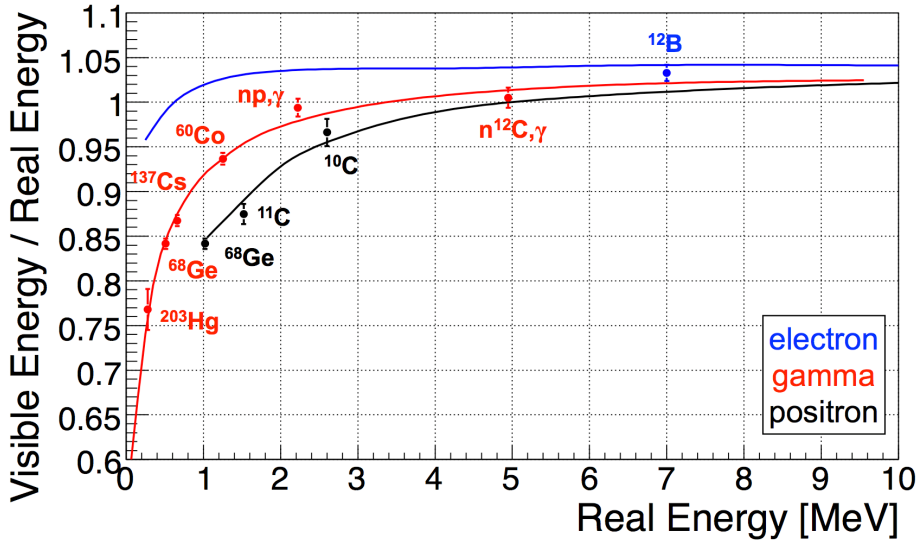

Figure 4.32: Detector energy scale model to various particle types after purifications(Nakajima 2009)

4.8 Vertex and Energy Uncertainty

4.8.1 Vertex Miss-Reconstruction Probability

There is a possibility that a vertex of a scintillation is reconstructed at a distance from its actual position. If an IBD event is reconstructed outside the effective volume, it makes an systematic bias in the antineutrino analysis. Therefore, the probability of miss reconstruction, or "miss-reconstruction probability", is estimated with ^{60}Co source calibration installed at the center of the ID. The miss-reconstruction probability is defined as

$$P_{\text{miss-recon.}} = \frac{N(^{60}\text{Co event with } \Delta R \geq \text{R}_{\text{cut}}) - N(\text{BG event with } \Delta R \geq \text{R}_{\text{cut}})}{N(^{60}\text{Co event}) - N(\text{BG event})} \tag{4.33}$$

where $\text{R}_{\text{cut}} = 300$ cm is determined enough larger than the ^{60}Co γ attenuation length. To account for only miss-reconstructed ^{60}Co events, the background (BG) contribution is evaluated in advance from special low-trigger-threshold run and subtracted.

Figure 4.33–4.35 show the estimation process and estimated miss-reconstruction probability for each source z-position. The miss-reconstruction probability is evaluate to be less than 0.2% in each period, which is assigned as a systematic uncertainty related to the vertex miss-reconstruction.

4.8.2 Fiducial Volume Uncertainty

In antienutrino analysis, a 6.0-m-radius spherical volume cut is applied as described in Sec.5.4. The exposure is calculated with a geometrical volume of 6-m-radius sphere and measured density of the liquid scintillator. If there is a bias in the reconstructed vertex, it leads to a difference between the calculated exposure and the actual exposure. So, the vertex bias is studied with 4-π calibration (Sec.3.3.7).

The 4-π calibration is a off-axis calibration and was performed in 2006, 2007 and 2011. Radioactive sources are deployed within 5.5 m radius in the ID. The uncertainty in 6 m radius, which is used in the antineutrino analysis, is calculated from the 4-π calibration result and scaling a factor from 5.5 m to 6 m studied using spallation products. Spallation ^{12}B/^{12}N is uniformly and constantly generated by cosmic muon and useful to study fiducial volume.

Fiducial volume uncertainty in Period1

The 4-π calibration in 2006 is used to estimate the uncertainty in Period1. See Sec.5.1.1 for the definition of "Period". Ichimura (2008) analyzed the 4-π calibration run in 2006 and obtained the reconstructed vertex bias within 5.5 m to be 3 cm, which corresponds to a 1.6% fiducial volume uncertainty. Using P_r as the number of protons in radius r [cm] spherical volume, it turns

$$\frac{\Delta P_{550}}{P_{550}} = 0.016 \tag{4.34}$$

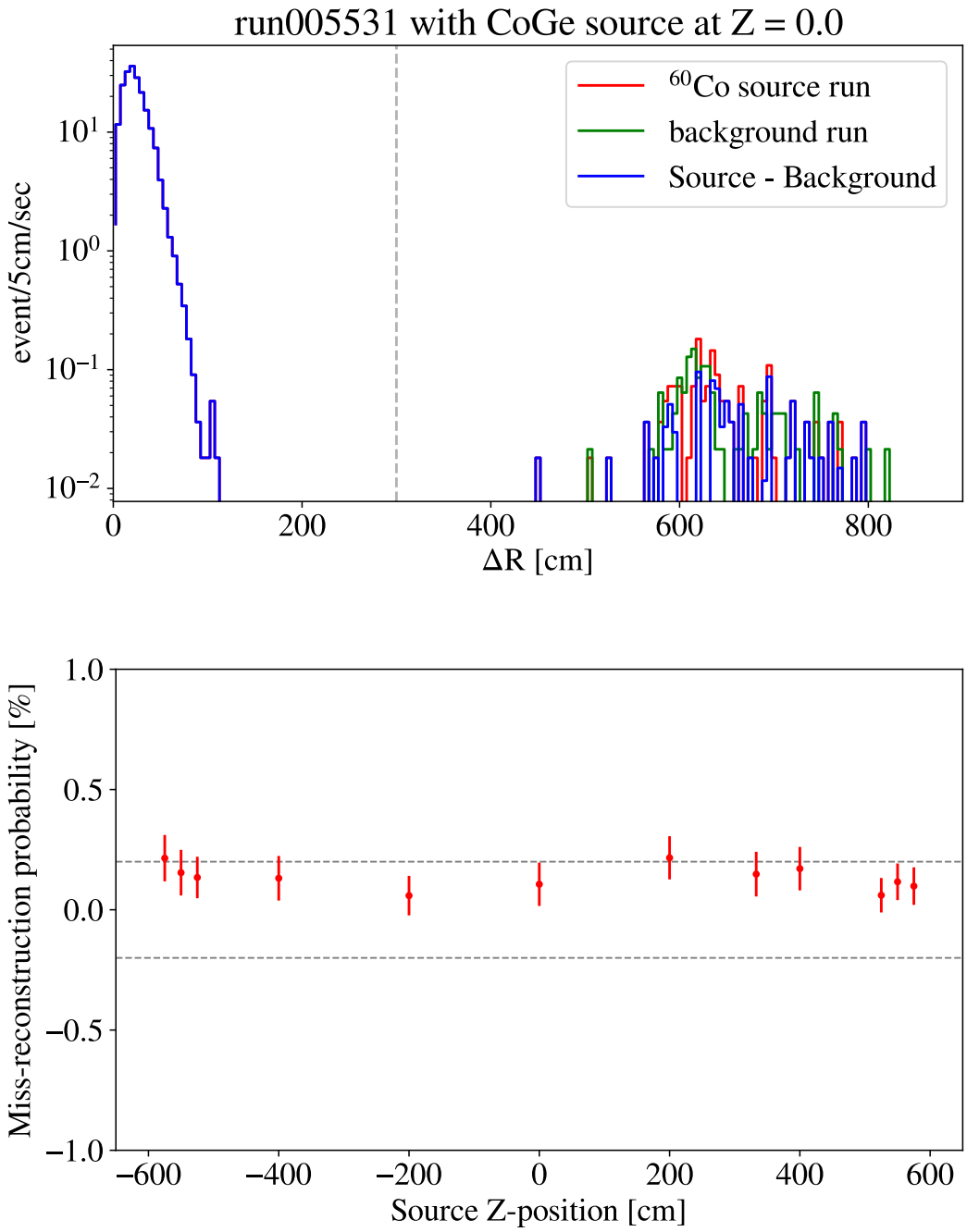

Figure 4.33: Miss-reconstruction probability estimation with ^{60}Co source in Period1

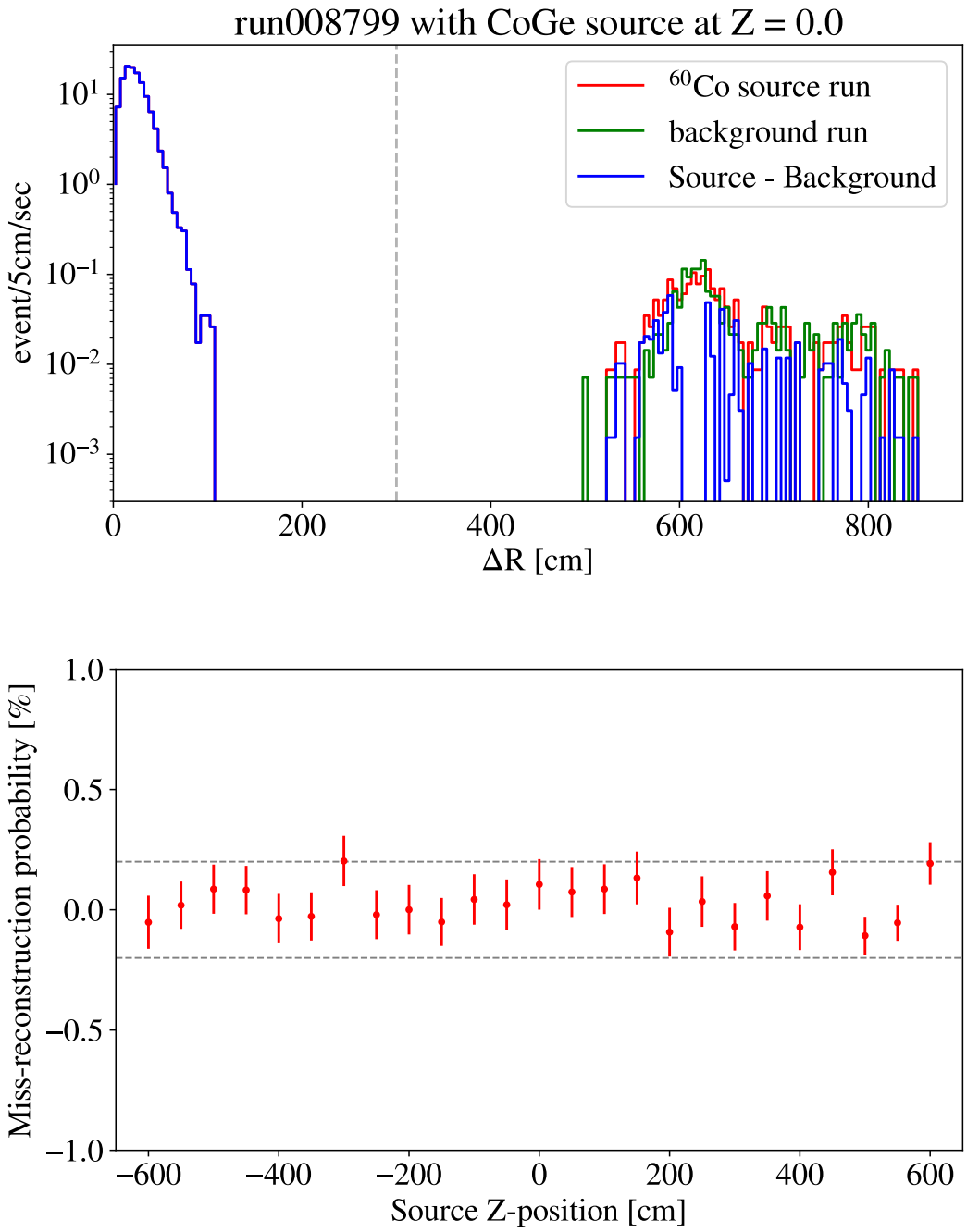

Figure 4.34: Miss-reconstruction probability estimation with ^{60}Co source in Period2

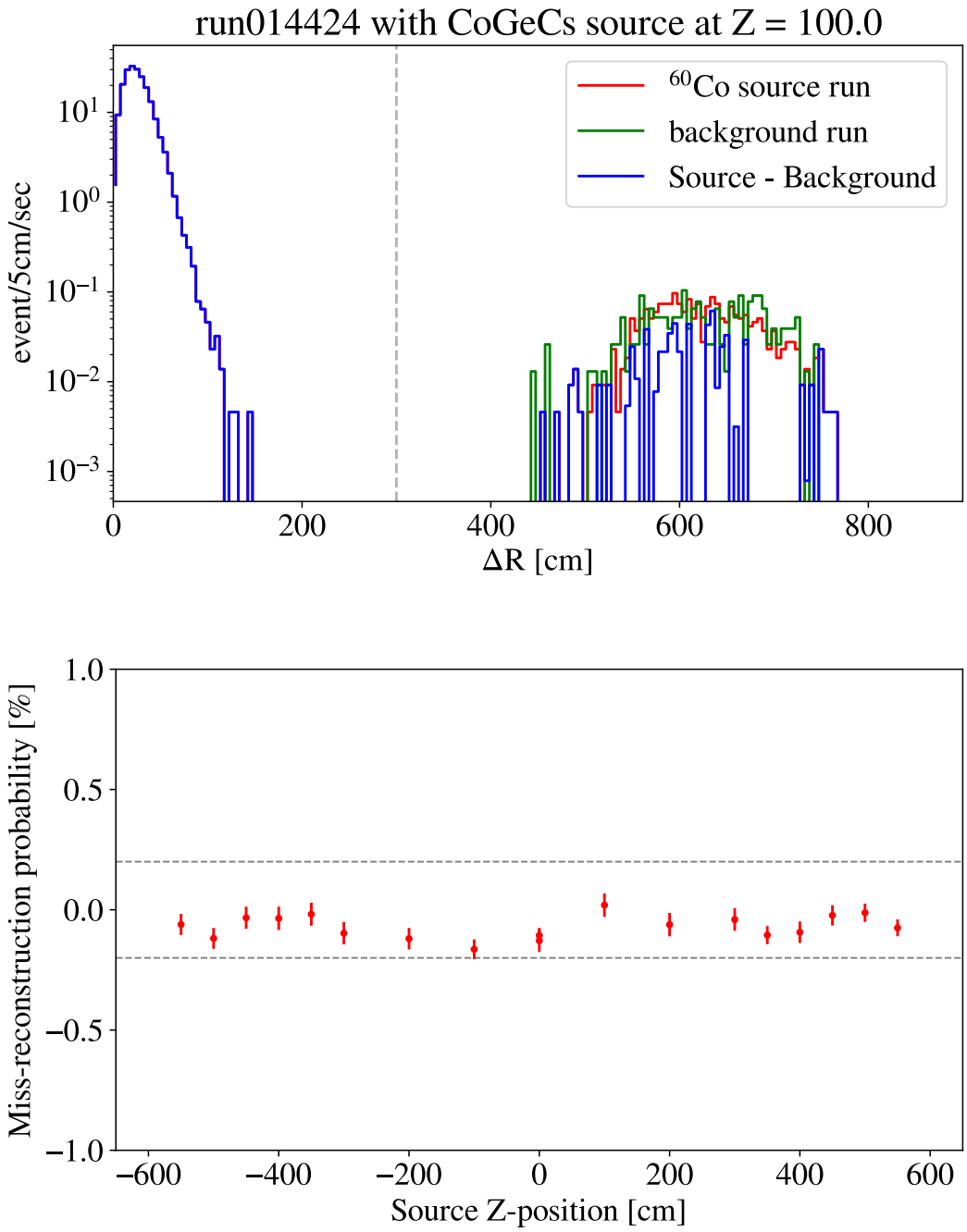

Figure 4.35: Miss-reconstruction probability estimation with ^{60}Co source in Period3

The scaling factor α in

$$P_{600} = \alpha P_{550} \tag{4.35}$$

is estimated using the number of spallation ^{12}B/^{12}N event within 550 cm and 600 cm (Figure 4.36). It gives

$$\begin{aligned} \frac{N_{550}}{N_{600}} &= 0.768 \pm 0.002 \\ \leftrightarrow \frac{N_{600}}{N_{550}} &= 1.302 \pm 0.003 \end{aligned} \tag{4.36}$$

On the other hand, a geometrical volume calculation gives

$$\frac{V_{600}}{V_{550}} = \frac{600^3}{550^3} = 1.2983 \tag{4.37}$$

From Eq. 4.36 and Eq. 4.37, the relative uncertainty of α is calculated to be

$$\frac{\Delta\alpha}{\alpha} = \frac{\sqrt{(1.302 - 1.2983)^2 + 0.003^2}}{1.2983} = 0.00367 \tag{4.38}$$

Finally, from Eq. 4.34 and Eq. 4.38, the fiducial volume uncertainty in Period1 is calculated as

$$\begin{aligned} \Delta P_{600} &= \sqrt{(P_{550} \cdot \Delta\alpha) + (\alpha \cdot \Delta P_{550})} \\ \frac{\Delta P_{600}}{P_{600}} &= \sqrt{\left(\frac{\Delta P_{550}}{P_{550}}\right)^2 + \left(\frac{\Delta\alpha}{\alpha}\right)^2} \\ &= 0.0165 \end{aligned} \tag{4.39}$$

A 1.65% systematic uncertainty from the fiducial volume uncertainty is assigned in Period1.

Fiducial volume uncertainty in Period2

The 4-π calibration in 2011 is available for Period2. It gives a fiducial volume uncertainty within 550 cm to be

$$\frac{\Delta P_{550}}{P_{550}} = 0.033 \tag{4.40}$$

The spallation ^{12}B/^{12}N event within 550 cm and 600 cm gives

$$\begin{aligned} \frac{N_{550}}{N_{600}} &= 0.77535 \pm 0.0106 \\ \leftrightarrow \frac{N_{600}}{N_{550}} &= 1.2897 \pm 0.01763 \end{aligned} \tag{4.41}$$

Then, the relative uncertainty of the 550-cm-to-600-cm scaling factor α is

$$\frac{\Delta\alpha}{\alpha} = \frac{\sqrt{(1.2897 - 1.2983)^2 + 0.0176^2}}{1.2983} = 0.01959 \tag{4.42}$$

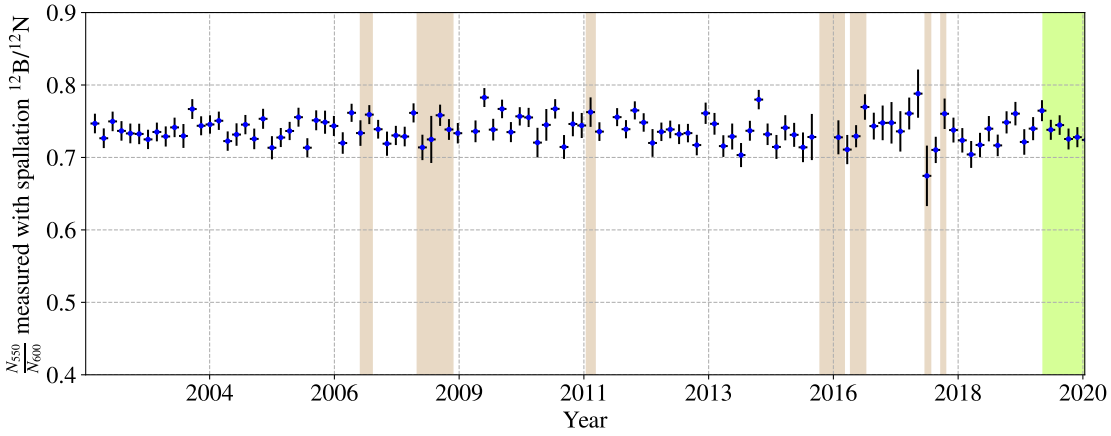

Figure 4.36: Time variation of spallation ^{12}B/^{12}N event rate ratio within 550 cm to 600 cm. Each point represent one-month-average. The value for each period is obtained by calculating the live-time-weighted average.

Finally, from Eq.4.40 and Eq.4.42, the fiducial uncertainty in Period2 is calculated as

$$\begin{aligned} \Delta P_{600} &= \sqrt{(P_{550} \cdot \Delta\alpha) + (\alpha \cdot \Delta P_{550})} \\ \frac{\Delta P_{600}}{P_{600}} &= \sqrt{\left(\frac{\Delta P_{550}}{P_{550}}\right)^2 + \left(\frac{\Delta\alpha}{\alpha}\right)^2} \\ &= 0.0386 \end{aligned} \tag{4.43}$$

A 3.86% systematic uncertainty from the fiducial volume uncertainty is assigned in Period2

Fiducial volume uncertainty in Period3

There are no 4-π calibration available in Period3. The fiducial volume uncertainty is estimated by adding the time variation of spallation ^{12}B/^{12}N event rate to the fiducial volume uncertainty in Period2.

Supposing the number of protons in the fiducial volume in Period3 is P_{600}^{Period3} and it is connected from P_{600} in Period2 as

$$P_{600}^{\text{Period3}} = \beta P_{600} \tag{4.44}$$

β is estimated with spallation ^{12}B/^{12}N events. The number of spallation ^{12}B/^{12}N events in 600-m-radius fiducial and in the total volume, i.e. no vertex cut, (Figure 4.37) are

$$\begin{aligned} \left(\frac{N_{600}}{N_{\text{total}}}\right)_{\text{Period2}} &= 0.7848 \pm 0.002151 \\ \left(\frac{N_{600}}{N_{\text{total}}}\right)_{\text{Period3}} &= 0.8001 \pm 0.001645 \end{aligned} \tag{4.45}$$

The errors in Eq. 4.45 are statistical error only because the others are canceled in the following calculation. Then, this gives

$$\beta = \frac{0.8001}{0.7848} = 1.01958 \tag{4.46}$$

and

$$\begin{aligned} \frac{\Delta\beta}{\beta} &= 0.0196 + \sqrt{\left(\frac{0.001645}{0.7848}\right)^2 - \left(\frac{0.8001 \times 0.002151}{0.7848^2}\right)^2} \\ &= 0.023 \end{aligned} \tag{4.47}$$

Thus, the fiducial volume uncertainty in Period3 is calculated as

$$\begin{aligned} \Delta P_{600}^{\mathrm{Period3}} &= \sqrt{(P_{600} \cdot \Delta\beta) + (\beta \cdot \Delta P_{600})} \\ \frac{\Delta P_{600}^{\mathrm{Period3}}}{P_{600}^{\mathrm{Period3}}} &= \sqrt{\left(\frac{\Delta P_{600}}{P_{600}}\right)^2 + \left(\frac{\Delta\beta}{\beta}\right)^2} \\ &= 0.045 \end{aligned} \tag{4.48}$$

Note that $\frac{\Delta P_{600}}{P_{600}}$ is the fiducial volume uncertainty in Period2.

A 4.50% systematic uncertainty from the fiducial volume is assigned in Period3.

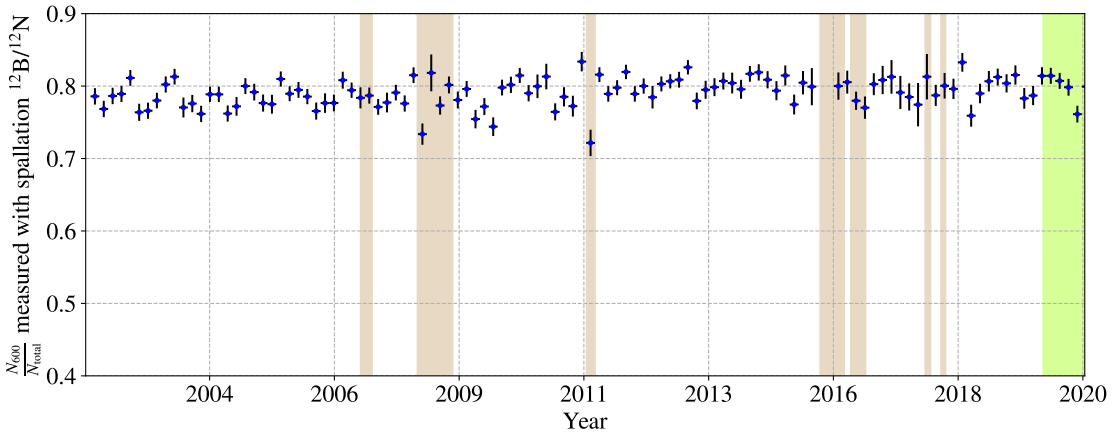

Figure 4.37: Time variation of spallation ^{12}B/^{12}N event rate ratio within 600 cm to the full volume. Each point represent one-month-average. The value for each period is obtained by calculating the live-time-weighted average.

Chapter 5

Anti-neutrino Event Selection

Anti-neutrino events are selected by various criteria described in this chapter. This study uses the acquired data from 2002 March to 2020 December, which include about 10 year of the low-reactor period. In advance of the event selection, the KamLAND observed data is classified by its "data quality", and a number of vetoes are applied to reject background contaminations. The anti-neutrino event, i.e. the inverse-beta decay, candidate is identified by the delayed-coincidence strategy as described in Sec.3.4. Furthermore, a likelihood-based event selection as applied to improve the purity of the antineutrino profiles. The Uncertainties of the selection is also described in this chapter.

5.1 Dataset

5.1.1 Data Periods

This study used the data acquired from 2002 March to 2020 December. The dataset is divided into three periods as shown in Table 5.1. The boundary between Period1 and Period2 is the start of the 1st purification campaign. Since the ^{210}Pb contamination in the liquid scintillator was effectively removed by the purifications(Sec.3.3.6), the $^{13}\mathrm{C}(\alpha, n)^{16*}\mathrm{O}$ background drastically decreased in Period2. The start of Period3 corresponds to the installation of the mini balloon described in Sec.3.5.2. It also coincidentally corresponds to the start of the low-reactor period, which started with the Japanese reactor's shutdown due to the Great East Japan Earthquake and the Fukushima-I reactor accident in 2011 March. Although the result of a great tragedy, this period provides us the opportunity to measure the geoneutino flux precisely. In particular, it enabled us to perform geoneutrino spectroscopy, separate the uranium and thorium contribution, thus probe the abundances of major heat-producing elements in the Earth independently from each other. This is a decisive key of this study.

Table 5.1: Summary of dataset

Period	date	live time [days]	detector status
1	2002 Mar. – 2007 May	1485.5	before purifications
2	2007 May – 2011 Aug.	1151.5	during and after purifications
3	2011 Aug. – 2020 Dec.	2590.0	after the start of KamLAND-Zen 400
total	2002 Mar. – 2020 Dec.	5227.0	

5.1.2 Run selection

The KamLAND DAQ is switched typically once every 24 hours, and each period is called a "run". This run switch is also performed when some troubles or on-side hardware changes happen. However, not all the data acquired is used in the analysis. Some runs are not appropriate for the physics analysis due to some fails of the high-voltage supplies, readout electronics, and data transition. Each run is checked for the following items, and runs with anomalies are excluded from the analysis to keep the data quality.

- Number of bad channels
  Runs with an abnormally large number of bad channels compared to the preceding and following runs are excluded from the analysis because they indicate some kind of hardware problem.

- Trigger rate, muon rate and low-energy event rate
  These parameters are monitored by online analysis in parallel with DAQ, and if they show unusually large values, such runs are excluded as it implies some anomalies in the data acquisition.

- Run time
  Runs with too short running time to apply run-by-run corrections described in Sec.4.3 can not be used for the analysis and not used.

There is a possibility that a run may have anomalies above in a part of the entire run time. Thus, the runs are classified into the following three categories.

- Good run
  No problem happened. These runs are used in the analysis.

- Half-bad run
  Partly problem happened. These runs are used in the analysis after cutting off the abnormal period as "dead time".

- Bad run
  Heavy problem happened. These runs are not used in the analysis.

5.1.3 Livetime Calculation

The live time is defined as the active time period of the detector for neutrino observation, and calculated run-by-run from the following items.

- Run time
  DAQ-running time defined as the time difference between the absolute time of the first event and the last event in the run
- Dead time
  Time of no-data taking or abnormal-data taking
- Veto time
  Time to be rejected by the muon veto (Sec.5.3) for the background rejection in offline analysis

The dead time is further categorized into and calculated by summing the followings

- Bad run
  As described above, bad runs are not used, i.e. the whole time of such run is treated as dead time.
- Half-bad run
  As described above, a part of half-bad run with low-data qualities are cut off as dead time. The past is used.
- Trigger disable period
  If the KamFEE Trigger module is busy and fails to issue a trigger correctly, it is recorded as an "trigger-disable flag". Such period is identified as dead time and excluded from the dataset.
- Trigger dead period
  Some network problem may cause broken data packets. Such incident is identified by searching for large time intervals more than 100 μs between each history trigger event.

The uncertainty of dead time is calculated by counting 1PPS trigger events. The 1PPS trigger is a forced trigger issued every seconds in sync with GPS, and thus the number of 1PPS-triggered event ideally corresponds to the veto-time-subtracted run time. The unknown dead time ratio is defined as

$$R \equiv= \left| 1 - \frac{(\text{Number of 1PPS trigger})}{(\text{run time}) - (\text{veto time})} \right| \tag{5.1}$$

Figure 5.1 and Figure 5.2 shows the distribution of the unknown dead time ratio before and after the purifications. The average unknown dead time ratio is estimated to be about 0.03% and 0.006%, respectively.

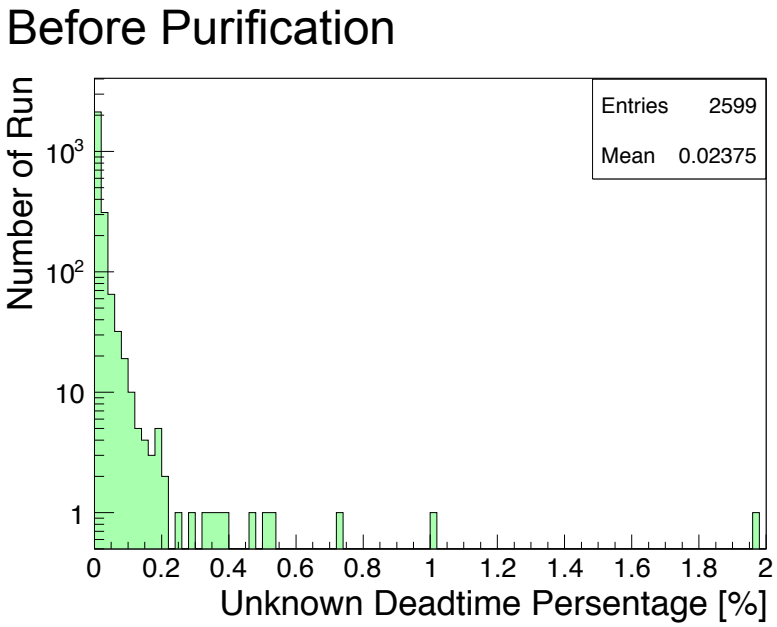

Figure 5.1: Unknown dead time ratio before the purifications(Watanabe 2012)

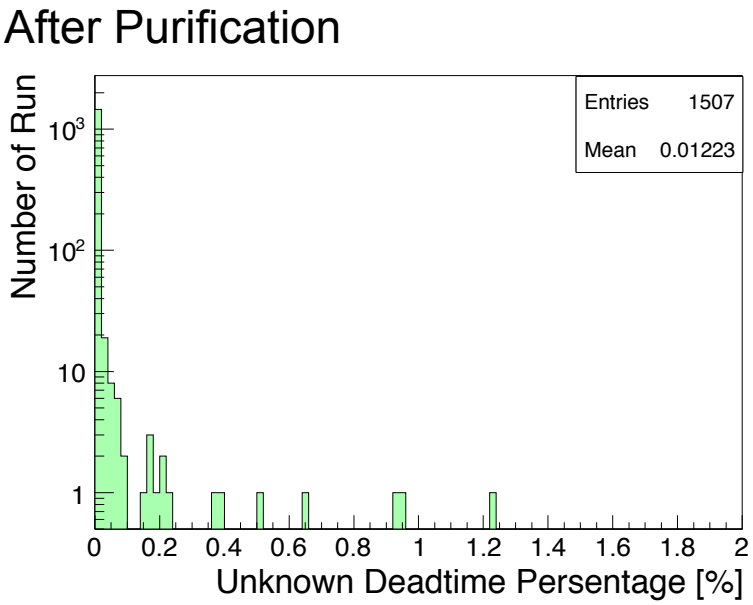

Figure 5.2: Unknown dead time ratio after the purifications(Watanabe 2012)

After all, the live time of each run is calculated from the run time, dead time and veto time. To take the overlaps of veto times into accounts, the live time is defined as follows using the pseudo dataset with an uniform time and vertex distribution.

$$(\text{live time}) = \frac{(\text{number of events after applying all cuts})}{(\text{number of the pseudo events})} \cdot (\text{run time}) \tag{5.2}$$

The cumulative live time against calendar time is plotted in Figure 5.3. Besides, the live time ratio to the run time is shown in Figure 5.4. Since recently KamLAND has increasing bad channels and trigger problems, the live time ratio has been gradually increasing.

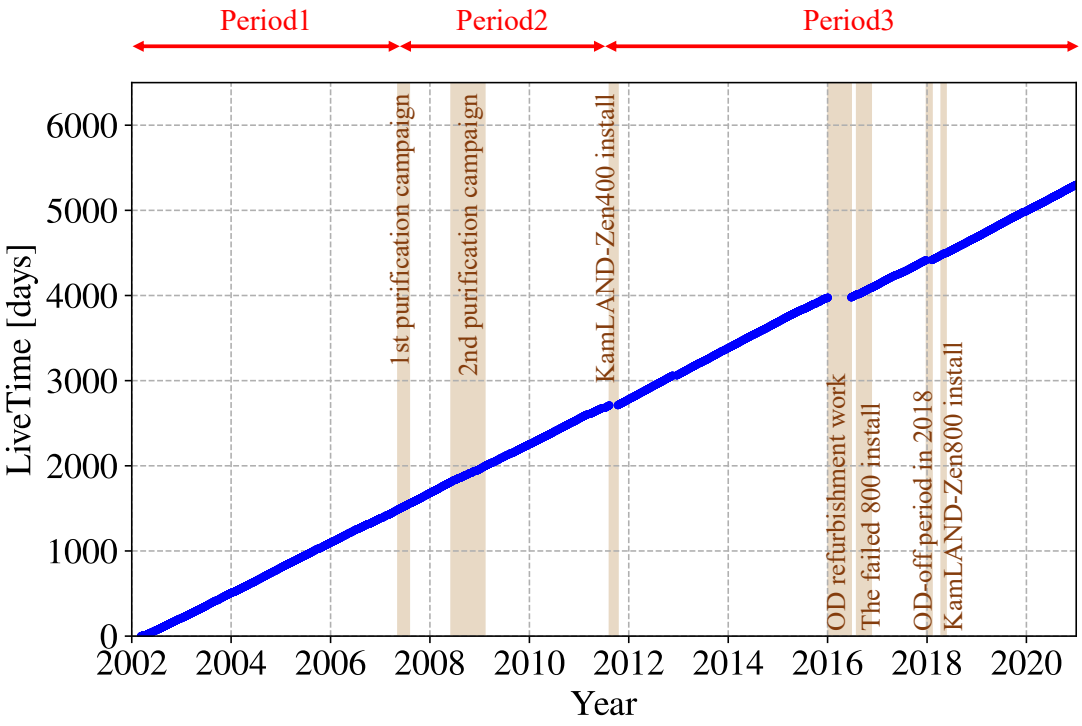

Figure 5.3: Year and cumulative livetime

The uncertainty of this calculation is evaluated from the statistical error. Given the number of the pseudo data is 10^7 for each run and the vetoed event is about 1% for good runs, the statistical uncertainty under the binominal distribution is about 0.003%, which is smaller than the unknown dead time ratio. Thus, the unknown dead time ratio for before and after the purifications, i.e. 0.03% and 0.006%, are assigned as the uncertainties of the live time.

5.2 Physics Event Selection

Non-physical events originating from electric noise, flasher PMTs and PMT ringings are also included in the KamLAND observation data. Those events are removed prior

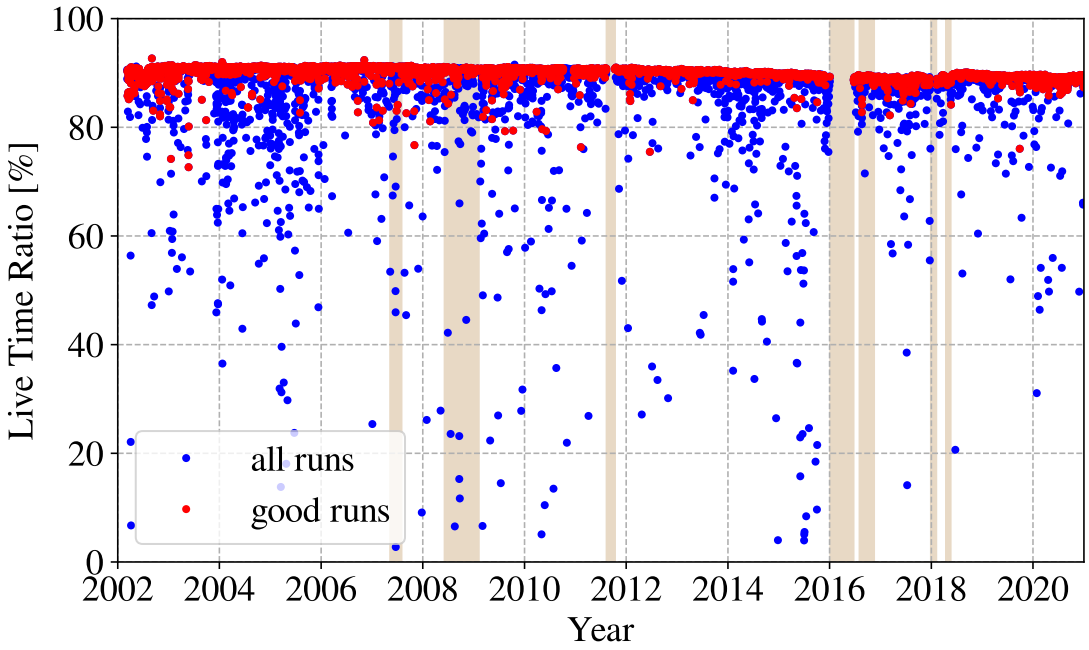

Figure 5.4: the livetime ratio to the run time

to the physics event selection by the methods described in this section.

The total charge distribution in various type of events are shown in Figure 5.5. The low-energy event, i.e. the antineutrino reaction candidates, have the charges around 10^2–10^3 photoelectrons. Most muon events have charges more than 10^3 photoelectron, whereas most of muon-related events have charge less than muon event but removed by the "2 msec after muon" veto. On the other hands, noise event originating from PMT or electronics noise is dominant in the charge region less than 10^2 photoelectrons.

5.2.1 Noise Event Cut

The non-physical noise event originating from PMT noise or electronics noise is characterized by their abnormal hit timing cluster. To find if a event has hit timing cluster, a parameter "N_{100}" is defined as the total number of hit PMT in a 100 ns time window. The time window for counting N_{100} is shifted in the event time window to get the largest value of N_{100}. The noise events are selected by the following criteria.

$$N_{100} \leq \frac{N_{\mathrm{hit}} + 50}{2} \tag{5.3}$$

where N_{hit} donates the number of PMT hit of the inner detector, including both 17inch and 20inch PMTs.

Figure 5.6 shows the corrections between N_{100} and N_{hit} in a source calibration run in 2017 with a Co-Ge-Cs composite source, where the noise cut criteria is shown as the green line.

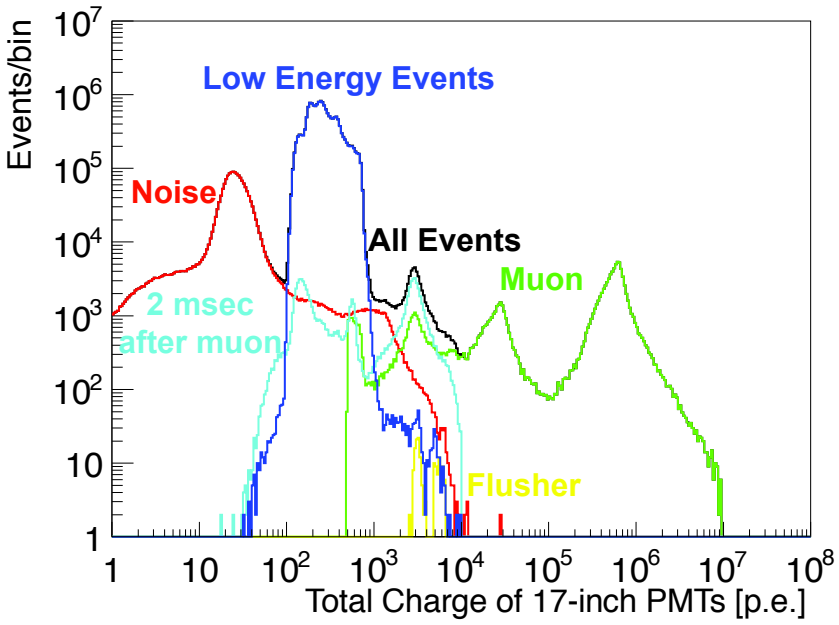

Figure 5.5: The total charge distribution of the 17inch PMTs in various type of events(Watanabe 2012)

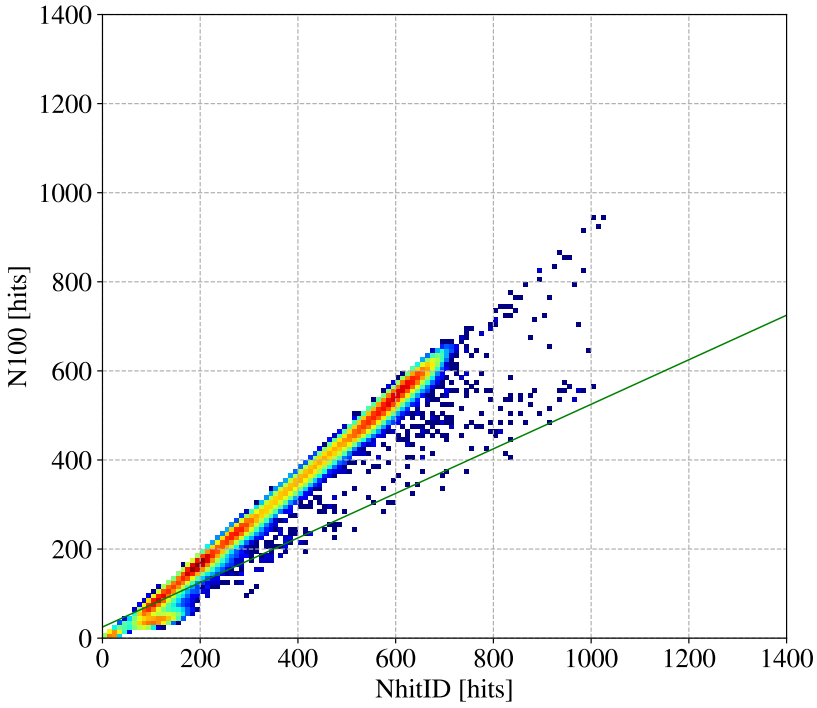

Figure 5.6: Noise event cut criteria

This cut criteria may accidentally remove an IBD event candidate with the incident neutrino energy near the reaction threshold. Therefore, the inefficiency by the noise cut is evaluated using source calibration data. ^{68}Ge is useful to check it since it emits thermal positron, i.e. annihilation 2 γ's, which has almost the same properties as the IBD prompt event with the least prompt scintillation.

The N_{100}-$N_{\rm hit}$ plots with the noise cut criteria for Period1 (2006/Apr., Co-Ge composite source), Period2 (2009/Jul., Co-Ge composite source) and Period3 (2017/Jul., Co-Ge-Cs composite source) are shown in Figure 5.7, Figure 5.8 and Figure 5.9, respectively. The ^{68}Ge events are easily selected by the reconstructed energy.

From these calibration data, the inefficiencies are found to be $< 2.7 \times 10^{-3}$% (upper limit), $< 4.9 \times 10^{-3}$% (upper limit) and $< 2.9 \times 10^{-2}$% for Period1, 2 and 3, respectively. These inefficiencies are assigned to the systematic uncertainties.

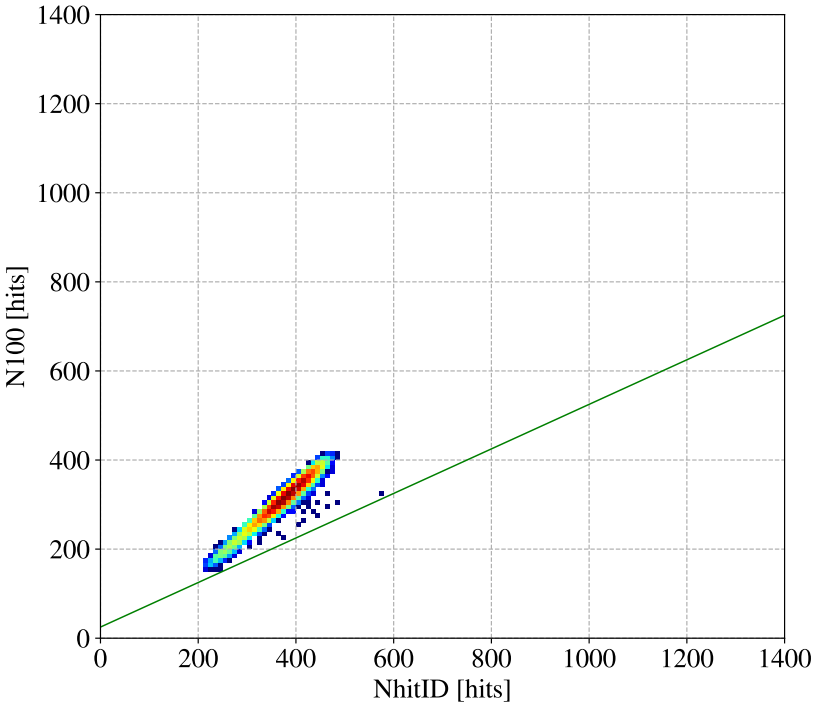

Figure 5.7: Noise event cut inefficiency check for Period1

5.2.2 Flasher Event Cut

PMTs may emit light from itself due to the discharge in the dynode. The emitted light is detected by the other PMTs and mimics a high energy event up to 20 MeV. This phenomenon is called "flasher event". Since the flashing PMT detect the most of detected charge in ID, the flasher events are easily selected by the following criteria.

- (Total charge of the 17inch and 20inch PMTs in the ID, $Q_{\rm ID}$) $\geq$ 2500 [p.e.]
- (Max PMT Charge) / $Q_{\rm ID} \geq 0.6$

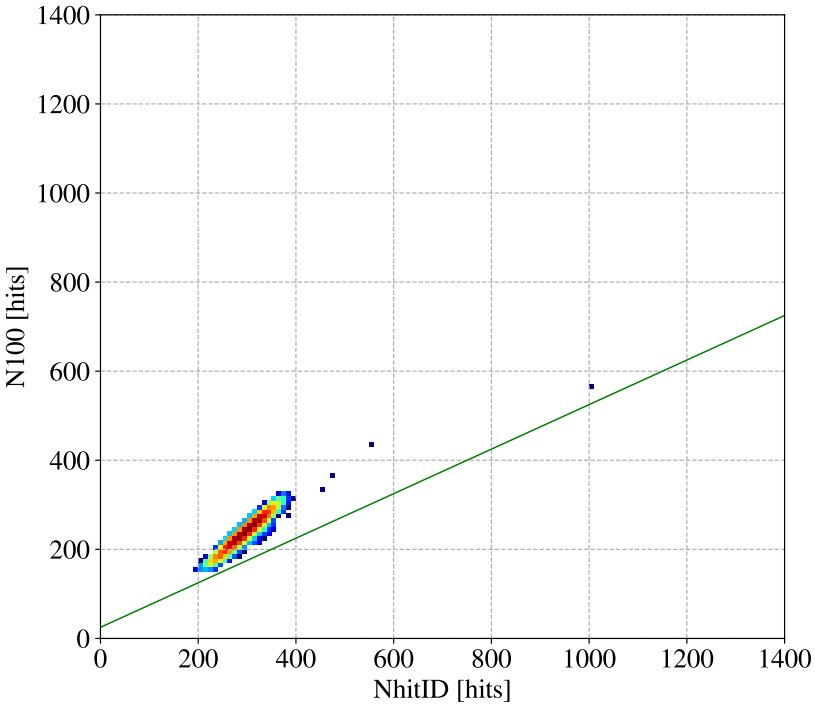

Figure 5.8: Noise event cut inefficiency check for Period2

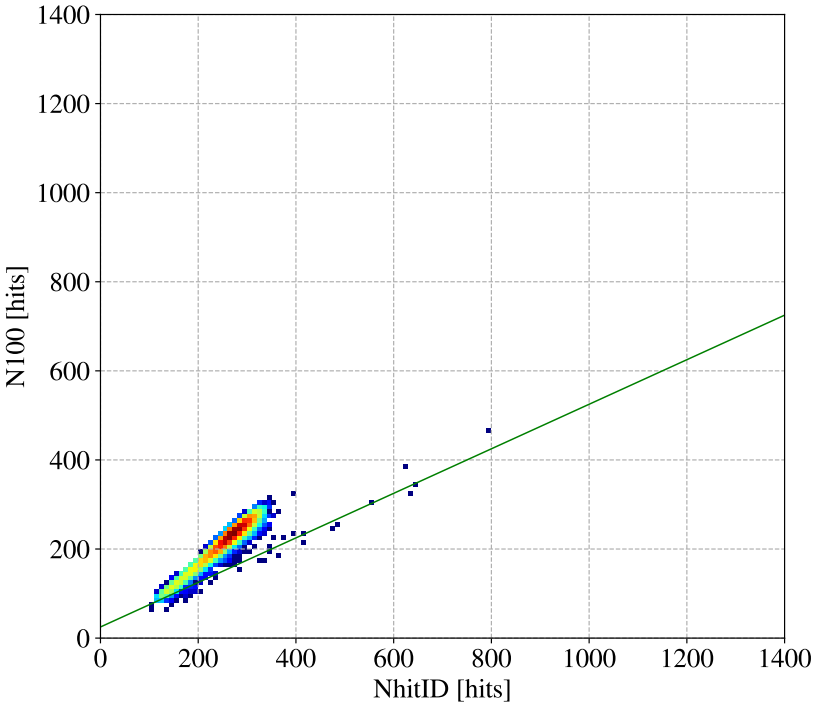

Figure 5.9: Noise event cut inefficiency check for Period3

- Not either a noise event (Sec.5.2.1) nor a muon event (Sec.4.6.1)

The flusher event are clearly separated from the other event as shown in Figure 5.10.

The flasher event rate is evaluated to be 2.9×10^{-3} [Hz] and 1.2×10^{-3} [Hz] for before and after the purifications. These corresponds to about 8×10^{-3}% and 9×10^{-3}% of the total low-energy events, which are much smaller than the rest of the systematic uncertainties and negligible.

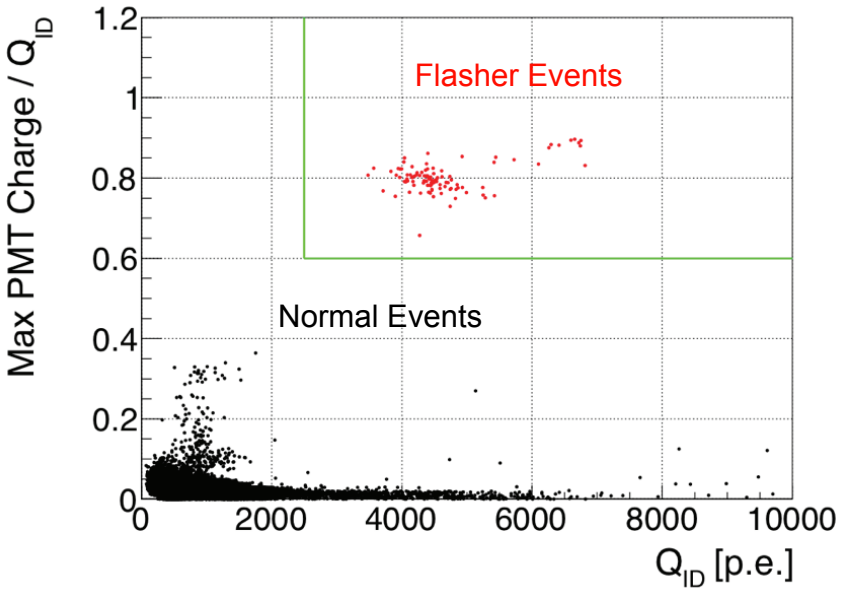

Figure 5.10: Flasher event profile and selection criteria(Watanabe 2012)

5.2.3 Ringing Event Cut

After a KamFEE upgrade campaign in 2003, fake muon events appears after muon events. These events are caused by instability of the KamFEE baseline, called "ringing", and thus, these fake muon events are called "ringing event".

As is shown in Figure 5.11, the ringing events are effectively rejected by

- $(N_{\rm hit} > 600)$ && $(\Delta T_{\rm muon} < 1\ [\mu{\rm s}])$

where $N_{\rm hit}$ is the total number of hit PMT in the ID and $\Delta T_{\rm muon}$ is the time difference from the last muon event.

5.3 Muon and Spallation Event veto

Cosmic muons generate various radioactive isotopes and neutrons via spallation in the KamLAND liquid scintillator. The major radioactive isotopes generated in the KamLAND is summarized in Table 5.2. Since we apply the delayed-coincidence method

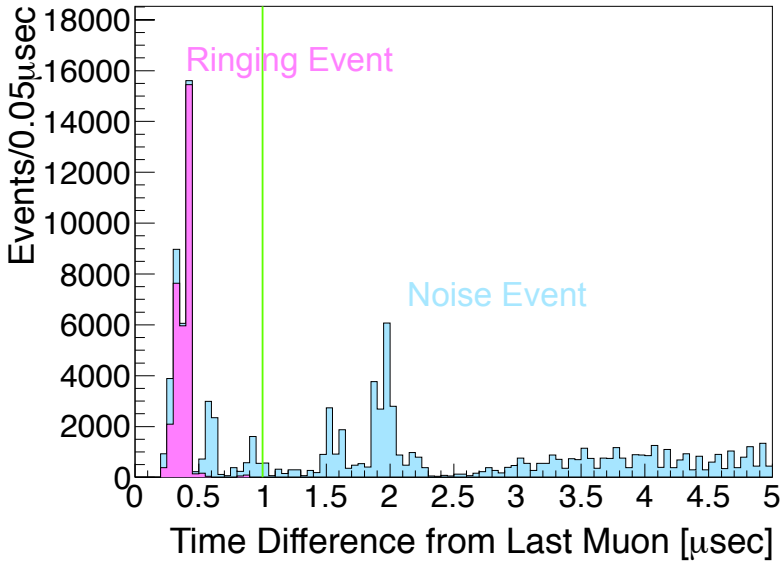

Figure 5.11: Time differences between muon events(ΔT_{muon}) and ringing event selection criteria. The vertical green line is the criteria.(Watanabe 2012)

to find the IBD candidates (Sec.5.4), there are not needs to apply spallation cuts described in Ozaki (2020) and Takeuchi (2022) to remove these isotopes. However, some of them, e.g. ^{8}He/^{9}Li, are generated with neutrons, and thus may mimics the IBD candidate. Such backgrounds are well studied and described in Sec.6.4.

Cosmic muons are detected as a huge scintillation and accompanied by multiple neutron capture events. This makes it challenging to reconstruct the correct vertex and energy of low-energy event immediately following the muon event. In addition, KamFEE cannot record all the data immediately after a muon event because of the ATWD dead time described in Sec.3.3.5.

To avoid muon-related backgrounds and get a high-quality antineutrino dataset, muon events tagged by the selection criteria described in Sec.4.6.1 and accompanying event selected by the following selections are removed. This cut is named "muon veto".

- Low-energy muon ($Q_{17} < 40000$[p.e.]) : 2 ms whole volume veto
- High-energy muon (40000[p.e.] $< Q_{17}$)
  - showering muon (10^6[p.e.] $\leq \Delta Q$) : 2 s whole volume veto
  - bad-reconstructed muon ($100 \leq$ Badness) : 2 s whole volume veto
  - well-reconstructed non-showering muon (Badness < 100 and $\Delta Q < 10^6$[p.e.]): 2 ms whole volume veto and 2 s veto in the cylindrical volume around the reconstructed muon track

where Q_{17} is the total observed change in the 17inch PMTs and ΔQ is the residual charge. Badness is a parameter for muon track reconstruction quality.

Table 5.2: Spallation products in KamLAND. The production rates are cited from Abe et al. (2010) except ^{6}He and ^{7}Be from Hagner et al. (2000). The other numbers are cited from Obara (2018)

Isotope	lifetime	Q-value [MeV]	mode	production rate [event/day/kt]
^{12}B	29.1 ms	13.4	β^-	58.7 ± 2.5
^{12}N	15.9 ms	17.3	β^+	2.1 ± 0.4
^{8}Li	1.21 s	16.0	$\beta^-\alpha$	27.3 ± 0.8
^{8}B	1.11 s	18.0	$\beta^+\alpha$	< 4.7
^{9}C	182.5 ms	16.5	β^+	7.4 ± 2.9
^{8}He/^{9}Li	171.7/257.2 ms	10.7/13.6	$\beta^-\gamma n$	2.7 ± 0.8
^{11}C	29.4 ms	1.98	β^+	1093 ± 176
^{10}C	27.8 s	3.65	$\beta^+\gamma$	21.6 ± 2.7
^{11}Be	19.9 s	11.5	β^-	< 2.2
^{6}He	1.16 s	3.51	β^-	19
^{7}Be	76.9 d	0.478	EC, γ	231

5.4 Delayed-Coincidence Selection for Inverse-Beta Decay

The selection criteria for the IBD event candidates is summarized in Table 5.3. The IBD event, i.e. the antineutrino event, is characterized by the time- and space-correlated two scintillations. The details of each criterion and its efficiency is discussed in this section.

Table 5.3: The selection criteria for the IBD candidate

parameter	criteria
prompt energy [MeV]	$0.9 \leq E_{\rm p} < 8.5$
delayed energy [MeV]	$1.8 \leq E_{\rm d} < 2.6$ $4.4 \leq E_{\rm d} < 5.6$
space correlation [m]	$\Delta R < 2.0$
time correlation [μs]	$0.5 \leq \Delta T < 1000$
fiducial volume [m]	$R_{\rm p} < 6$ & $R_{\rm d} < 6$

Energy Selection

The lower boundary of the prompt energy cut corresponds to the IBD reaction threshold, whereas the upper boundary is selected to cover the whole energy range of reactor neutrinos shown in Sec.6.1.

The delayed energy criterion is optimized to effectively find the neutron capture γ on a proton (2.2 [MeV], 99.48%) and ^{12}C (4.9 [MeV], 0.51%). The ratio of neutron captures on the other nuclei, e.g. ^{13}C, is less than $\mathcal{O}(10^{-3})$%, and thus negligible.

The selection efficiencies of the delayed energy cut depend on the energy resolution as

$$\varepsilon_{\text{1.8-2.6MeV}} = \frac{1}{\sqrt{2\pi\sigma^2}} \int_{\text{1.8MeV}}^{\text{2.6MeV}} \left(-\frac{(x-2.211)^2}{2\sigma^2} \right) \mathrm{d}x$$
$$\varepsilon_{\text{4.4-5.6MeV}} = \frac{1}{\sqrt{2\pi\sigma^2}} \int_{\text{4.4MeV}}^{\text{2.6MeV}} \left(-\frac{(x-5.061)^2}{2\sigma^2} \right) \mathrm{d}x \tag{5.4}$$

where σ is the estimated energy resolution, 2.211 and 5.061 are the visible energy converted from neutron capture 2.2 MeV and 4.9 MeV, respectively. The evaluated selection efficiency is summarized in Table 5.4.

Table 5.4: Delayed energy selection efficiency

Period	parameter	17inch	20inch
before purification	$\sigma[\%/\sqrt{E[\text{MeV}]}]$	7.0 ± 0.1	6.1 ± 0.1
	efficiency (1.8–2.6 MeV)	99.99%	100%
	efficiency (4.4–5.6 MeV)	100%	100%
after purification	$\sigma[\%/\sqrt{E[\text{MeV}]}]$	8.2 ± 0.1	7.0 ± 0.1
	efficiency (1.8–2.6 MeV)	99.98%	99.99%
	efficiency (4.4–5.6 MeV)	99.99%	100%

Space Correlation

The time and space difference between the prompt and delayed scintillation essentially depends on the neutron diffusion and capture process. It also depends on the detector response, i.e. the detector vertex resolution.

AmBe composite source emits 4.4 MeV γ-ray and neutron, thus which is useful to verify the selection for the space correlation. Figure 5.12 shows the coincidence properties of AmBe source calibration installed at the center of the detector in 2003 August. Each panel except the ΔT panel shows the selection criteria by red dashed lines. The blue dashed line in the ΔT panel shows the off-time window, whereas the red dashed line implies the on-time window. The rest histograms are created by subtracting the off-time histograms from the on-time histograms. Furthermore, these are the "N-1 plot", that is, each panels show the histograms where the criteria for other parameters have been already applied.

From this test, the selection efficiency for the space correlation is evaluated to be 99.84%. In addition, the mean neutron capture time is evaluated to be 207.87 ± 1.14 [μs] from this fitting, which is well consistent to the spallation neutron data discussed below.

The AmBe source emits fast neutron, whereas the IBD by $\mathcal{O}(1)$ MeV antineutron emits thermal neutron. The difference in the diffusion process is verified by comparing the AmBe data and IBD MC, and assigned as the systematic uncertainties.

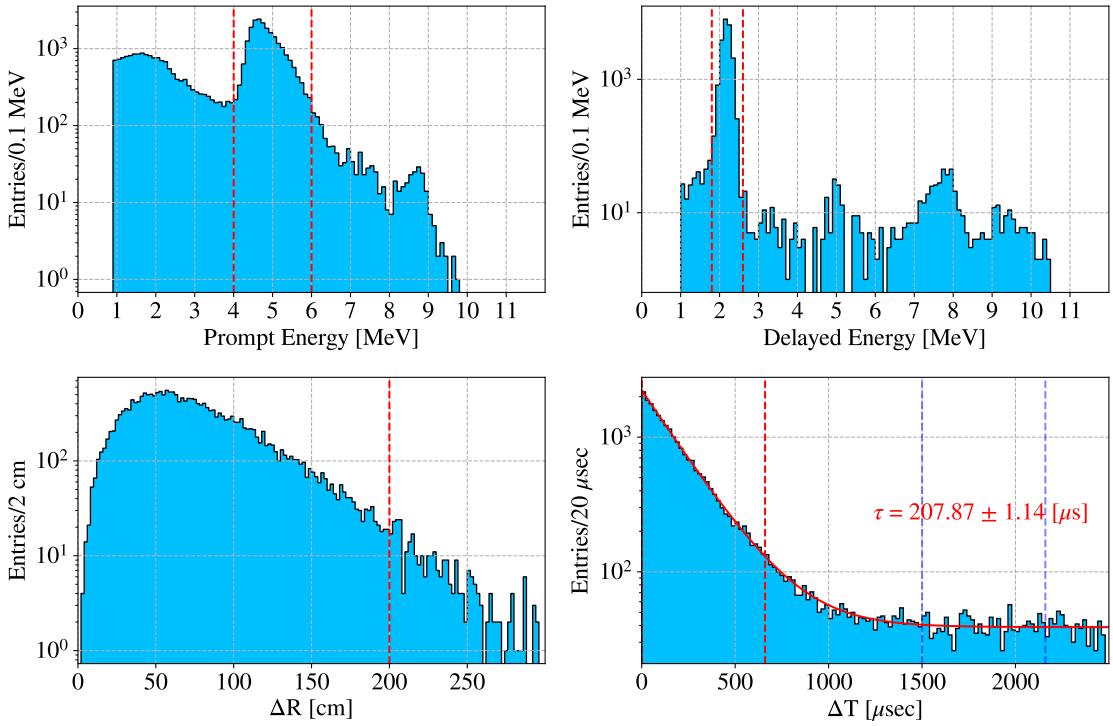

Figure 5.12: Delayed-coincidence property of AmBe composite source at the center of the detector in 2003 August

Time Correlation

The time correlation selection can be verified by the spallation neutron event accompanying muon events. Figure 5.13 and Figure 5.14 show the distributions of the time difference between muon events and accompanying neutron capture events. To avoid the busy electronics condition due to the multiple neutrons, high charge muons ($0 < \Delta Q$) are not used in this analysis. Besides, the neutron events are selected by $350 <$ NsumMax < 550, where NsumMax means the number of KamFEE channel which detected PMT hit. From this analysis, The mean capture time is fitted to be $\tau = 209.0 \pm 2.7$ [μs] and $\tau = 209.5 \pm 3.9$ [μs] for before and after the purifications, respectively.

The time correlation cut lower boundary 0.5 [μs] is applied to avoid systematic biases due to multiple neutrons and electronics dead time.

The selection efficiency of the time correlation cut is computed with the fitted function as

$$\begin{aligned} \varepsilon_{\text{time-correlation}} &= \frac{1}{\tau}\int_{0.5\mu s}^{1000\mu s} \exp\left(-\frac{t}{\tau}\right) \mathrm{d}t \\ &= 98.91 \pm 0.04\% \quad \text{(before purification)} \\ &= 98.93 \pm 0.04\% \quad \text{(after purification)} \end{aligned} \tag{5.5}$$

The status of the KamLAND liquid scintillator has not been changed after the purifications, even if there is some on-site activities for the KamLAND-Zen. The change of detector response is accounted for by changing effective quenching factor in the analysis. So, this estimation is valid also for Period3.

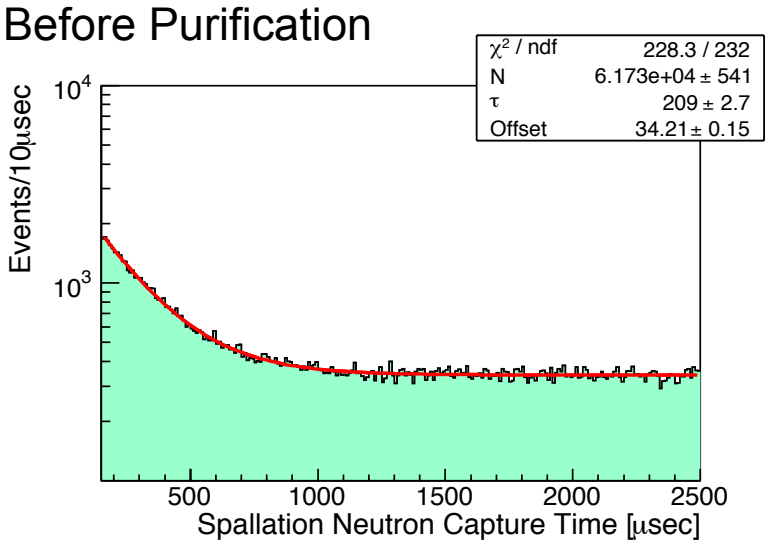

Figure 5.13: Time differences between a muon event and accompanying neutron capture event before purifications(Watanabe 2012)

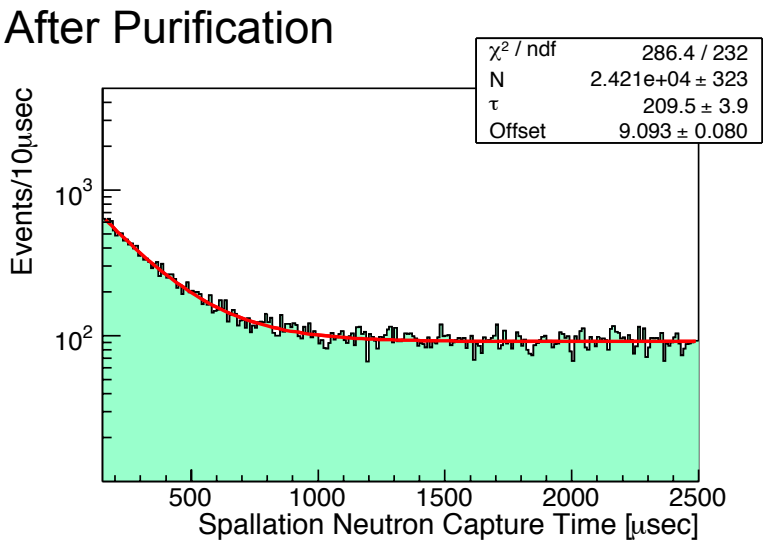

Figure 5.14: Time differences between a muon event and accompanying neutron capture event after purifications(Watanabe 2012)

Multiple Coincidence Cut

The IBD reaction emits only one neutron. Therefore, if a prompt event is accompanied by multiple delayed event candidates, it is vetoed from the IBD candidate to keep the purity of the antineutrino dataset. Such multiple coincidence event can be created by the spontaneous fission of ^{238}U in the detector or neutral current interaction by the atmospheric neutrinos.

Zen Volume Cut

As is mentioned in Sec.3.5, the LS volume with the KamLAND-Zen equipments installed is excluded from the effective volume of the antineutrino observation.

Figure 5.15 shows the schematic view of the zen volume cut. During the KamLAND-Zen400 period (from 2011 August to 2015 December), the failed800 period (from 2016 August to 2016 November) and the KamLAND-Zen800 period (from 2018 May to present), a $r < 250$ [cm] cylindrical volume in the upper hemisphere and a $r < 250$ [cm] volume in the lower hemisphere is excluded from the effective volume. The delayed events reconstructed in this zen volume cut region are vetoed.

The decrease of the exposure is accounted for as by changing the selection efficiency.

5.5 Likelihood Selection

The delayed-coincidence method is a powerful tool to improve the purity of the antineutrino dataset. However, the accidental coincidence can contaminate and is one

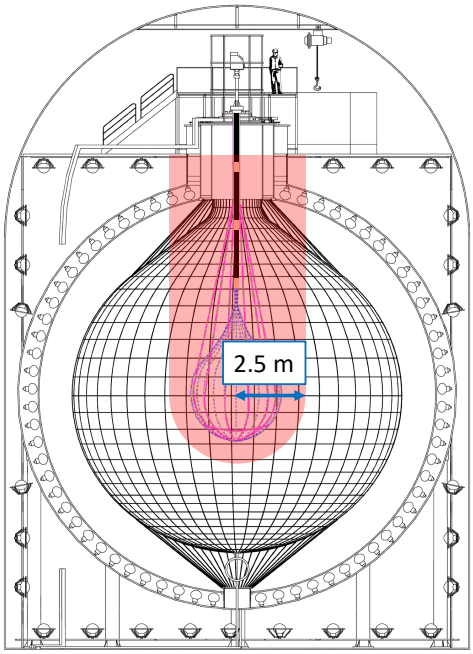

Figure 5.15: Schematic view of Zen-volume cut. The red region is excluded from the effective volume. The drawn mini balloon is that for KamLAND-Zen 800, while the veto region is identical in Zen400 and Zen800 period.

of the dominant backgrounds to find the antineutrino candidate. In order to further improve the signal-to-background ratio, a likelihood based event selection is applied. This section describes the procedure and efficiency of the likelihood selection.

The procedure of the likelihood selection is as follows.

1. perform the delayed-coincidence selection (described in Sec.5.4)
2. construct probability density function (PDF) of the parameter set ($E_{\rm p}$, $E_{\rm d}$,ΔR, ΔT, $R_{\rm p}$, $R_{\rm d}$) for the antineutrino signal ($f_{\overline{\nu}_{\rm e}}$) and for the accidental coincidence background ($f_{\rm accidental}$)
3. find likelihood ratio thresholds that maximize the likelihood ratio for each $E_{\rm p}$
4. apply the likelihood ratio cut to the antineutrino candidate

5.5.1 Likelihood Period

The likelihood selection depends on the accidental background rate, which has time variation due to the changing status of the detector. Figure 5.16 and Figure 5.17 show the time variation of the accidental coincidence event rates selected by almost the same criteria as the IBD candidate, whereas the ΔT selection window is shifted and extended to 0.2–1.2 [sec] from the prompt event.

That is why the KamLAND dataset is divided into 8 likelihood periods (LH-period) as Table 5.5, and the likelihood selection criteria are prepared independently for each period. Hereafter, a notation "LH-X" refers to the X-th LH period.

Table 5.5: Dataset classification for the likelihood selection

Period	date	run	detector status
LH-0	2002/Mar./9 – 2003/Oct./31	220–2985	before purifications
LH-1	2003/Nov./1 – 2007/May/12	2986–6801	before purifications
LH-2	2007/May/12 – 2007/Aug./5 2008/Jul./7 – 2009/Apr./7	6802–6953 7872–8501	during purifications
LH-3	2007/Aug./6 – 2008/Jul./7	6954–7871	between purifications
LH-4	2008/Apr./8 – 2011/Aug./12	8502–10675	after purifications
LH-5	2011/Aug./13 – 2015/Dec./15 2016/Aug./3 – 2016/Nov./22	10676–13414 13786–13962	during Zen400 and failed800
LH-6	2015/Dec./15 – 2016/Aug./2 2016/Nov./22 – 2018/May/10	13415–13785 13963–14990	after Zen400
LH-7	2018/May/19 – 2020/Dec./31	14991–16597	during Zen800

5.5.2 Probability Density Function

The probability density function for the antineutrino signal, $f_{\overline{\nu}_e}$, is constructed based on a Geant4 simulation(Agostinelli et al. 2003). The prompt event are generated uniformly in the liquid scintillator with proper charge dispersion, vertex resolution and energy resolution for each likelihood period. The delayed event is also generated considering the neutron diffusion, γ-ray diffusion and vertex/energy resolution. The time correlation is independently simulated from the measured neutron capture data.

On the other hands, the probability density function for the accidental coincidence background, $f_{\text{accidental}}$, can be easily created from the data as described in Sec.5.5.1.

The probability density functions for signal and background are defined in $1200 = (76 \times 3 \times 16 \times 1 \times 5 \times 5)$ bins as follows.

- E_{p} : 76 bins
  0.9 – 8.5 [MeV] with 0.1 [MeV] bin width

- E_{d} : 3 bins
  a. 2.0 – 2.4 [MeV]
  b. 1.9 – 2.0 [MeV] and 2.4 – 2.5 [MeV]
  c. 1.8 – 1.9 [MeV] and 2.5 – 2.6 [MeV]

- ΔR : 16 bins
  a. 0 – 50 [cm]
  b. 50 – 600 [cm] with 25 [cm] bin width

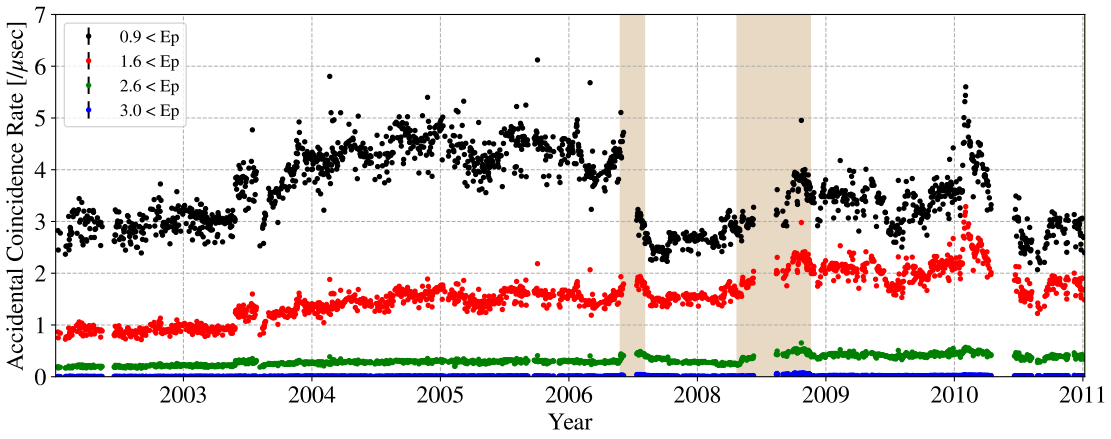

Figure 5.16: Time variation of the accidental coincidence rate in Period1 and Period2. The accidental coincidence events are selected by the delayed-coincidence method and the likelihood selection has not been applied.

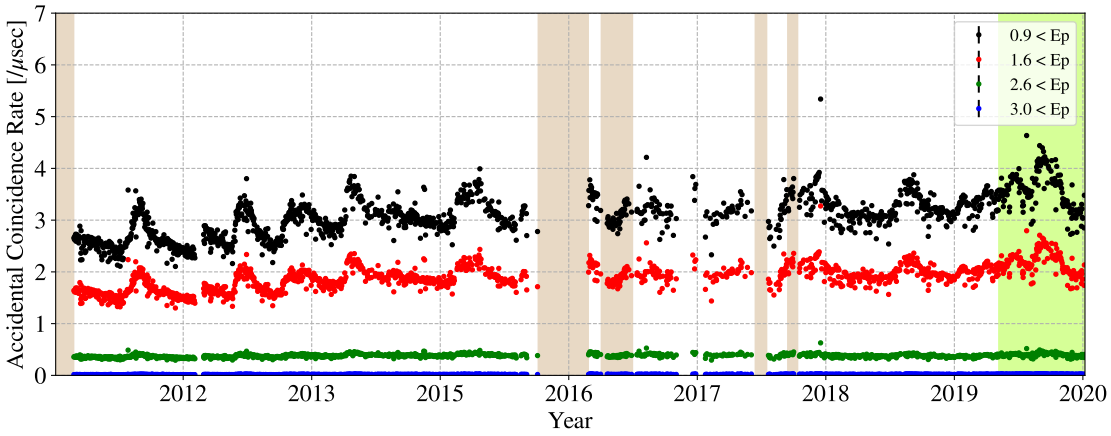

Figure 5.17: Time variation of the accidental coincidence rate in Period3. The accidental coincidence events are selected by the delayed-coincidence method and the likelihood selection has not been applied.

- ΔT : 1 bins
  (signal) : un-binned assuming an exponential distribution $\exp(-t/211.1[\mu s])$ in 0.5 – 1000 [μs]
  (accidental) : un-binned assuming an uniform distribution in 0.5 – 1000 [μs]

- $R_{\rm p}$: 5 bins
  a. 0 – 500 [cm]
  b. 500 – 600 [cm] with 25 [cm] bin width

- $R_{\rm d}$: 5 bins
  a. 0 – 500 [cm]
  b. 500 – 600 [cm] with 25 [cm] bin width

5.5.3 Likelihood Ratio

The Likelihood function constructed in Sec.5.5.2, $f_{\overline{\nu}_{\rm e}}(f_{\rm accidental})$, means the probability that a antineutrino signal (accidental coincidence background) has a parameter set ($E_{\rm p}$, $E_{\rm d}$,ΔR, ΔT, $R_{\rm p}$, $R_{\rm d}$).

Therefore, the probability that a delayed-coincidence pair with a parameter set ($E_{\rm p}$, $E_{\rm d}$,ΔR, ΔT, $R_{\rm p}$, $R_{\rm d}$) is a antineutrino signal, or the likelihood ratio $\mathcal{L}_{\rm ratio}$, is defined as a function of the prompt energy like,

$$\mathcal{L}_{\rm ratio}(E_{\rm p}) = \frac{f_{\overline{\nu}_{\rm e}}}{f_{\overline{\nu}_{\rm e}} + f_{\rm accidental}} \tag{5.6}$$

Ideally, $\mathcal{L}_{\rm ratio}$ for signal distributes near 1, whereas that for accidental background near 0. So, $\mathcal{L}_{\rm ratio}$ is useful to discrete the antineutrino signals from the accidental coincidence backgrounds.

Figure 5.18–5.23 show the procedure of the likelihood selection. For each $E_{\rm p}$ bins, the distribution of $\mathcal{L}_{\rm ratio}$ for signal and background is calculated as the top panels. Hereafter, these distributions are referred to as $S'(\mathcal{L}_{\rm ratio})$ and $B'(\mathcal{L}_{\rm ratio})$, respectively.

The threshold for the likelihood ratio, $\mathcal{L}_{\rm cut}$, is determined to maximize a figure of merit defined as

$$\mathrm{FoM}(\mathcal{L}_{\rm cut}) = \frac{S(\mathcal{L}_{\rm cut})}{S(\mathcal{L}_{\rm cut}) + B(\mathcal{L}_{\rm cut})} \tag{5.7}$$

where $S(\mathcal{L}_{\rm cut})$ and $B(\mathcal{L}_{\rm cut})$ account for the residual signal and accidental background events calculated as

$$\begin{aligned} S(\mathcal{L}_{\rm cut}) &= \mathrm{N}_{\rm signal} \int_{\mathcal{L}_{\rm cut}}^{1} S'(\mathcal{L}_{\rm ratio})\, \mathrm{d}\mathcal{L}_{\rm ratio} \\ B(\mathcal{L}_{\rm cut}) &= \mathrm{N}_{\rm accidental} \int_{\mathcal{L}_{\rm cut}}^{1} B'(\mathcal{L}_{\rm ratio})\, \mathrm{d}\mathcal{L}_{\rm ratio} \end{aligned} \tag{5.8}$$

Here $\mathrm{N}_{\rm signal}$ is the expected antineutrino signal rate in the $E_{\rm p}$ bin of the interest, calculated considering non-oscillating reactor neutrino spectrum described in Sec.6.1 and the geoneutrino flux modeled by Enomoto (2006). Whether the oscillation is assumed or not and the choice of geoneutrino spectrum model do not matter here

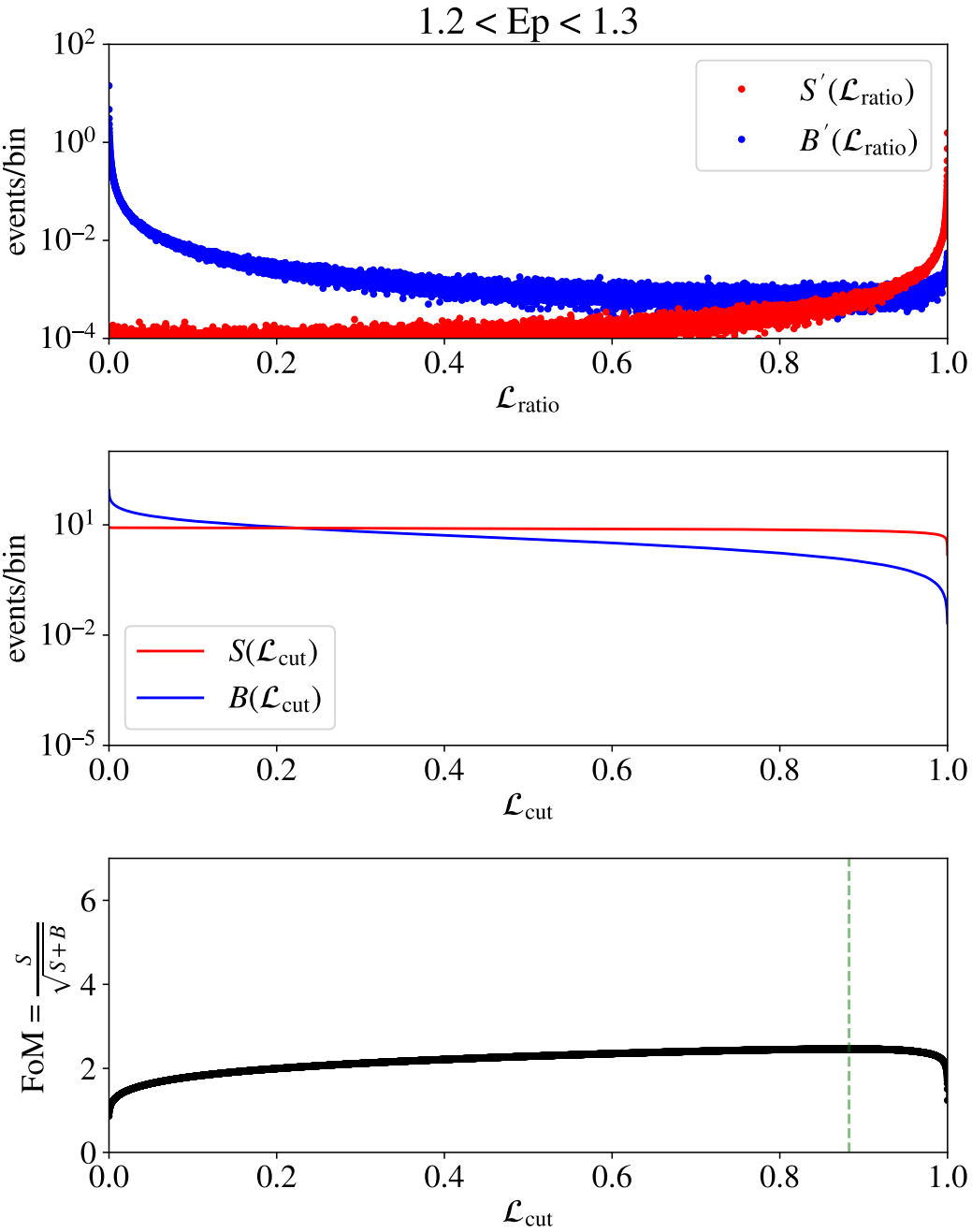

Figure 5.18: Likelihood selection procedure for $1.2 < E_{\text{p}} < 1.3$ in LH-0. (top)$\mathcal{L}_{\text{ratio}}$ distribution for signal (red) and accidental background (blue). (middle)integrated $\mathcal{L}_{\text{ratio}}$ as $S(\mathcal{L}_{\text{ratio}})$ for signal and $B(\mathcal{L}_{\text{ratio}})$ for accidental background. (bottom) FoM as a function of $\mathcal{L}_{\text{ratio}}$. The $\mathcal{L}_{\text{ratio}}$ that gives the maximum FoM is shown as green dashed line.

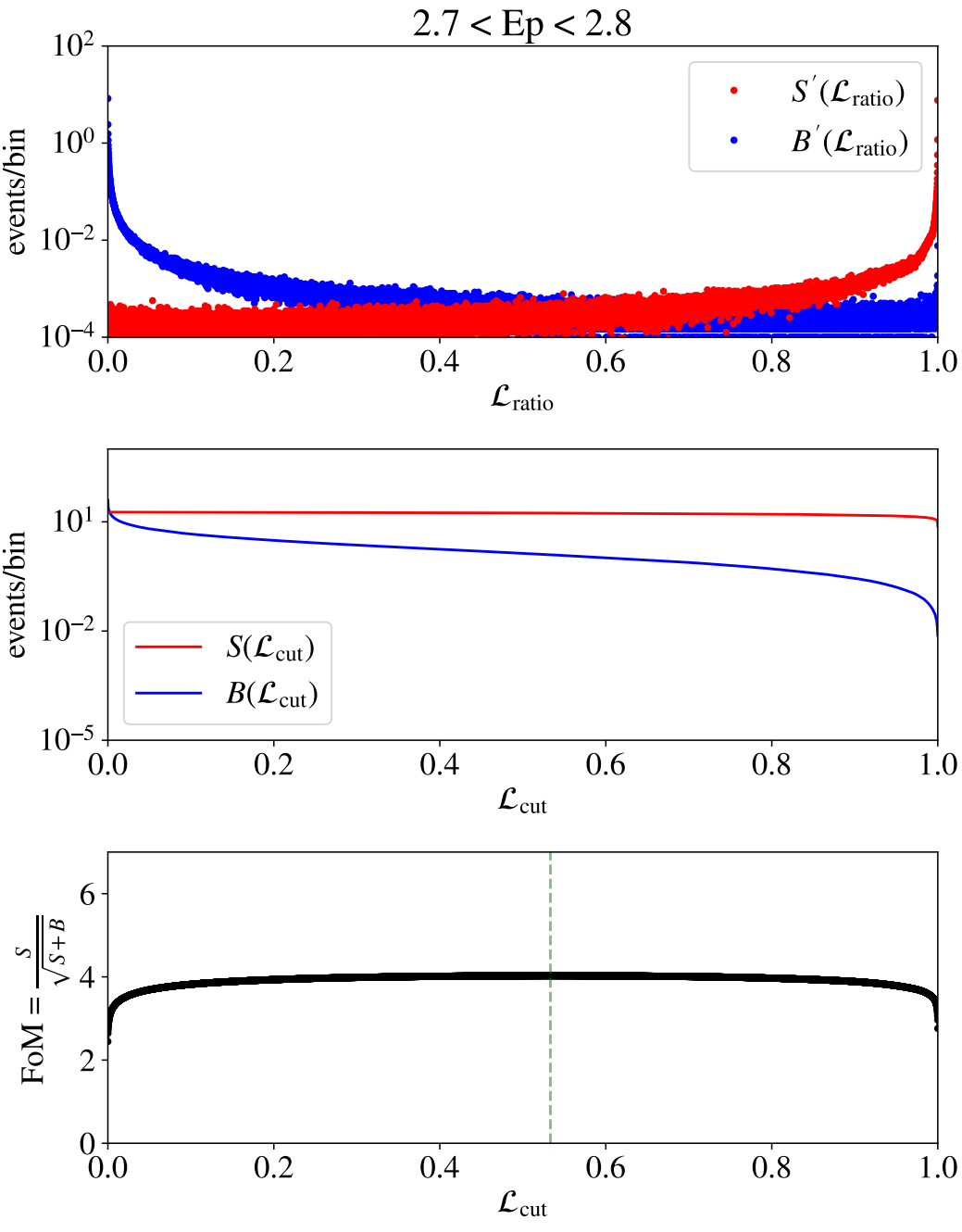

Figure 5.19: Likelihood selection procedure for $2.7 < E_{\text{p}} < 2.8$ in LH-0

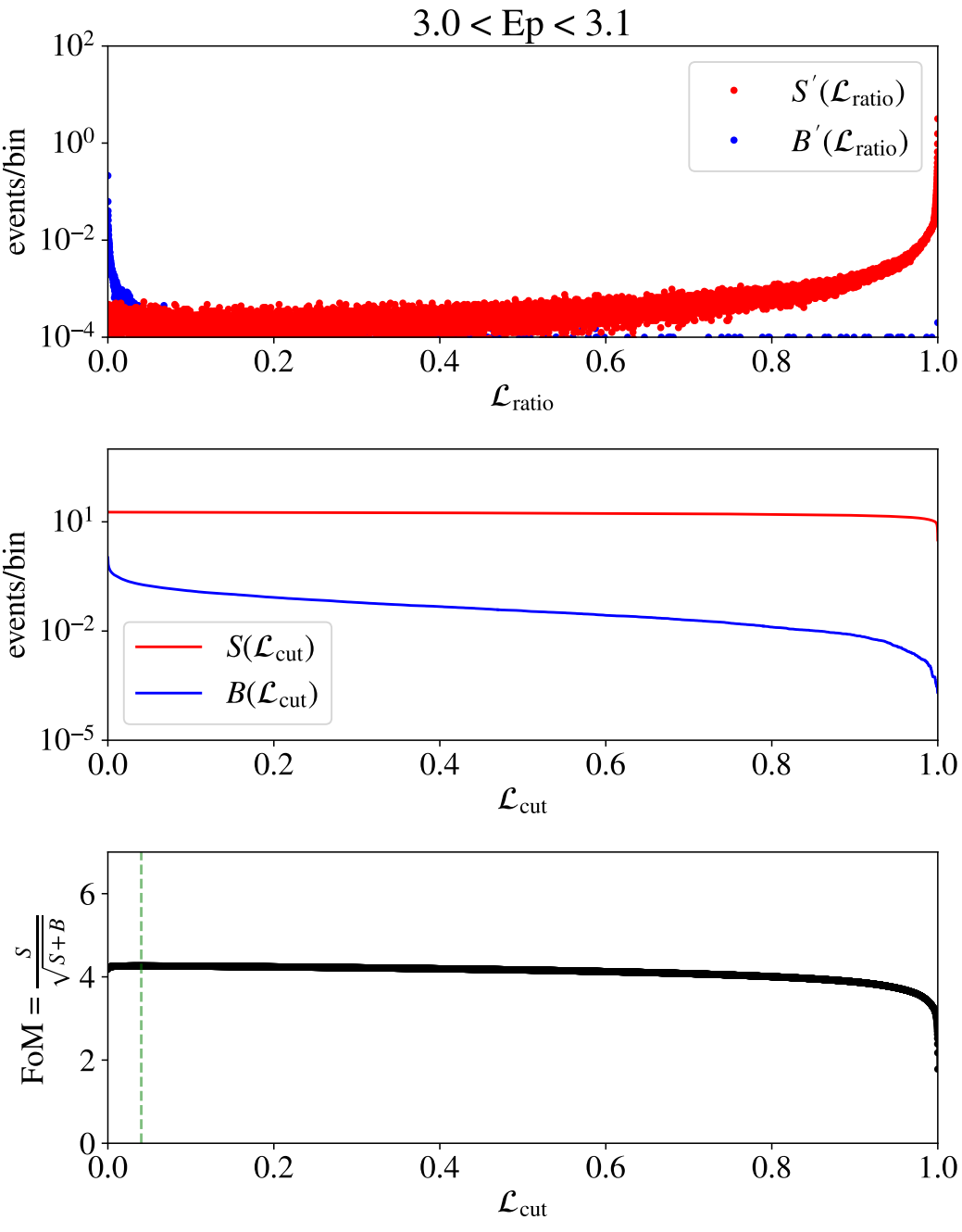

Figure 5.20: Likelihood selection procedure for $3.0 < E_{\text{p}} < 3.5$ in LH-0

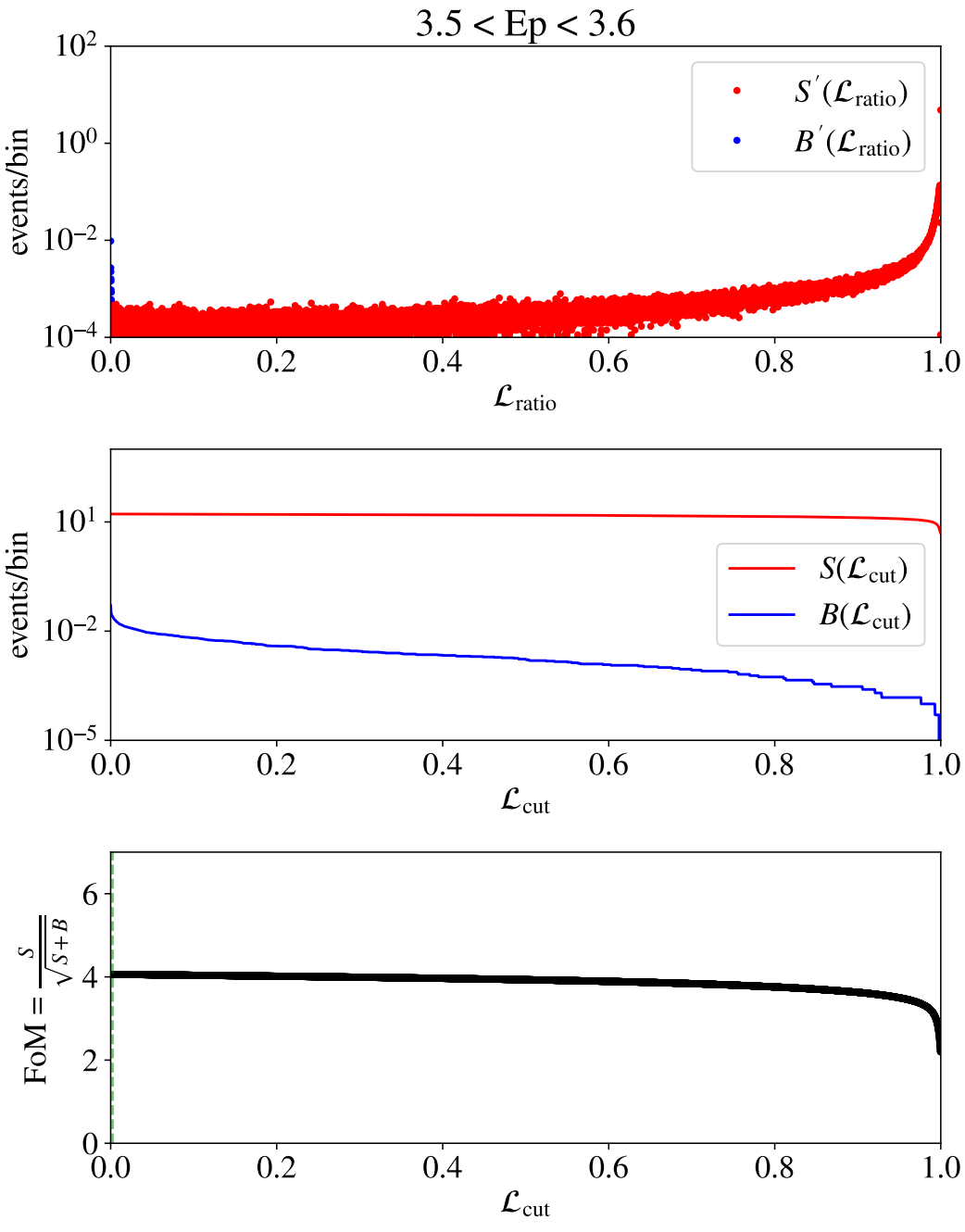

Figure 5.21: Likelihood selection procedure for $1.2 < E_{\text{p}} < 1.3$ in LH-0

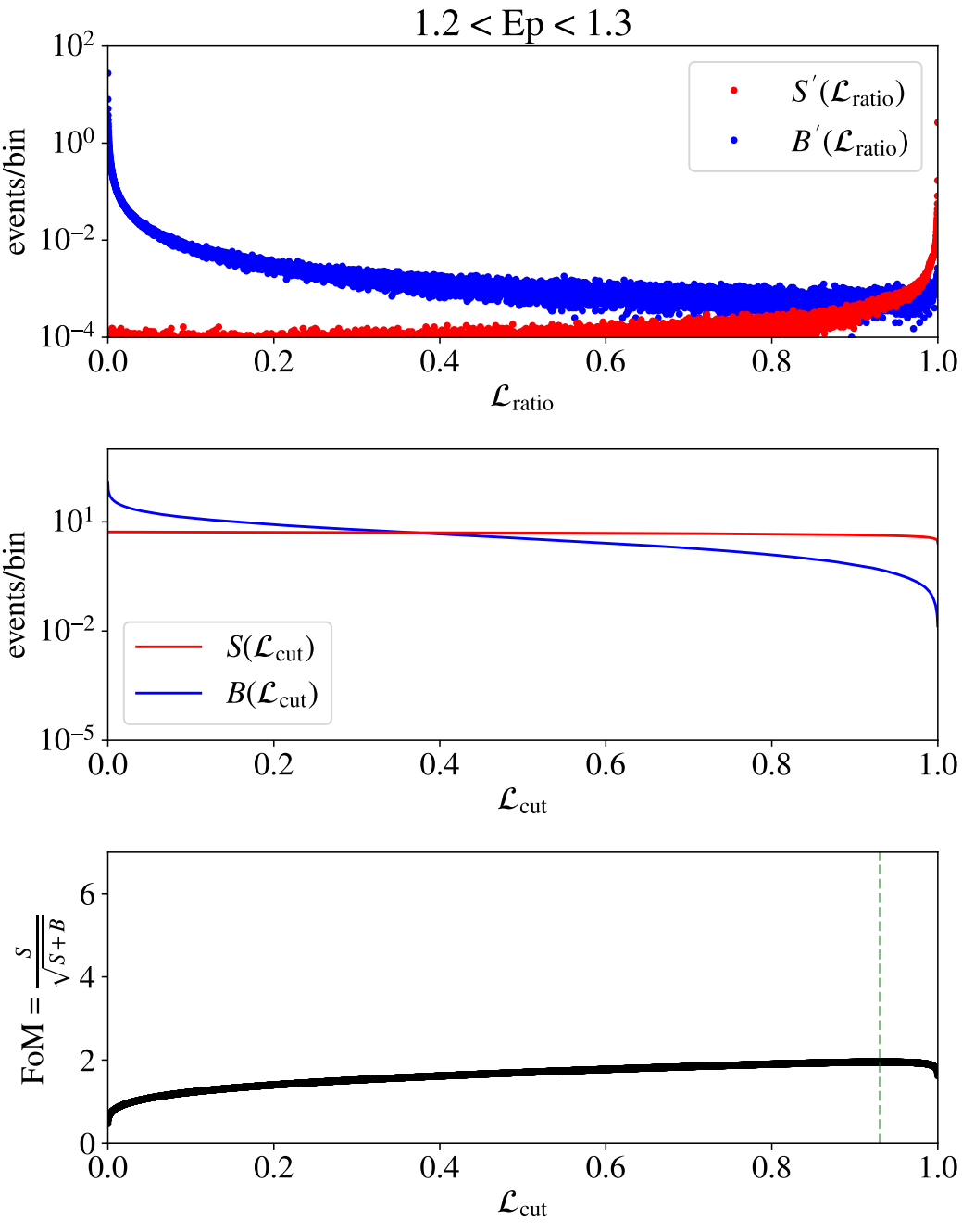

Figure 5.22: Likelihood selection procedure for $1.2 < E_{\text{p}} < 1.3$ in LH-7

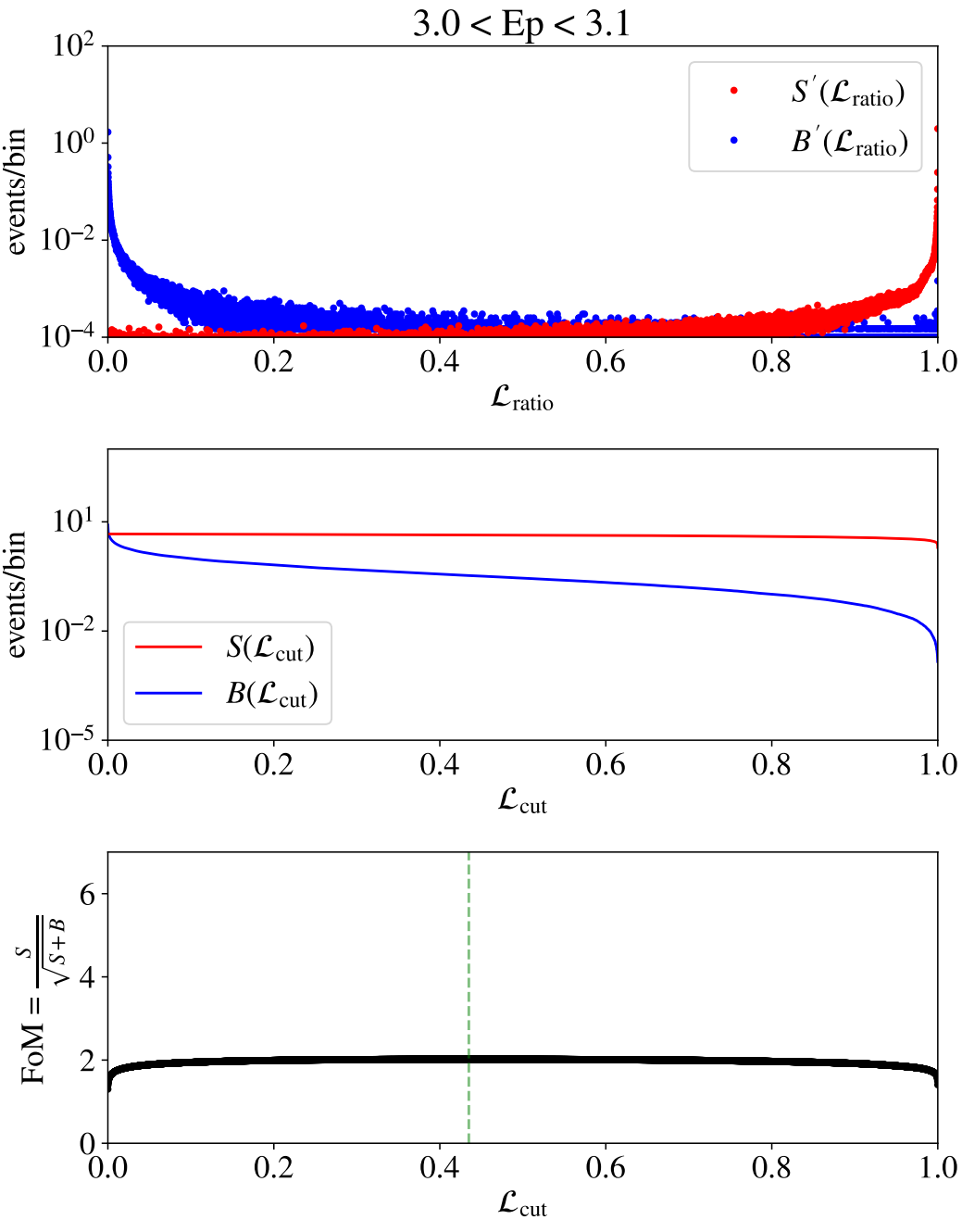

Figure 5.23: Likelihood selection procedure for $3.0 < E_{\text{p}} < 3.5$ in LH-7

because the selection efficiencies are evaluated independently as described in Sec.5.5.4. Besides, $N_{accidental}$ means the accidental coincidence background rate evaluated from the data. The middle panels of Figure 5.18–5.23 show $S(\mathcal{L}_{cut})$ and $B(\mathcal{L}_{cut})$ for some E_p and likelihood period.

The bottom panels show the figure of merit as a function of $\mathcal{L}_{cut}$. The optimized likelihood ratio cut criteria are determined by finding the maximum point of this curve as shown with green lines.

Figure 5.24 shows the maximum figure of merit as a function of the prompt energy for each likelihood period. Besides, Figure 5.25 shows the optimized likelihood ratio cut threshold for each prompt energy.

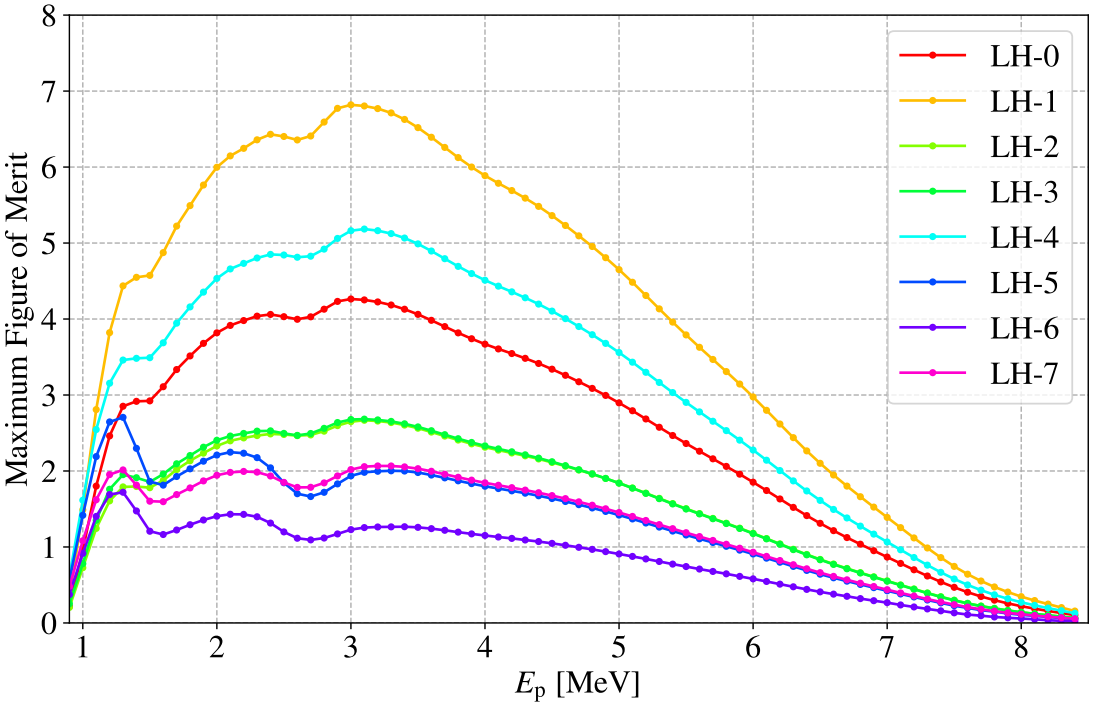

Figure 5.24: Maximum figure of merit for each the prompt energy

5.5.4 Selection Efficiency

The selection efficiency of the likelihood selection is estimated using pseudo antineutrino dataset generated with the Geant4(Agostinelli et al. 2003) MC simulation. 1.0×10^7 antineutrino events are generated uniformly in the 750 cm radius volume for each prompt energy bin, and the delayed-coincidence selection and likelihood selection are applied. Then, the selection efficiency, $\varepsilon(E_p)$, is calculated as

$$\varepsilon(E_p) = \frac{N_{survived}}{N_{R<600}} \tag{5.9}$$

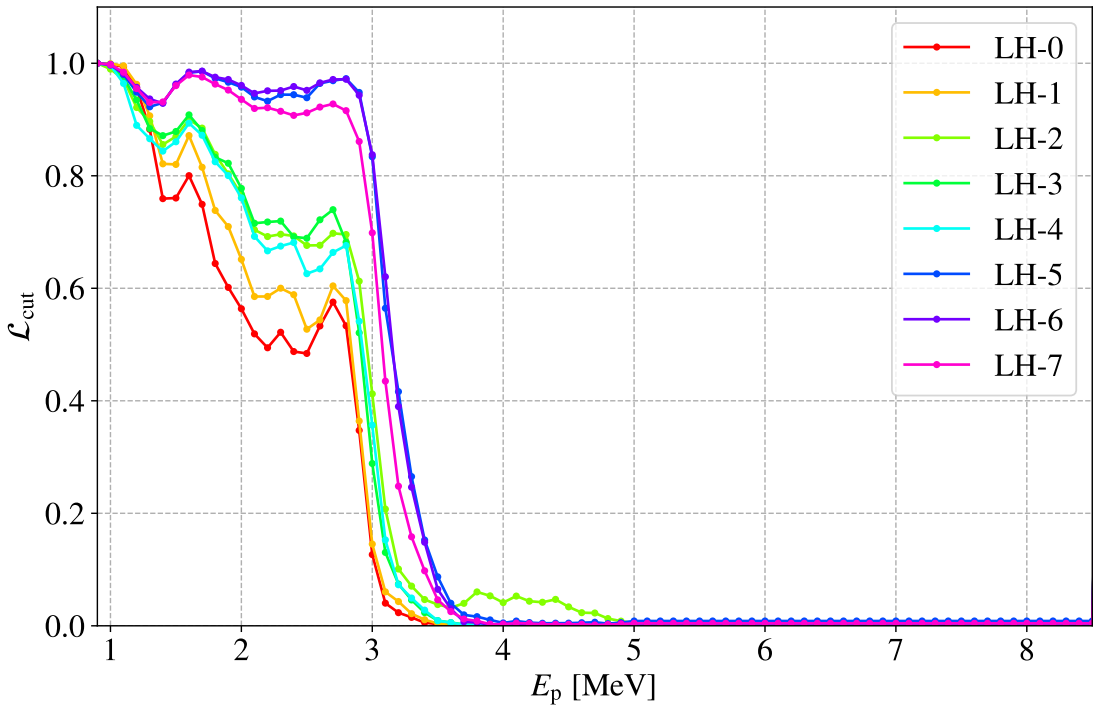

Figure 5.25: $\mathcal{L}_{\rm cut}$ for each the prompt energy

where $N_{\rm R<600}$ is the number of pseudo events generated within the 600 cm fiducial volume, whereas $N_{\rm survived}$ is the number of survived events after the likelihood selection. This calculation is performed for each $E_{\rm p}$ bin and for each likelihood period.

The Geant4 simulator is tuned to reproduce the observed data before the purifications. However, the detector response, i.e. the vertex and energy resolution, is changing. Especially, the two purification campaigns changed the LS transparency and worsened the resolutions since the resolutions are ideally determined by the statistical uncertainties of the light yield. Moreover, the increase of the bad channels starting from 2011 is decreasing the effective light yield of the detector.

To offset these impacts on the selection efficiency estimation, the change of relative light yield is studied using periodical source calibrations and $^{40}\gamma$-rays from ^{40}K impurities on the outer balloon. The decrease of effective light yield by the increasing bad channels is also taken into consideration. Figure 5.26 shows the result of these studies in "relative quench factor" with respect to calibration data before purification. The relative quench factor works like a quench factor of the scintillator. That is, the larger the relative quench factor is, the fewer the effective light yield is and the worse the resolution is.

The energy and vertex resolution is corrected to be

$$\begin{aligned}\sigma_{\rm energy}(E) &= \sigma_{\rm energy}^{\rm calibration} \times \sqrt{E \times F_\epsilon} \quad [\%/\sqrt{E[\mathrm{MeV}]}] \\ \sigma_{\rm vertex}(E) &= \sigma_{\rm vertex}^{\rm calibration} / \sqrt{E/F_\epsilon} \quad [\% \cdot \sqrt{E[\mathrm{MeV}]}]\end{aligned} \tag{5.10}$$

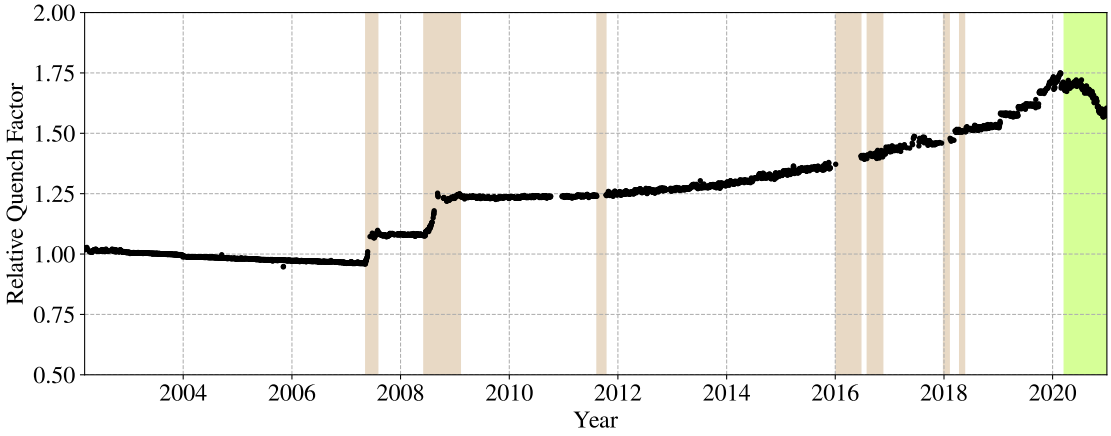

Figure 5.26: Time variation of the relative quench factor

where F_ϵ is the relative quench factor. The pseudo dataset is corrected using these resolution values before the efficiency estimation.

The selection efficiency in each likelihood period is shown in Figure 5.27 as a function of the prompt energy. The efficiency curves have dumps at 0.9 [MeV], 1.6 [MeV] and 2.8 [MeV]. These are due to accidental coincidence backgrounds originated from ^{210}Bi, ^{40}K and ^{208}Tl, respectively. On the other hand above 3.0 [MeV], the efficiency curves are flat since there are no serious radioactive impurities making accidental coincidence background.

The selection efficiency in the low energy region, $0.9 < E_{\rm p} < 3.5$ [MeV], differs by likelihood period because of the different Japanese reactor operation status and different reactor neutrino flux expectations. LH-2, LH-3 and LH-4 have lower efficiencies than LH-0 and LH-1 because the Kashiwazaki-Kariwa nuclear power station, which is the most effective reactor neutrino source for KamLAND, stopped due to an earthquake in 2007. LH-5, LH-6, and LH-7 also have lower efficiency for the same reason with the Great East Japan Earthquake in 2011.

In addition, the efficiencies in LH-5 and LH-7 is decreased by the Zen Volume Cut (Sec.5.4) in all energy region.

Figure 5.28 shows the livetime-weighted average efficiency curve for each dataset period. As is discussed above, Period1 has the largest efficiency except for energy region lower than 1.4 [MeV]. Period2 is superior in this energy region since the purification campaigns reduced the ^{210}Bi background. Period3 has the lowest efficiency since the smallest reactor neutrino expectations and Zen Volume Cut.

5.5.5 Systematic Uncertainty

Binning Effect

The likelihood selection is implemented with 0.1 MeV binning for the prompt energy. In other words, the selection does not consider the shape of the antineutrino energy spectrum within each bin and assumes that the selection efficiency is constant within

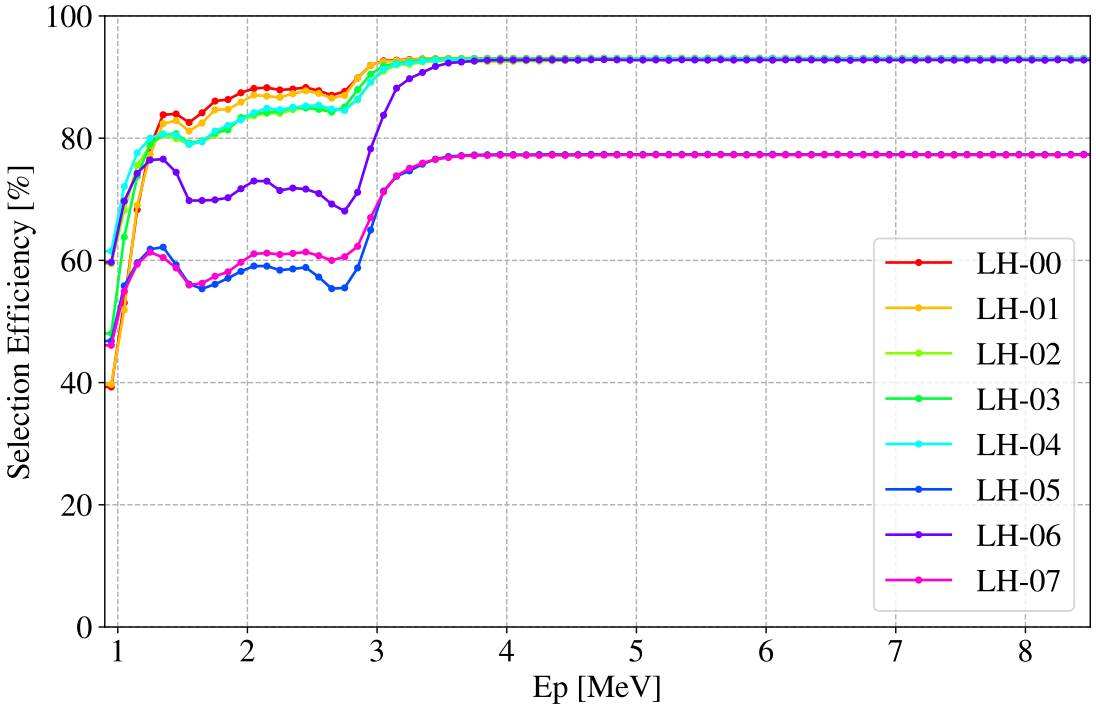

Figure 5.27: Selection efficiency for each the prompt energy in each likelihood period

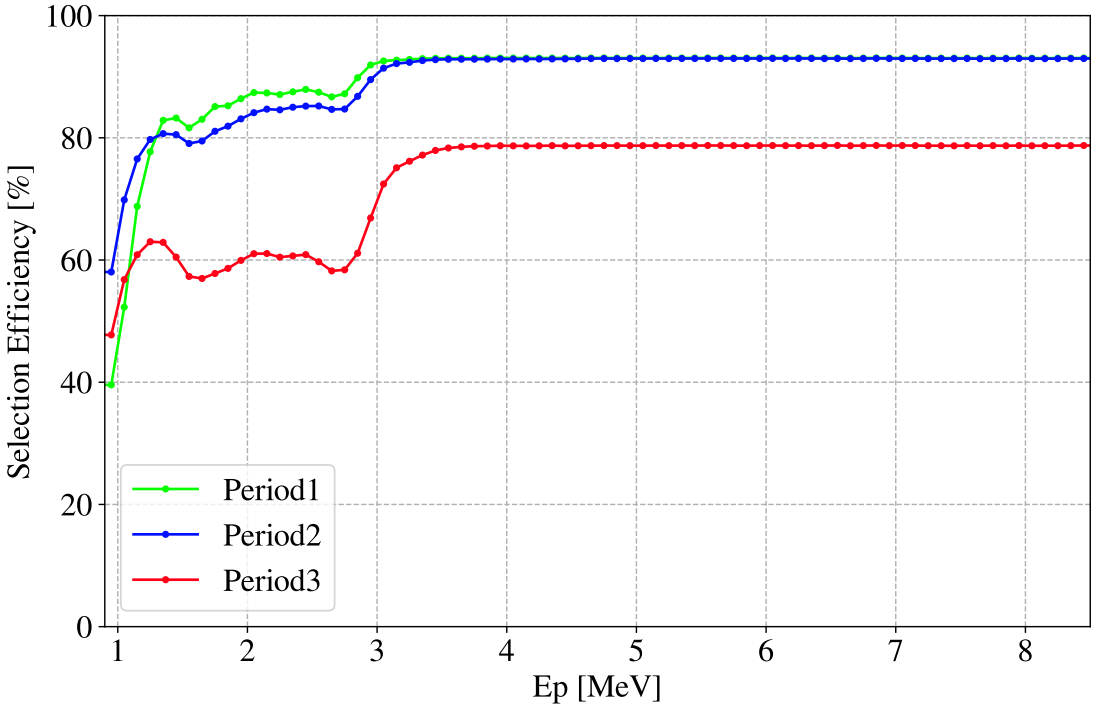

Figure 5.28: Selection efficiency for each the prompt energy in each dataset period

each bin. However, the actual reactor antineutrino and geoneutrino have continuous spectral shape.

The possible distortion originating from this difference is called "binning effect" and evaluated as

$$\sigma_{\text{binning}} = \frac{N_{\text{unbinned}} - N_{\text{binned}}}{N_{\text{binned}}} \tag{5.11}$$

where

$$\begin{aligned} N_{\text{binned}} &= \sum_{E_{\text{p}}\text{-bins}} F_{\text{binned}}(E_{\text{p}}) S_{\text{binned}}(E_{\text{p}}) \Delta E_{\text{p}} \\ N_{\text{unbinned}} &= \int F_{\text{unbinned}}(E_{\text{p}}) S_{\text{unbinned}}(E_{\text{p}})\, \mathrm{d}E_{\text{p}} \end{aligned} \tag{5.12}$$

Here, $F_{\text{binned}}(E_{\text{p}})$ is the binned antineutrino spectrum including non-oscillating reactor neutrino and geoneutrino(Enomoto 2006), and $S_{\text{binned}}(E_{\text{p}})$ is the selection efficiency as a function of the prompt energy. Whereas $F_{\text{unbinned}}(E_{\text{p}})$ is the continuous antineutrino energy spectrum and $S_{\text{unbinned}}(E_{\text{p}})$ is the corresponding selection efficiency generated by interpolating $S_{\text{binned}}(E_{\text{p}})$. Figure 5.29 shows the comparisons of the binned and continuous spectrum multiplied the energy dependent selection efficiencies.

The binning effect is evaluated in different energy regions by varying the range of summation and integration in Eq.5.12 as summarized in Table 5.6.

Delayed Energy Selection

The energy resolution implemented into the Geant4 simulation is estimated from the observed calibration data, and it is accompanied by an uncertainty. The uncertainty of the likelihood selection efficiency from this resolution uncertainty is evaluated from the difference between the efficiency curves in case of $\sigma_{\text{vertex}} = \sigma^{\text{mean}}_{\text{vertex}} + \sigma^{\text{stat}}_{\text{vertex}}$ and $\sigma_{\text{vertex}} = \sigma^{\text{mean}}_{\text{vertex}} - \sigma^{\text{stat}}_{\text{vertex}}$, where $\sigma^{\text{mean}}_{\text{vertex}}$ is the initially implemented vertex resolution and $\sigma^{\text{stat}}_{\text{vertex}}$ is its statistical uncertainty.

Space Correlation

The uncertainty of the space correlation cut is evaluated from the deviation between the Geant4 simulation and observed data. The pseudo "observed data" of IBD reaction is constructed by combining the ^{68}Ge source calibration data (0.511×2 MeV γ) as a prompt event and AmBe composite source calibration data (2.2 MeV neutron capture γ selected by the delayed coincidence) as a delayed event.

Time Correlation

The uncertainty related to the time correlation is evaluated in the same strategy as that of delayed energy selection, changing the half life of neutron capture within its measured statistical uncertainty.

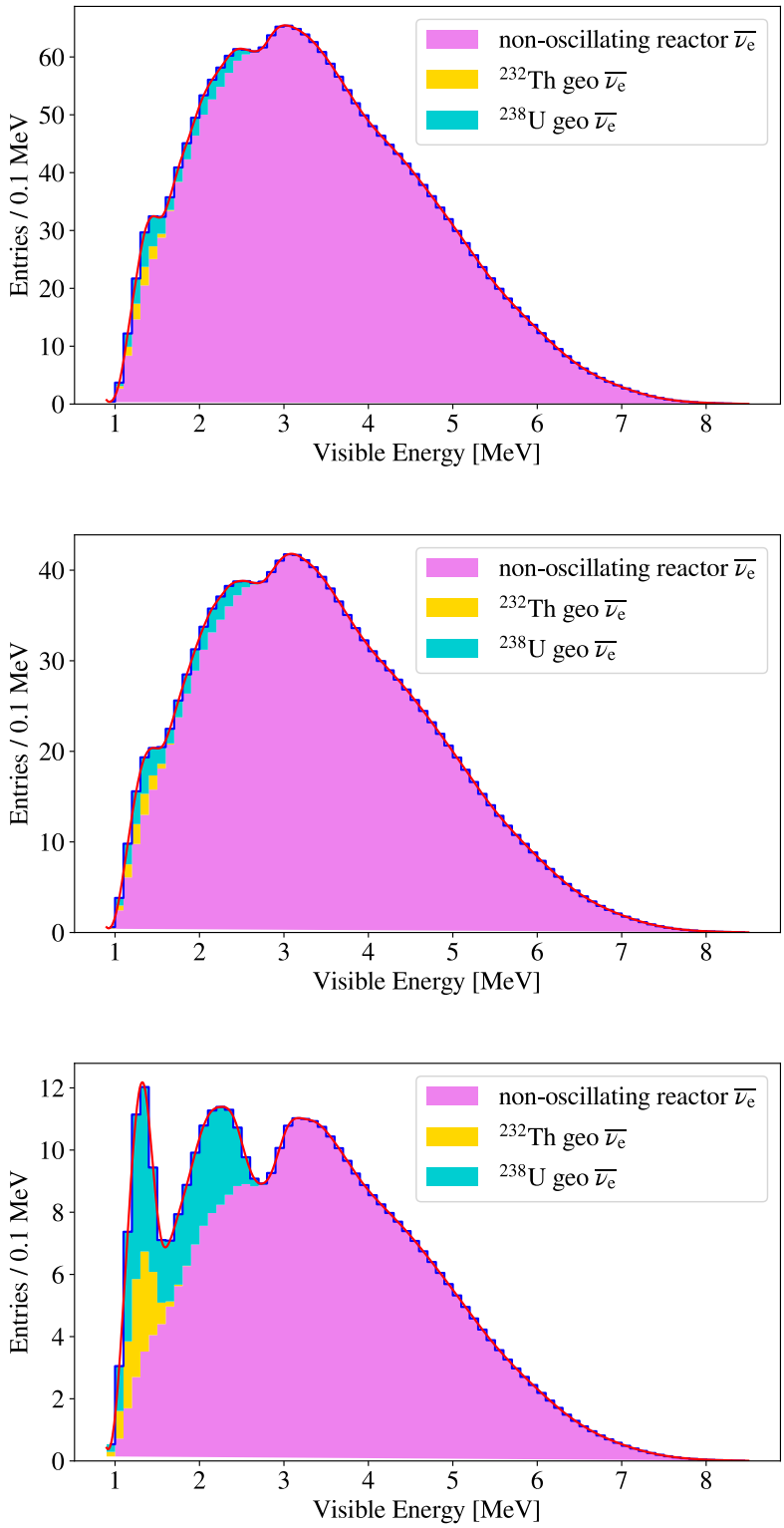

Figure 5.29: binning effect calculation for period1 (top), period2 (middle) and period3 (bottom). The non-oscillating reactor neutrino spectrum is described in Sec.6.1. The geoneutrino spectrum originating from ^{238}U (lime green) and ^{232}Th (yellow) are the model expectation by Enomoto (2006).

Total Likelihood Selection Uncertainty

Figure 5.30 shows the uncertainties from above three components and the sum of them as a function of the prompt energy in each data period.

The systematic uncertainty for reactor and geo neutrino is calculated by convolving the expected energy spectrum by these curves in different energy ranges and summarized in Table 5.6 as "Likelihood selection".

5.6 Detector-related Systematic Uncertainties

This section summarizes the detector-related, or selection-related, systematic uncertainties.

Table 5.6 is the summary of the detector-related systematic uncertainties. The uncertainty of "Livetime Calculation" was described in Sec.5.1.3. The uncertainties of "Miss-recon. probability", "Energy scale" and "Fiducial volume cut" were discussed in Sec.4.8. The uncertainty of "Noise cut" is discussed in Sec.5.2.1. The uncertainties of "Binning effect" and "Likelihood selection" were shown in Sec.5.5.4. The rest is discussed later in this section.

Table 5.6: Summary of detector-related systematic uncertainties

	Period1		Period2		Period3	
energy range [MeV]	0.9–8.5	0.9–2.6	0.9–8.5	0.9–2.6	0.9–8.5	0.9–2.6
– Target proton –						
Number of target proton	0.1%		0.1%		0.1%	
– Cross section –						
Cross section of IBD	0.2%		0.2%		0.2%	
– Detector operation –						
Livetime Calculation	0.030%		0.006%		0.006%	
Trigger efficiency	0.0114%		0.0956%		0.0147%	
– Event reconstruction –						
Miss-recon. probability	0.2%		0.2%		0.2%	
Energy scale	1.1%	1.6%	1.2%	2.3%	1.2%	2.3%
– Event selection –						
Noise cut	0.0027%		0.0049%		0.029%	
OD-hit event cut	0.3%		0.2%		0.2%	
Fiducial volume cut	1.65%		3.86%		4.50%	
Binning effect	0.0026%	0.0061%	0.0028%	0.0068%	0.0048%	0.0064%
Likelihood selection	1.172%	1.363%	0.944%	0.890%	1.679%	1.963%
Total	2.342%	2.706%	4.168%	4.596%	4.964%	5.434%

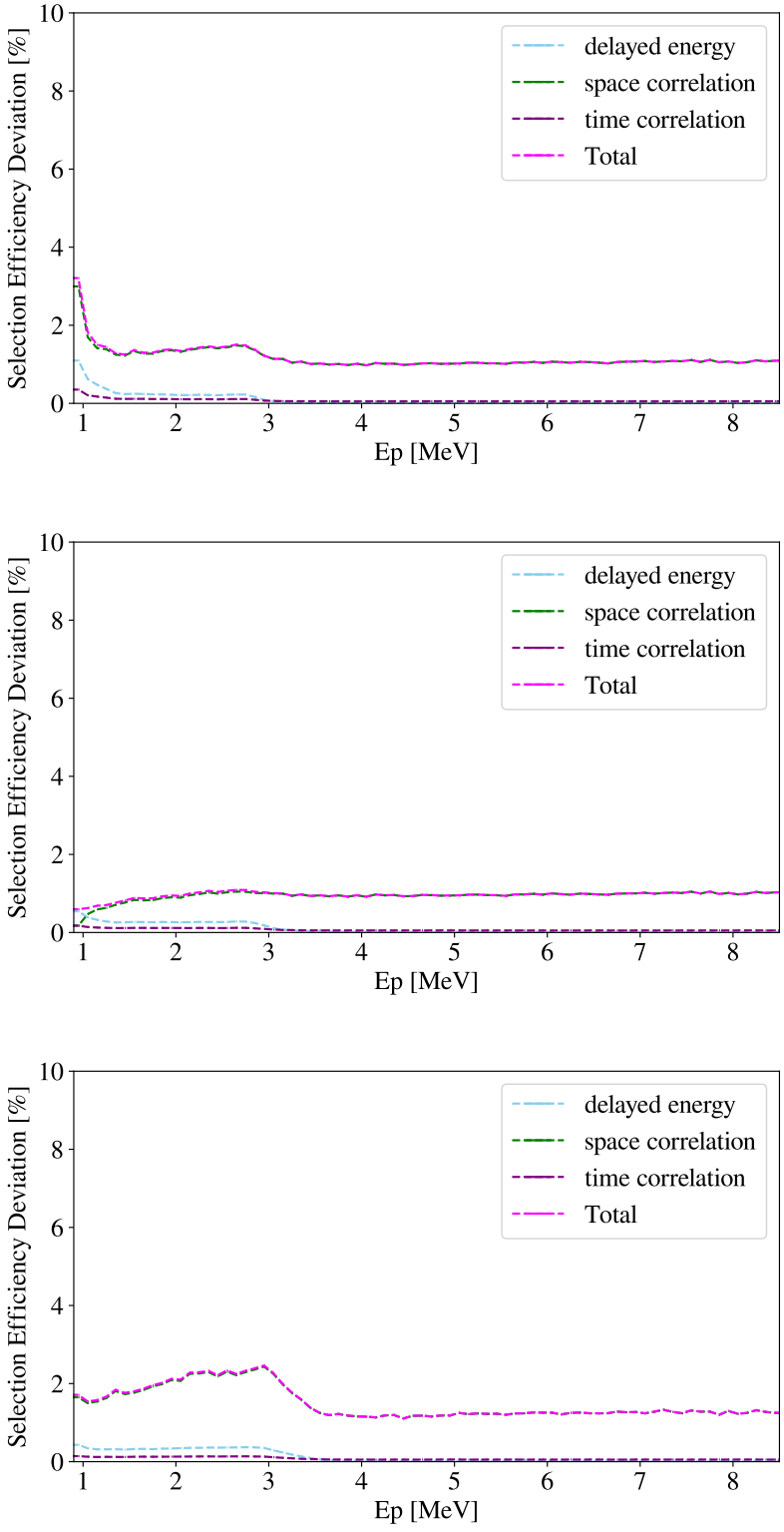

Figure 5.30: Uncertainty of likelihood selection efficiency in period1 (top), period2 (middle) and period3 (bottom)

5.6.1 Number of Target Proton

Antineutrinos are detected via the inverse-beta decay on proton in the liquid scintillator. Therefore, the number of target proton in the 6.0 m fiducial volume is calculated from the chemical composition of the liquid scintillator and density measurement.

Originally the measured density of the KamLAND liquid scintillator was 0.77754± 0.00010 [g/cm^3] at 15 °C. The temperature coefficient of density expansion is measured to be 7.14×10^{-4} [g/cm^3/K]. The temperature of the KamLAND scintillator is controlled at 11.5±1.5 °C. Thus, the actual density is estimated to be 0.78013 [g/cm^3], and the ±1.5 °C temperature uncertainty corresponds to 0.1% density uncertainty. This number is assigned as the systematic uncertainty in Table 5.6. (Ichimura 2008)

Though there were two purification campaigns, the density of filled liquid scintillator was precisely controlled, and the temperature uncertainty discussed above is still dominant. (Watanabe 2012, Obara 2018)

The ratio of H/C, H/N and H/O in the KamLAND liquid scintillator are given from the chemical composition to be 1.96908, 17842.0, 17842.0, respectively. So, the number of ^{1}H in the unit mass is calculated as

$$\begin{aligned} N_{^1\mathrm{H}} &= \frac{\mathrm{N_A}}{1.00794 + 12.001/1.96908 + 14.00674/17842.0 + 15.9994/17842.0} \\ &= 8.471 \times 10^{22} [/\mathrm{g}] \end{aligned} \tag{5.13}$$

where $\mathrm{N_A} = 6.02 \times 10^{23}$ is the Avogadro constant. Therefore, the number of target proton in the 6.0 m fiducial volume (904.78 m^3) is estimated to be

$$\begin{aligned} N_{\mathrm{proton}} &= (8.471 \times 10^{22}/\mathrm{g}) \times (904.78 \times 10^6 \mathrm{cm}^3) \times (0.78013 \mathrm{g/cm}^3) \times (0.99985) \\ &= 5.978 \times 10^{31} \qquad \text{(Ichimura 2008)} \end{aligned} \tag{5.14}$$

This value is used in this study.

5.6.2 Trigger Efficiency

The trigger efficiencies of the prompt and delayed trigger (Sec.3.3.5) is evaluated as

$$\varepsilon_{\mathrm{prompt}}(E_{\mathrm{vis}}) = \frac{\text{number of delayed-triggered events with NsumMax} \geq N_{\text{prompt-threshold}}}{\text{number of delayed-triggered events}} \tag{5.15}$$

$$\varepsilon_{\mathrm{delayed}}(E_{\mathrm{vis}}) = \frac{\text{number of prescale-triggered events with NsumMax} \geq N_{\text{delayed-threshold}}}{\text{number of prescale-triggered events}} \tag{5.16}$$

where $N_{\text{prompt-threshold}}$ and $N_{\text{delayed-threshold}}$ are the prompt and delayed trigger threshold, respectively. These values are evaluated against the visible energy for each period with different trigger threshold presets. Figure 5.31 shows the prompt trigger estimation of average in each data period. The blue stair plots show the

delayed-triggered energy spectrum. The blue filled step plots show the energy spectrum with NsumMax$\geq N_{\text{prompt-threshold}}$. The black stair plots show the prompt trigger efficiencies as a function of the visible energy. The prompt energy corresponding to the IBD reaction threshold, 0.9 MeV, is shown as red dashed vertical lines. Since period1 had higher prompt threshold (see Figure 3.14), the prompt trigger threshold at E_{vis} =0.9 MeV is less than 100% in period1, whereas it is almost 100% in period2 and period3. The delayed trigger threshold is set equal to or lower than the prompt energy threshold, and is used for the neutron capture 2.2 MeV γ, in this study. The (α, n) backgrounds (Sec.6.2) are studied using the prescale threshold. Therefore, the delayed trigger inefficiencies are negligible in this study.

The statistical uncertainties of the trigger efficiencies are calculated from the same dataset assuming the binominal distribution. Finally, the systematic uncertainty of the number of the antineutrino candidates coming from the trigger efficiency uncertainty is estimated by convolving the expected antineutrino spectrum by the trigger efficiency uncertainty curve as shown in Figure 5.32. The mean deviation between $\pm 1\sigma$ of the integration of the convolved spectrum is assigned as the systematic uncertainty.

5.6.3 OD Miss-Tagging Probability

As described in Sec.4.6.1, a cut for N_{200OD} is applied to tag clipping-muon events. However, this criteria might tag a non-muon event with accidental OD hits as a muon event. Such probability is named "OD miss-tagging probability" and estimated using 1PPS trigger data as

$$P_{\text{OD-miss-tagging}} = \frac{\text{number of 1PPS-triggered event with } \text{N}_{\text{200OD}} \geq \text{N}_{\text{200OD-threshold}}}{\text{number of 1PPS-triggered event}} \tag{5.17}$$

where $\text{N}_{\text{200OD-threshold}}$ is the threshold for N_{200OD}.

The OD cut inefficiency, which refers to the probability that the OD miss a muon event, is also evaluated with muon data as

$$\text{(OD cut inefficiency)} = \frac{\text{number of events with } \text{Q}_{17} \geq 10^6 \text{ and } \text{N}_{\text{200OD}} < \text{N}_{\text{200OD-threshold}}}{\text{number of events with } \text{Q}_{17} \geq 10^6} \tag{5.18}$$

These two parameters are evaluated for each run as Figure 5.33. The statistical uncertainties are calculated with the binominal distribution. The vertical green dashed line represents $\text{N}_{\text{200OD-threshold}}$ for this run.

Figure 5.34 shows the time variation of the OD miss-tagging probability (left axis) and the OD cut inefficiency (right axis). From this test, 0.3%, 0.2% and 0.2% are conservatively assigned as the systematic uncertainty from the OD miss-tagging for period1, period2 and period3, respectively.

Due to incompatible trigger presets, this test can not be applied for data taken before 2004. Instead, the values above is checked with source calibration data, and confirmed to be consistent.

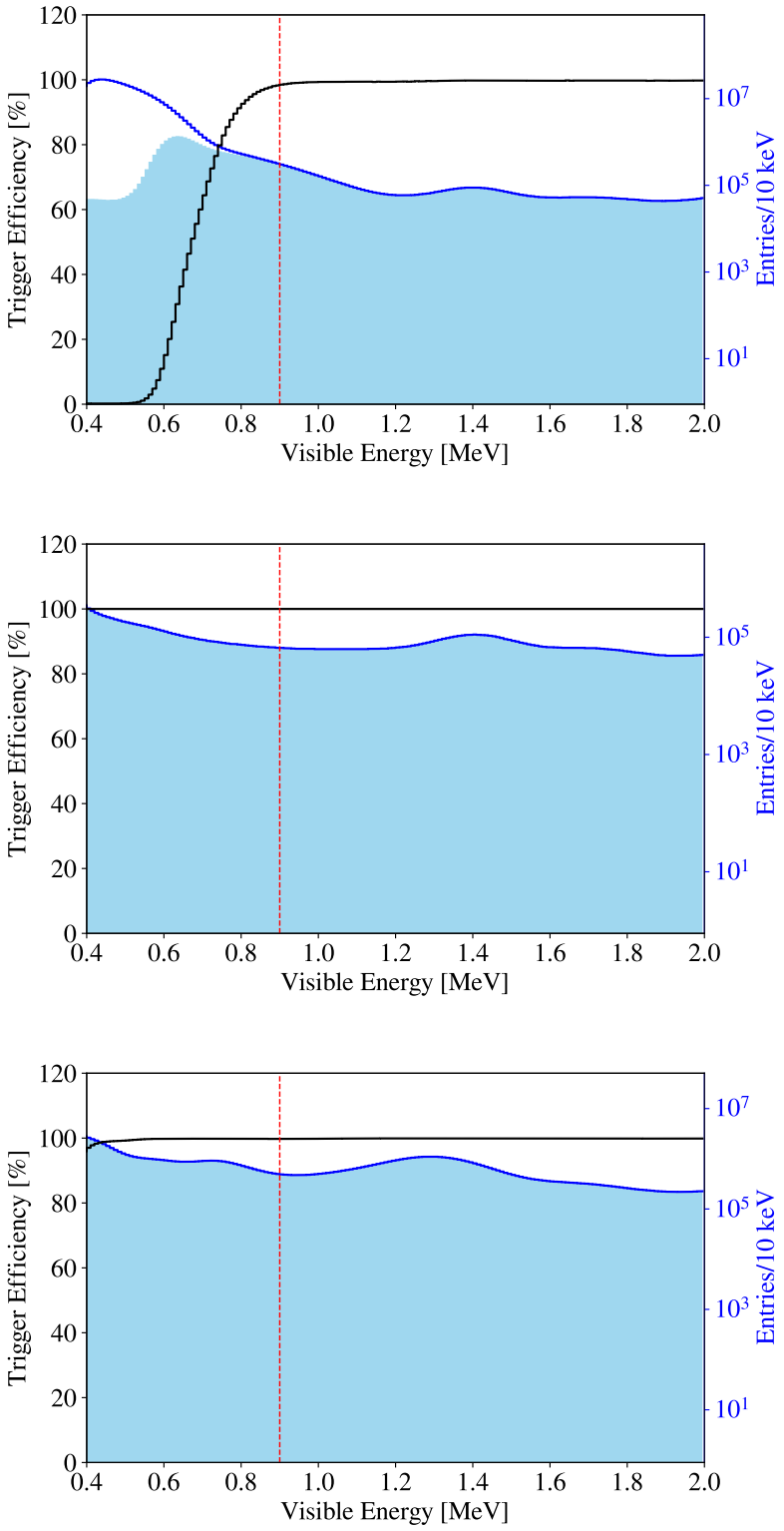

Figure 5.31: Estimation of prompt trigger efficiency in period1 (top), period2 (middle) and period3 (bottom).

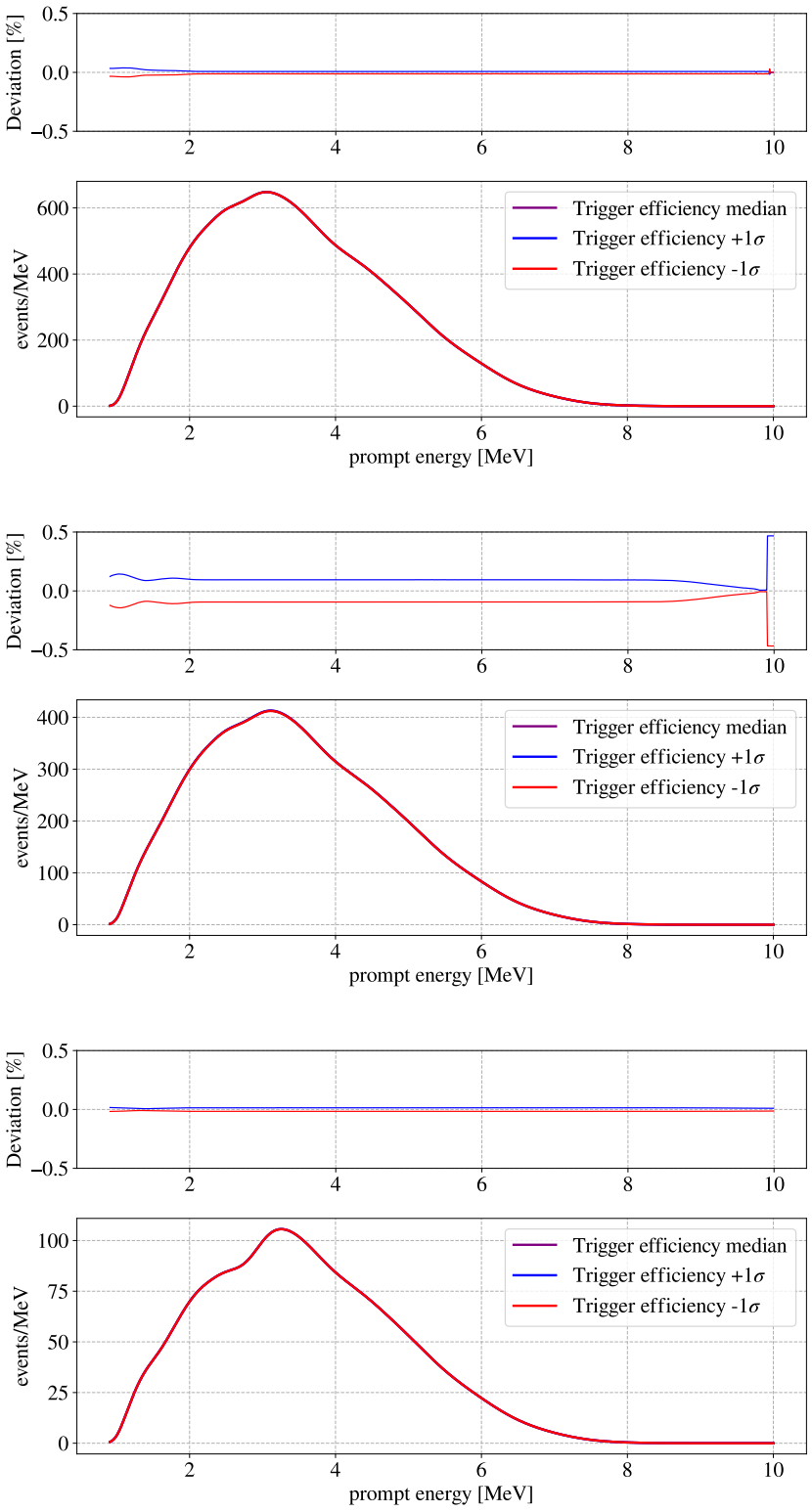

Figure 5.32: Expected energy spectrum convolved by the trigger efficiency uncertainty in period1 (top), period2 (middle) and period3 (bottom).

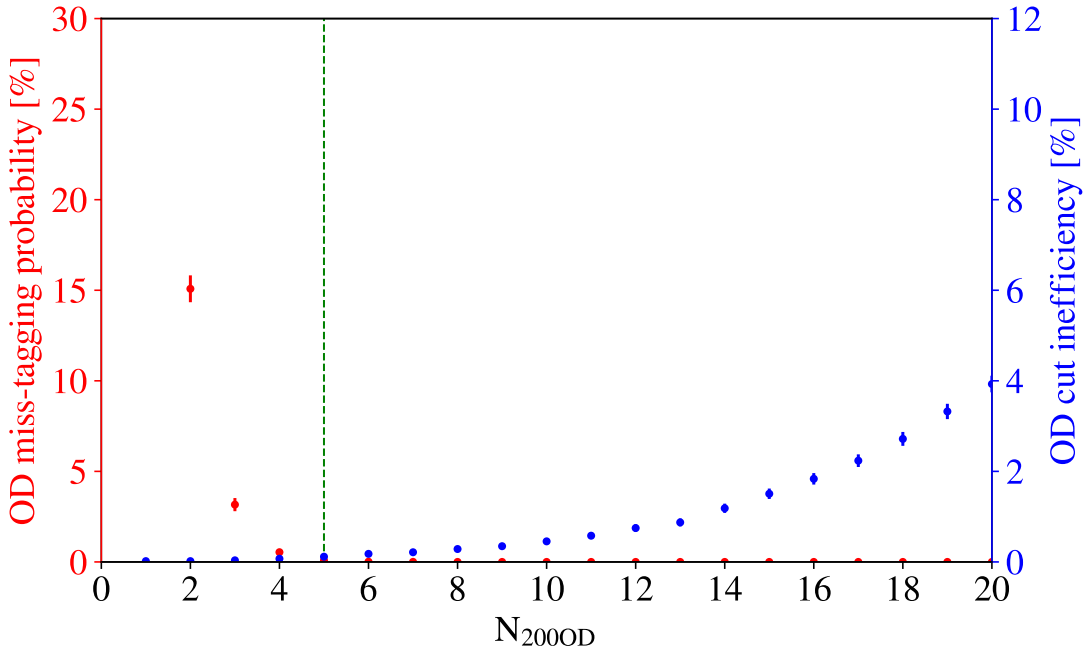

Figure 5.33: OD miss-tagging probability (left axis) and OD cut inefficiency in a run before purification (right axis) as a function of N_{200OD}

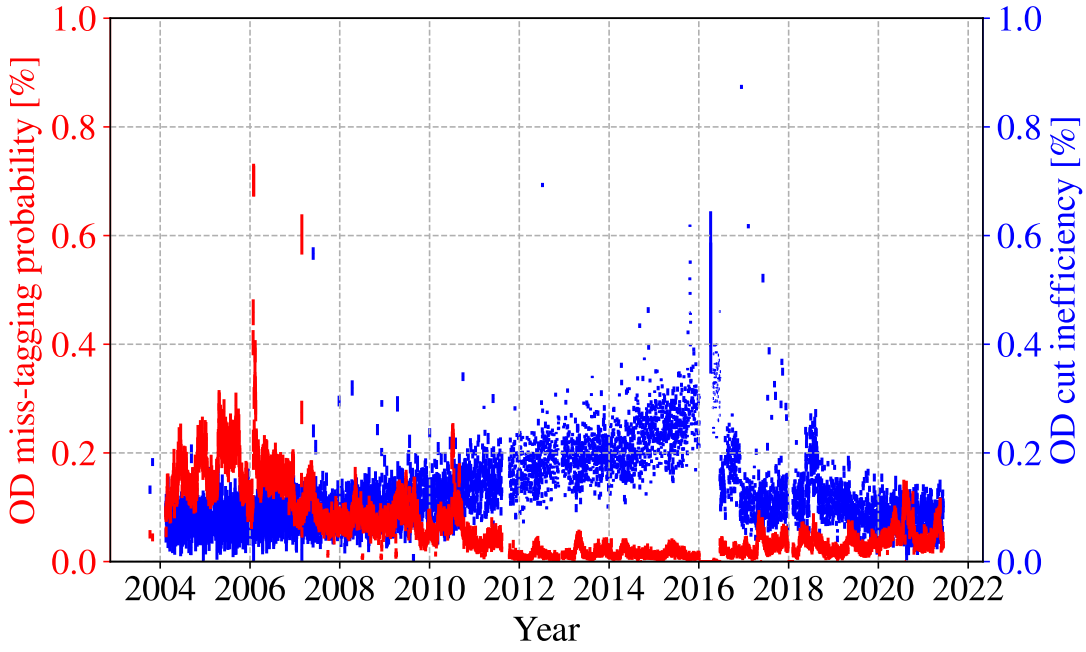

Figure 5.34: time variation of the OD miss-tagging probability (left axis) and the OD cut inefficiency (right axis).

5.7 Anti-neutrino Candidates

This section summarizes the antineutrino signal candidate profile.

There are 23339 delayed-coincidence pairs in the entire dataset and in the energy region $0.9 \leq E_{\rm p} \leq 8.5$. From those, the likelihood selection identified 2964 events as the antineutrino signal candidate. In the geoneutrino energy region, i.e. $0.9 \leq E_{\rm p} \leq 2.6$, 19485 delayed-coincidence pairs were reduced to 1178 antineutrino signal candidates.

Figure 5.35 shows the delayed-coincidence profiles of the candidates in the entire dataset. The blue stair plots show the delayed-coincidence pairs, whereas the blue filled histograms show the remaining signal candidates after the likelihood selection. It is clear that the accidental coincidence backgrounds are effectively rejected by the likelihood selection below 3.0 MeV.

Figure 5.36 shows the vertex distribution of th prompt (left) and delayed (right) events. The final candidates are shown as red points whereas the histograms imply the rejected events by the likelihood selection. From these plots, it is also clear that the likelihood selection effectively rejects the accidental coincidence backgrounds originating from the impurities on the outer balloon.

The number of antineutrino signal in each period are summarized in Table 5.7. Besides, the delayed-coincidence profiles and vertex distributions of each period are shown in Figure 5.37–5.42.

In Figure 5.42, the Zen Volume Cut region is illustrated with blue dashed line. However, some candidates are in this line because period3 includes some dataset without Zen Volume Cut, i.e. the period between KamLAND-Zen 400 and 800.

Table 5.7: The number of antineutrino signal candidates in each period

	Period1		Period2		Period3	
energy range [MeV]	0.9–8.5	0.9–2.6	0.9–8.5	0.9–2.6	0.9–8.5	0.9–2.6
Delayed-coincidence selection	8201	6771	5502	4309	9636	8405
Likelihood selection	1608	651	1022	363	334	164

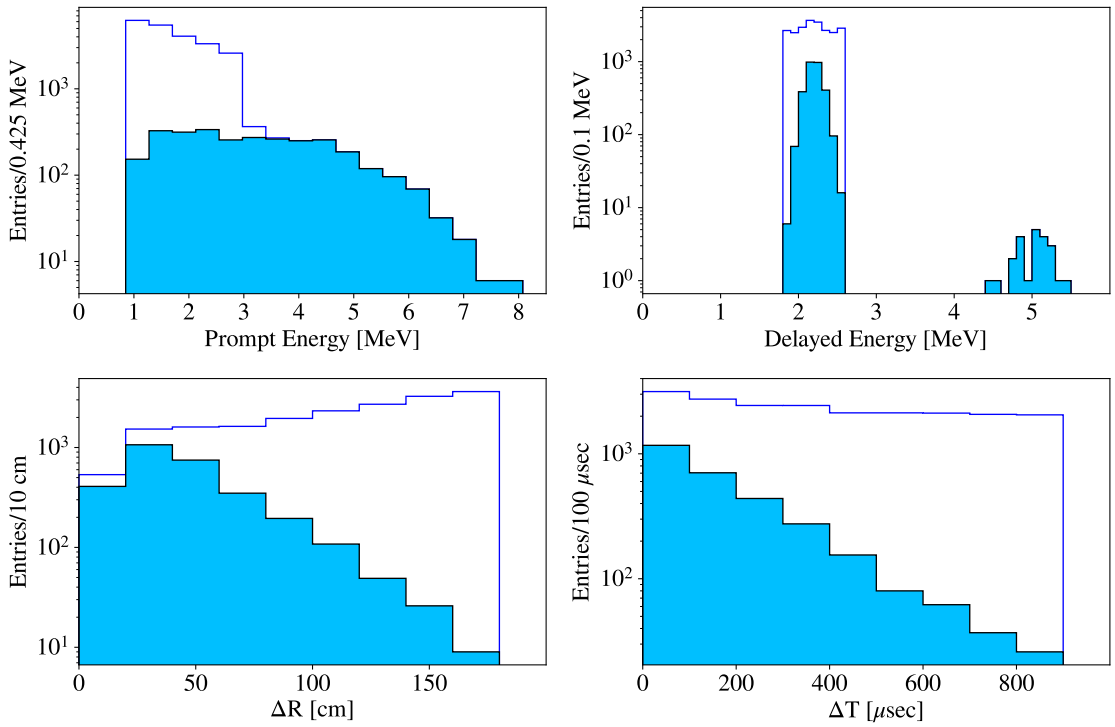

Figure 5.35: Delayed-coincidence profile of the antineutrino candidates in the entire dataset

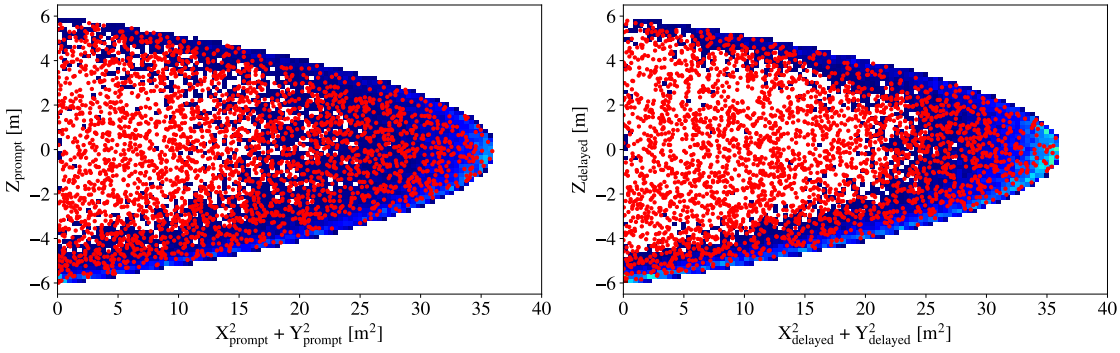

Figure 5.36: Vertex distribution of the antineutrino candidates in the entire dataset

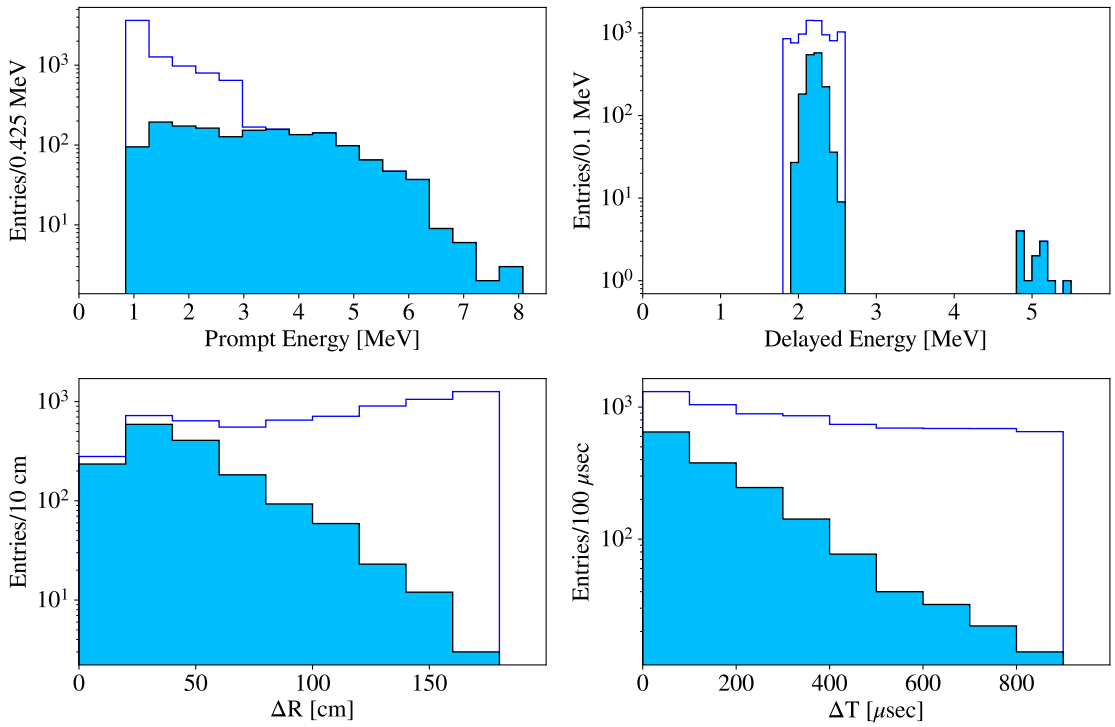

Figure 5.37: Delayed-coincidence profile of the antineutrino candidates in Period1

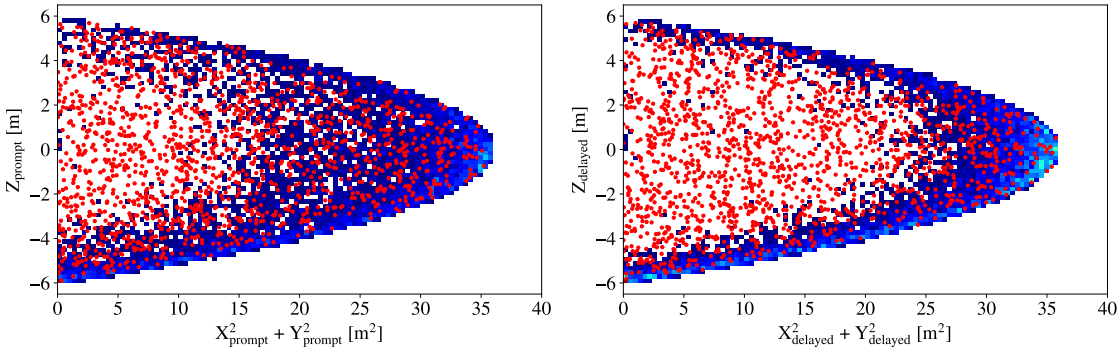

Figure 5.38: Vertex distribution of the antineutrino candidates in Period1

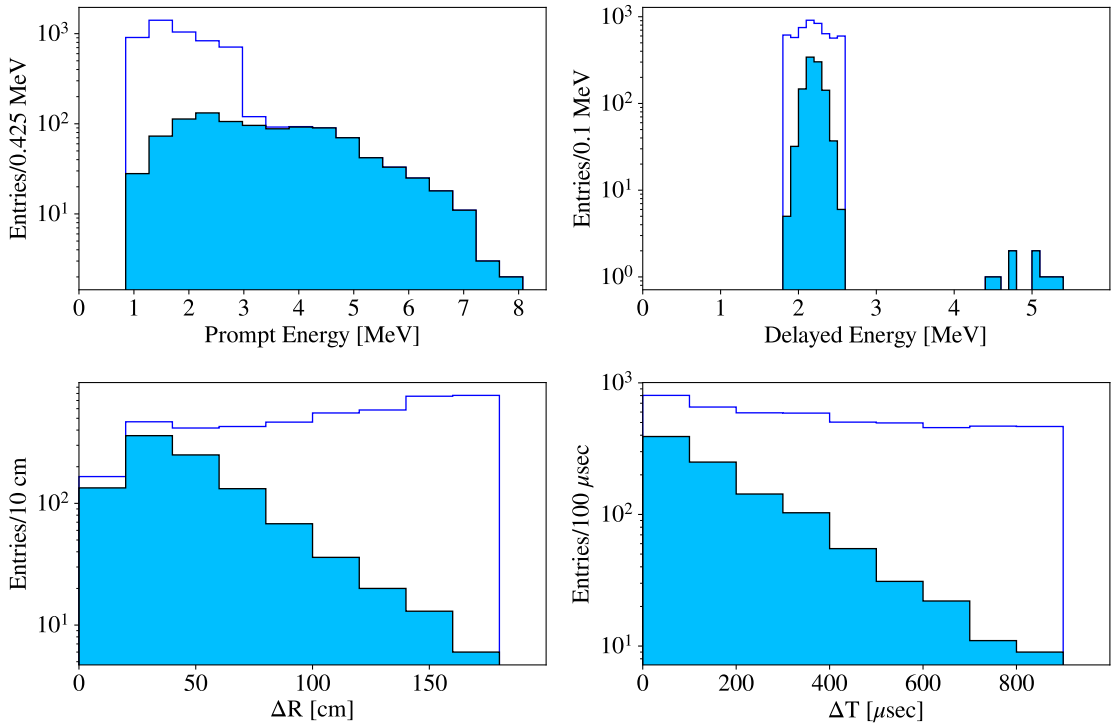

Figure 5.39: Delayed-coincidence profile of the antineutrino candidates in Period2

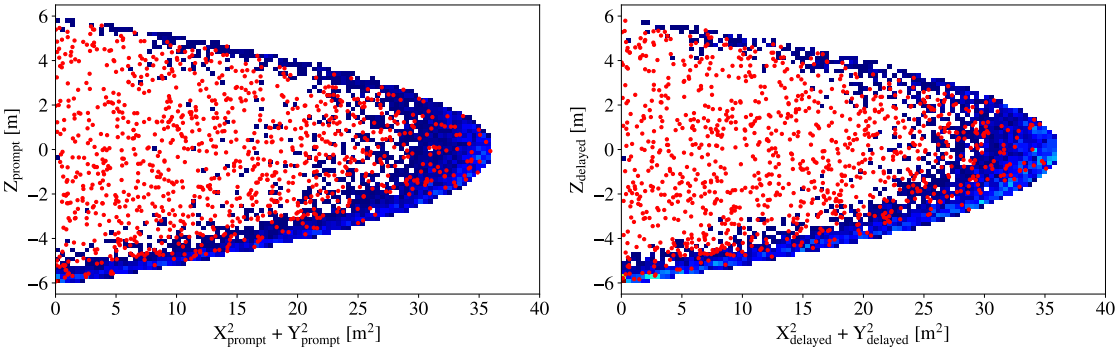

Figure 5.40: Vertex distribution of the antineutrino candidates in Period2

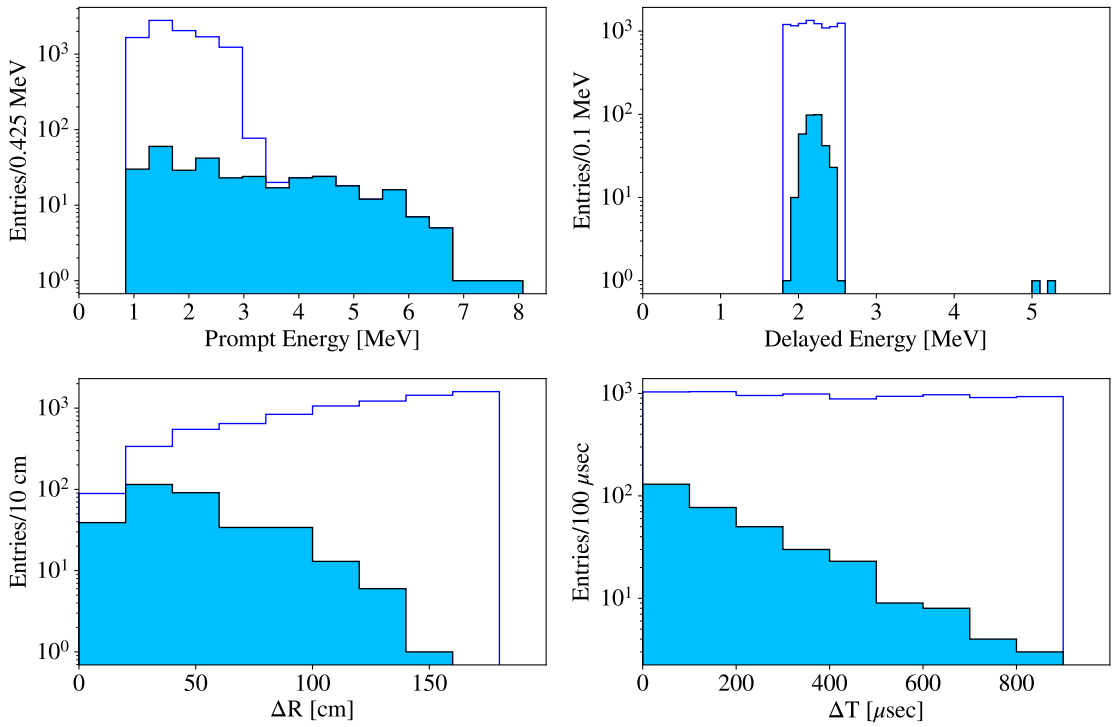

Figure 5.41: Delayed-coincidence profile of the antineutrino candidates in Period3

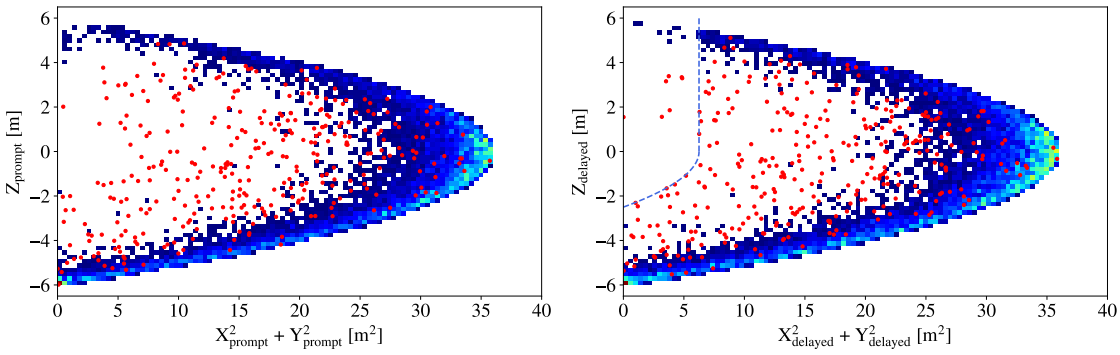

Figure 5.42: Vertex distribution of the antineutrino candidates in Period3

Chapter 6

Background Estimation

The electron antineutrino signal is selected by the delayed-coincidence method. The backgrounds for the geoneutrino signal is classified into three categories.

The first and dominant background is antineutrinos originating from the reactors. These events shall have exactly the same event profile in the detector, and cannot be distinguished by any event selection criteria. So, it is necessary to evaluate the abundance and energy spectrum of the reactor antineutrinos in advance.

The second one is time-correlated sequential events associated with the muon-spallation product accompanying neutron captures, radioactive decays with neutron emitter, or short life nuclei.

The third one is uncorrelated events which accidentally tagged by the delayed-coincidence selection.

6.1 Antineutrinos from Reactors

The KamLAND detector was originally designed to detect antineutrinos from Japanese commercial reactors aiming at demonstrating the neutrino oscillation. Therefore, the site is chosen to have enough reactor neutrino flux. Although reactor neutrino is of great interest as described in Chap.7, it is the most serious backgrounds for geoneutrino observation.

Reactor neutrinos are mainly generated by β-decays of short-lived isotopes (^{235}U, ^{238}U, ^{239}Pu and ^{241}Pu) in nuclear fuels. Since the reactor neutrinos are by-product of the thermal power from nuclear reactors, the abundance of reactor antineutrino can be estimated using the correlation between the reactor power output and number of fissions of these elements.

There also be a small amount of long-lived nuclei (e.g. ^{106}Ru, ^{144}Ce, ^{90}Sr) which are produced by fissions and decays of short-lived elements. Such isotopes are accumulated in the nuclear fuel and make a small but constant antineutrino emission uncorrelated with the reactor operation status, even after the fuel is removed from the reactor. The amount of such isotopes are also calculated.

6.1.1 Antineutrino Flux from Japanese reactors

There are 56 commercial nuclear reactors and 2 research nuclear reactors in Japan which are in operation in the KamLAND running time as listed in Table 6.1–6.3. The fission-flux-weighted average of distance between these reactors and the KamLAND site is $\sim$ 180 km. Figure 6.1 shows the positions of Japanese commercial reactors. The precise position of these reactors are provided from Tokyo Electric Power Company (TEPCO). The uncertainty of the reactor position is found to be within 70 m from the comparison between the provided coordinate and coordinate taken from a topological map. This position uncertainty corresponds to the distance uncertainty less than 0.1%.

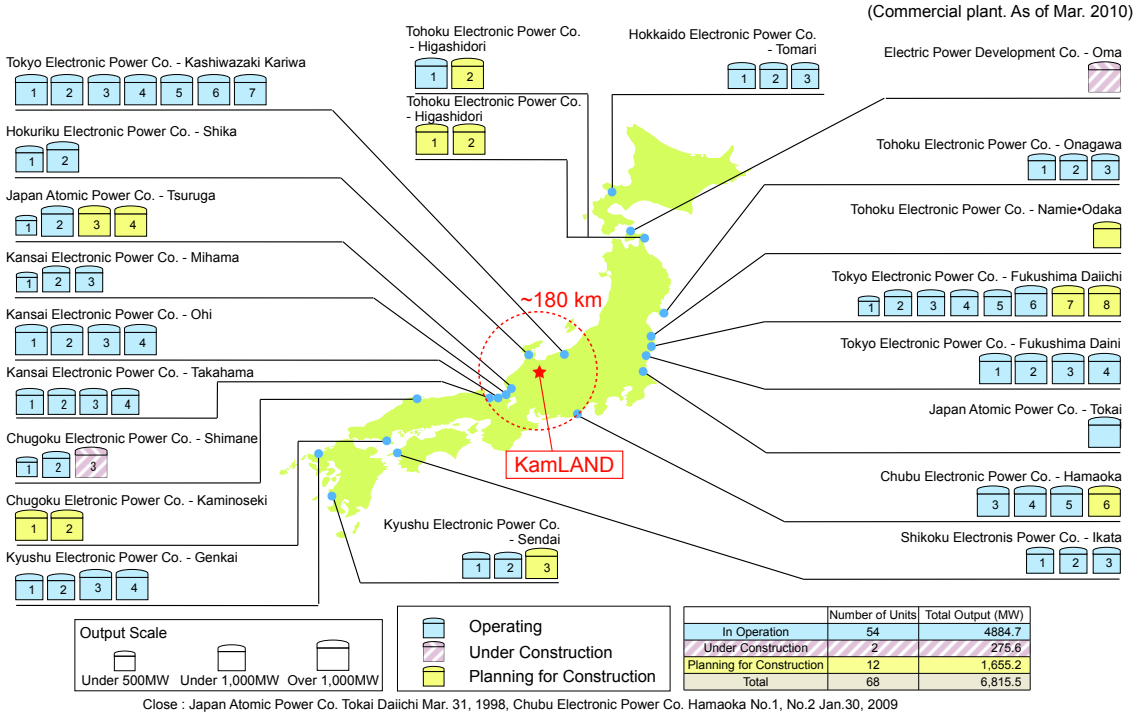

Figure 6.1: Positions of Japanese reactors. The data is as of 2010. The figure is cited from Watanabe (2012) but the original data is provided from the Foundation of Electric Power Companies of Japan.

Nuclear reactors are categorized by the type of fuel coolant and neutron moderator. All commercial reactors in Japan are light-water reactor (LWR), whereas graphite-moderated reactor and heavy-water reactor is in operation oversea. A large majority of LWR is further categorized in to two types, boiling-water reactor (BWR) and pressurized-water reactor (PWR). Figure 6.2 shows the schematic view of BWR and PWR. The main difference between BWR and PWR is the process of generating steam. In a BWR, coolant water is converted to steam and directly send to a stem turbine. On the other hand, heated water in PWR is kept liquid under high pressure and sent to a steam generator, where the heat is transferred the secondary water system. The secondary water system then converted water to steam for tur-

Table 6.1: List of Japanese reactors (1)

operator	reactor name	distance [km]	type	thermal power [MW]	electrical power [MW]
Chubu	Hamaoka-1	213.723	BWR	1593	540
	Hamaoka-2	213.799	BWR	2436	840
	Hamaoka-3	214.005	BWR	3293	1100
	Hamaoka-4	214.145	BWR	3293	1137
	Hamaoka-5	214.523	BWR	3926	1380
Chugoku	Shimane-1	401.072	BWR	1380	460
	Shimane-2	401.218	BWR	2436	820
Genden	Tokai2	295.371	BWR	3293	1100
	Tsuruga-1	138.467	BWR	1064	357
	Tsuruga-2	138.484	PWR	3423	1160
Hokkaido	Tomari-1	783.041	PWR	1650	579
	Tomari-2	782.923	PWR	1650	579
	Tomari-3	782.735	PWR	2660	912
Hokuriku	Shika-1	87.675	BWR	1593	540
	Shika-2	87.719	BWR	3926	1358
Kansai	Mihama-1	145.719	PWR	1031	340
	Mihama-2	145.768	PWR	1456	500
	Mihama-3	145.833	PWR	2440	826
	Ohi-1	178.75	PWR	3423	1175
	Ohi-2	178.826	PWR	3423	1175
	Ohi-3	179.041	PWR	3423	1180
	Ohi-4	179.159	PWR	3423	1180
	Takahama-1	191.239	PWR	2440	826
	Takahama-2	191.271	PWR	2440	826
	Takahama-3	191.682	PWR	2660	870
	Takahama-4	191.714	PWR	2660	870
Kyusyu	Genkai-1	754.402	PWR	1650	559
	Genkai-2	754.514	PWR	1650	559
	Genkai-3	754.629	PWR	3423	1180
	Genkai-4	754.74	PWR	3423	1180
	Sendai-1	830.381	PWR	2660	890
	Sendai-2	830.302	PWR	2660	890
Shikoku	Ikata-1	560.79	PWR	1650	566
	Ikata-2	560.845	PWR	1650	566
	Ikata-3	560.703	PWR	2660	890

Table 6.2: List of Japanese reactors (2)

operator	reactor name	distance [km]	type	thermal power [MW]	electrical power [MW]
Tohoku	Onagawa-1	430.48	BWR	1593	524
	Onagawa-2	430.604	BWR	2436	825
	Onagawa-3	430.51	BWR	2436	825
	Higashidori-1	635.891	BWR	3293	1100
Tokyo	Fukushima1-1	349.425	BWR	1380	460
	Fukushima1-2	349.374	BWR	2381	784
	Fukushima1-3	349.338	BWR	2381	784
	Fukushima1-4	349.301	BWR	2381	784
	Fukushima1-5	349.553	BWR	2381	784
	Fukushima1-6	349.59	BWR	3293	1100
	Fukushima2-1	345.341	BWR	3293	1100
	Fukushima2-2	345.398	BWR	3293	1100
	Fukushima2-3	345.439	BWR	3293	1100
	Fukushima2-4	345.472	BWR	3293	1100
	KashiwazakiKariwa-1	159.105	BWR	3293	1100
	KashiwazakiKariwa-2	159.225	BWR	3293	1100
	KashiwazakiKariwa-3	159.336	BWR	3293	1100
	KashiwazakiKariwa-4	159.538	BWR	3293	1100
	KashiwazakiKariwa-5	160.619	BWR	3293	1100
	KashiwazakiKariwa-6	160.519	BWR	3926	1356
	KashiwazakiKariwa-7	160.399	BWR	3926	1356

Table 6.3: List of Japanese research reactors

operator	reactor name	distance [km]	type	thermal power [MW]	electrical power [MW]
Japan Nuclear Cycle	Fugen	138.505	ATR	557	165
	Monju	141.51	FBR	714	280

bine. However, the differences between BWR and PWR do not matter in calculating reactor neutrino flux because the thermal output of the reactor is directly measured and used in the calculation.

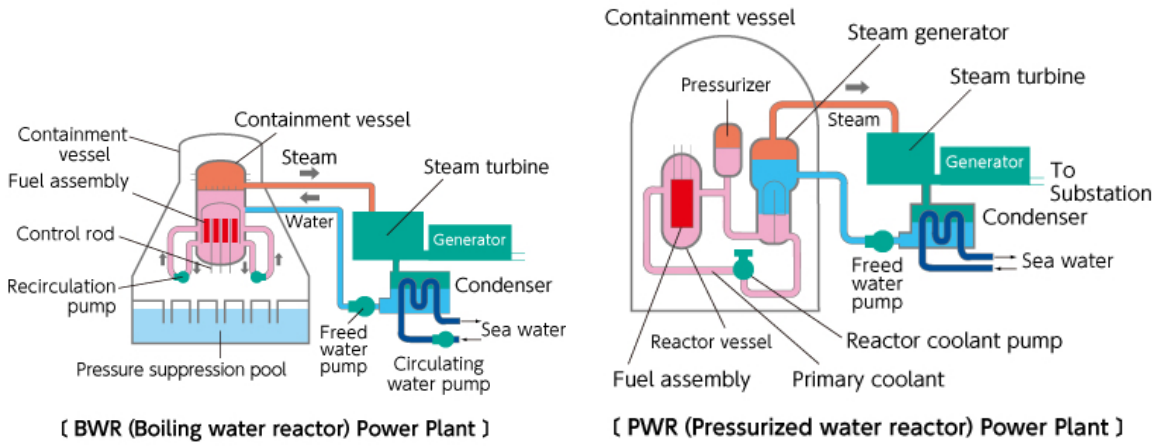

Figure 6.2: Schematic view of BWR (left) and PWR (right)(Fuel)

Reactor cores consist of fuel rods and control rod. The normal fuel rods contains uranium oxide where ^{235}U is enriched to 3–5% as main heat producing isotope and the rest is ^{238}U. The composition of the fuel changes as the burn progress, i.e. ^{235}U decrease and ^{238}U, ^{239}Pu and ^{241}Pu increase. This process is called "burnup". The MOX fuels have different initial compositions, and then, the different burnup effect as discussed in Sec.6.1.4.

Under the special agreement between Tohoku University and the Japanese nuclear power reactor operators, detailed reactor operation data is provided, including thermal power and burnup status at each time. Figure 6.3 and Figure 6.4 show examples of the provided reactor operation data. The data is typically provided at weekly frequency during regular operation. Thermal power of reactors are measured via flow meter of coolant with precision of 2%, which is assigned as the uncertainty for $\overline{\nu}_e$ flux from Japanese reactor's thermal power. The fuel composition is evaluated using a simple and practical modeling of the reactor core developed by TEPCO(Nakajima et al. 2006). The uncertainty for $\overline{\nu}_e$ flux from fuel composition is estimated to be 1.0% by comparing with a detailed simulation by TEPCO. The fission rate of each isotope is then calculated from the thermal output, estimated fuel composition and released energy per fission of each isotope (Table 6.4) studied by Declais et al. (1994). Figure 6.5 and Figure 6.6 show examples of the calculated fission rate of each isotope.

Critical reaction in reactors achieve equilibrium within one day for reactor $\overline{\nu}_e$ above 2 MeV. So, the systematic uncertainty from time lag of the provided data is estimated to be 0.01% for $\overline{\nu}_e$ flux by the difference between original reactor $\overline{\nu}_e$ yield and the yield shifting the run time by one day.

The reactor neutrino flux is calculated from the fission rate of each isotopes and distance from each reactor. Figure 6.7 shows the time variation of the estimated $\overline{\nu}_e$ flux from Japanese and Korean reactors. Japanese reactors had a dominant contribution until 2011. By the Great East Japan Earthquake in 2011, almost all Japanese

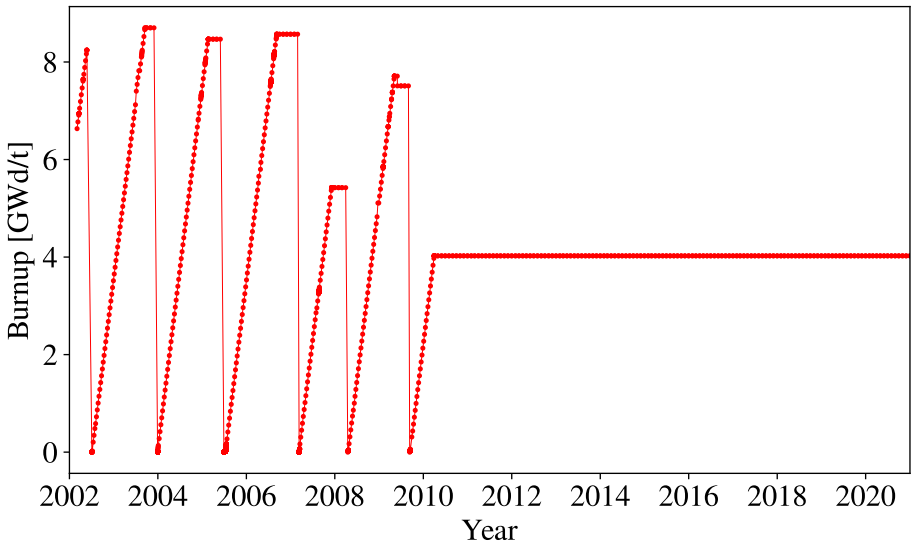

Figure 6.3: Example of provided burnup data (An anonymous nuclear power plant A, BWR). This data is provided according to a special agreement between Tohoku University and the Japanese nuclear power reactor operators.

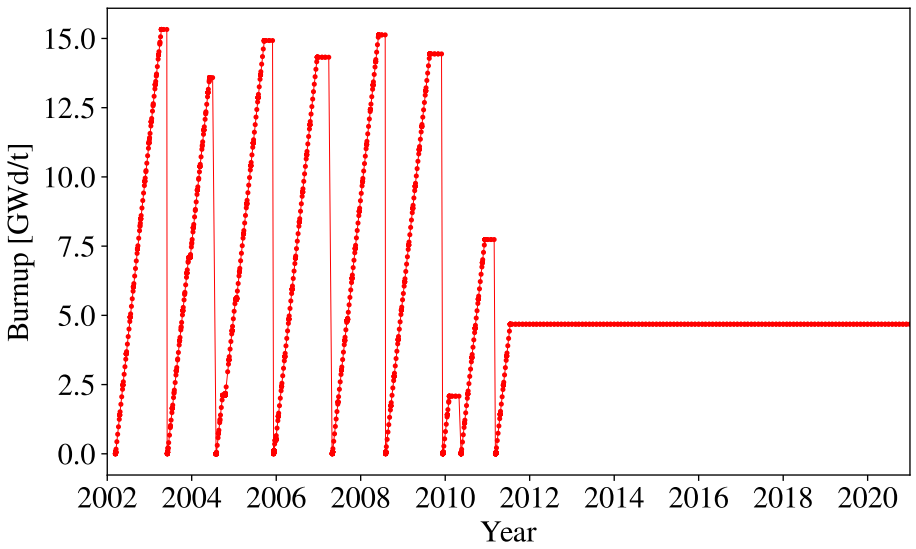

Figure 6.4: Example of provided burnup data (An anonymous nuclear power plant B, PWR). This data is provided according to a special agreement between Tohoku University and the Japanese nuclear power reactor operators.

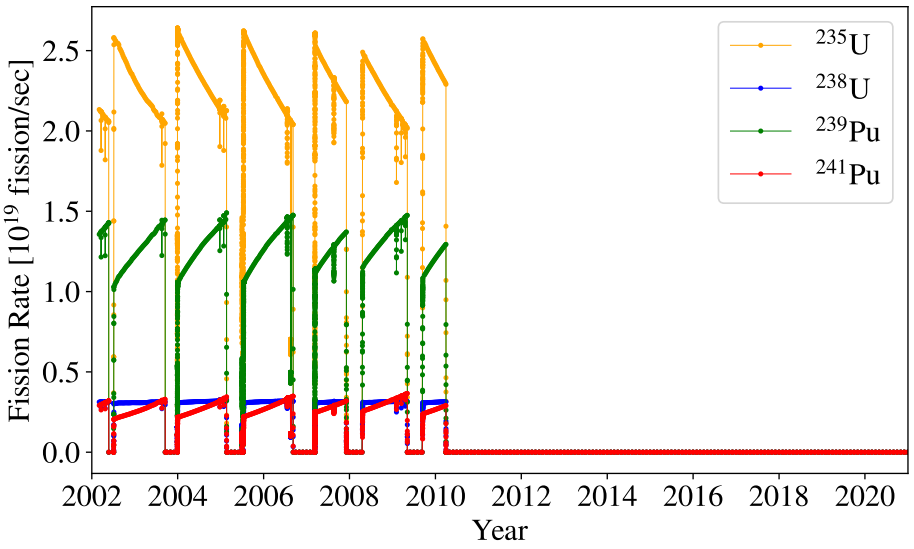

Figure 6.5: Example of calculated fission rate (An anonymous nuclear power plant A, BWR).

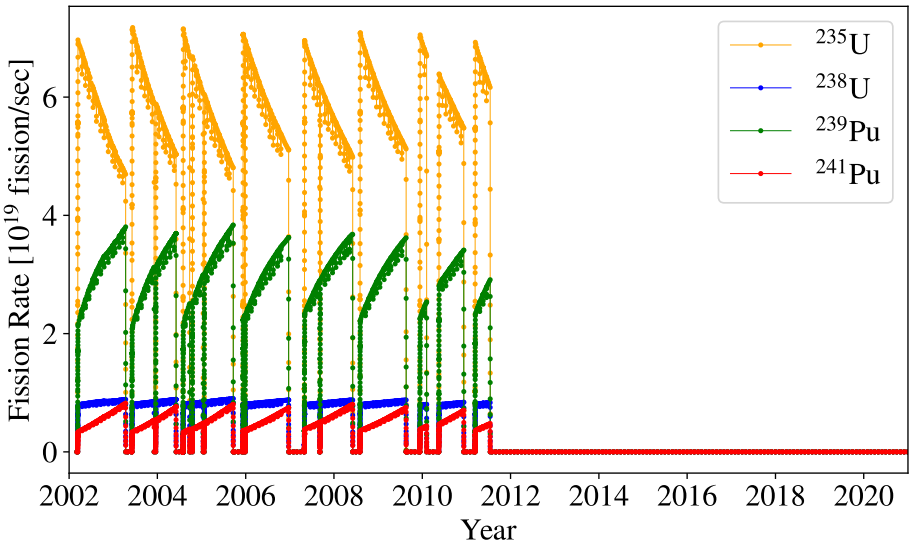

Figure 6.6: Example of calculated fission rate (An anonymous nuclear power plant B, PWR).

Table 6.4: Energy release per fission

isotope	released energy per fission [MeV]
^{235}U	201.8 ± 0.5
^{238}U	205.0 ± 0.7
^{239}Pu	210.3 ± 0.6
^{241}Pu	212.6 ± 0.7

reactors stopped. Because of this, the contribution of the Korean nuclear reactor became larger than before and dominant. Therefore, the precise estimation of the $\overline{\nu}_e$ flux from foreign reactors is important especially in the low-reactor period.

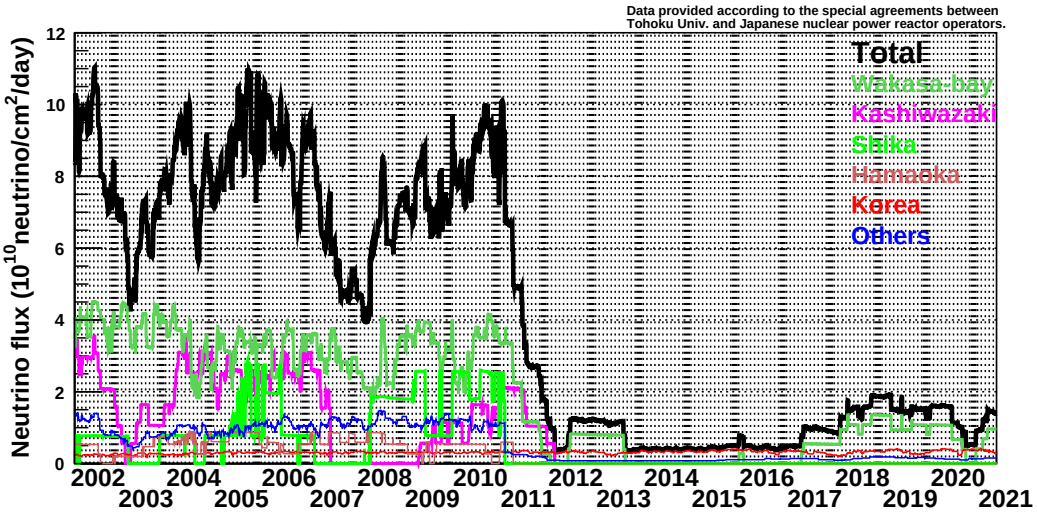

Figure 6.7: Time variation of reactor $\overline{\nu}_e$ flux

6.1.2 Antineutrino Flux from Korean reactors

There are 26 commercial reactors in Korea which are in operation in the KamLAND running time as listed in Table 6.5. However, the operational data of these reactors are neither provided from the operating company nor publicly available. Therefore, the thermal output of Korean reactors is calculated by converting the public electric output data to the thermal output data with a 10% conversion uncertainty. The fission rate of each heat producing isotope is estimated from the thermal output assuming the relative fission yield (^{235}U : ^{238}U : ^{239}Pu : ^{241}Pu) = (0.574 : 0.081 : 0.293 : 0.052), which are average values for Japanese reactors.

The ratio of the $\overline{\nu}_e$ from Korean reactors to the total expected flux is 3.655%, 4.738% and 33.38% in Period1, 2 and 3, respectively.

Table 6.5: List of Korean reactors

operator	reactor name	distance [km]	type	thermal power [MW]	electrical power [MW]
KHNP (Korea)	Kori-1	734.518	PWR	1727	587
	Kori-2	734.518	PWR	1913	650
	Kori-3	734.518	PWR	2796	950
	Kori-4	734.518	PWR	2796	950
	Ulchin-1	711.813	PWR	2796	950
	Ulchin-2	711.813	PWR	2796	950
	Ulchin-3	711.813	PWR	2943	1000
	Ulchin-4	711.813	PWR	2943	1000
	Wolsong-1	708.579	PWR	1995	678
	Wolsong-2	708.579	PWR	2060	700
	Wolsong-3	708.579	PWR	2060	700
	Wolsong-4	708.579	PWR	2060	700
	Yonggwang-1	986.409	PWR	2796	950
	Yonggwang-2	986.409	PWR	2796	950
	Yonggwang-3	986.409	PWR	2943	1000
	Yonggwang-4	986.409	PWR	2943	1000
	Yonggwang-5	986.409	PWR	2943	1000
	Yonggwang-6	986.409	PWR	2943	1000
	Ulchin-5	711.813	PWR	2943	1000
	Ulchin-6	711.813	PWR	2943	1000
	ShinKori-1	733.609	PWR	2825	1038
	ShinKori-2	733.609	PWR	2825	1000
	ShinKori-3	733.609	PWR	3983	1400
	ShinKori-4	733.609	PWR	3983	1400
	ShinWolsong-1	709.378	PWR	2825	1000
	ShinWolsong-2	709.378	PWR	2825	1000

6.1.3 Antineutrino Flux from Global Reactors

In the low-reactor period, not only Korean reactor but also reactors in the other countries (global reactors) have larger contribution than before 2011. Figure 6.8 shows the positions of global reactors in 2010. A number of reactors are operating in Europe and North America, but the $\overline{\nu}_e$ flux from these reactors is almost negligibly small due to their distance from Japan. However, the number of reactors in China and Taiwan is increasing since 2010, whose impact on the $\overline{\nu}_e$ flux is not ignorable.

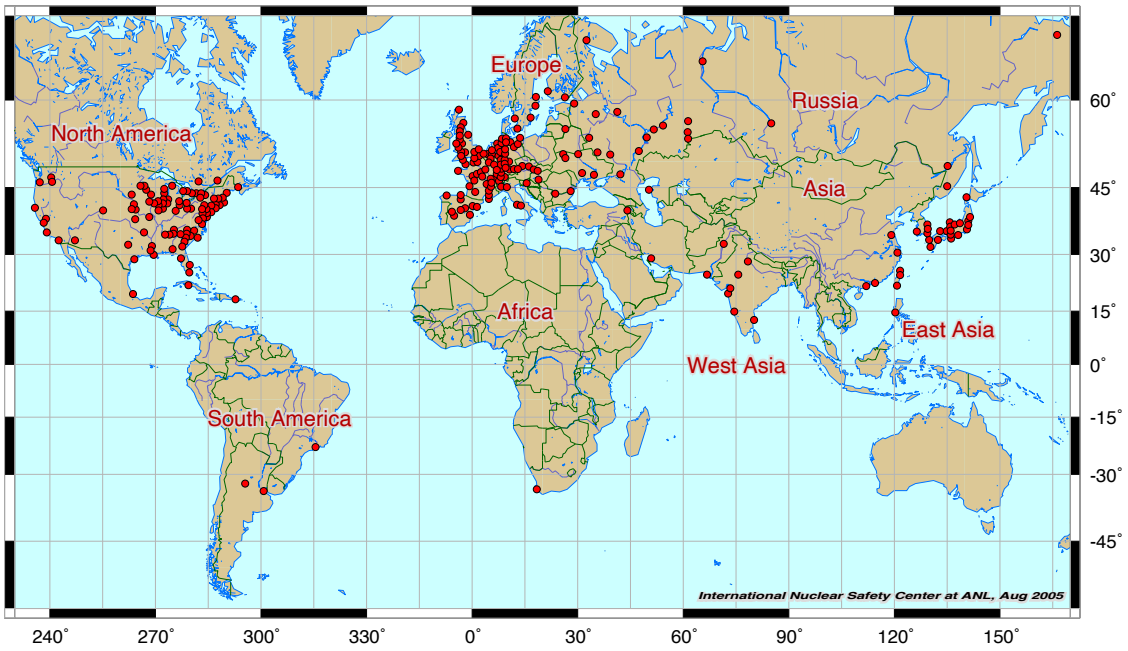

Figure 6.8: Positions of reactors around the world. The data is as of 2010. The figure is cited from Shimizu (2010) but the original data is provided from the International Nuclear Safety Center.

As with the Korean reactors, thermal output record for Chinese and Taiwanese reactors are not available. Thus, the $\overline{\nu}_e$ flux from the global nuclear reactors other than from Japanese and Korean reactors is calculated from the monthly reactor operation data of the global reactor published by IAEA. Operating Experience with Nuclear Power Stations in Member States (OPEX, IAEA (2021)) is published every year and contains various data including reactor type, thermal/electric capacity and monthly electric output. The monthly electric output is converted to the thermal output using the maximum thermal/electric capacity. The conversion uncertainty is estimated to be 10%, which is confirmed using the Korean reactor data from OPEX and calculated in Sec.6.1.2.

Figure 6.10 shows the time variation of calculated ^{235}U fission flux from reactors in Taiwan and China, compared to the Korean reactor. All data shown in this figure is from IAEA (2021). It is clear that the contribution of Chinese reactors is increasing in recent years. On the other hand, the contribution from Taiwanese reactor is negligibly small compared to the Korean flux. The ratio of the $\overline{\nu}_e$ from Taiwanese and Chinese

reactors to the total expected flux is 0.71%, 1.01% and 10.45% in Period1, 2 and 3, respectively. Since the fission flux estimated using OPEX bear 10% uncertainty from the conversion uncertainty, 0.071%, 0.101% and 1.045% is assigned as the $\overline{\nu}_e$ flux uncertainty in each period.

Figure 6.11 shows the breakdown of "The others" in Figure 6.10. A majority of "The other" comes from reactors in the US, France and Russia. However, as with Taiwanese reactors, the contribution from these states is small by order compared to the Korean reactor.

The antineutrino spectrum from East Asia states and the other states in Period3 is calculated using a method described in Sec.6.1.5 and shown in Figure 6.9.

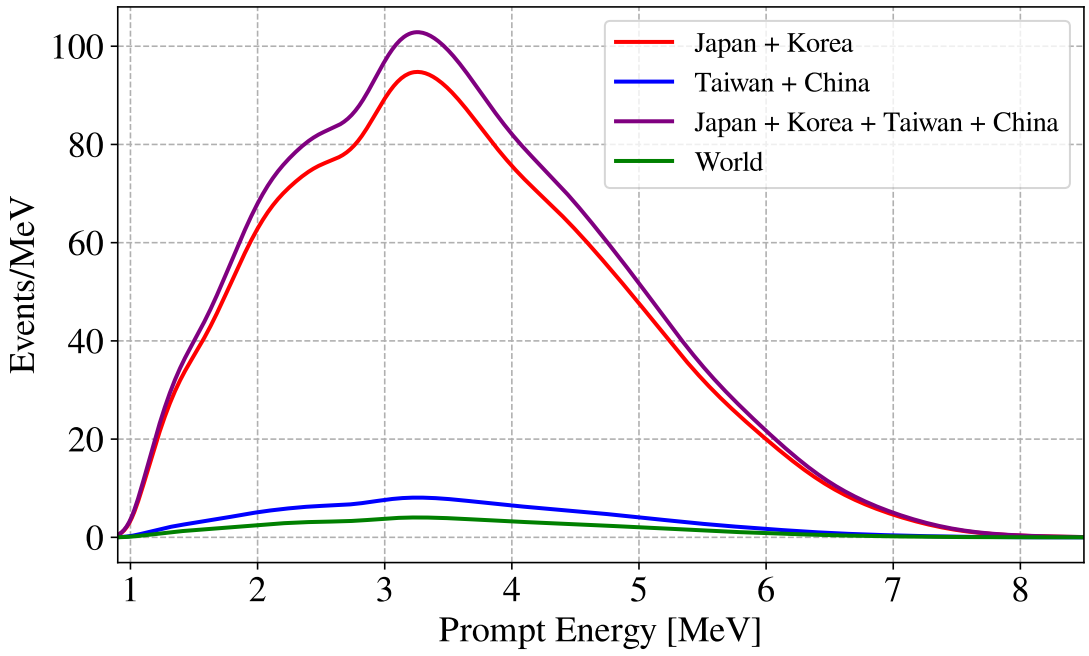

Figure 6.9: Expected antineutrino spectrum from East Asia states and the other states in Period3

Although the $\overline{\nu}_e$ flux from the global nuclear reactors other than Japan, Korea, Taiwan and China is far smaller than the Korean contribution, all the data read from IAEA (2021) is compiled for $\overline{\nu}_e$ flux and input to the analysis described in Chap.7 and Chap.8. Using the calculation described in Sec.6.1.5, the ratio of the $\overline{\nu}_e$ flux from the global reactors to the total expected flux is 0.42%, 0.51% and 3.51% in Period1, 2 and 3, respectively. As with the Taiwanese and Chinese reactors, 10% of above is assigned as the $\overline{\nu}_e$ flux uncertainties in each period.

6.1.4 MOX Fuel Effect

Mixed-OXide fuel (MOX fuel) is nuclear fuel that contains more than one oxide of fissile materials. In this study, unless otherwise specified, MOX fuel refers to nuclear

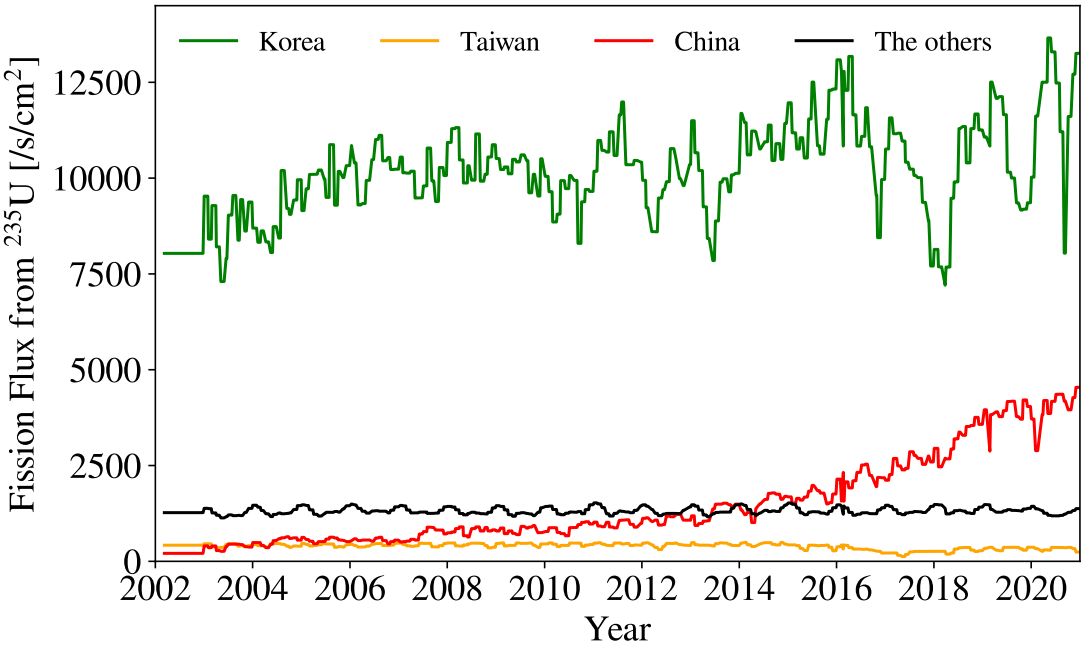

Figure 6.10: Time variation of ^{235}U fission flux from Korean, Taiwanese and Chinese reactors compiled from OPEX.

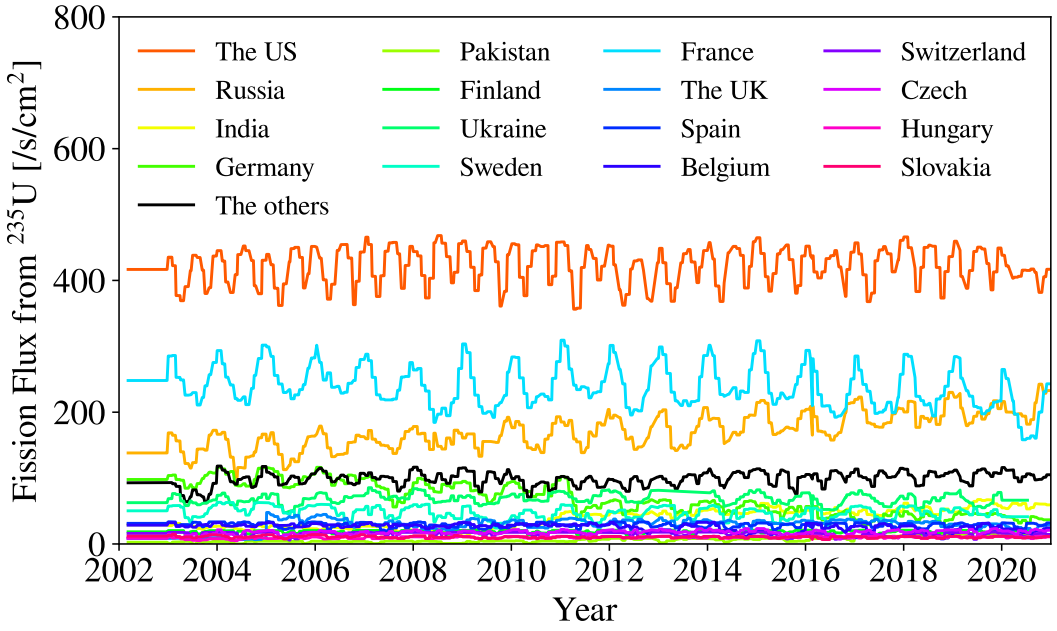

Figure 6.11: Time variation of ^{235}U fission flux from reactors in the other states compiled from OPEX.

fuel which contain 4–9% of $^{239(241)}$Pu in place of ^{235}U contained in normal fuel as uranium dioxide (UO_2). MOX fuel is manufactured from plutonium recovered from used nuclear fuel mixed with depleted or recycled uranium.

Due to different initial quantity of plutonium, ^{239}Pu and ^{241}Pu account for a larger portion of the total power generation in MOX fuel operation than in normal UO_2 fuel operation. As is shown in Table 6.4, a fission of plutonium generates more thermal power than uranium. In other words, MOX fuel needs fewer fissions than UO_2 fuel. In addition, plutonium fission emits fewer neutrinos than uranium fission as shown in Figure 6.20. Therefore, the use of MOX fuel decrease the reactor $\overline{\nu}_e$ flux. This effect is called "MOX fuel effect" and estimated based on MOX operation information reported from reactor operators and fission fractions of the major heat producing isotopes in MOX fuel calculated by TEPCO.

Japanese commercial reactors which have used MOX fuel are listed in Table 6.6. MOX operation in Japanese commercial reactor started in 2009. So, this estimation is effective especially in the low-reactor period.

Table 6.6: Japanese commercial reactors with MOX fuel. Note that some of these reactor are not in operation or under decommission process without announcement of MOX fuel removal.

reactor name	installation date	removal date	total assemblies	MOX assemblies	MOX ratio [%]
Genkai-3	2009 Oct. 08	present	16	193	8.29
Ikata-3	2010 Feb. 09	present	16	157	10.2
Fukushima1-3	2010 Aug. 21	-	32	548	5.84
Takahama-3	2010 Dec. 05	2016-01-28	8	157	5.10
Takahama-3	2016 Jan. 29	2018-11-06	24	157	15.3
Takahama-3	2018 Nov. 07	present	28	157	17.8
Takahama-4	2017 May 17	2018-08-30	4	157	2.5
Takahama-4	2018 Aug. 31	2020-01-29	16	157	10.2
Takahama-4	2020 Jan. 30	present	20	157	12.7

Figure 6.12–6.15 show fission fractions of ^{235}U, ^{238}U, ^{239}Pu and ^{241}Pu, respectively, as functions of burnup calculated by a simple simulation and verified by a detailed simulation by TEPCO. As discussed in Sec.6.1.1, the uncertainty of chemical composition prediction is small enough, and the MOX fuel effect is also very small as descussed later, the uncertainty of these simulation is negligible in this study. The provided data is ploted as dots, where different colors refer to different ratio of MOX assemblies in the total fuel assemblies. The data is interpolated for burnup and MOX ratio to get fission fraction for accutual MOX ratio in the Japanese reactors.

Using burnup at each time discussed in Sec.6.1.1 and fission fraction of each isotope in UO_2 fuel and MOX fuel discussed above, The fission rate of each isotope is corrected for MOX fuel as

$$R_X^{\mathrm{MOX}} = \frac{F_X^{\mathrm{MOX}}}{\sum_i F_i^{\mathrm{UO_2}}} \sum_i R_i^{\mathrm{UO_2}} \tag{6.1}$$

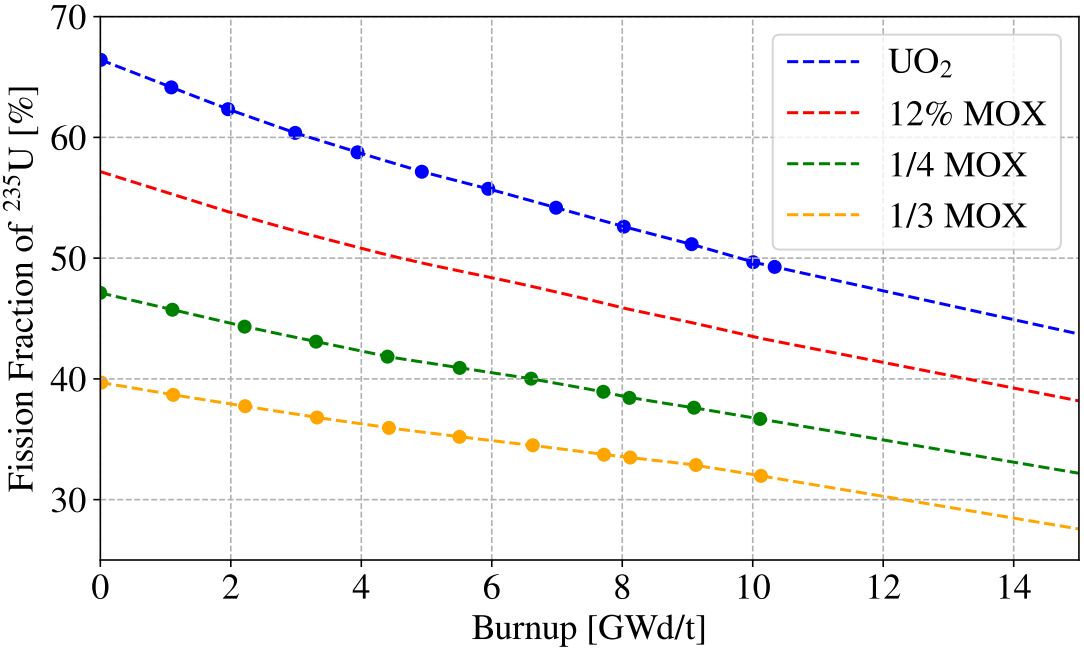

Figure 6.12: Fission fraction of ^{235}U as a function of fuel burnup in various MOX ratio.

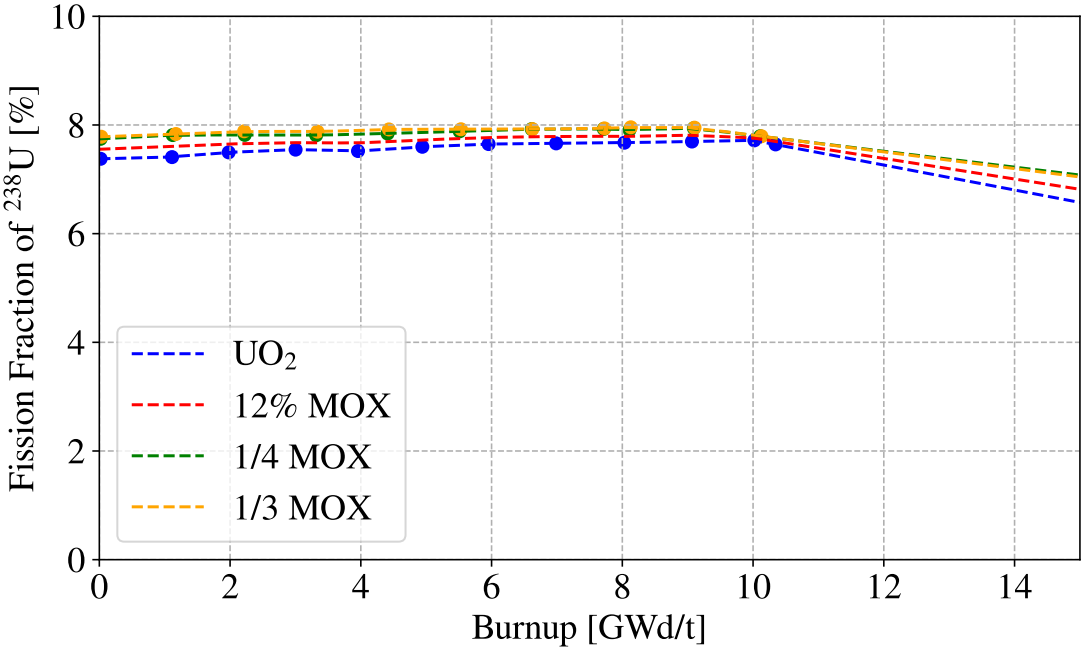

Figure 6.13: Fission fraction of ^{238}U as a function of fuel burnup in various MOX ratio.

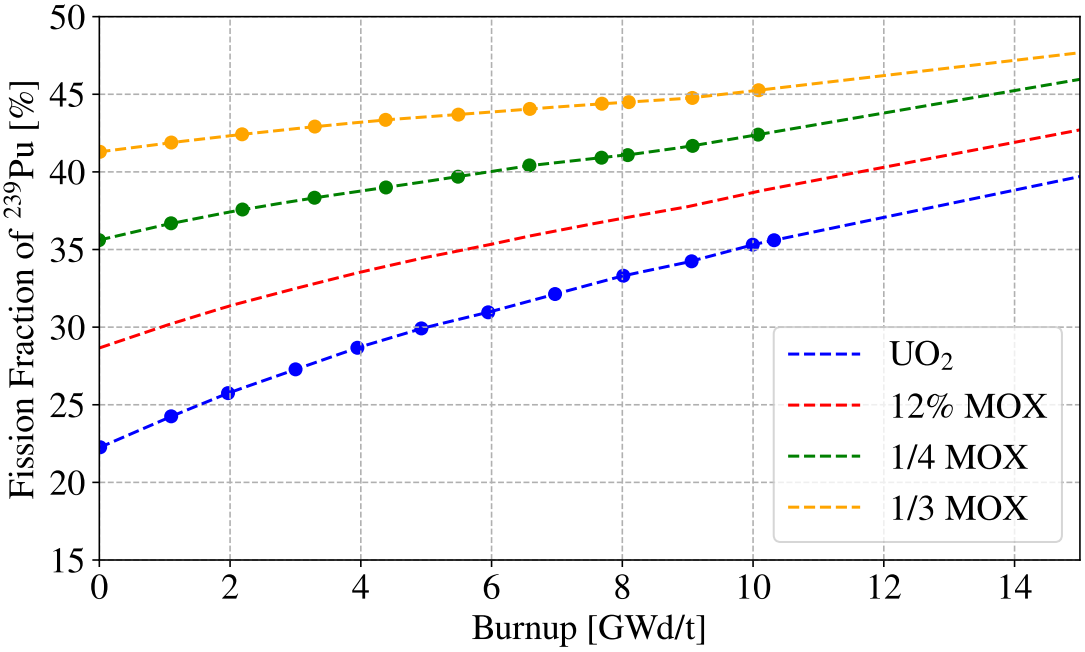

Figure 6.14: Fission fraction of ^{239}Pu as a function of fuel burnup in various MOX ratio.

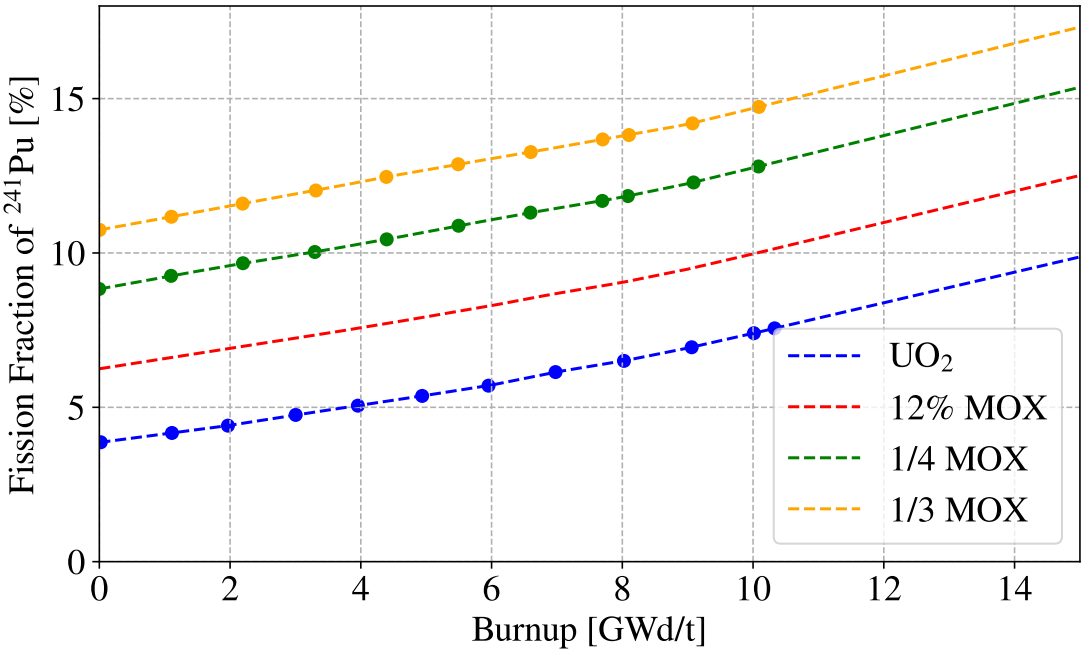

Figure 6.15: Fission fraction of ^{241}Pu as a function of fuel burnup in various MOX ratio.

where $X = (^{235}\mathrm{U}, ^{238}\mathrm{U}, ^{239}\mathrm{Pu}, ^{241}\mathrm{Pu})$, $R_X^{\mathrm{UO_2(MOX)}}$ is the fission rate of isotope X and $F_X^{\mathrm{UO_2(MOX)}}$ is the fission fraction of isotope X in $\mathrm{UO_2}$(MOX) fuel.

Figure 6.16 and Figure 6.17 show comparisons of the total $\overline{\nu}_\mathrm{e}$ spectrum emitted from a reactor with various MOX ratio at burnup = 0 GWd/t and burnup = 10 GWd/t, respectively. The differences is relatively more pronounced in a higer energy region, e.g. about 10% negative shift is expected around 7 MeV from 25% MOX fuel at burnup = 0 GWd/t. As the burnup progresses, the difference become smaller. However, it does not follows that the observed reactor neutrino flux at KamLAND decrease by $\mathcal{O}(1)$% by MOX fuel effect, since not all reactors uses MOX fuel.

Figure 6.18 and Figure 6.19 show comparisons of expected $\overline{\nu}_\mathrm{e}$ spectrum at KamLAND without and with the MOX fuel effect. The calculation method will be described later in Sec.6.1.5. There were no MOX fuel installed in Period1. Taking integral of the spectrum, MOX fuel effect is less than 0.001% in Period2 and 0.306% in Period3. Conservatively 100% error is assigned to these effects, that is, 0.001% and 0.306% is assigned as the systematic uncertainties for $\overline{\nu}_\mathrm{e}$ flux in Period2 and Period3, respectively.

6.1.5 Neutrino from Short-Lived Isotope

The four main fissile isotopes (^{235}U, ^{238}U, ^{239}Pu, ^{241}Pu) contribute to 99.9% of reactor antineutrino emission.

- ^{235}U

  ^{235}U in the core absorbs a thermal neutron and fissions. Electron antineutrinos are emitted from beta decays of unstable fission fragments.

$$^{235}\mathrm{U} + \mathrm{n} \rightarrow \mathrm{A} + \mathrm{B} + 6.1\beta^- + 6.1\overline{\nu}_\mathrm{e} + 202\ [\mathrm{MeV}] + 2.4n \tag{6.2}$$

- ^{238}U

  ^{238}U in the core absorbs a fast neutron and fissions.

$$^{238}\mathrm{U} + \mathrm{n} \rightarrow \mathrm{C} + \mathrm{D} + 5 \sim 7\beta^- + 5 \sim 7\overline{\nu}_\mathrm{e} + 205\ [\mathrm{MeV}] + x\ n \tag{6.3}$$

  ^{238}U also captures a thermal neutron and undergoes two beta decay to generate ^{239}Pu.

$$^{238}\mathrm{U} + \mathrm{n} \rightarrow {}^{239}\mathrm{U} \xrightarrow[\mathrm{T_{1/2}=23.5\ min}]{\beta^-} {}^{239}\mathrm{Np} \xrightarrow[\mathrm{T_{1/2}=2.356\ day}]{\beta^-} {}^{239}\mathrm{Pu} \tag{6.4}$$

- ^{239}Pu

  ^{239}Pu absorbs a thermal neutron and fissions.

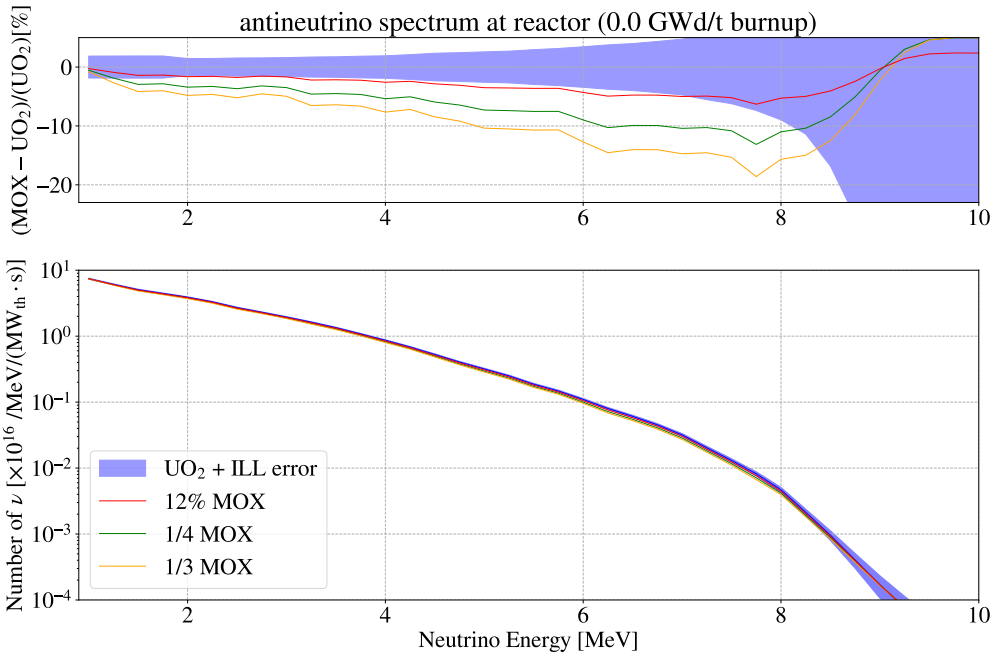

Figure 6.16: Emitted antienutrino spectrum from reactor with various MOX ratio at 0.0 GWd/t burnup

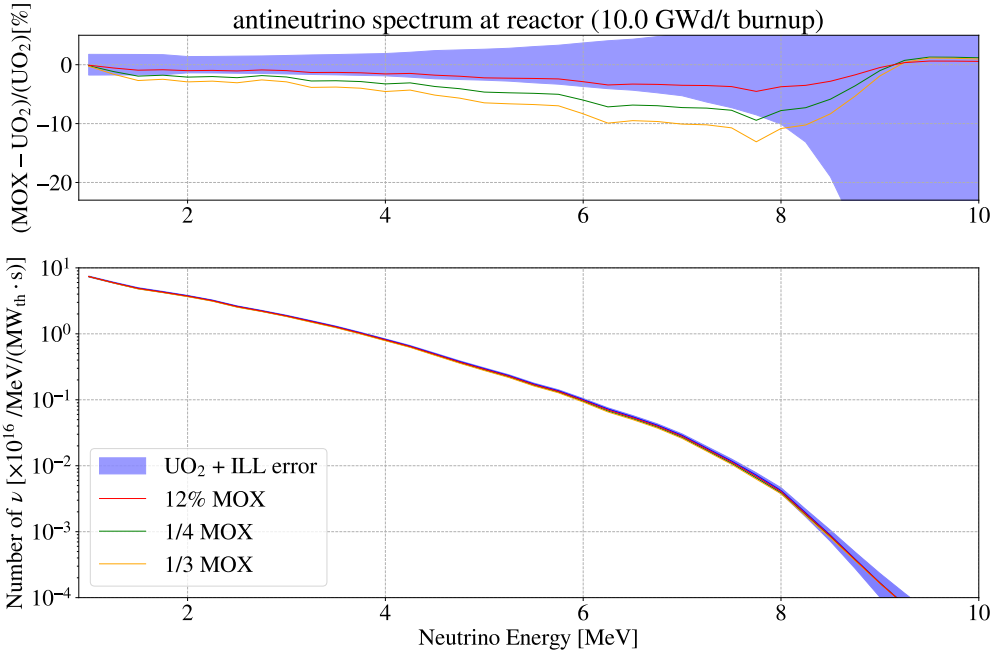

Figure 6.17: Emitted antienutrino spectrum from reactor with various MOX ratio at 10.0 GWd/t burnup

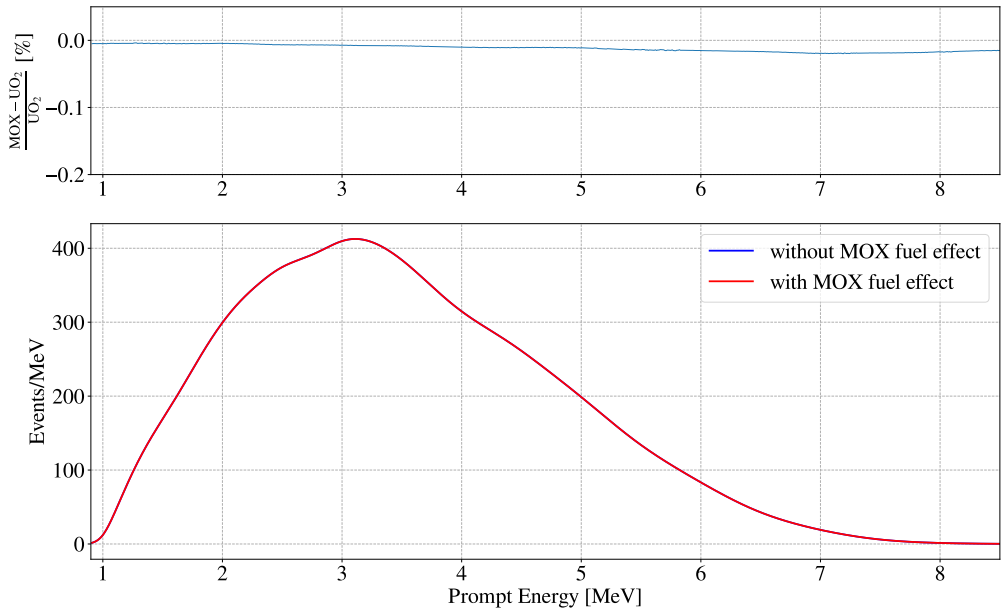

Figure 6.18: MOX fuel effect on reactor $\overline{\nu}_e$ spectrum at KamLAND in Period2

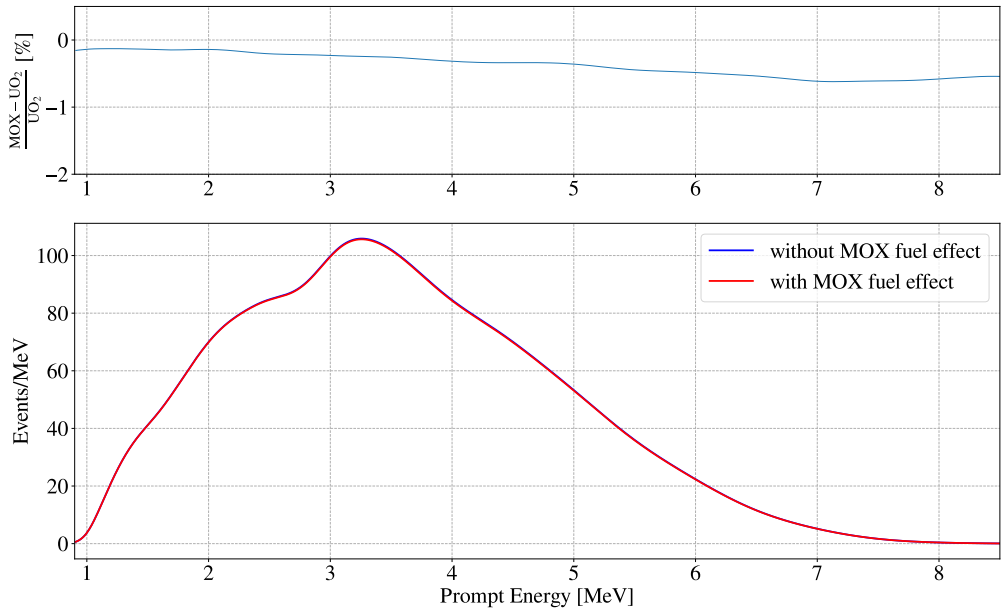

Figure 6.19: MOX fuel effect on reactor $\overline{\nu}_e$ spectrum at KamLAND in Period3

$$^{239}\mathrm{Pu} + \mathrm{n} \rightarrow \mathrm{E} + \mathrm{F} + 5.6\beta^- + 5.6\overline{\nu}_\mathrm{e} + 210\ [\mathrm{MeV}] + 2.9\ n \tag{6.5}$$

^{239}Pu also captures two thermal neutron to generate ^{241}Pu.

$$\begin{aligned} ^{239}\mathrm{Pu} + \mathrm{n} &\rightarrow {}^{240}\mathrm{Pu} \\ ^{240}\mathrm{Pu} + \mathrm{n} &\rightarrow {}^{241}\mathrm{Pu} \end{aligned} \tag{6.6}$$

The neutron capture cross section of ^{240}Pu is 289.5 barn, whereas the thermal neutron fission cross section is 0.064 barn. Therefore, the fission of ^{240}Pu is almost negligible compared to that of ^{239}Pu and ^{241}Pu.

- ^{241}Pu

^{241}Pu absorbs a thermal neutron and fissions.

$$^{241}\mathrm{Pu} + \mathrm{n} \rightarrow \mathrm{G} + \mathrm{H} + 6.4\beta^- + 6.4\overline{\nu}_\mathrm{e} + 212\ [\mathrm{MeV}] + 2.9\ n \tag{6.7}$$

Neutrino spectra from these isotopes per fission is a key input of calculating the neutrino spectrum at KamLAND site.

Antineutrino spectrum from ^{235}U fission was studied by measuring β spectrum of ^{235}U fission products. Schreckenbach et al. (1985) exposed 93% enriched ^{235}U dioxide to thermal neutrons from the Institut Laue-Langevin (ILL) reactor for total 15 hours and measured the β spectrum of the fission products with a magnetic beta spectrometer. Antineutrino spectrum was then obrained by fitting the measured β spectrum with 30 hypothetical β branches.

The same method can not be applied for ^{238}U because ^{238}U fission occours by only fast neutron capture. Vogel (1981) studied antineutrino spectrum from ^{238}U fission by a theoretical calculation considering a process of fission, subsequent β decay and possible neutron capture by fissile fragments based on the data set in the ENDF/B-V Fission Product Library of the Evaluated Nuclear Data File, Version V.

Antineutrino spectrum from ^{239}Pu and ^{241}Pu were studied by Hahn et al. (1989) in a similar method as ^{235}U. For ^{239}Pu, the dioxide was evaporated on a thin Ni foil and exposed to thermal neutrons from the ILL reactor. The β spectrum was fitted with 25 hypothetical β branches. For ^{241}Pu, 83% enriched ^{241}Pu dioxide was exposed to thermal neutrons and fitted with 30 branches.

Huber (2011) and Mueller et al. (2011) improved these studies by re-evaluating the ILL data with 845 nuclei and 10000 β branches, introducing a new ab-initio conversion method from β to ν and including full error propagation and correlation. They found about 3% upward shift with respect to the previous studies. Figure 6.20 shows the Huber-Mueller prediction of neutrino spectrum from ^{235}U, ^{239}Pu and ^{241}Pu with the Vogel (1981) prediction of ^{238}U spectrum.

Ideally, total reactor antineutrino spectrum can be calculated by summing up spectrum from each isotope with accutual fission ratio in the reactor. However, recent

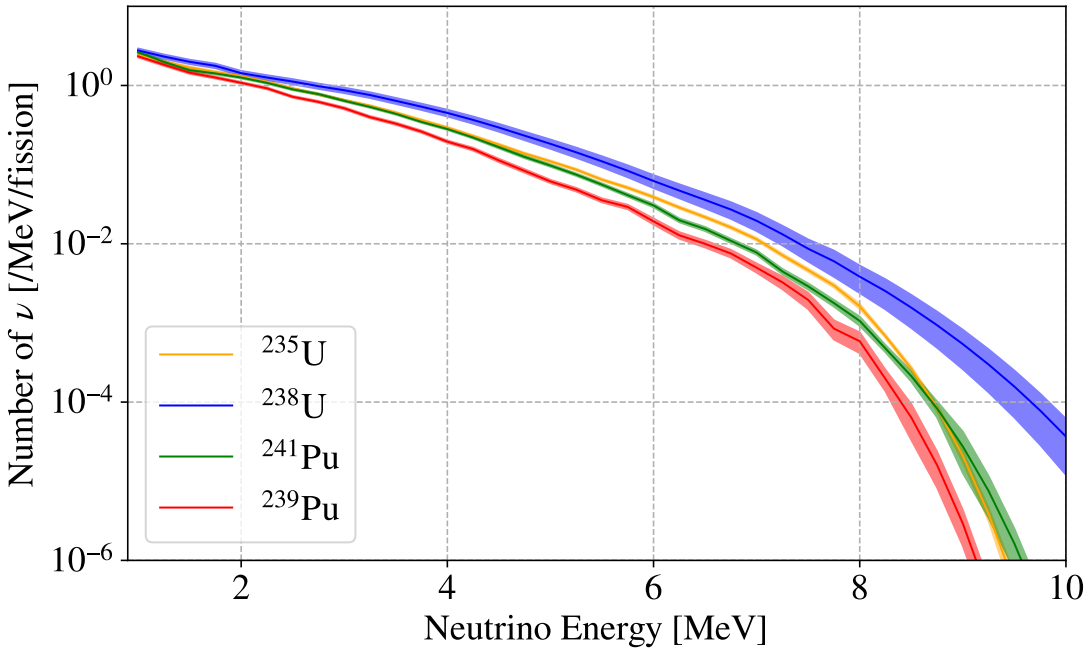

Figure 6.20: $\overline{\nu}_e$ spectrum per fission of major heat producing isotope in reactor(Huber 2011, Mueller et al. 2011, Vogel 1981).

short-baseline reactor neutrino experiment(An et al. 2017) found an exess of reactor neutrino spectrum in a energy region of 4–6 MeV by about 10% from the Huber-Mueller prediction as shown in Figure 6.21. They extracted reactor neutrino spectrum from each fissil isotope taking advantage of huge statistics and time variation of the spectrum shape by burnup. This model-observed distortion is called "reactor neutrino anomaly" and indicating a need of revising the reactor neutrino modeling (Adey et al. 2019).

To minimize the systematic uncertainties from the reactor neutrino anomaly, the total reactor neutrino spectrum from each reactor is calculated by correcting the DayaBay spectrum for the accutual fission ratio in each reactor as

$$S(E_\nu) = S_{\mathrm{DB}}(E_\nu) + \sum_{x\in\mathrm{isotope}} (f_i^x - f_{\mathrm{DB}}^x) S_{\mathrm{HM}}^x(E_\nu)\sigma_{\mathrm{IBD}}(E_\nu) \tag{6.8}$$

where $S_{\mathrm{DB}}(E_\nu)$ is the reactor antineutrino spectrum per fission measured by the DayaBay experiment (Figure 6.21(a)), f_{DB}^x is an average fission ratio of isotope x in the reactors near DayaBay, f_i^x is a fission ratio of isotope x in reactor i, $S_{\mathrm{HM}}^x(E_\nu)$ is the fission spectrum model of each isotope (Huber 2011, Mueller et al. 2011, Vogel 1981) and $\sigma_{\mathrm{IBD}}(E_\nu)$ is the IBD cross section(Strumia and Vissani 2003).

The second term of Eq. (6.8) is typically small and the dominant uncertainty of $S(E_\nu)$ comes from the uncertainty of $S_{\mathrm{DB}}(E_\nu)$. Therefore, the statistical uncertainty of $S_{\mathrm{DB}}(E_\nu)$, 2.03%, is assigned as the systematic uncertainty for the reactor neutrino flux related to the antineutrino spectra.

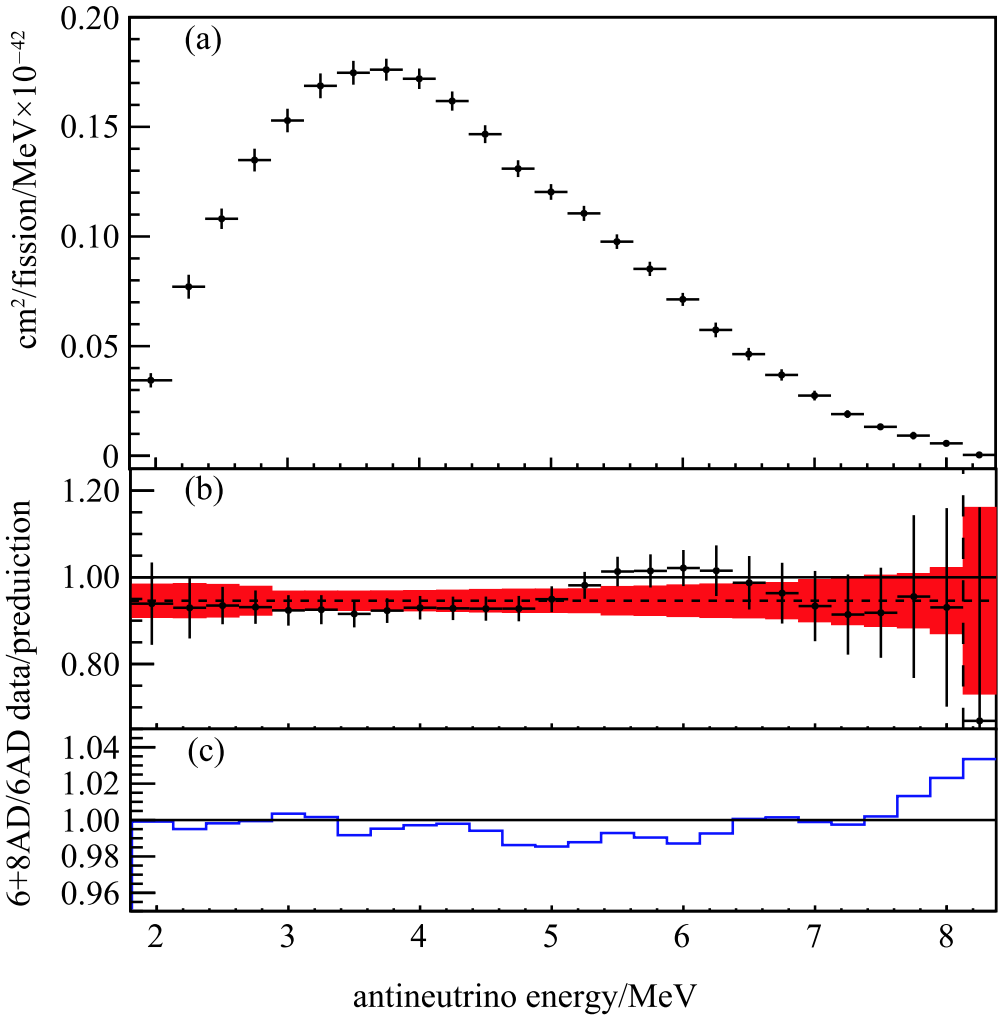

Figure 6.21: Antineutrino spectrum observed by the DayaBay experiment(An et al. 2017). (a)Antineutrino spectrum weighted with the IBD cross section (b)Ratio of the extracted reactor antineutrino spectrum to the Huber-Mueller prediction

The reactor neutrino flux at the KamLAND site is then calculated geometrically as

$$\frac{\mathrm{d}\Phi}{\mathrm{d}E_\nu} = \sum_{i\in\text{reactor}} P_{\text{ee}}(E_\nu, L_i)\frac{1}{4\pi L_i^2}\cdot\frac{W_i}{\sum_{x\in\text{isotope}} f_i^x e_x}S(E_\nu) \tag{6.9}$$

where L_i is the distance from reactor i to the KamLAND site, W_i is the thermal power of reactor i, e_x is the energy released per fission of isotope x (listed in Table 6.4) and $P_{\text{ee}}(E_\nu, L_i)$ is the neutrino survival probability.

The observed spectrum at KamLAND is finally calculated by integrating for time and multiplying the number of target, N_{proton} (Sec.5.6.1), and selection efficiency, $\varepsilon(E_\nu)$ (Sec.5.5.4), as

$$\frac{\mathrm{d}N}{\mathrm{d}E_\nu} = N_{\text{proton}}\cdot\varepsilon(E_\nu)\int\frac{\mathrm{d}\Phi}{\mathrm{d}E_\nu}\mathrm{d}t \tag{6.10}$$

6.1.6 Neutrino from Long-Lived Isotope

Fission products whose lifetime is shorter than a few hours are included in the short-lived isotope spectrum discussed in Sec.6.1.5. On the other hand, fission products whose lifetime is longer than ∼10 hours and maximum antineutrino energy is greater than 1.8 MeV, called "long-lived isotope", is not included and need to be calculated from the past reactor operation data and the location of spent fuels. Kopeikin et al. (2001) listed six long-lived isotopes as summarized in Table 6.7.

Table 6.7: Long-lived fission products (Kopeikin et al. 2001)

fission fragment	half file	E_{max} [MeV]	yield [%]			
			^{235}U	^{238}U	^{239}Pu	^{241}Pu
^{97}Zr	16.91 hour	1.922	5.95	5.50	5.30	4.89
^{132}I	2.295 hour	2.104	4.30	5.16	5.40	4.14
^{93}Y	10.18 hour	2.890	6.40	4.97	3.89	3.51
^{106}Ru	373 day	3.541 (^{106}Rh)	0.40	2.55	4.31	6.18
^{144}Ce	285 day	2.994 (^{144}Pr)	5.48	4.50	3.74	4.39
^{90}Sr	28.8 year	2.279 (^{90}Y)	5.82	2.10	1.57	3.12

Of these six isotopes, ^{97}Zr, ^{132}I and ^{93}Y achieve equilibrium within ten days. So, the antineutrino from from these three isotopes do not affect seriously on the KamLAND experiment. The rest three isotopes have longer half lives than 100 days and the daughter nuclei have larger β decay Q-value than 1.8 MeV. Eq. (6.11) shows details of β decay process of these isotopes. Besides, Figure 6.22 shows the antineutrino spectrum from these isotopes.

$$
\begin{aligned}
^{106}\mathrm{Ru} &\xrightarrow[\mathrm{T}_{1/2}=373.6\ \mathrm{day}]{\mathrm{Q}_\beta=0.0394\ \mathrm{MeV}} {}^{106}\mathrm{Rh} \xrightarrow[\mathrm{T}_{1/2}=29.8\ \mathrm{sec}]{\mathrm{Q}_\beta=3.541\ \mathrm{MeV}} {}^{106}\mathrm{Pd} \\
^{144}\mathrm{Ce} &\xrightarrow[\mathrm{T}_{1/2}=284.9\ \mathrm{day}]{\mathrm{Q}_\beta=0.3187\ \mathrm{MeV}} {}^{144}\mathrm{Pr} \xrightarrow[\mathrm{T}_{1/2}=12.3\ \mathrm{sec}]{\mathrm{Q}_\beta=2.9975\ \mathrm{MeV}} {}^{144}\mathrm{Nd} \\
^{90}\mathrm{Sr} &\xrightarrow[\mathrm{T}_{1/2}=22.8\ \mathrm{day}]{\mathrm{Q}_\beta=0.546\ \mathrm{MeV}} {}^{90}\mathrm{Y} \xrightarrow[\mathrm{T}_{1/2}=64.1\ \mathrm{sec}]{\mathrm{Q}_\beta=2.282\ \mathrm{MeV}} {}^{90}\mathrm{Zr}
\end{aligned}
\tag{6.11}
$$

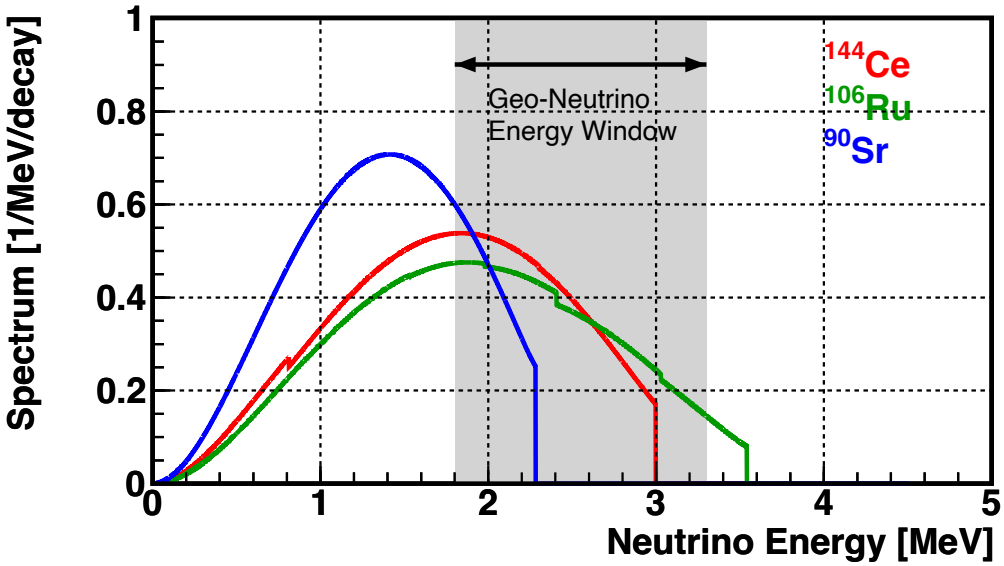

Figure 6.22: Neutrino energy spectrum from long-lived fission products(Enomoto 2005)

The yield rate and fission rate of these three isotopes are estimated from published reactor operation data with assuming typical fuel composition and thermal efficiency of BWR. In addition, the contribution from spent fuel is also estimated assuming they are stored just near the reactor. This assumption is reasonable because in general the spent fuel is stored for about ten years in a pool of a reactor facility and then transferred for permanent strage or fuel recycling, whereas the half life of ^{90}Sr is much longer but it contributes only 2.4% of the all long-lived isotope event for KamLAND.

The ratio of antineutrino flux from long-lived isotopes to the total flux estimate is calculated to be 2.184%, 2.258% and 4.078%, respectively, and their relative uncertainty 50% is conservatively assumed. Thus, 1.092%, 1.129% and 2.044% are assigned as the systematic uncertainty of antineutrino flux in each period.

6.1.7 Reactor-related Systematic Uncertainties

Table 6.8 summarizes the systematic uncertainty related to the reactor $\overline{\nu}_\mathrm{e}$ spectrum and flux estimation. Uncertainties of distance, Japanese reactor's thermal power,

chamical composition and time lag were discussed in Sec.6.1.1. Uncertainties of Korean, Taiwanese, Chinese and the other country's reactor thermal power were discussed in Sec.6.1.2–6.1.3. Uncertainties of MOX fuel effect, antineutrino spectra and long-lived nuclei were discussed in Sec.6.1.4, Sec.6.1.5 and Sec.6.1.6, respectively.

Table 6.8: Summary of reactor-related systematic uncertainties

	Period1	Period2	Period3
energy range [MeV]	0.9–8.5	0.9–8.5	0.9–8.5
Distance	0.1%	0.1%	0.1%
– Termal power –			
Japan	2.0%	2.0%	2.0%
Korea	0.365%	0.474%	3.338%
Taiwan/China	0.071%	0.101%	1.045%
The others	0.042%	0.051%	0.351%
Chemical composition	1.0%	1.0%	1.0%
MOX fuel effect	0.0000%	0.001%	0.306%
long-lived nuclei	1.092%	1.129%	2.044%
antineutrino spectra	2.03%	2.03%	2.03%
time lag	0.01%	0.01%	0.01%
Total	3.235%	3.262%	5.075%

6.2 $^{13}C(\alpha, n)^{16}O$ Reaction

$^{13}C(\alpha, n)^{16}O$ interaction is the second largest background for geoneutrino observation. This section describes the overview of this reaction and its expectation.

6.2.1 Overview of (α, n) Reaction

(α, n) interaction is triggered by α particle as Eq. (6.12) and mimic an antineutrino event.

$$(Z, A) + \alpha \rightarrow (Z + 2, A + 3) + n \tag{6.12}$$

The neutron from this reaction is often a fast neutron and deposites energy in thermalization process. Otherwise, the generated nuclei goes to an excited state and emit γ-ray in de-excitation. The neutron is finally captured and emit 2.2 MeV γ-ray, which mimic a delayed-coincidence candidate.

Since this reaction has almost the same event profile as the IBD reaction, the rate and energy spectrum need to be estimated in advance from the number of α decay, (α, n) reaction cross section, α quenching in the liquid scintillator and the energy and anglar distribution of the neutron.

6.2.2 α Source in the KamLAND Liquid Scintillator

There are various α particle sources in the KamLAND liquid scintillator. However, according to Ichimura (2008), α decays of ^{210}Po account for more than 99% of all α activities in the KamLAND liquid scintillator as shown in Figure 6.23.

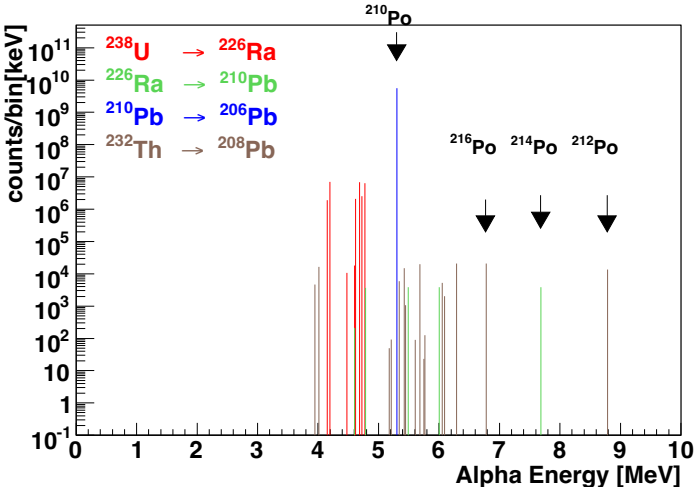

Figure 6.23: α activities in the KamLAND liquid scintillator classified into four groups(Ichimura 2008)

6.2.3 Reaction Cross Section

(α, n) reaction occours on various nuclei. Table 6.9 summarizes the target nuclei of (α, n) rection in the KamLAND liquid scintillator. In KamLAND, 5.304 MeV α particle from ^{210}Po decay is the dominant α activity. So, the contribution from nuclei whose (α, n) reaction threshold is greater than 5.304 MeV or small natural abundance is negligible.

Table 6.9: Target nuclei of (α, n) reaction(Ichimura 2008). The original data of Q value and reaction threshold are calculated in On-Line Q-Value Calculation.

target nuclei	Q value [MeV]	threshold [MeV]	natural abundance [%]
^{1}H	-23.68	115.4	99.985
^{2}H	-4.190	12.50	0.015
^{3}H	-4.783	11.12	-
^{12}C	-8.502	11.34	98.90
^{13}C	2.216	0	1.10
^{14}C	-1.818	2.337	-
^{14}N	-4.735	6.088	99.634
^{15}N	-6.419	8.131	0.366
^{16}N	1.526	0	-
^{16}N	-12.13	15.17	99.762
^{17}N	5.867	0	0.038
^{18}N	-0.6962	0.8510	0.200
^{19}N	5.713	0	-

Figure 6.24 shows the total cross section of (α, n) reaction as a function of incident α energy for various nuclei normalized to natural carbon considering the chemical composition of the KamLAND liquid scintillator and their natural isotopic abundance. From this figure, the dominant α target in KamLAND is ^{13}C. Hereafter in this study, only ^{13}C$(\alpha, n)^{16}$O is considered.

6.2.4 ^{13}C$(\alpha, n)^{16}$O Reaction

^{13}C$(\alpha, n)^{16}$O produces the ground state or four excited states of ^{16}O as shown in Figure 6.25 The 0^+ state decay by pair emission of e^+-e^-, whereas the other three decays by γ emission. Figure 6.26 shows the cross section of ^{13}C$(\alpha, n)^{16}$O to different final statesas a function of incident α energy. Considering 5.304 MeV α from ^{210}Po, the ground state, the first excited state and the second excited state are candidates of interest in this study.

These three final states make different event property in KamLAND as follows.

- ^{13}C$(\alpha, n)^{16}$O (ground state, g.s.)
  Neutron have the energy equivalent to the Q value of the reaction. This neutron

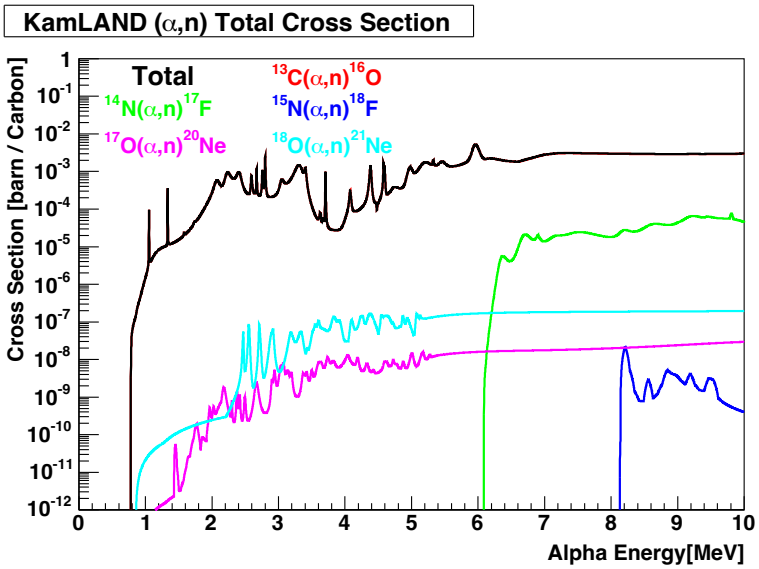

Figure 6.24: Total cross section of (α, n) reaction for various nuclei. The figure is cited from (Ichimura 2008). The original data is calculated based on JENDLE (2005).

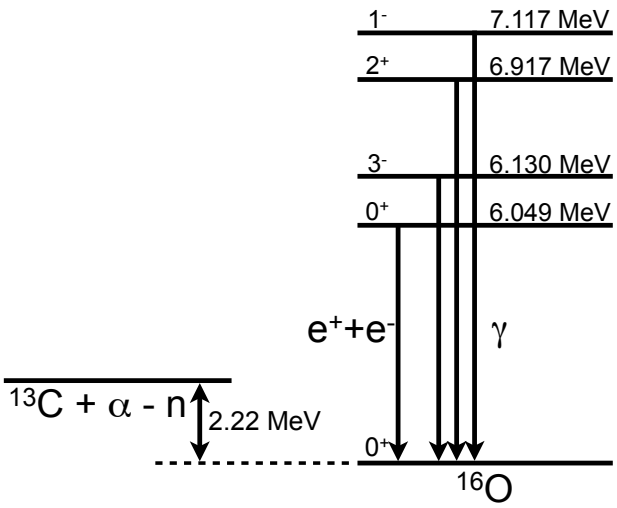

Figure 6.25: Energy levels of ^{16*}O(Watanabe 2012)

recoil protons in the liquid scintillator and make a prompt scintillation labeled as "prompt event(3)" in Figure 6.27.
The neutron sometimes exites ^{12}C, which emits de-excitation 4.438 γ-ray. The rest neutron energy is deposited via proton recoils. This process is labeled as "prompt event(2)" in Figure 6.27. Although the total deposite energy does not depend on if the neutron exite ^{12}C or not, the total amount of scintillation is different because neutron, proton and γ have different quenching in the liquid scintillator.

- ^{13}C$(\alpha, n)^{16*}$O (first excited state)
  If ^{16}O goes to the first excited state, it de-exites by emitting e^+-e^- pair, whose total energy is 6.046 MeV. The rest energy is given to neutron and deposited via proton recoil. This process is labeled as "prompt event(1)" in Figure 6.27.

- ^{13}C$(\alpha, n)^{16*}$O (second excited state)
  If ^{16}O goes to the second excited state, it de-exites by emitting a 6.129 MeV γ ray. The rest energy is given to neutron and deposited via proton recoil. This process is also labeled as "prompt event(1)" in Figure 6.27.

In any case, the neutron capture 2.2 MeV γ makes delayed scintillation.

6.2.5 Rate and Spectrum Expectation

^{210}Po α decay rate measurement

^{210}Po α decay rate is measured by fitting energy spectrum taken in special low trigger-threshold run (background run). Figure 6.28 and Figure 6.29 show the observed energy spectrum in a background run before and after the purifications, respectively.

In the low-energy region, backgrounds are dominated by the radioactive noble gasses such as ^{85}Kr (Eq. 6.13) and ^{222}Rn (^{210}Bi and ^{210}Po in decay chain, Eq. 6.14). However, the purifications effectively removed the radioactive impurities and suppressed these backgrounds. ^{85}Kr is further suppressed by the N_2 purge after the distillation(Nakajima 2009).

$$^{85}\mathrm{Kr} \xrightarrow[\mathrm{T}_{1/2}=10.76\ \mathrm{year}]{\mathrm{Q}_\beta=0.678\ \mathrm{MeV}} {}^{85}\mathrm{Rb} \tag{6.13}$$

$$\begin{aligned} {}^{210}\mathrm{Pb} &\xrightarrow[\mathrm{T}_{1/2}=22.3\ \mathrm{year}]{\mathrm{Q}_\beta=0.0635\ \mathrm{MeV}} {}^{210}\mathrm{Bi} \\ &\xrightarrow[\mathrm{T}_{1/2}=5.013\ \mathrm{day}]{\mathrm{Q}_\beta=1.162\ \mathrm{MeV}} {}^{210}\mathrm{Po} \\ &\xrightarrow[\mathrm{T}_{1/2}=138.4\ \mathrm{day}]{\mathrm{Q}_\alpha=5.304\ \mathrm{MeV}} {}^{206}\mathrm{Pb} \end{aligned} \tag{6.14}$$

Figure 6.30 shows the time variation of fitted ^{210}Bi and ^{210}Po rate.

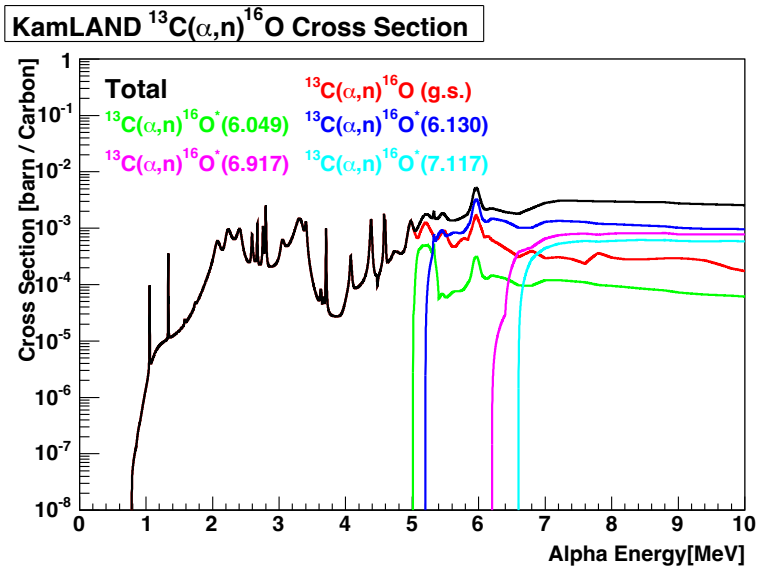

Figure 6.26: Total cross section of (α, n) reaction for carbon isotopes nuclei. The figure is cited from (Ichimura 2008). The original data is calculated based on JENDLE (2005).

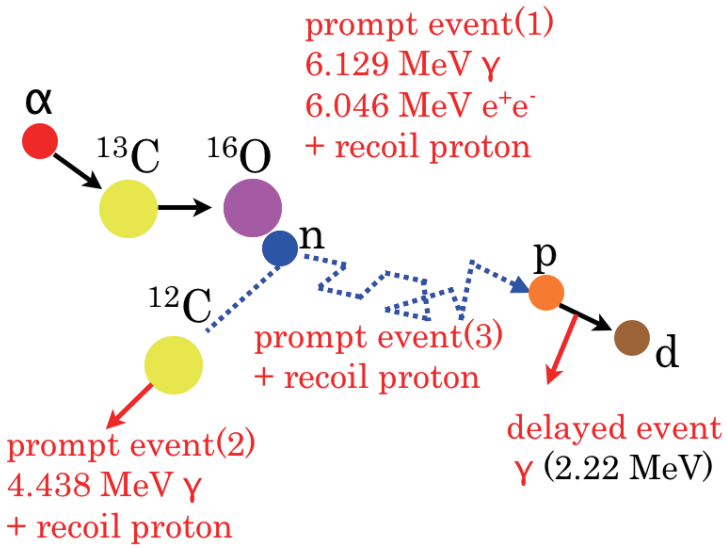

Figure 6.27: ^{13}C$(\alpha, n)^{16*}$O reaction(Ichimura 2008)

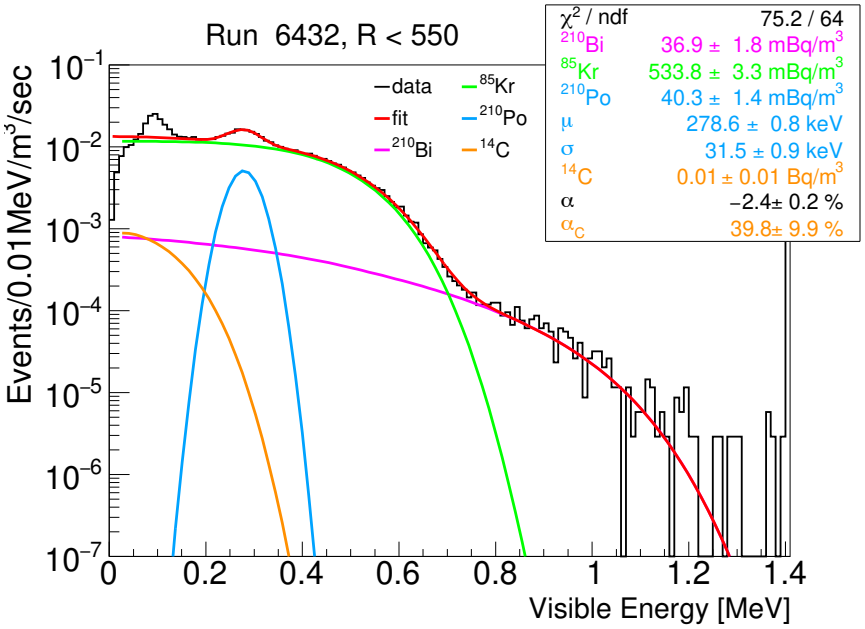

Figure 6.28: Energy spectrum fitting to estimate ^{210}Po rate before purifications

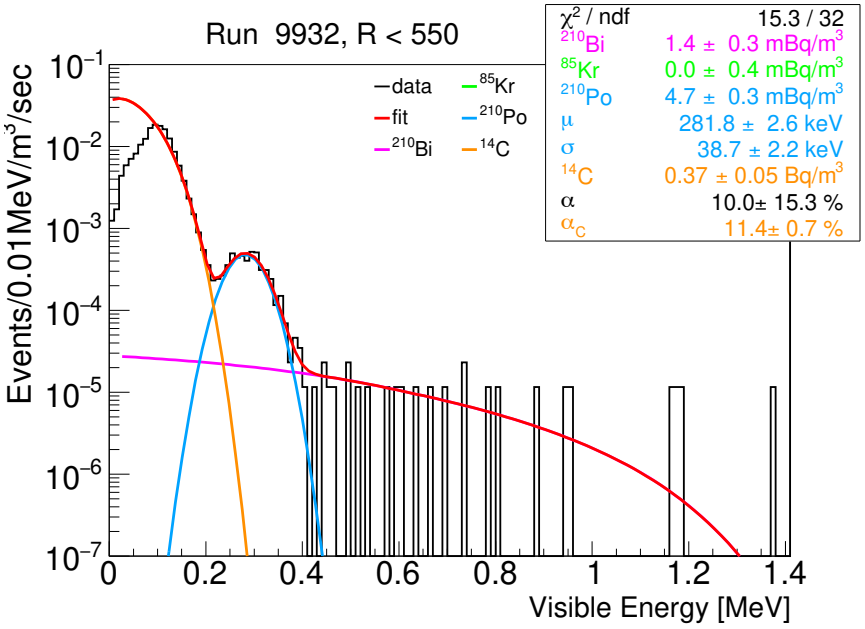

Figure 6.29: Energy spectrum fitting to estimate ^{210}Po rate after purifications

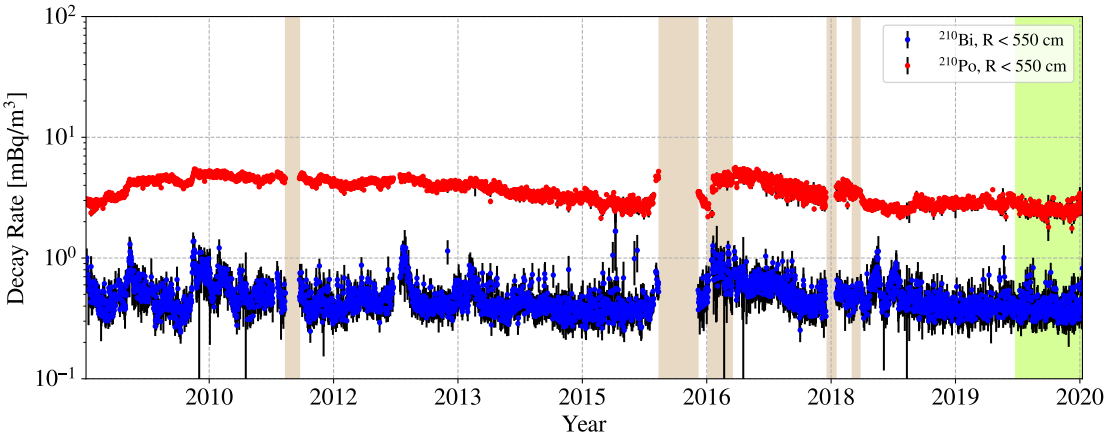

Figure 6.30: Time variation of ^{210}Bi and ^{210}Po rate. This figure includes not only background run but also physics run analyzed with prescale-triggered events. See Watanabe (2012) for the time variation before the purification.

^{13}C$(\alpha, n)^{16}$O rate estimation

α from ^{210}Po initially have 5.304 MeV energy and deposites energy to the scintillator before finally it stops. Thus, the rate of $^{13}\mathrm{C}(\alpha, n)^{16}\mathrm{O}$ reaction is calculated as follows.

$$
\begin{aligned}
N &= \int_{E_0}^{0} \mathrm{d}E_\alpha \left(-\frac{\mathrm{d}N}{\mathrm{d}E_\alpha}\right) \\
-\frac{\mathrm{d}N}{\mathrm{d}E_\alpha} &= n_{\mathrm{target}} I_{\mathrm{source}} \sigma(E_\alpha) \left(-\frac{\mathrm{d}X}{\mathrm{d}E_\alpha}\right)
\end{aligned}
\tag{6.15}
$$

where E_α is the α energy, E_0 is the initial α energy, n_{target} is the number density of ^{13}C nuclei in the KamLAND liquid scintillator, I_{source} is the α source intensity discussed above, $\sigma(E_\alpha)$ is the cross section (Sec.6.2.3) and $-\frac{\mathrm{d}X}{\mathrm{d}E_\alpha}$ is a stopping power for α calculated with GEANT4(Agostinelli et al. 2003) as shown in Figure 6.31.

Neutron Spectrum Calculation

The observed energy spectrum is calculated based on the energy deposites. While the γ energy from ^{16*}O depends on the excitation energy levels, the neutron energy depends on the incident α energy and the scattering angle as shown in Figure 6.32. The angular distribution of neutron is parameterized by Legendre-polynominals(Walton et al. 1957, Kerr et al. 1968) as a function of the energy. Then, the neutron energy spectrum in the lab frame is calculated as

$$
\begin{aligned}
n(E) &= \int_{E_0}^{0} \mathrm{d}E_\alpha \int \mathrm{d}\Omega\, \delta(\Omega, E_\alpha, E_n) n_{\mathrm{target}} I_{\mathrm{source}} \frac{\mathrm{d}\delta}{\mathrm{d}\Omega} \left(-\frac{\mathrm{d}X}{\mathrm{d}E_\alpha}\right) \\
\frac{\mathrm{d}\delta}{\mathrm{d}\Omega} &= \sum_l A_l P_l(\cos\theta)
\end{aligned}
\tag{6.16}
$$

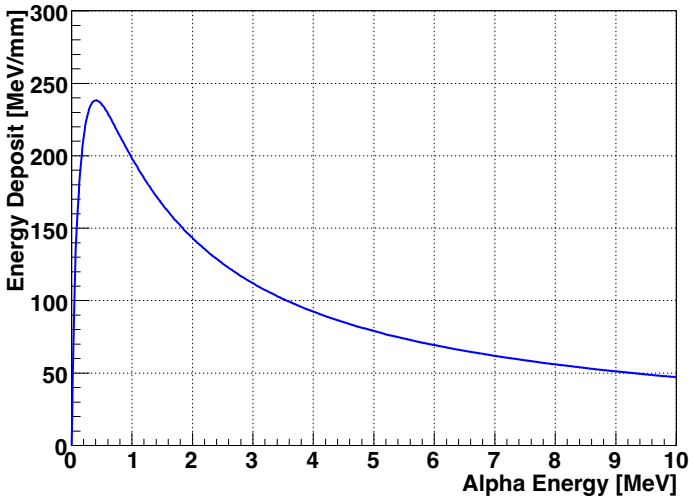

Figure 6.31: α particle energy deposition per unit length in the KamLAND liquid scintillator(Ichimura 2008)

where Ω is the scattering solid angle, E_n is the neutron energy, $\delta(\Omega, E_\alpha, E_n)$ is a delta function expressing the conservation of momentum, A_l is coefficient of Legendre-polynominal and $P_l(\cos\theta)$ is Legendre-polynominal. Figure 6.33 shows the neutron energy spectrum for each final state.

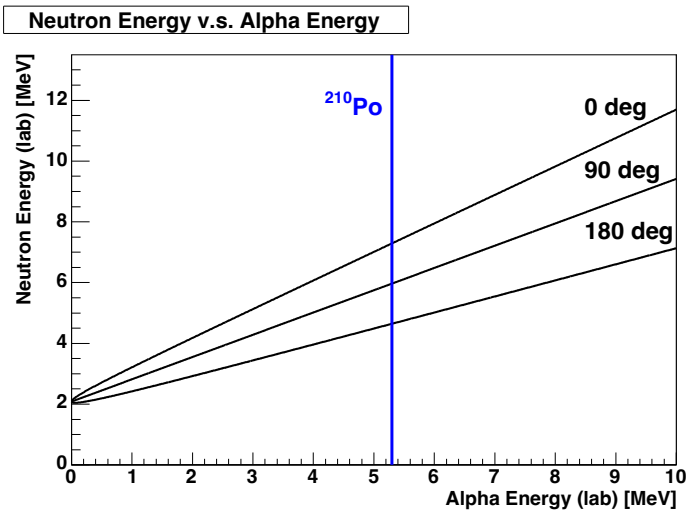

Figure 6.32: Correlation between neutron energy and incident α energy with different scattering angles(Ichimura 2008)

Proton Quench Effect

Neutron from $^{13}\mathrm{C}(\alpha, n)^{16}\mathrm{O}$ reaction recoils protons, which deposite energy to the scintillator. Therefore, a study of proton quench effect is necessary to estimate the visible energy spectrum of $^{13}\mathrm{C}(\alpha, n)^{16}\mathrm{O}$ reaction in KamLAND.

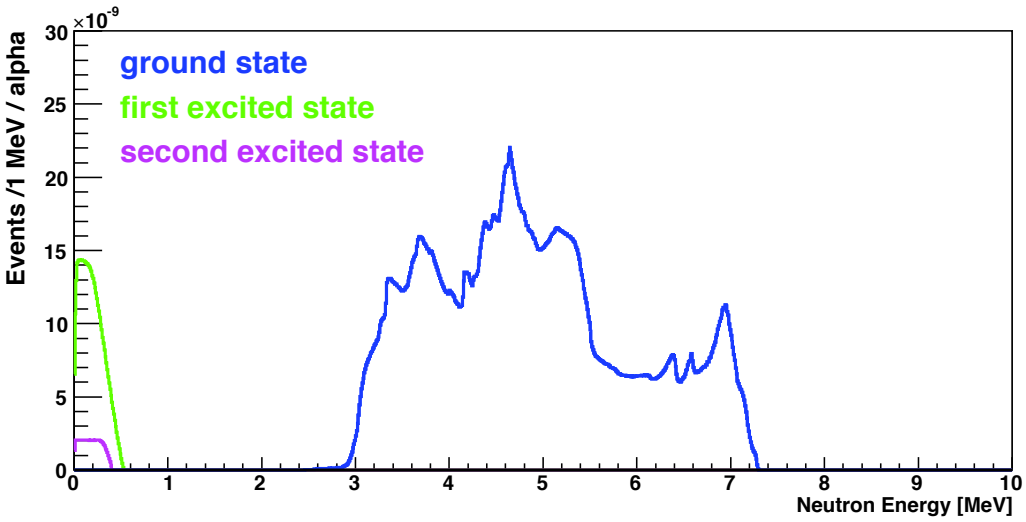

Figure 6.33: Neutron energy spectrum from $^{13}C(\alpha, n)^{16}O$ reaction(Watanabe 2012)

Yoshida et al. (2010) measured the proton quench effect in the OKTAVIAN facility, Osaka University with a deuteron bean and a tritium target to generate monochromatic neutron beam. Figure 6.34 shows the schematic view of the experimantal setup at OKTAVIAN facility. Neutron beam of monochromatic 14.4 MeV energy is hit to a liquid scintillator material target, which was sampled from the center of the kamLAND detector. The recoil proton energy is changed by changeing the scattering angle.

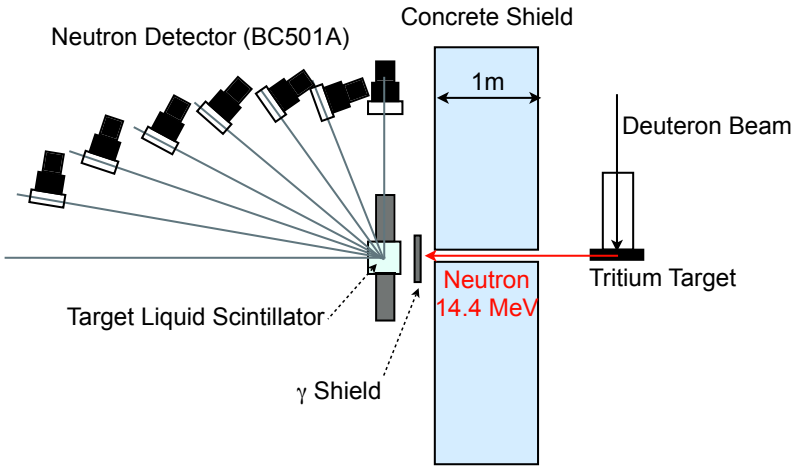

Figure 6.34: Schematic view of the experimantal setup at OKTAVIAN facility(Watanabe 2012)

Figure 6.35 shows the proton quench factor measured in OKTAVIAN facility as a function of the proton energy. The accuracy of the quench factor measuring is 2%(Yoshida et al. 2010).

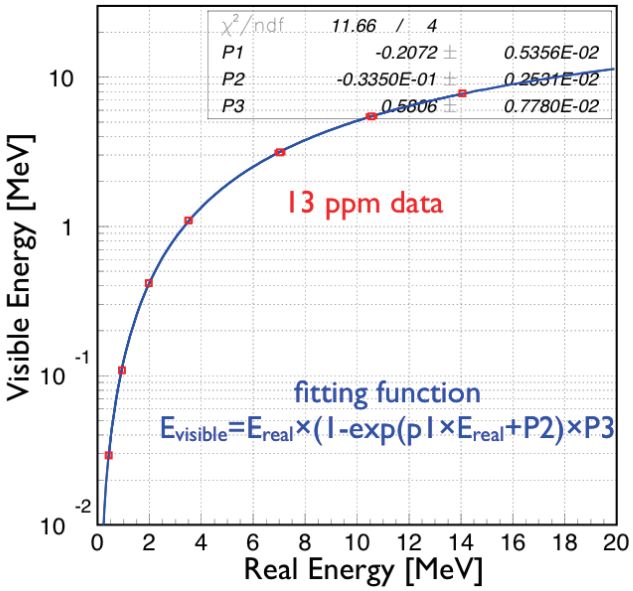

Figure 6.35: Proton quench factor as a function of recoil proton energy(Ichimura 2008)

The visible energy spectrum of the prompt scintillation of $^{13}C(\alpha, n)^{16}O$ reaction is calculated using GEANT4(Agostinelli et al. 2003) based on the neutron energy discussed in Sec.6.2.5 and the proton quench effect discussed above.

Branching Ratio

There are a large uncertainty in the branching ratio to each final state of $^{13}C(\alpha, n)^{16}O$ reaction due to the calculation model. A $^{210}Po^{13}C$ source calibration was performed to study the branching ratio.

Figure 6.36 shows the schematic view of $^{210}Po^{13}C$ source(McKee et al. 2008). The source mixture is produced by adding a polonium solution to an approximately 0.3 g of ^{13}C powder, dried completely, tamped with a Delrin spacer and sealed in an adhesive container.

Figure 6.37 shows the delayed-coincidence profile of the $^{210}Po^{13}C$ source calibration data installed at the center of the detector. The peaks of ^{12}C de-excitation, 4.438 MeV γ, and ^{16}O de-excitation from the second excited state, 6.129 MeV γ, were clearly observed. The first excited state of ^{16}O emits e^+-e^- pair but they are absorbed by the source contair. Instead, pair annihilation 1.022 MeV γ is detected.

Figure 6.38 shows the comparison between the $^{210}Po^{13}C$ source calibration data and the expected spectrum. The rate of the second excited state is consistent with the JENDLE (2005) prediction. The expected rate of the first excited state is scaled by 0.6 to reproduce the source data. The expected rate of the ground state is in good agreement with the data after scaled by 1.05.

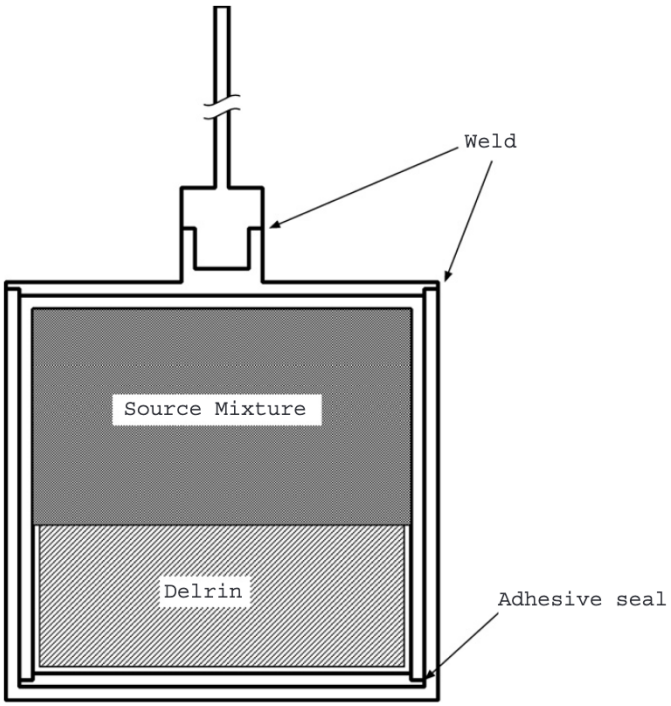

Figure 6.36: $^{210}Po^{13}C$ source geometry(McKee et al. 2008). The radioactive source material is loaded in "Source Mixture" part. The source countair is 13-mm-diameter × 13-mm-height.

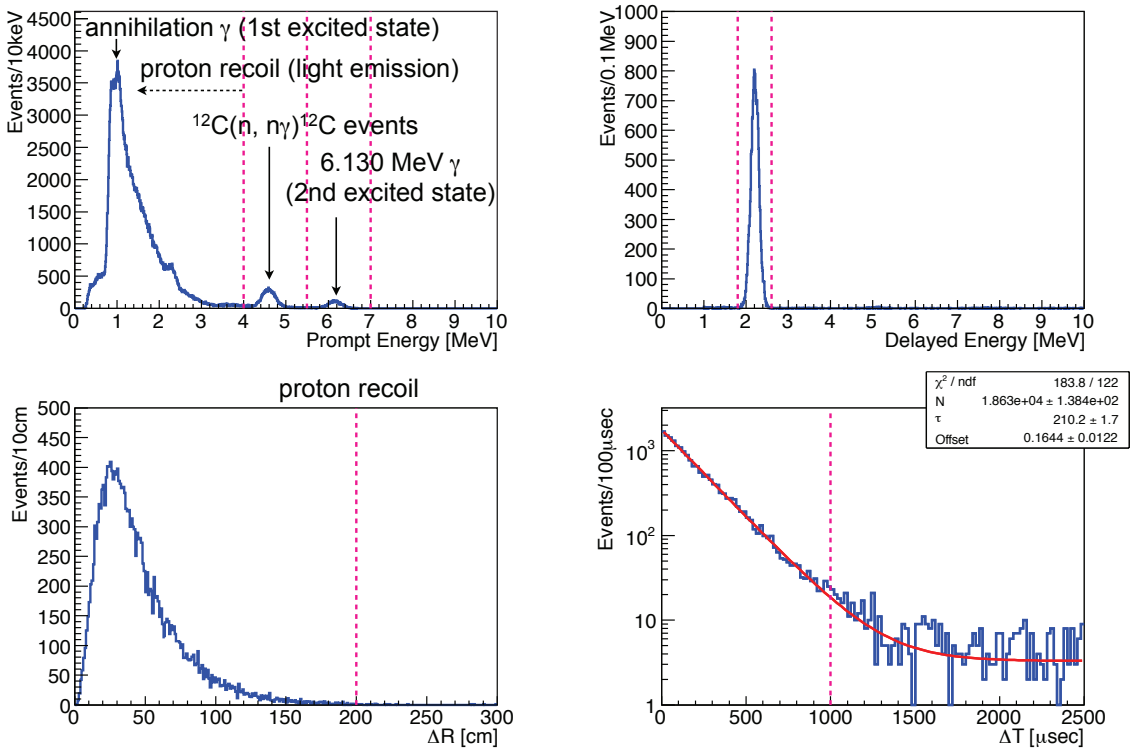

Figure 6.37: Delayed-coincidence profile of the ^{210}Po^{13}C source calibration data installed at the center of the detector(Watanabe 2012).

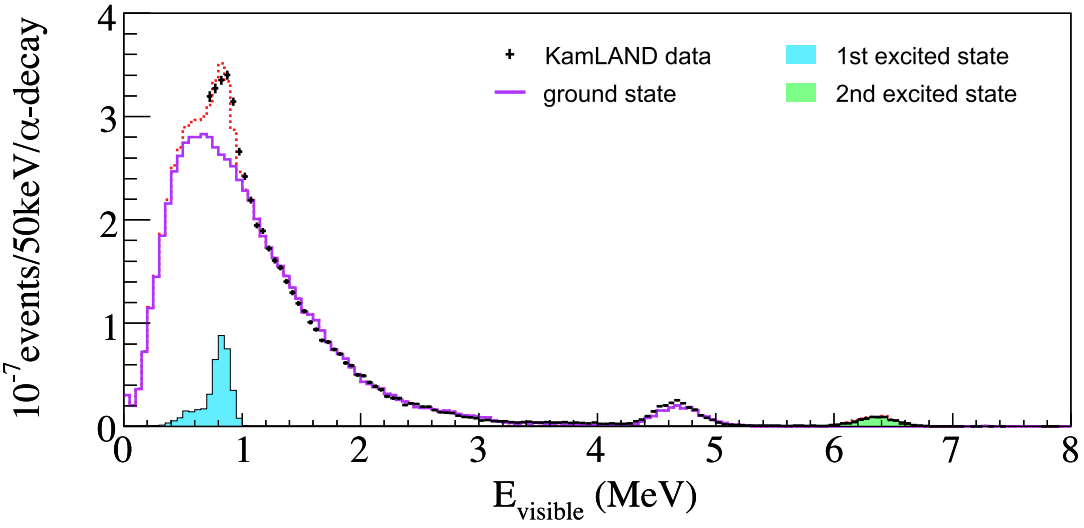

Figure 6.38: Comparison between the ^{210}Po^{13}C source calibration data and the expected spectrum(Watanabe 2012).

6.2.6 Uncertainties Estimation

The uncertainties of (α, n) background rate come from the ^{210}Po α decay rate measurement and the difference between the simulated spectrum and the ^{210}Po^{13}C source data, i.e. the cross section uncertainty.

^{210}Po α decay rate uncertainty

The ^{210}Po α decay rate is measured by fitting observed energy spectrum as shown in Figure 6.28 and Figure 6.29. This measurement is performed with a 550-cm-radius fiducial volume cut to avoid radioactive impurities coming from the outer balloon and γ radiation from outside the ID. Then the measured rate in the 550-cm-radius fiducial volume is scaled to the rate in a 600-cm-radius volume. However, there is a radius dependence of ^{210}Po α decay rate. Therefore, an uncertainty related to this scaling, or "fiducial volume dependence", need to be estimated. This uncertainty is studied by comparing the ^{210}Po α decay rate within 550-cm-radius volume and 600-cm-radiums volume as shown in Figure 6.39. After the first purification, the ^{210}Po α decay rate around fiducial radius 600 cm is affected by radioactivity from the outer-balloon, which is reconstructed inside fiducial cut due to fitite vertex resolution. Therefore, the fiducial radius dependence of such events are simulated with GEANT4(Agostinelli et al. 2003) and subtracted from the observed radius dependence. The uncertainty from the volume dependence after the second purification is much larger than before the second purification. This is because ^{210}Po in the liquid scintillator was effectively removed by the purification and is not be a problem.

The fiducial volume dependence estimation is affected by the fiducial volume uncertainty, which is verified by the time variation of estimated dependences as shown in Figure 6.40.

The ^{210}Po α decay rate measurement assumed uniform distribution of ^{210}Po α decay rate, whereas it has position dependence as shown in Figure 6.41. An independent measurement assuming the position dependence found a 0.5% downward-shift in the total ^{210}Po α decay number after the first purification(Watanabe 2021). Thus 0.5% is added to the ^{210}Po α decay rate uncertainty as "^{210}Po non-uniformity".

Table 6.10 summarizes the uncertainties of ^{210}Po α decay rate.

Table 6.10: Uncertainty of ^{210}Po decay rate (Shimizu 2010, Watanabe 2012, 2021)

	before purif.	after 1st purif.	after 2nd purif.
fiducial volume dependence	2.0%	2.8%	37.7%
dependence uncertainty	1.0%	0.8%	2.0%
^{210}Po non-uniformity	-	0.5%	0.5%
total	2.2%	3.0%	37.8%

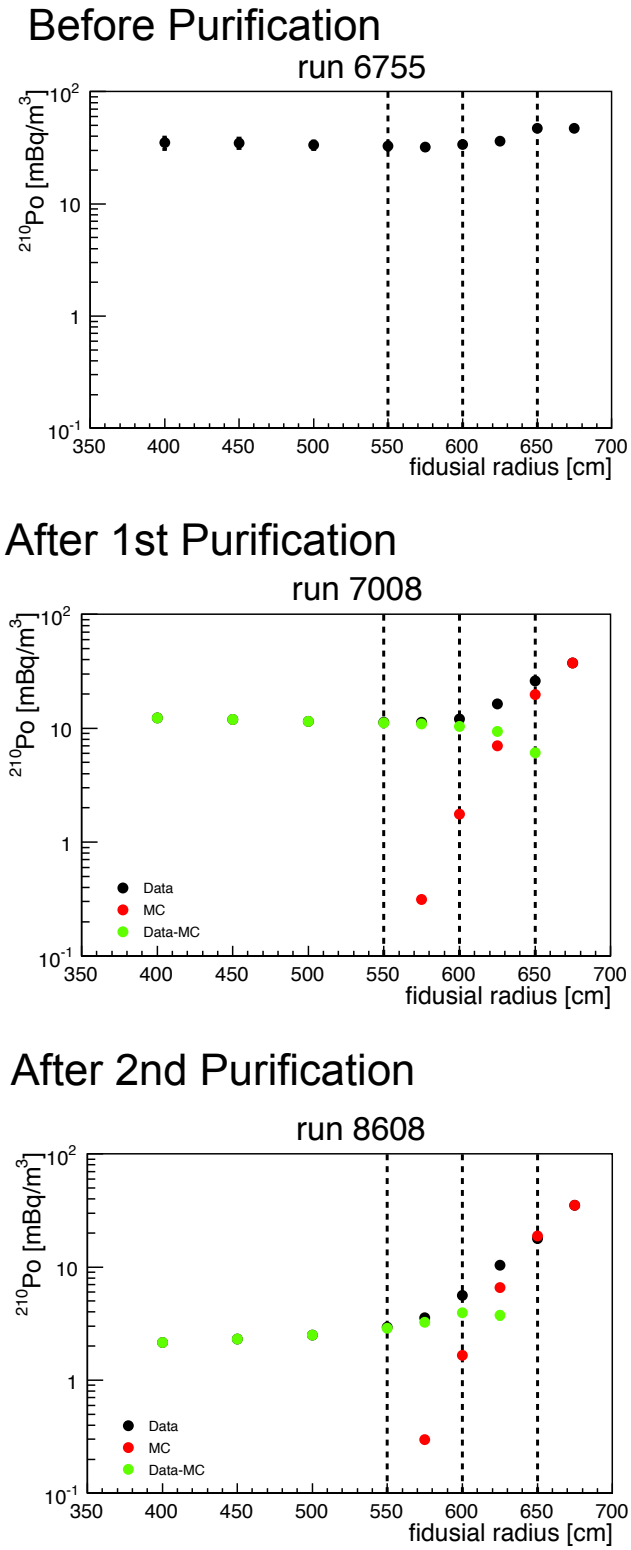

Figure 6.39: Fiducial radius dependence of ^{210}Po α rate with MC (top) before purifications, (middle) after the first purification and (bottom) after the second purifications (Watanabe 2012).

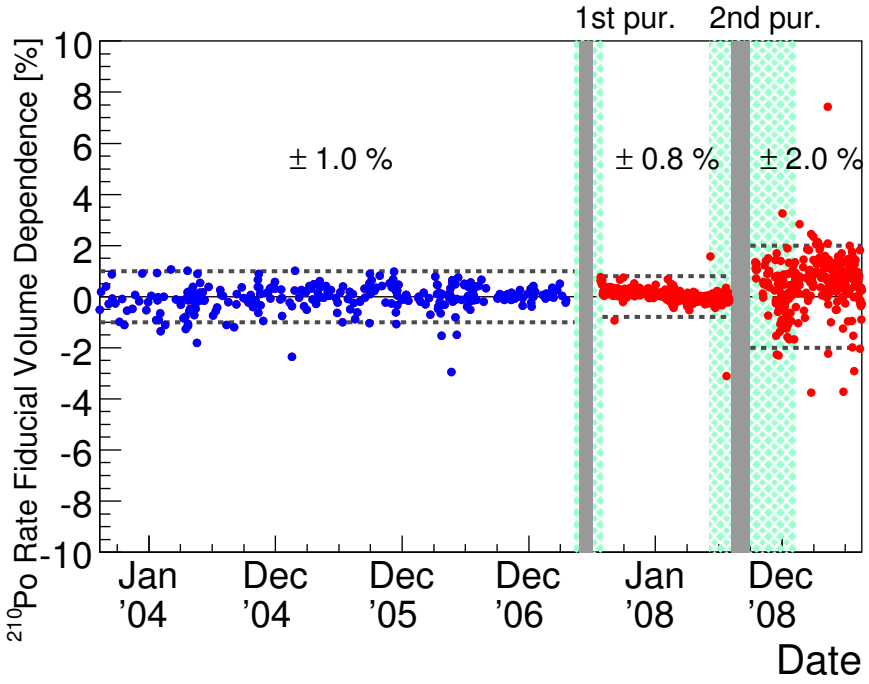

Figure 6.40: Time variation of the fiducial volume dependence of ^{210}Po α decay rate (Watanabe 2012)

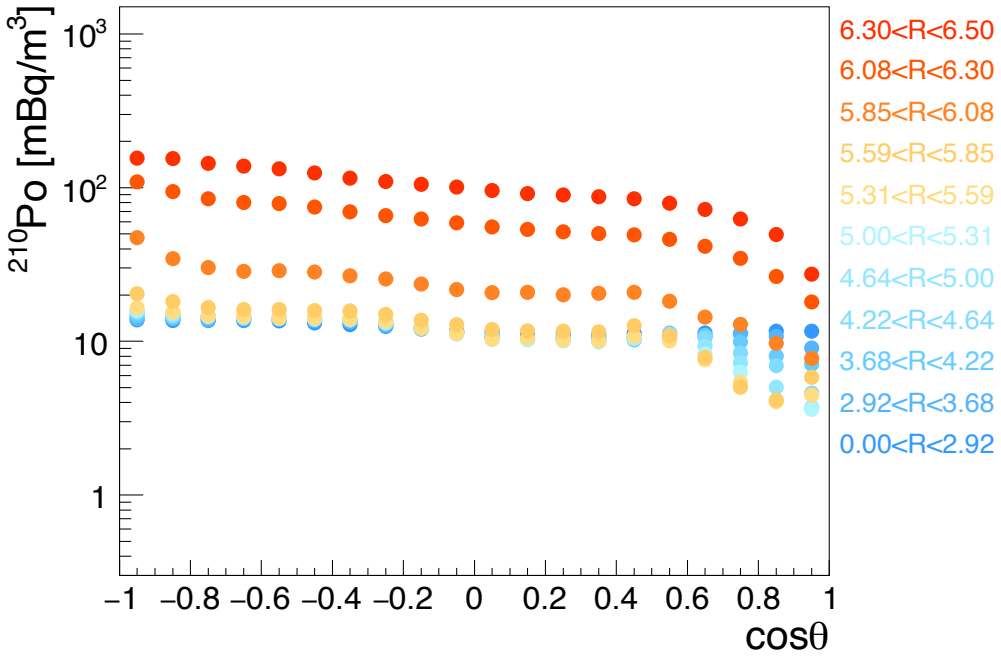

Figure 6.41: Position dependence of ^{210}Po α decay rate (Watanabe 2021)

$^{13}C(\alpha, n)^{16}O$ cross section uncertainty

The uncertainty of the cross section is estimated from the difference between simulated rate by GEANT4(Agostinelli et al. 2003) and the observed rate in the $^{210}Po^{13}C$ source calibration. It is found to be 10% and 20% for the ground state and for the excited states, respectively.

Table 6.11 is the summary of $^{13}C(\alpha, n)^{16}O$ rate uncertainty.

Table 6.11: Uncertainty of $^{13}C(\alpha, n)^{16}O$ rate

	before purif.	after 1st purif.	after 2nd purif.
^{210}Po decay rate	2.2%	3.0%	37.8%
$^{13}C(\alpha, n)^{16}O$ cross section	10% / 20% (ground state / excited states)		
total	10.2%/20.1%	10.4%/20.2%	39.1%/42.8%

6.3 Accidental Coincidence

As is discussed in Sec.5.5.1, the accidental coincidence event is selected by almost the same criteria as the IBD candidates, except shifted and extended time-correlation selection. For the accidental background estimation, the likelihood selection is also applied. Data-driven estimation of accidental coincidence background is performed for each run.

Figure 6.42–6.43 show the time variation of the accidental coincidence background rate after the likelihood selection in each data period. The accidental coincidence rate in period3 is lower by factor than those in the other periods. This is because the expected reactor neutrino flux is smaller in period3. Since the likelihood selection adopts a FoM-based strategy, the cut for likelihood ratio is set to be tight in period3, that is, the smaller expected signal rate prefers the more accidental background supression.

6.4 Muon-Spallation Products

6.4.1 Overview of Muon-Spallation Background

As discussed in Sec.5.3, cosmic muon generate various radioactive isotopes via spallation in the liquid scintillator (Table 5.2). Isotopes whose lifetime is less than $\mathcal{O}(10^{-3})$ sec are effectively rejected with the muon veto. Besides, most of muon-spallation products do not contaminate the signal since the delayed-coincidence selection and the likelihood selection are applied.

However, isotopes that emit neutrons need to be estimated carefully because their β-decays accompanied with neutron emission mimic a delayed-coincidence event.

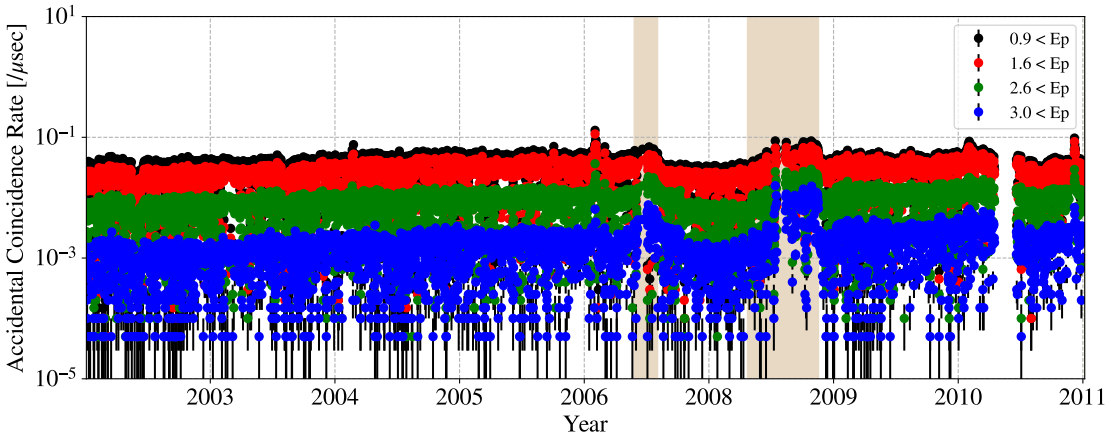

Figure 6.42: Time variation of the accidental coincidence background rate after Likelihood cut in Period1 and Period2.

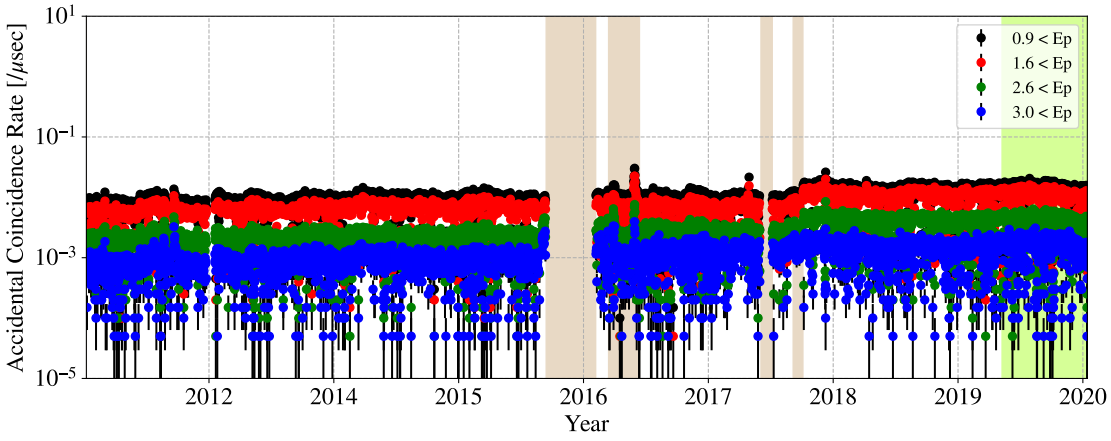

Figure 6.43: Time variation of the accidental coincidence background rate after Likelihood cut in Period3

6.4.2 Neutron Emitters

Table 6.12 summarizes isotopes which are accompanied by neutron emission after their β decay. An experiment using muon bean by Hagner et al. (2000) and a measurement by KamLAND(Abe et al. 2010) reported that ^{8}He and ^{9}Li are the dominant neutron-emitting isotope. Indeed, ^{11}Li have not been observed in KamLAND. Besides, Bergmann et al. (1999) reported that the fraction of neutron-emission mode for ^{12}Be is 0.5%. Thus, ^{11}Li and ^{12}Be are negligible.

Table 6.12: List of isotopes which emit β-ray and neutron (Ichimura 2008). The decay mode fractions for ^{12}Be is provided by Bergmann et al. (1999).

isotope	production reaction	life time [msec]	decay mode	energy [MeV]	fraction
^{8}He	^{12}C$(\gamma, 4\mathrm{p})^{8}$He,^{12}C$(\pi^-, \mathrm{n3p})^{8}$He	171.7	β^-	10.7	0.84
			$\beta^- + \mathrm{n}$		0.16
^{9}Li	^{12}C$(\gamma, 3\mathrm{p})^{9}$Li,^{12}C$(\pi^-, \mathrm{n2p})^{9}$Li	257.2	β^-	13.6	0.52
			$\beta^- + \mathrm{n}$		0.48
^{11}Li	^{12}C$(\gamma, 2\pi^+\mathrm{p})^{11}$Li,^{12}C$(\pi^-, \pi^+\mathrm{p})^{11}$Li	12.3	β^-	20.6	0.07
			$\beta^- + x\mathrm{n}$		0.92
^{12}Be	^{12}C$(\gamma, 2\pi^+)^{12}$Be,^{12}C$(\pi^-, \pi^+)^{12}$Be	14.6	β^-	11.7	0.995
			$\beta^- + \mathrm{n}$		0.005

6.4.3 Rate Estimation

^{8}He and ^{9}Li events are selected with almost the same criteria as the IBD candidates except the prompt energy range and the muon veto as summarized in Table 6.13. Muon vetos other than 2 msec veto after muon are not applied to get a large statistics of ^{8}He and ^{9}Li events.

Table 6.13: Selection criteria for ^{8}He/^{9}Li events

parameter	criteria
prompt energy [MeV]	$0.9 \leq E_\mathrm{p} < 20$
delayed energy [MeV]	$1.8 \leq E_\mathrm{d} < 2.6$
space correlation [m]	$\Delta R < 2.0$
time correlation [μs]	$0.5 \leq \Delta T < 1000$
fiducial volume [m]	$R_\mathrm{p} < 6$ & $R_\mathrm{d} < 6$
muon veto	2 msec veto after muon

Prompt energy spectrum of ^{8}He or ^{9}Li is shown in Figure 6.44. The KamLAND data is consistent with the expected ^{9}Li β decay spectrum. Though this figure just

lays the data on the expected spectrum, an extended likelihood analysis (Watanabe 2012) indicates that ^{9}Li accounts for almost all of the observed neutron emitters, whereas the contribution of ^{8}He is negligible as shown in Figure 6.45.

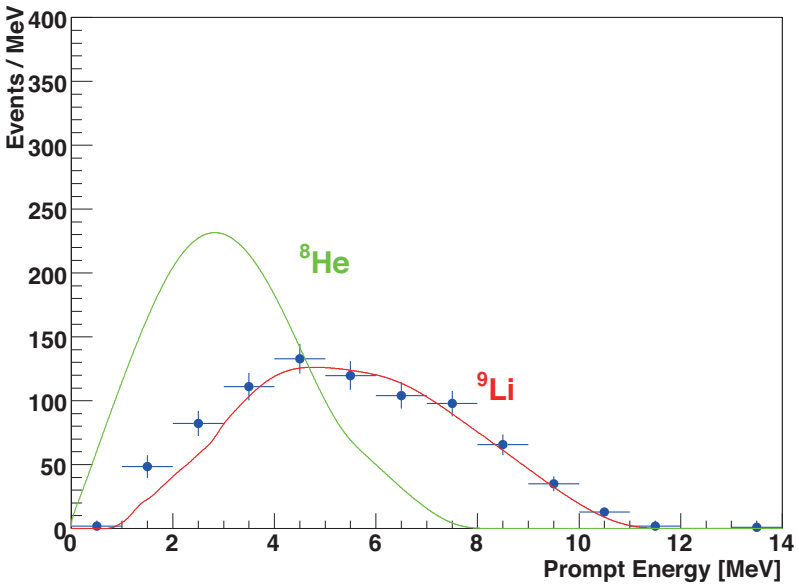

Figure 6.44: Energy spectrum of ^{8}He/^{9}Li β decay candidates. ^{8}He and ^{9}Li β decay spectra are normalized with the integral. Data is consistent with ^{9}Li. This figure is cited from Obara (2018) whereas the original data is from Ichimura (2008)

The event rate of ^{9}Li with neutron emission is measured by fitting the time difference distribution from last muon event shown in Figure 6.46. The decreasing curves imply decays of ^{9}Li. Each curve is fitted with an exponential function of ^{9}Li decay and a constant offset. Besides, the efficiency of 3-m-cylindrical track cut is estimated with the same dataset as shown in Figure 6.47.

The selection of the IBD candidates includes 2 sec whole volume veto for showering muon and 2 sec 3-m-cylindrical volume veto along reconstructed muon track for non-showering muon. Thus, the number of ^{9}Li backgrounds is estimated from the total event rate and cylindrical cut efficiency by calculating the number of ^{9}Li which survive more than 2 sec or escape from the 3-m-cylindrical volume. The uncertainty of the ^{9}Li background rate is estimated to be 20% from the deviation of the track cut efficiency along time.

6.5 Miscellaneous Negligible Backgrounds

6.5.1 Fast Neutron

Cosmic muon spallation is tagged by the OD, and muon-induced neutron and short-lived spallation products are effectively rejected with muon veto. However, in case a muon goes through the OD insensitive region or goes through just outside the OD, fast

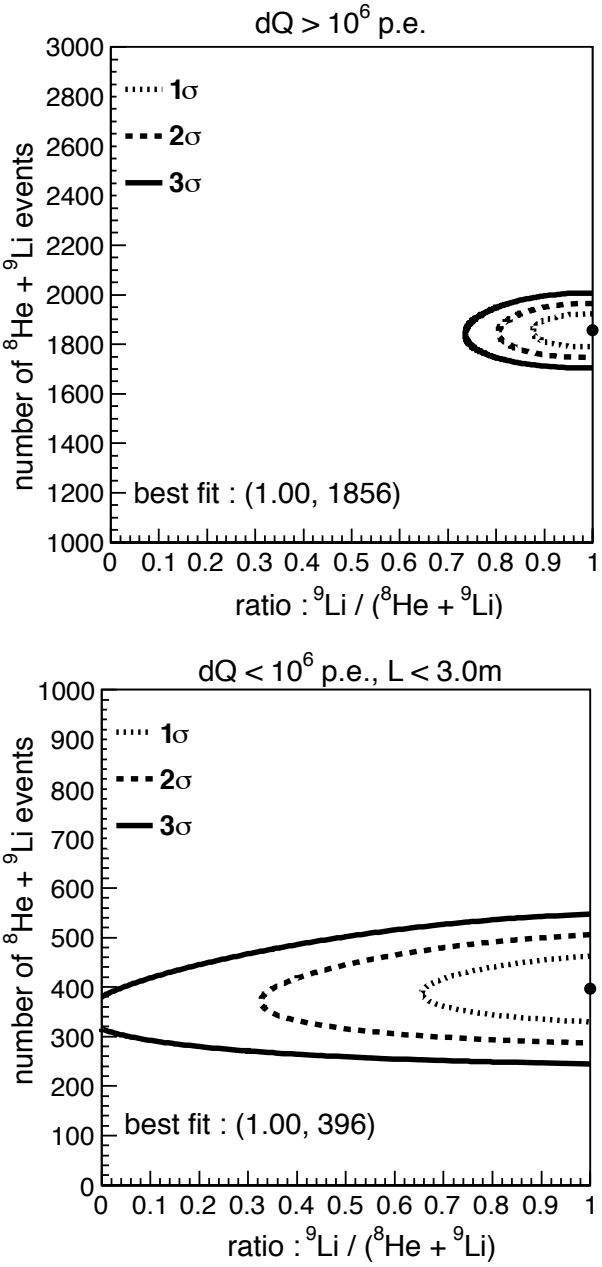

Figure 6.45: Allowed reigon from extended likelihood analysis of the number of ^{8}He and ^{9}Li events againt the ratio of ^{9}Li for (top) showering muon and (bottom) non-showering muon (Watanabe 2012). The life time of ^{8}He and ^{9}Li are fixed in this analysis.

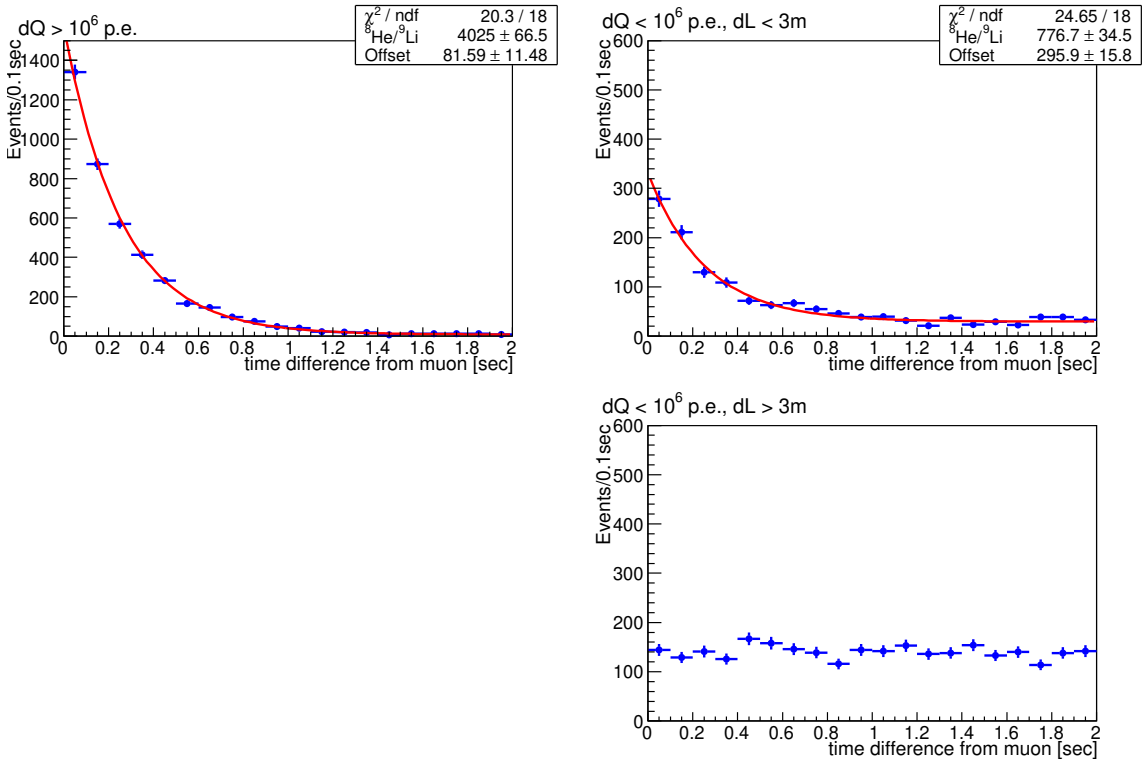

Figure 6.46: Time distributions of ^{8}He or ^{9}Li β decay candidates from last muon event after (upper left) showering muon (upper right) non-showering muon within 3 m from muon track and (lower right) non-showering muon 3 m or further from muon track

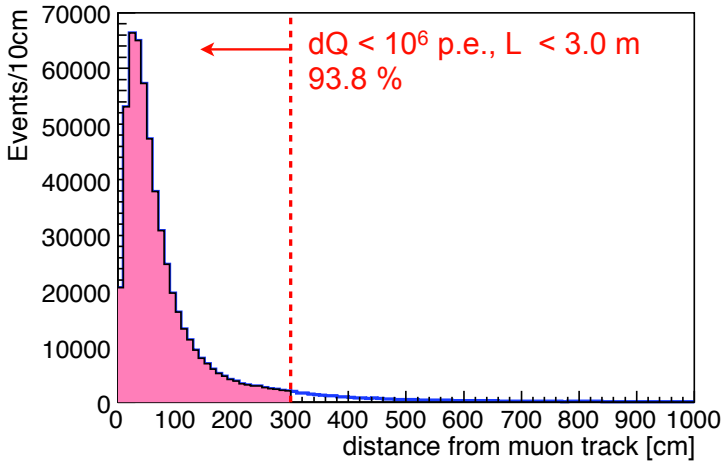

Figure 6.47: Distance of ^{9}Li candidates from muon track(Watanabe 2012). The efficiency of the 3-m-cylindrical track cut for muon veto is estimated to be 93.8%.

neutron generated by such muon can enter the detector without get tagged with the OD. Once a fast neutron is emitted to the liquid scintillator, it mimic an IBD signal just as the same as the (α, n) background to the ground state of ^{16}O. Figure 6.48 shows schematic of such "fast neutron" background.

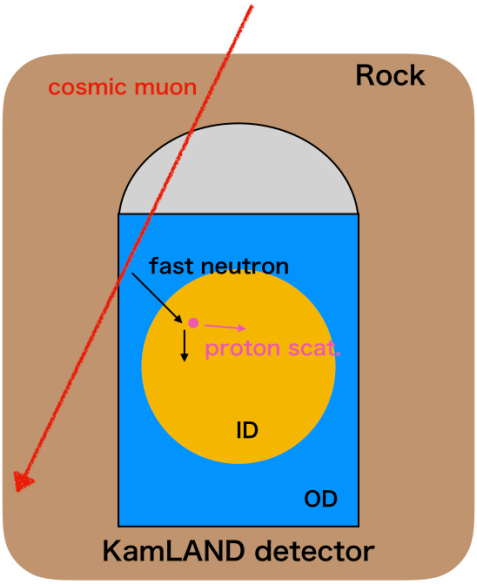

Figure 6.48: Schematic of fast neutron background (Obara 2018)

To estimate the fast neutron background, MUSIC muon propagation simulator (Antonioli et al. 1997) is tuned to reproduce the muon angler distribution at KamLAND as shown in Figure. 6.49. In addition, the rate and obseved event properties, e.g. energy or radius distribution, are estimated using GEANT4 (Agostinelli et al. 2003).

Based on the estimation result reported by Obara (2018), the number of fast neutron backgrounds in the geoneutrino energy region is calculated to be 0.31 ± 0.07 event and negligible.

6.5.2 Atmospheric Neutrino

Atmospheric neutrinos are generated in the cascade shower in the atmosphere and cause charged current or neutral current interaction in the ID. Honda et al. (2001) simulated the atomospheric neutrino flux at Kamioka site with NUANCE neutrino physics simulator (Casper 2002) as shown in Figure. 6.50. This spectral model is input to GEANT4 simulator for KamLAND to estimate the number of atomospheric neutrino background. Based on the estimation result reported by Watanabe (2012), the number of atomospheric neutrino backgrounds in the geoneutrino energy region is calculated to be 6.72 and negligible.

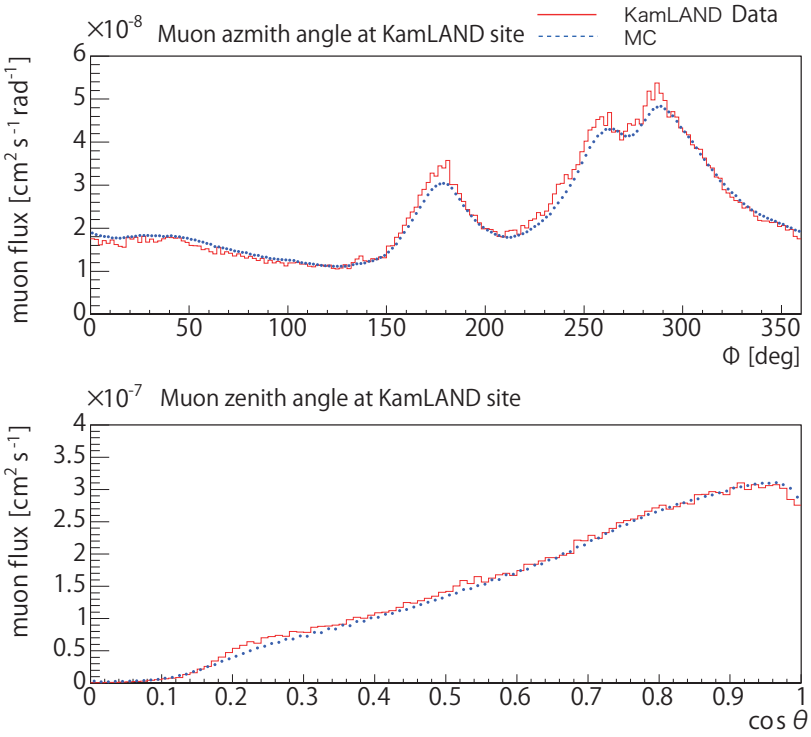

Figure 6.49: The comparison of muon track direction from simulation and the KamLAND data. This figure is cited from Obara (2018). The original data is compiled by Minekawa (2008)

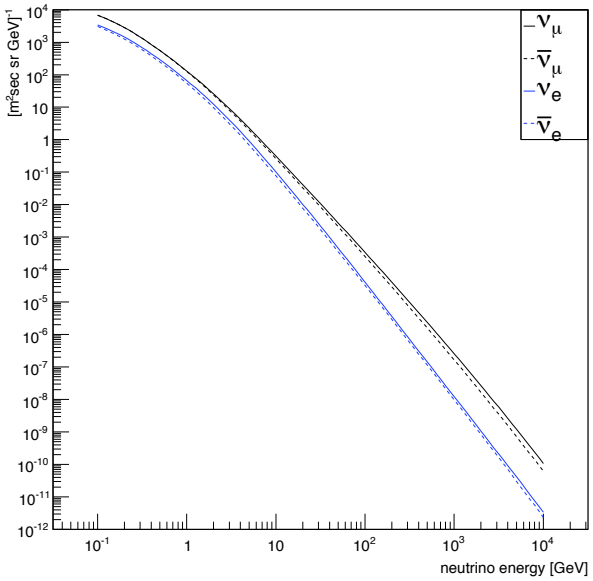

Figure 6.50: Atomospheric neutrino flux simulated with NUANCE (Casper 2002) simulator. This figure is cited from Watanabe (2012). The original data is provided by Honda et al. (2001).

6.6 Background Summary

The expected numbers of various backgrounds are summarized in Table 6.14. The backgrounds are calculated in a neutrino-oscillation analysis region, i.e. 0.9–8.5 MeV, and a geoneutrino analysis region, i.e. 0.9–2.9 MeV. In this calculation, the oscillation parameters were set to the best-fit value in a previous work in 2013 (Gando et al. 2013a).

Table 6.14: The expected number of backgrounds in each period. Reference geo $\overline{\nu}_e$ is calculated from Enomoto et al. (2007).

	Period1		Period2		Period3	
energy range [MeV]	0.9–8.5	0.9–2.6	0.9–8.5	0.9–2.6	0.9–8.5	0.9–2.6
Reactor $\overline{\nu}_e$	1261.50	331.51	765.94	220.54	209.26	53.04
$^{13}C(\alpha, n)^{16}O$	186.38	155.99	18.94	15.33	18.08	14.50
Accidental	76.82	59.35	57.40	40.53	33.92	24.79
Spallation ($^{8}He/^{9}Li$)	18.76	1.52	13.28	1.05	24.10	1.69
Reference geo $\overline{\nu}_e$	72.79	72.55	55.11	54.87	96.02	95.53
Total	1616.24	620.91	910.66	332.32	381.38	189.55

Figure 6.51 shows the expected event rate of each background between 0.9 MeV and 8.5 MeV. The dominant background vary from period to period. In Period1, $^{13}C(\alpha, n)^{16}O$ is dominant, whereas it is significantly suppressed by the two pufification campaigns and accidental background is dominant in Period2. As described in Sec.6.3, the likelihood selection can suppress the accidental coincidence background further due to smaller reactor neutrino flux. So, for reactor neutrino in Period3, geoneutrino signal is the dominant background. In the oscillation analysis, the geoneutrino contribution from ^{232}Th and ^{238}U are floated as free parameters.

Figure 6.52 shows the expected event rate of each background between 0.9 MeV and 2.6 MeV. In Period1 and Period2, reactor neutrino is the dominant background. In Period3, i.e the low-reactor period, though the reactor is the largest background, the expected number of reactor neutrino background is smaller than the geoneutrino reference model (Enomoto et al. 2007).

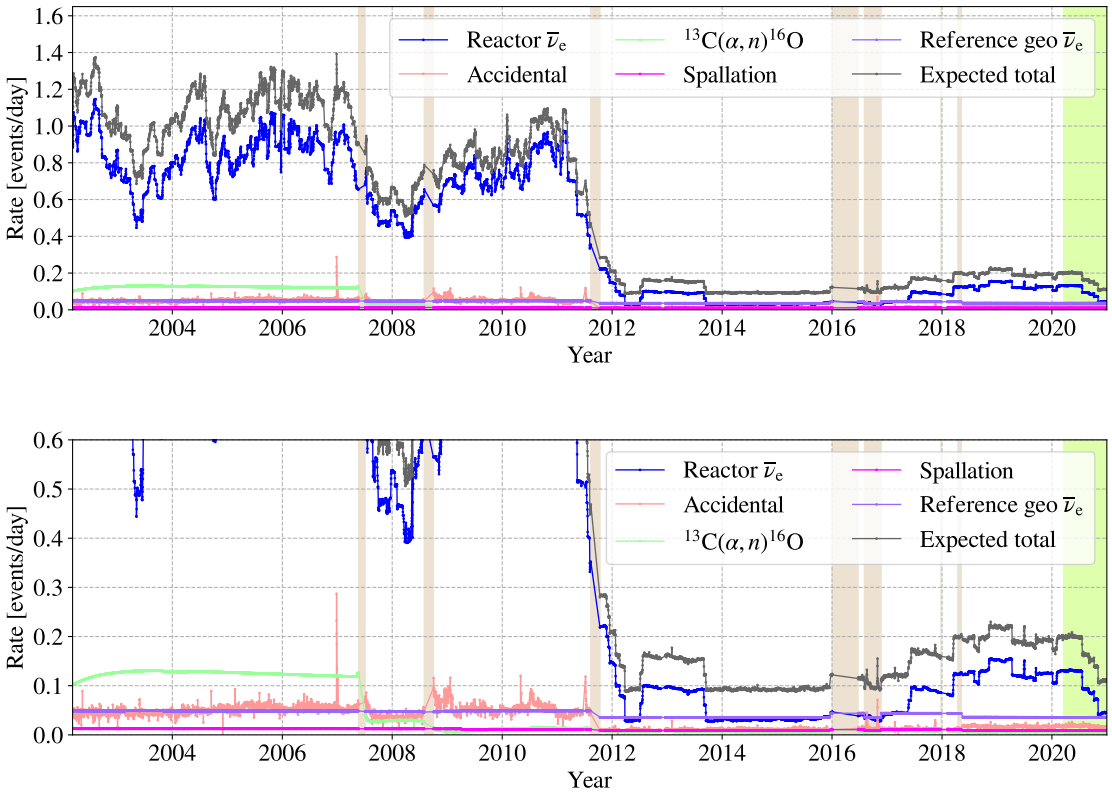

Figure 6.51: Time variation of expected background rate between 0.9 MeV and 8.5 MeV. Reference geoneutrino contribution is calculated from Enomoto et al. (2007). The bottom figure is the same figure as the top figure in a different vertical scale.

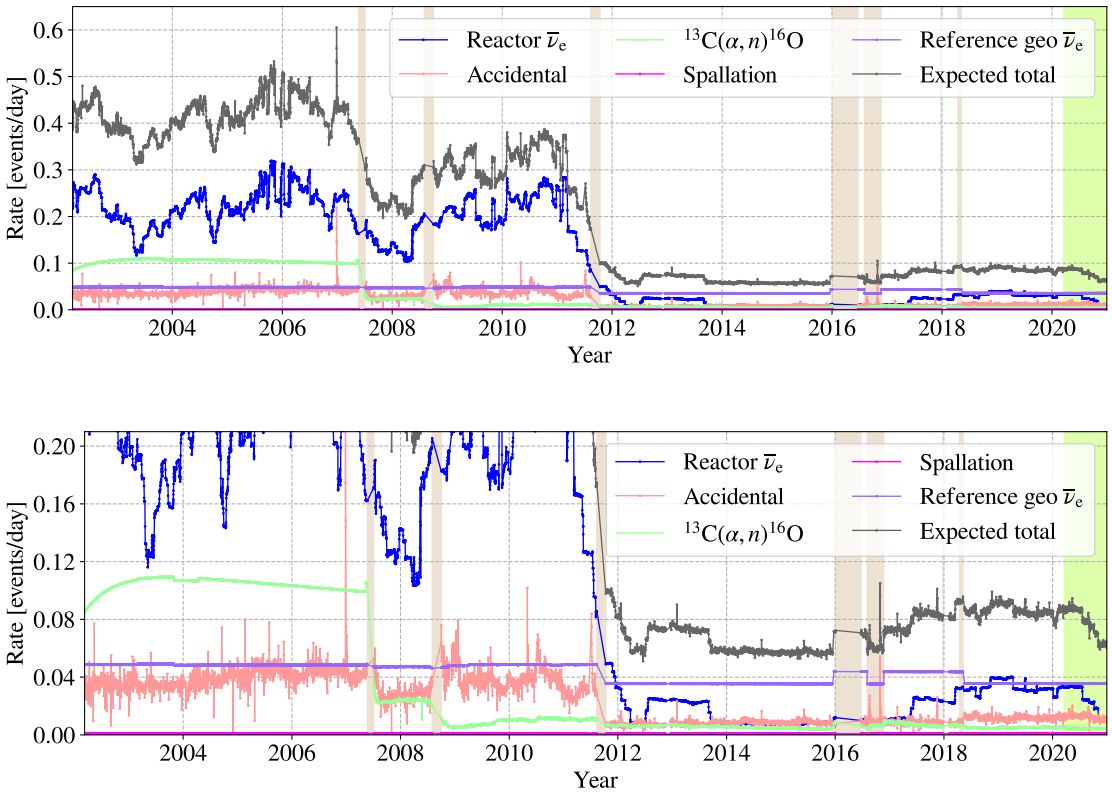

Figure 6.52: Time variation of expected background rate between 0.9 MeV and 2.6 MeV. Reference geoneutrino contribution is calculated from Enomoto et al. (2007). The bottom figure is the same figure as the top figure in a different vertical scale.

Chapter 7

Neutrino-oscillation Analysis

7.1 Oscillation Analysis in 3 Generation

The KamLAND data is analyzed with an unbinned likelihood method using event rate, spectral shape and time information. For neutrino oscillation analysis, the IBD candidates with prompt energies from 0.9 MeV to 8.5 MeV and corresponding background models described in Chap.6 are input, while reactor neutrino is dealt with not as background but as signal of interest after applying oscillation effect and geoneutrinos are floated as free parameters.

Reactor neutrinos propagate in earth for typically $\mathcal{O}(10^2)$ km to reach KamLAND. In this distance scale, three-flavor survival probability including matter effect are considered and written as

$$\begin{aligned} P_{ee}^{3\nu} &= \cos^4\theta_{13}\widetilde{P}_{ee}^{2\nu} + \sin^4\theta_{13} \\ \widetilde{P}_{ee}^{2\nu} &= 1 - \sin^2\left(2\widetilde{\theta}_{12}\right)\sin^2\left(\frac{\Delta\widetilde{m}_{21}^2 L}{E_\nu}\right) \end{aligned} \tag{7.1}$$

where $\widetilde{\theta}_{12}$ and $\Delta\widetilde{m}_{21}^2$ are ν_1-ν_2 oscillation parameters with a modified electron density $\widetilde{N}_e = N_e\cos^2\theta_{13}$ (Goswami and Smirnov 2005).

7.2 Rate + Shape + Time Analysis Scheme

The χ^2 for the Rate + Shape + Time analysis is defined as

$$\chi^2 = \chi^2_{\text{rate}} + \chi^2_{\text{shape}} + \chi^2_{\text{penalty}} + \chi^2_{\text{solar}} + \chi^2_{\theta_{13}\text{-constraint}} \tag{7.2}$$

The rate term, χ^2_{rate} is written as

$$\chi^2_{\text{rate}} = \frac{(N_{\text{obs}} - n_{\text{reactor}} - n_{\text{BG}})^2}{\sigma^2_{\text{stat}}} \tag{7.3}$$

where

$$\begin{aligned} N_{\rm obs} &: \text{number of observed events} \\ n_{\rm reactor} &: \text{number of reactor } \overline{\nu_{\rm e}} \text{ events for each set of oscillation parameter} \\ n_{\rm BG} &: \text{number of background events} \\ \sigma_{\rm stat} &: \text{statistical error, i.e. the square root of } (n_{\rm reactor} + n_{\rm BG}) \end{aligned} \tag{7.4}$$

The shape term includes energy and time information as

$$\chi^2_{\rm shape} = -2 \log \prod_{i=1}^{N_{\rm obs}} \mathcal{L}(E_i, T_i) \tag{7.5}$$

where $\mathcal{L}(E_i, T_i)$ is a normalized probability density function for prompt energy and time of the antineutrino candidates, which considers rector neutrinos, geoneutrinos, all background contributions and systematic uncertainties.

The penalty term provides constraints from background rate estimation and systematic uncertainties as

$$\begin{aligned} \chi^2_{\rm penalty} =& \frac{(n_{(\alpha,n),\text{g.s.}} - N_{(\alpha,n),\text{g.s.}})^2}{{\sigma_{(\alpha,n),\text{g.s.}}}^2} \\ &+ \frac{(n_{(\alpha,n),\text{e.s.}} - N_{(\alpha,n),\text{e.s.}})^2}{{\sigma_{(\alpha,n),\text{e.s.}}}^2} \\ &+ \frac{(n_{^9\text{Li}} - N_{^9\text{Li}})^2}{{\sigma_{^9\text{Li}}}^2} \\ &+ \alpha^2_{\text{reactor,Period1}} + \alpha^2_{\text{reactor,Period2}} + \alpha^2_{\text{reactor,Period3}} \\ &+ \alpha^2_{\rm geo} + \alpha^2_{\rm flux} + \alpha^2_{\rm efficiency} + \alpha^2_{\text{energy scale}} \end{aligned} \tag{7.6}$$

where $N_{\rm x}$ and $\sigma_{\rm x}$ are the expected rate and its uncertainty of background x, $n_{\rm x}$ is a variable parameter as the number of background x, $\alpha_{\rm y}$ is the deviation from the estimated systematic uncertainty y. The penalty terms for reactor-related systematic uncertainty are implemented independently for each period since the dominant uncertainty factor varies from period to period. The penalty terms for reactor neutrino flux and selection efficiency are added because these uncertainties have energy dependence.

Using deviation parameters in Eq. 7.6, $n_{\rm reactor}$ for Period-s is calculated as

$$\begin{aligned} n_{\text{reactor,Period-}s} = N_{\text{reactor,Period-}s} &\times (1 + \alpha_{\text{reactor,Period-}s}\sigma_{\text{reactor,Period-}s}) \\ &\times (1 + \alpha_{\rm flux}\sigma_{\text{flux,Period-}s}) \\ &\times (1 + \alpha_{\rm efficiency}\sigma_{\text{efficiency,Period-}s}) \\ &\times (1 + \alpha_{\text{energy scale}}\sigma_{\text{energy scale,Period-}s}) \end{aligned} \tag{7.7}$$

where $\sigma_{\rm reactor}$, $\sigma_{\rm flux}$, $\sigma_{\rm efficiency}$ and $\sigma_{\text{energy scale}}$ for each period are given in columns labeled as "0.9–8.5" of Table 5.6 and Table 6.8.

As with reactor neutrino signal, the number of geoneutrino background $n_{\mathrm{U,Th}}$ for each period, which is a part of n_{BG}, is calculated as

$$\begin{aligned} n_{\mathrm{U,Th}} = N_{\mathrm{U,Th}} &\times (1 + \alpha_{\mathrm{geo}}\sigma_{\mathrm{detector,Period\text{-}}s}) \\ &\times (1 + \alpha_{\mathrm{efficiency}}\sigma_{\mathrm{efficiency,Period\text{-}}s}) \\ &\times (1 + \alpha_{\mathrm{energy\ scale}}\sigma_{\mathrm{energy\ scale,Period\text{-}}s}) \end{aligned} \tag{7.8}$$

where $\sigma_{\mathrm{detector}}$, $\sigma_{\mathrm{efficiency}}$ and $\sigma_{\mathrm{energyscale}}$ for each period are given in columns labeled as "0.9–2.6" of Table 5.6. Although N_{U} and N_{Th} float as free parameters, this term provides a constraint that the geoneutrino flux should be constant over the observation period.

KamLAND analysis employs some constraints on the oscillation parameters from solar neutrino data (Cleveland et al. 1998, Abdurashitov et al. 2009, Bellini et al. 2011, Hosaka et al. 2006, Aharmim et al. 2013) represented by χ^2_{solar}. Besides, θ_{13} is constrained by a global fit result by Gonzalez-Garcia et al. (2012) based on short-baseline oscillation experiments (Abe et al. 2012, An et al. 2013, Ahn et al. 2012) and accelerator neutrino experiments (Abe et al. 2011a, Adamson et al. 2011) as $\sin\theta_{13} = 0.0227 \pm 0.0023$, which $\chi^2_{\theta_{13}\text{-constraint}}$ refers to.

The χ^2 is minimized for various set of $(\Delta m^2_{12}, \theta_{12}, \theta_{13})$ and the best fit oscillation parameters are obtained by finding a set of oscillation parameter which yield minimum χ^2.

7.3 Oscillation Analysis Result

Figure 7.1 shows the confidence level contours and best fit point for $\tan^2\theta_{12}$ and Δm^2_{12} from the KamLAND Rate + Shape + Time analysis. The KamLAND result, black contour and point, employs the constraint on θ_{13} from short-baseline reactor neutrino data and accelerator neutrino data as shown in Figure 7.2. Compared to the solar constraint, blue contour and point, the KamLAND data is superior to determine Δm^2_{12}. The combined result is shown in red. The best oscillation parameter is summarized in Table 7.1.

Table 7.1: Oscillation parameter scan result

	$\tan^2\theta_{12}$	Δm^2_{12} [10^{-4} eV^2]
KamLAND	$0.434^{+0.053}_{-0.046}$	$0.754^{+0.018}_{-0.018}$
Solar	$0.431^{+0.038}_{-0.038}$	$0.660^{+0.171}_{-0.060}$
KamLAND + Solar	$0.432^{+0.026}_{-0.025}$	$0.753^{+0.018}_{-0.018}$

Figure 7.3 shows the best fit energy spectrum in all data period. The reactor neutrino spectrum after the best fit oscillation well reproduces the observed spectrum. Besides, Figure 7.4 shows the best fit spectrum in each period. The reactor neutrino spectrum and background spectra are calculated using the best fit values in the all-period analysis.

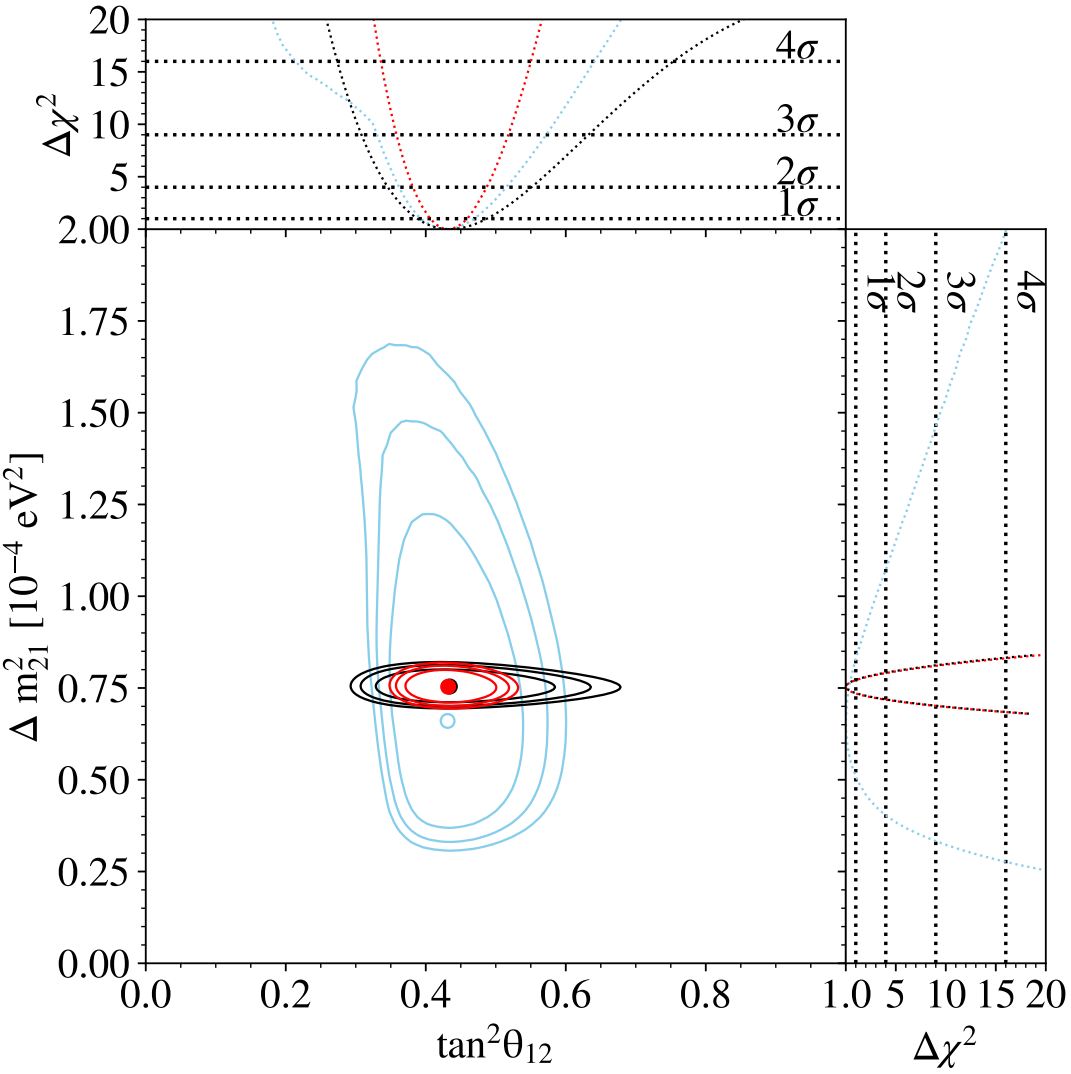

Figure 7.1: Confidence level contours (68.3%, 95.4% and 99.7% from inside) and best fit point for $\tan^2\theta_{12}$ and Δm^2_{12}. The KamLAND result employing a θ_{13} constraint by Gonzalez-Garcia et al. (2012) is drawn in black. The blue contour presents a constraint from solar neutrino global analysis. The red ones are the combined result. The top and right sub panes are projections to each axis.

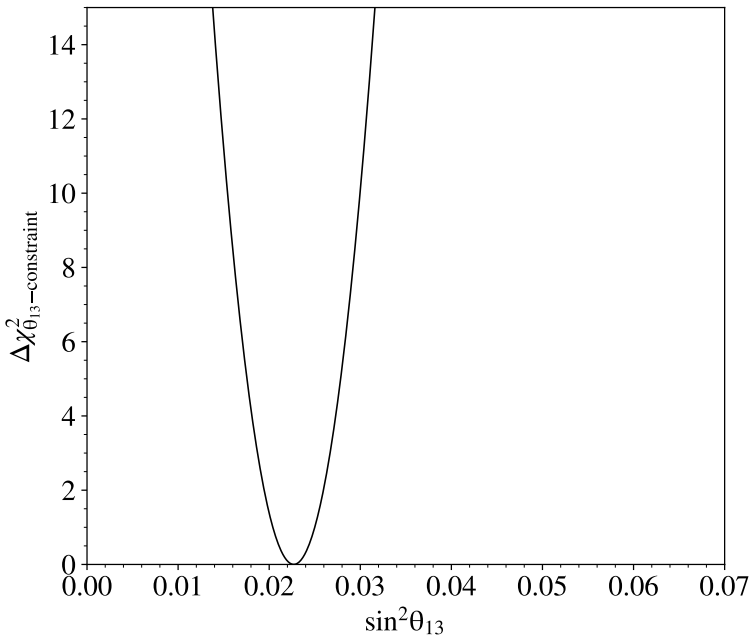

Figure 7.2: θ_{13} constraint from a global fit by Gonzalez-Garcia et al. (2012) based on short-baseline oscillation experiments (Abe et al. 2012, An et al. 2013, Ahn et al. 2012) and accelerator neutrino experiments (Abe et al. 2011a, Adamson et al. 2011)

Though geoneutrinos are floated in this analysis, Period3 data well determine the geoneutrinos's contribution and constraint it due to the low-reactor condition. Therefore, the low-reactor period is also helpful for the oscillation analysis.

The time variation of the best fit reactor neutrino and background rate is shown in Figure 7.5.

Figure 7.6–7.8 show the confidence level contours and best fit point for $\tan^2\theta_{12}$, $\sin^2\theta_{13}$ and Δm^2_{12} from the KamLAND Rate + Shape + Time analysis without the θ_{13} constraint. As in Figure 7.1, the black, blue and red contours represent the KamLAND result, solar constraint and the combined result, respectively.

The best oscillation parameter without θ_{13} constraint is summarized in Table 7.2. Though the statistical accuracy is poor than the short-baseline experiments, the KamLAND analysis demonstrated a evidence of non-zero θ_{13} at a confidence level of 1.0σ. Combined with the solar data, the significance is improved to 2.8σ.

Table 7.2: Oscillation parameter scan result without θ_{13} constraint

	$\tan^2\theta_{12}$	$\sin^2\theta_{13}$	Δm^2_{12} [10^{-4} eV^2]
KamLAND	$0.424^{+0.078}_{-0.065}$	$0.030^{+0.029}_{-0.030}$	$0.754^{+0.018}_{-0.018}$
Solar	$0.431^{+0.038}_{-0.038}$	$0.012^{+0.028}_{-0.012}$	$0.660^{+0.171}_{-0.060}$
KamLAND + Solar	$0.432^{+0.027}_{-0.025}$	$0.024^{+0.014}_{-0.015}$	$0.753^{+0.018}_{-0.018}$

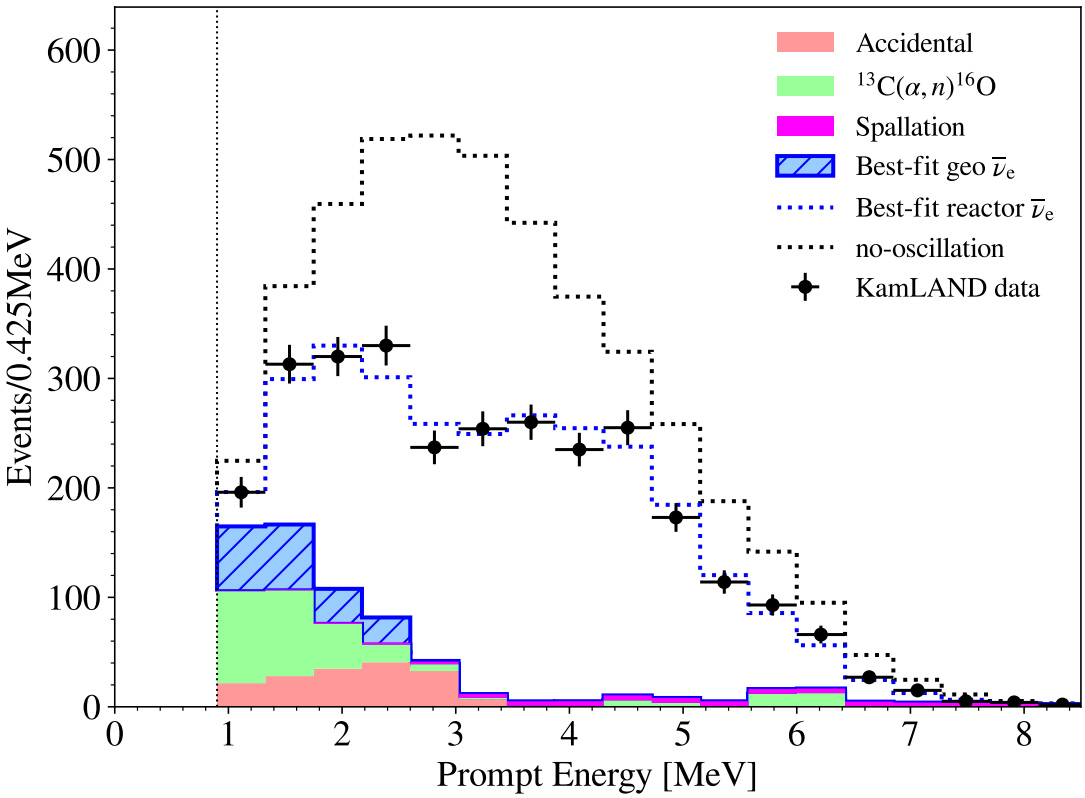

Figure 7.3: Best fit prompt energy spectrum of antineutrino candidates within 0.9–8.5 MeV in all dataset

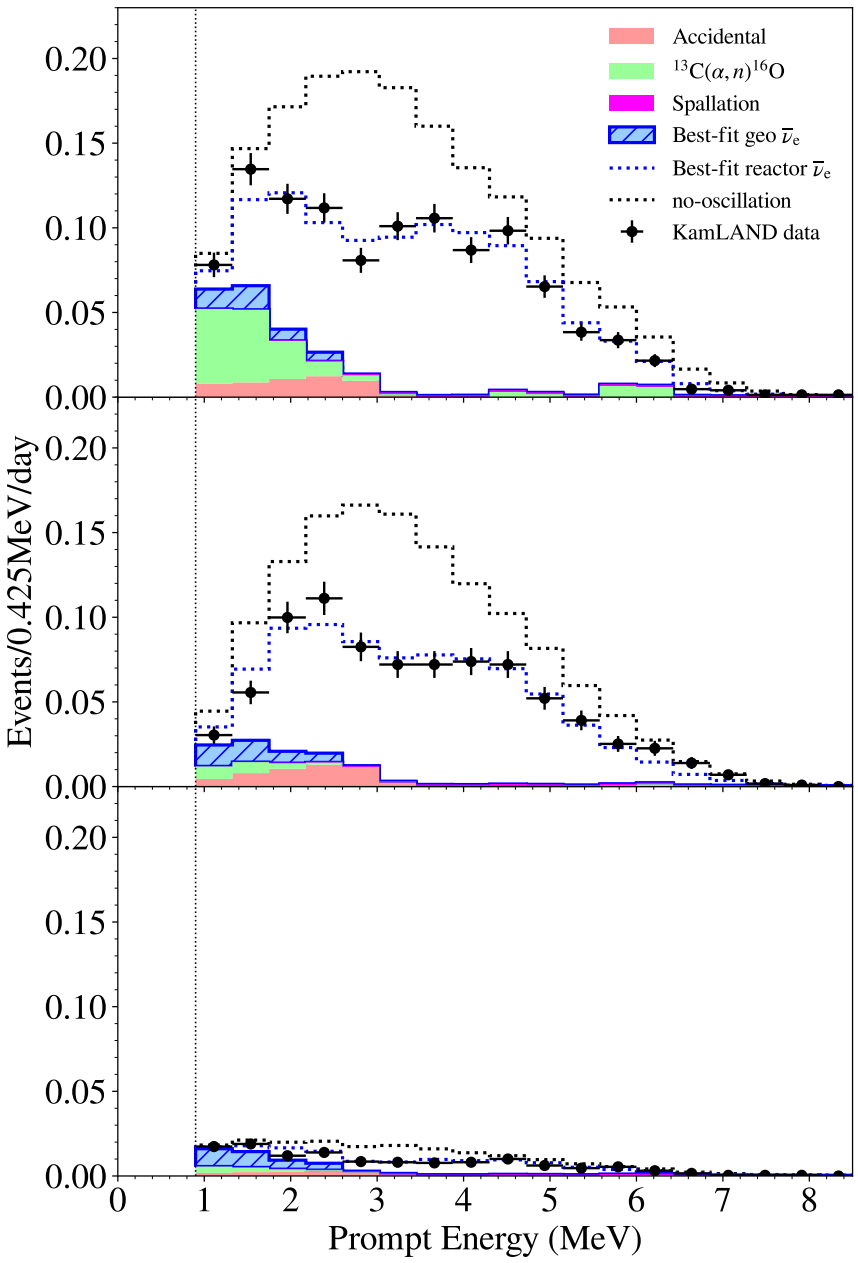

Figure 7.4: Best fit prompt energy spectrum of antineutrino candidates within 0.9–8.5 MeV in each data period (top:Period1, middle:Period2 and bottom:Period3)

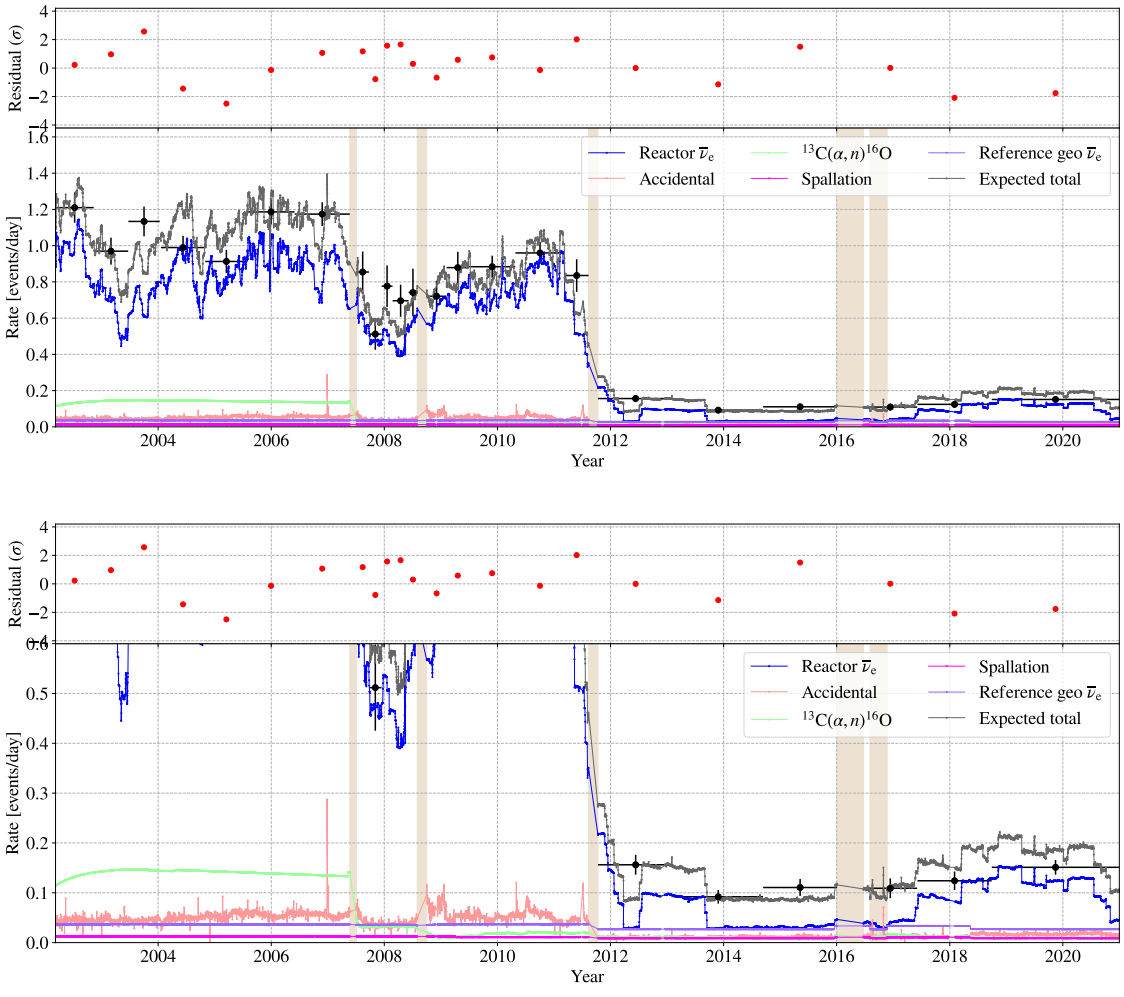

Figure 7.5: Time variation of best fit background rate between 0.9 MeV and 8.5 MeV. The bottom figure is the same figure as the top figure in a different vertical scale.

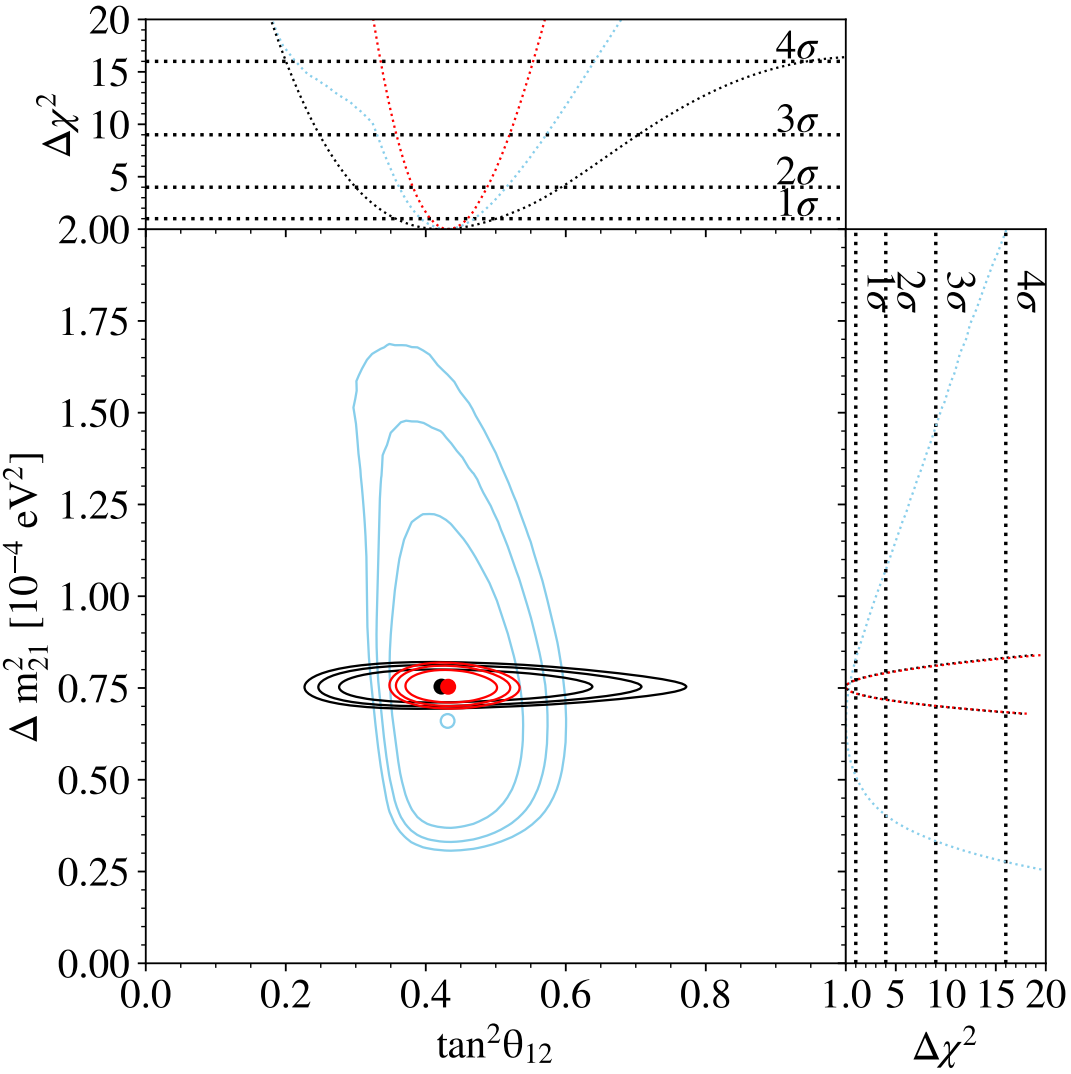

Figure 7.6: Confidence level contours (68.3%, 95.4% and 99.7% from inside) and best fit point for $\tan^2\theta_{12}$ and Δm^2_{12} without θ_{13} constraint. The KamLAND result is drawn in black. The blue contour presents a constraint from solar neutrino global analysis. The red ones are the combined result. The top and right sub panes are projections to each axis.

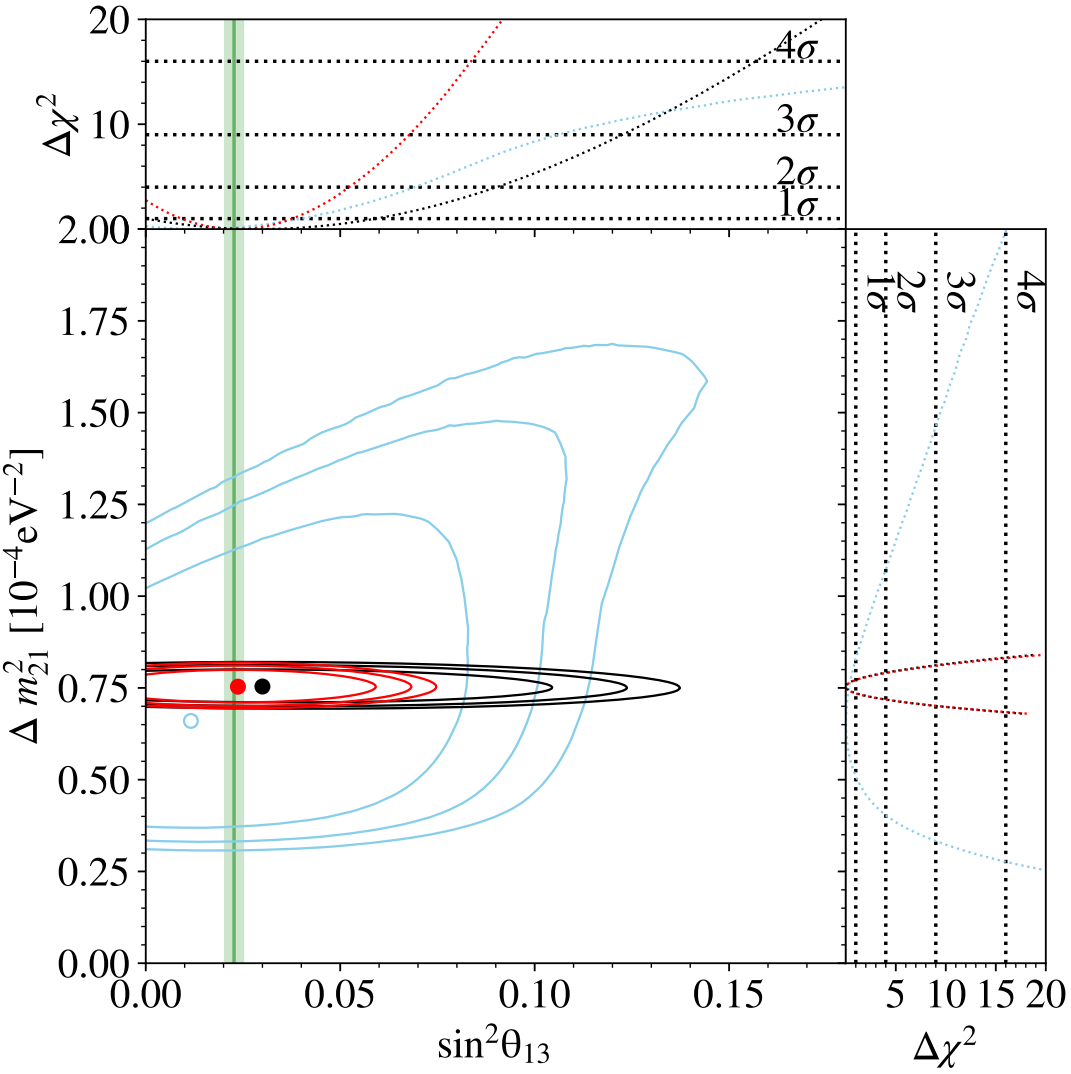

Figure 7.7: Confidence level contours (68.3%, 95.4% and 99.7% from inside) and best fit point for $\sin^2\theta_{13}$ and Δm^2_{12} without θ_{13} constraint. The KamLAND result is drawn in black. The blue contour presents a constraint from solar neutrino global analysis. The red ones are the combined result. The green band represents the θ_{13} constraint ($\sin^2\theta_{13} = 0.0227 \pm 0.0023$). The top and right sub panes are projections to each axis.

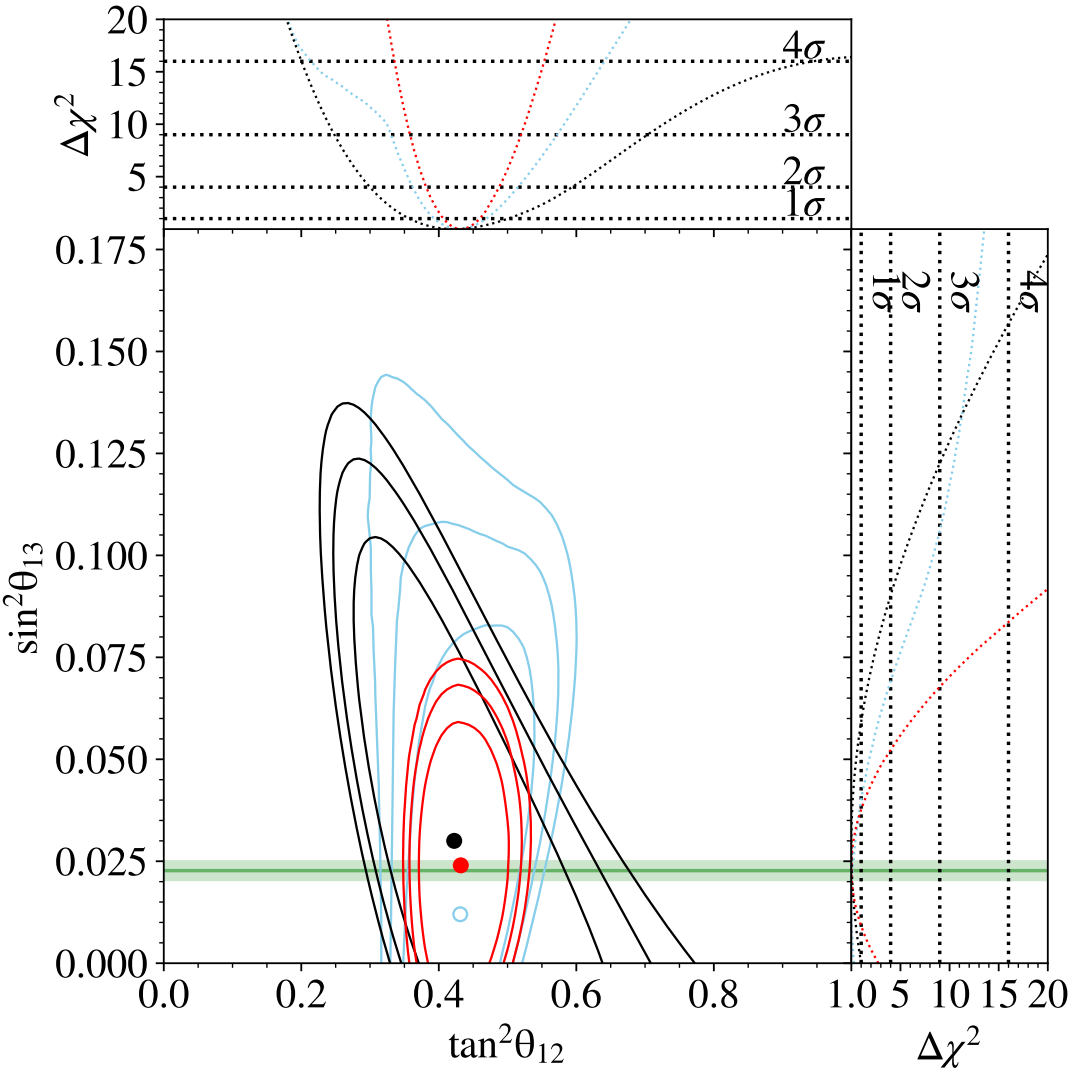

Figure 7.8: Confidence level contours (68.3%, 95.4% and 99.7% from inside) and best fit point for $\tan^2\theta_{12}$ and $\sin^2\theta_{13}$ without θ_{13} constraint. The KamLAND result is drawn in black. The blue contour presents a constraint from solar neutrino global analysis. The red ones are the combined result. The green band represents the θ_{13} constraint ($\sin^2\theta_{13} = 0.0227 \pm 0.0023$). The top and right sub panes are projections to each axis.

Chapter 8

Geoneutrino Analysis

8.1 Simultaneous scan of oscillation parameters and geoneutrino signals

The KamLAND data is also analyzed for geoneutrino signal with an unbinned likelihood method using event rate, energy spectral shape and time information. Since reactor neutrino is one of major backgrounds of geoneutrino signals due to shared energy range, the geoneutrino event rate and the oscillation parameters are evaluated simultaneously within prompt energy range 0.9 MeV to 8.5 MeV.

This analysis adopts almost the same strategy as the oscillation analysis discussed in Chap.7, except that reactor neutrino is dealt with as background and the assumed signal is geoneutrinos.

8.2 Rate + Shape + Time Analysis Scheme

The χ^2 for the Rate + Shape + Time analysis is defined as

$$\chi^2 = \chi^2_{\text{rate}} + \chi^2_{\text{shape}} + \chi^2_{\text{penalty}} + \chi^2_{\text{solar}} + \chi^2_{\theta_{13}\text{-constraint}} \tag{8.1}$$

The rate term, χ^2_{rate} is written as

$$\chi^2_{\text{rate}} = \frac{(N_{\text{obs}} - n_{\text{U}} - n_{\text{Th}} - n_{\text{BG}})^2}{\sigma^2_{\text{stat}}} \tag{8.2}$$

where

$$\begin{aligned}
N_{\text{obs}} &: \text{number of observed events} \\
n_{\text{U}} &: \text{number of geoneutrino signals from } ^{238}\text{U} \\
n_{\text{Th}} &: \text{number of geoneutrino signals from } ^{232}\text{Th} \\
n_{\text{BG}} &: \text{number of background events including reactor neutrino} \\
\sigma_{\text{stat}} &: \text{statistical error, i.e. the square root of } (n_{\text{U}} + n_{\text{Th}} + n_{\text{BG}})
\end{aligned} \tag{8.3}$$

The shape term and penalty term are defined as in the oscillation analysis.

$$\chi^2_{\text{shape}} = -2\log\prod_{i=1}^{N_{\text{obs}}}\mathcal{L}(E_i, T_i) \tag{8.4}$$

where $\mathcal{L}(E_i, T_i)$ is a normalized probability density function for prompt energy and time of the antineutrino candidates, which considers geoneutrinos, reactor neutrinos, all other background contributions and systematic uncertainties.

The penalty term provides constraints from background rate estimation and systematic uncertainties as

$$\begin{aligned}\chi^2_{\text{penalty}} =& \frac{(n_{(\alpha,n),\text{g.s.}} - N_{(\alpha,n),\text{g.s.}})^2}{{\sigma_{(\alpha,n),\text{g.s.}}}^2} \\ &+ \frac{(n_{(\alpha,n),\text{e.s.}} - N_{(\alpha,n),\text{e.s.}})^2}{{\sigma_{(\alpha,n),\text{e.s.}}}^2} \\ &+ \frac{(n_{^9\text{Li}} - N_{^9\text{Li}})^2}{{\sigma_{^9\text{Li}}}^2} \\ &+ \alpha^2_{\text{reactor,Period1}} + \alpha^2_{\text{reactor,Period2}} + \alpha^2_{\text{reactor,Period3}} \\ &+ \alpha^2_{\text{geo}} + \alpha^2_{\text{flux}} + \alpha^2_{\text{efficiency}} + \alpha^2_{\text{energy scale}}\end{aligned}$$

where N_{x} and σ_{x} are the expected rate and its uncertainty of background x, n_{x} is a variable parameter as the number of background x, α_{y} is the deviation from the estimated systematic uncertainty y. The penalty terms for reactor-related systematic uncertainty are implemented independently for each period since the dominant uncertainty factor varies from period to period. The penalty terms for reactor neutrino flux and selection efficiency are added because these uncertainties have energy dependence.

The number of reactor neutrino background for period-s is calculated as

$$\begin{aligned}n_{\text{reactor,Period-}s} = N_{\text{reactor,Period-}s} &\times (1 + \alpha_{\text{reactor,Period-}s}\sigma_{\text{reactor,Period-}s}) \\ &\times (1 + \alpha_{\text{flux}}\sigma_{\text{flux,Period-}s}) \\ &\times (1 + \alpha_{\text{efficiency}}\sigma_{\text{efficiency,Period-}s}) \\ &\times (1 + \alpha_{\text{energy scale}}\sigma_{\text{energy scale,Period-}s})\end{aligned} \tag{8.5}$$

where σ_{reactor}, σ_{flux}, $\sigma_{\text{efficiency}}$ and $\sigma_{\text{energy scale}}$ for each period are given in columns labeled as "0.9–8.5" of Table 5.6 and Table 6.8.

The number of geoneutrino signals from ^{238}U and ^{232}Th for period-s is calculated as

$$\begin{aligned}n_{\text{U,Th}} = N_{\text{U,Th}} &\times (1 + \alpha_{\text{geo}}\sigma_{\text{detector,Period-}s}) \\ &\times (1 + \alpha_{\text{efficiency}}\sigma_{\text{efficiency,Period-}s}) \\ &\times (1 + \alpha_{\text{energy scale}}\sigma_{\text{energy scale,Period-}s})\end{aligned} \tag{8.6}$$

where σ_{detector}, $\sigma_{\text{efficiency}}$ and $\sigma_{\text{energyscale}}$ for each period are given in columns labeled as "0.9–2.6" of Table 5.6.

As in the oscillation analysis, some constraints on the oscillation parameters are employed in this analysis. Details are described in Sec.7.2.

The χ^2 is minimized for various set of $(N_{\rm U}, N_{\rm Th})$ and the best fit geoneutrino signals are obtained by finding a set of $(N_{\rm U}, N_{\rm Th})$ which yield minimum χ^2.

8.3 Best fit geoneutrino signals

Figure 8.1 shows the allowed region of $(N_{\rm U}, N_{\rm Th})$ from the Rate + Shape + Time analysis. From this scan, the number of observed geoneutrino signals from ^{238}U and ^{232}Th in the whole data set and their uncertainties are obtained as Table 8.1. The number of geoneutrino signals are converted to flux using the number of target protons (Sec.5.6.1), total live time (Sec.5.1.3) and selection efficiency (Sec.5.5.4). The flux are also represented in Terrestrial Neutrino Unit (TNU). 1 TNU corresponds to one IBD event by geoneutrino in 1-year live time on 10^{32} target protons assuming 100% detection efficiency. The conversion factor from [cm^{-2}s^{-1}] to [TNU] is unique for each isotope due to different neutrino energy spectrum and energy-dependent IBD reaction cross section.

Table 8.1: Best fit and uncertainty of geoneutrino signals

	$N_{\rm U/Th}$	flux		0-signal
	[event]	[$\times 10^5$ cm^{-2}s^{-1}]	[TNU]	rejection
U	117^{+41}_{-39}	$14.7^{+5.2}_{-4.8}$	$19.1^{+6.7}_{-6.3}$	3.3σ
Th	58^{+25}_{-24}	$23.9^{+10.2}_{-10.0}$	$9.7^{+4.1}_{-4.1}$	2.4σ
U + Th	174^{+31}_{-29}	$32.1^{+5.8}_{-5.3}$	$28.6^{+5.1}_{-4.8}$	8.5σ

The best fit background model is summarized in Table 8.2. The number of reactor $\overline{\nu}_{\rm e}$ backgrounds is also evaluated from the oscillation analysis. Figure 8.2 shows a contour of the number of reactor $\overline{\nu}_{\rm e}$ events in the geoneutrino energy region ($0.9 \leq E_{\rm p} \leq 2.6$ [MeV]) assuming various set of oscillation parameters, which is overlaid on the confidence level contour of the oscillation parameters from Figure 7.1. For each colored curve in Figure 8.2, the minimum χ^2 value is searched for as shown in Figure 8.3. By interpolating the $\Delta\chi^2$ curve, the number of reactor neutrino backgrounds in the geoneutrino energy region is evaluated to be 608^{+11}_{-13}, which is well consistent to the geoneutrino analysis result (Table 8.2).

Figure 8.4 shows the best fit event rate time variation in 0.9–2.6 MeV. A constant contribution over time, drawn in purple, is interpreted as geoneutrino signal. The geoneutrino contribution clearly appears in the correlation plot (Figure 8.5). The ratio of geoneutrino signal over background for Period1, Period2 and Period3 are 0.10, 0.15 and 0.74, respectively. Thus, the time information is highly advantageous for discriminating the geoneutrino contribution from the reactor $\overline{\nu}_{\rm e}$ and $^{13}{\rm C}(\alpha, {\rm n})^{16}{\rm O}$ backgrounds, which vary with time.

The event energy information is important to discriminate geoneutrino signals, and also to determine the relative contribution of geoneutrino signals from ^{238}U and

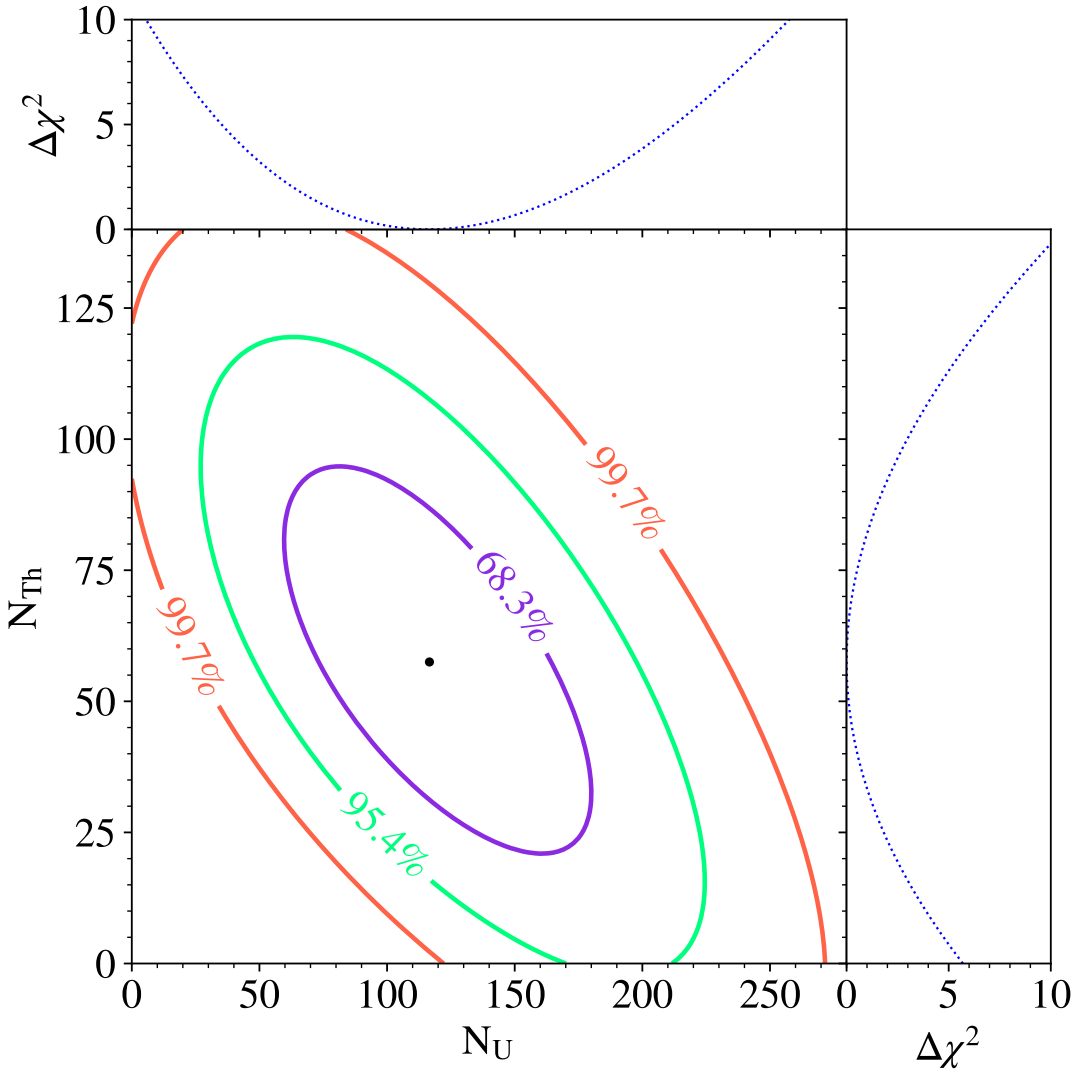

Figure 8.1: Confidence level contour of geoneutrino signals from ^{238}U and ^{232}Th. The top and right panes show projections to each axis.

Table 8.2: The best fit background model in geoneutrino scan

	Period1	Period2	Period3	All Period
energy range [MeV]	0.9–2.6	0.9–2.6	0.9–2.6	0.9–2.6
live time [day]	1485.5	1151.5	2590.0	5227.0
Reactor $\overline{\nu}_e$	325.75	229.64	48.97	604.36
$^{13}C(\alpha, n)^{16}O$	177.66	20.42	22.18	222.26
Accidental	59.35	40.53	24.79	124.67
Spallation (^{8}He/^{9}Li)	1.52	1.05	1.69	4.26
Background total	620.21	334.07	171.98	1126.26
observed	651	363	164	1178

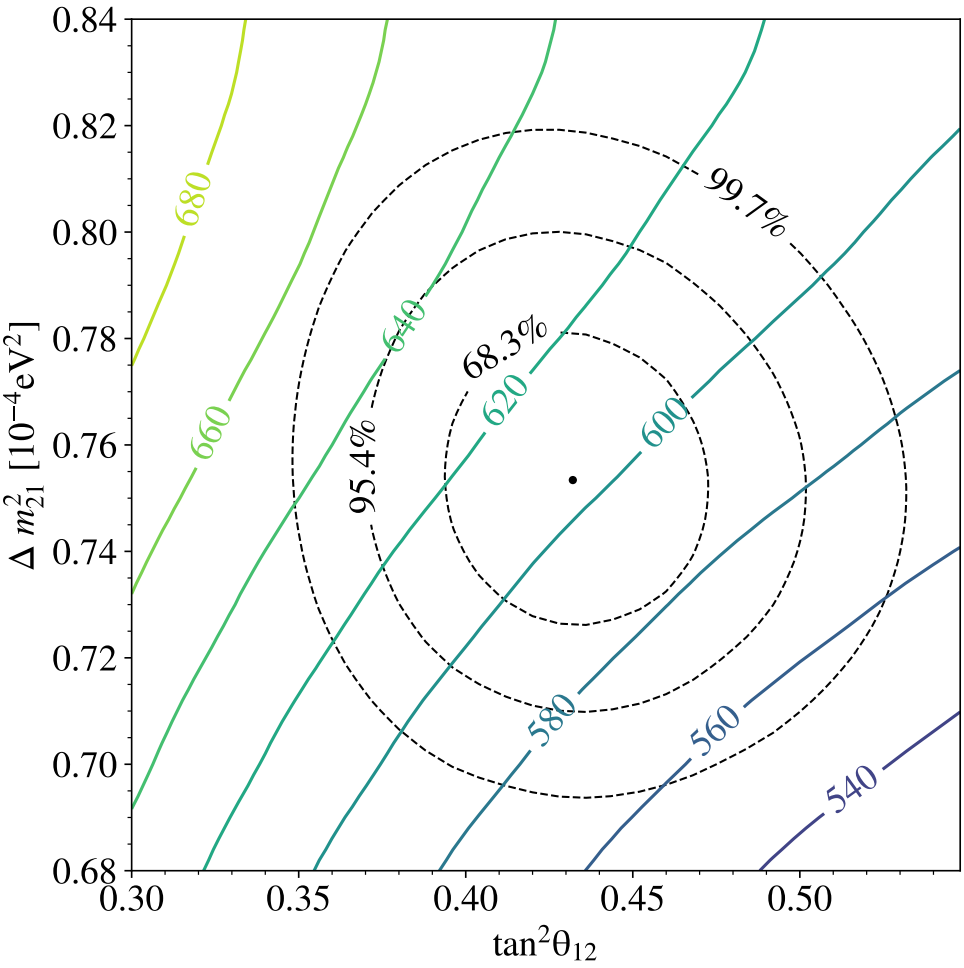

Figure 8.2: Neutrino oscillation parameters and the number of reactor neutrino events in the geoneutrino energy region (colored contour) overlaid on the confidence level contour of the oscillation parameters (dashed black contour)

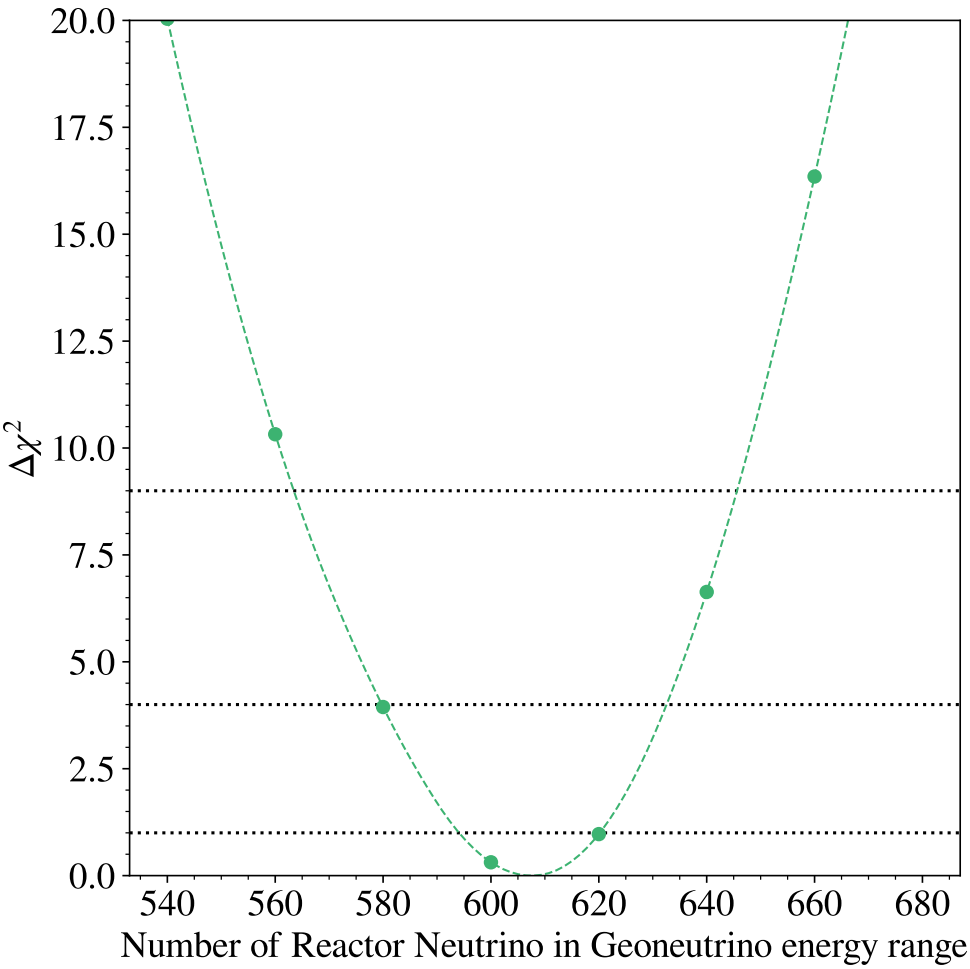

Figure 8.3: Confidence level of the number of reactor neutrino events in the geoneutrino energy region

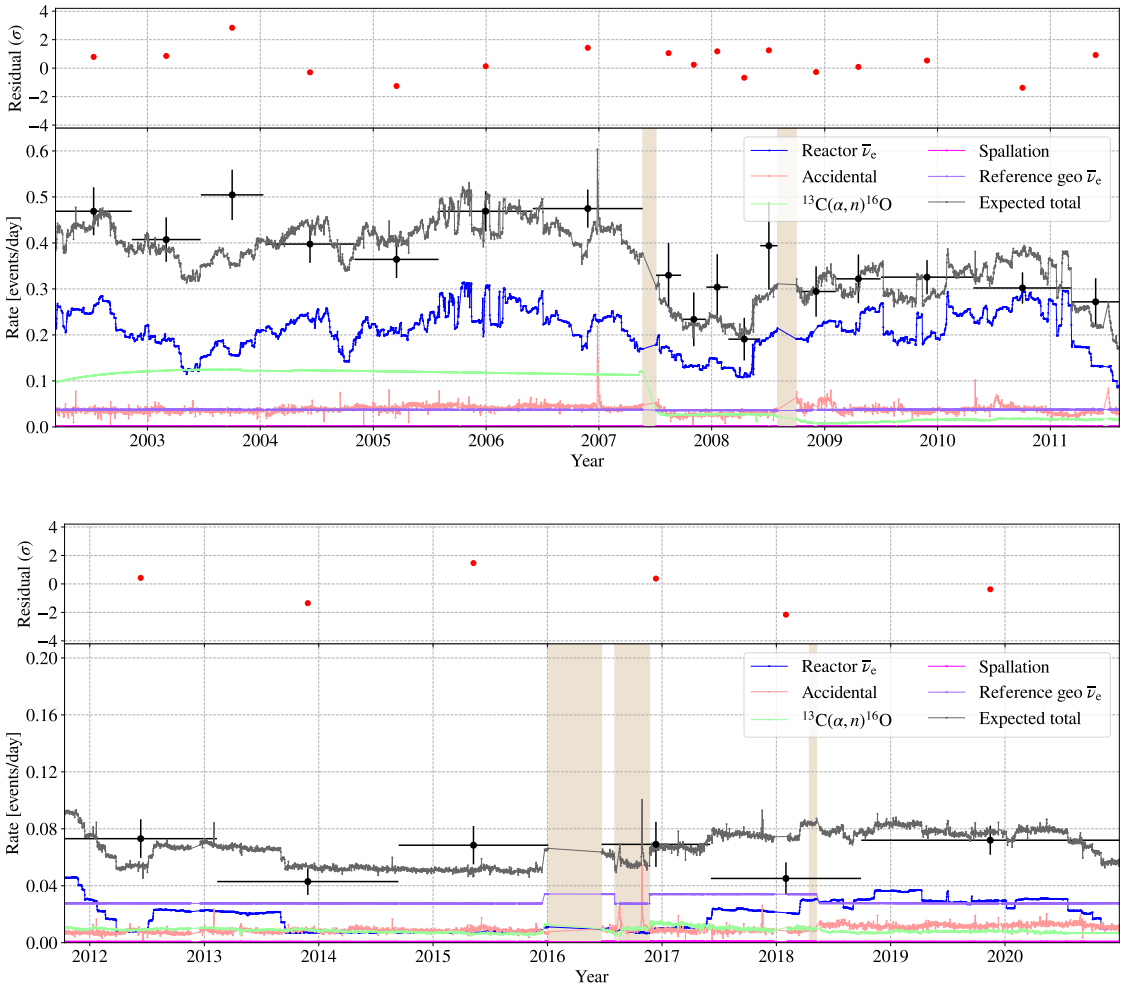

Figure 8.4: Time variation of best fit background rate between 0.9 MeV and 2.6 MeV (top:Period1+Period2, bottom:Period3)

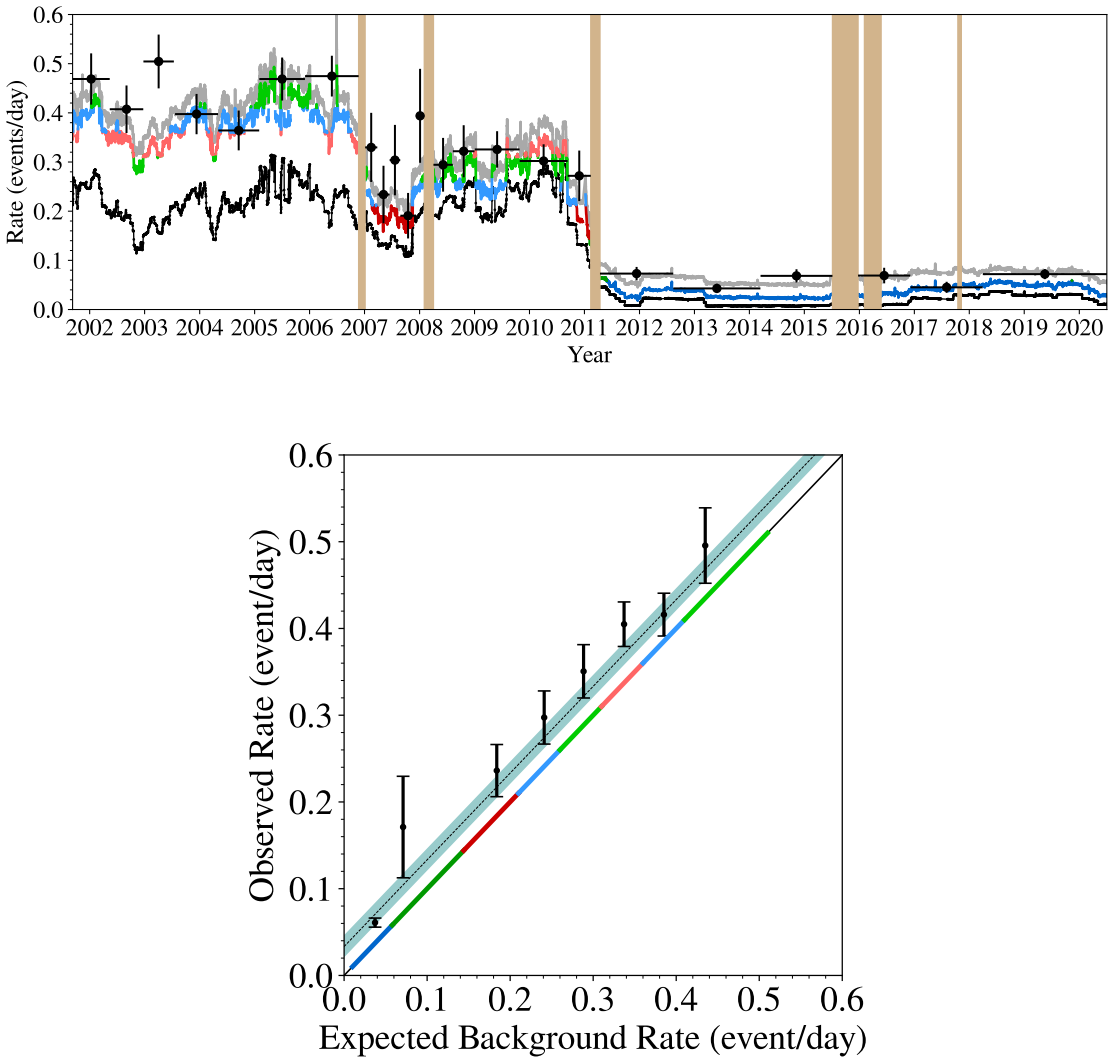

Figure 8.5: Time variation of best fit background rate between 0.9 and 8.5 MeV focusing the reactor $\overline{\nu}_e$, accompanied with the comparison of observed rate versus best fit background rate. In the top figure, the colored segments represent reactor $\overline{\nu}_e$ + other backgrounds, which is binned to different colors as the expected background rate. The data in the bottom figure are integrated within the each colored segments in the top figure. The best fit value of the geoneutrino contribution from the Rate + Shape + Time analysis is shown as black dashed line together with the $\pm 2\sigma$ C.I. (shaded region).

^{232}Th, whose spectral shapes are characterized by the effective end point of 3.272 MeV and 2.254 MeV in the neutrino energy, respectively. The best fit energy spectrum for each period is shown in Figure 8.6. The $^{13}\mathrm{C}(\alpha, \mathrm{n})^{16}\mathrm{O}$ background, which is prominent in Period1 (the top pane), was drastically reduced by the purification campaigns in Period2 (the middle pane). As shown in the bottom pane, the observed spectrum in Period3 shows a clear peak at 1.3 MeV consistent with the geoneutrino signal shape, and also shows the low background rate. Figure 8.7 shows the confidence level contour of $(N_{\mathrm{U}}, N_{\mathrm{Th}})$ for each period. It is clear that Period3 has outstanding statistical power, and this enabled the separate measurement, or spectroscopic measurement, of geoneutrinos originating from uranium and thorium. Figure 8.8 shows the livetime-weighted average of the background-subtracted observed energy spectrum overlaid on the best fit geoneutrino spectrum accompanied with the energy-dependent selection efficiency.

8.4 Radiogenic Heat

The primary motivation of geoneutrino measurement is to understand the radiogenic heat production in the Earth. Our previous study (Gando et al. 2013a) verified a partial radiogenic heat model for Earth, implying the global cooling of our planet. This study improved the accuracy of geoneutrino measurement by a significant reduction of reactor $\overline{\nu}_{\mathrm{e}}$ backgrounds and related uncertainties, which enabled a better constraint on the radiogenic heat amount and even a spectroscopic separation of heat producing elements in earth.

The observed geoneutrino flux is converted to radiogenic heat in a framework of Earth models. The radiogenic heat and geoneutrino from crust is estimated by a geological study (Enomoto et al. 2007). Uranium and thorium are generally assumed to be absent in the core. This is a reasonable assumption because these elements are not soluble in metals. Therefore, the radiogenic heat from mantle is our interest. In the differentiation history of mantle and crust, the highly insoluble elements, including uranium and thorium, are circulated inside earth and concentrated near the surface. The compositional heterogeneity of the mantle depends on the structure of mantle convection, whereas there are various models (Fukao and Obayashi 2013, Rudolph et al. 2015, Ballmer et al. 2017) but it is still a open question. Henceforth in this section, an uniform distribution of the heat producing elements in the mantle is assumed.

The radiogenic heat from the mantle, $Q^{\mathrm{U,Th}}_{\mathrm{mantle}}$, is calculated from the observed geoneutrino flux after subtracting expected geoneutrino flux from the crust and multiplying by an coefficient between flux and radiogenic heat in the mantle. Then, the total radiogenic heat amount from ^{238}U and ^{232}Th, $Q^{\mathrm{U,Th}}$, is obtained by adding expected radiogenic heat from the crust as

$$\begin{aligned} Q^{\mathrm{U,Th}} &= Q^{\mathrm{U,Th}}_{\mathrm{crust}} + Q^{\mathrm{U,Th}}_{\mathrm{mantle}} \\ &= Q^{\mathrm{U,Th}}_{\mathrm{crust}} + (\Phi^{\mathrm{U,Th}} - \Phi^{\mathrm{U,Th}}_{\mathrm{crust}}) \frac{\mathrm{d}Q^{\mathrm{U,Th}}_{\mathrm{mantle}}}{\mathrm{d}\Phi^{\mathrm{U,Th}}_{\mathrm{mantle}}} \end{aligned} \tag{8.7}$$

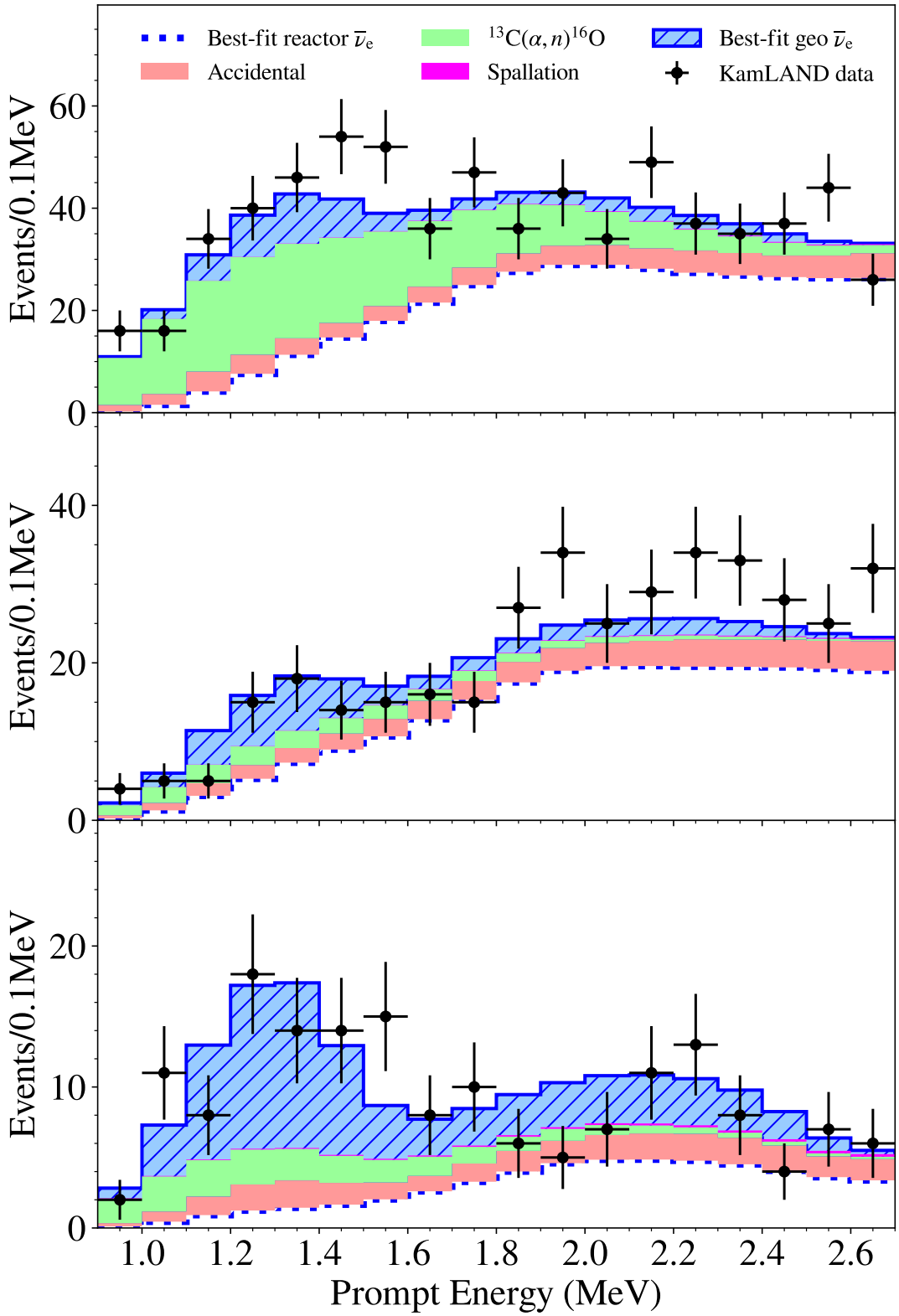

Figure 8.6: Best fit prompt energy spectrum of antineutrino candidates within 0.9–2.6 MeV in each data period (top:Period1, middle:Period2 and bottom:Period3)

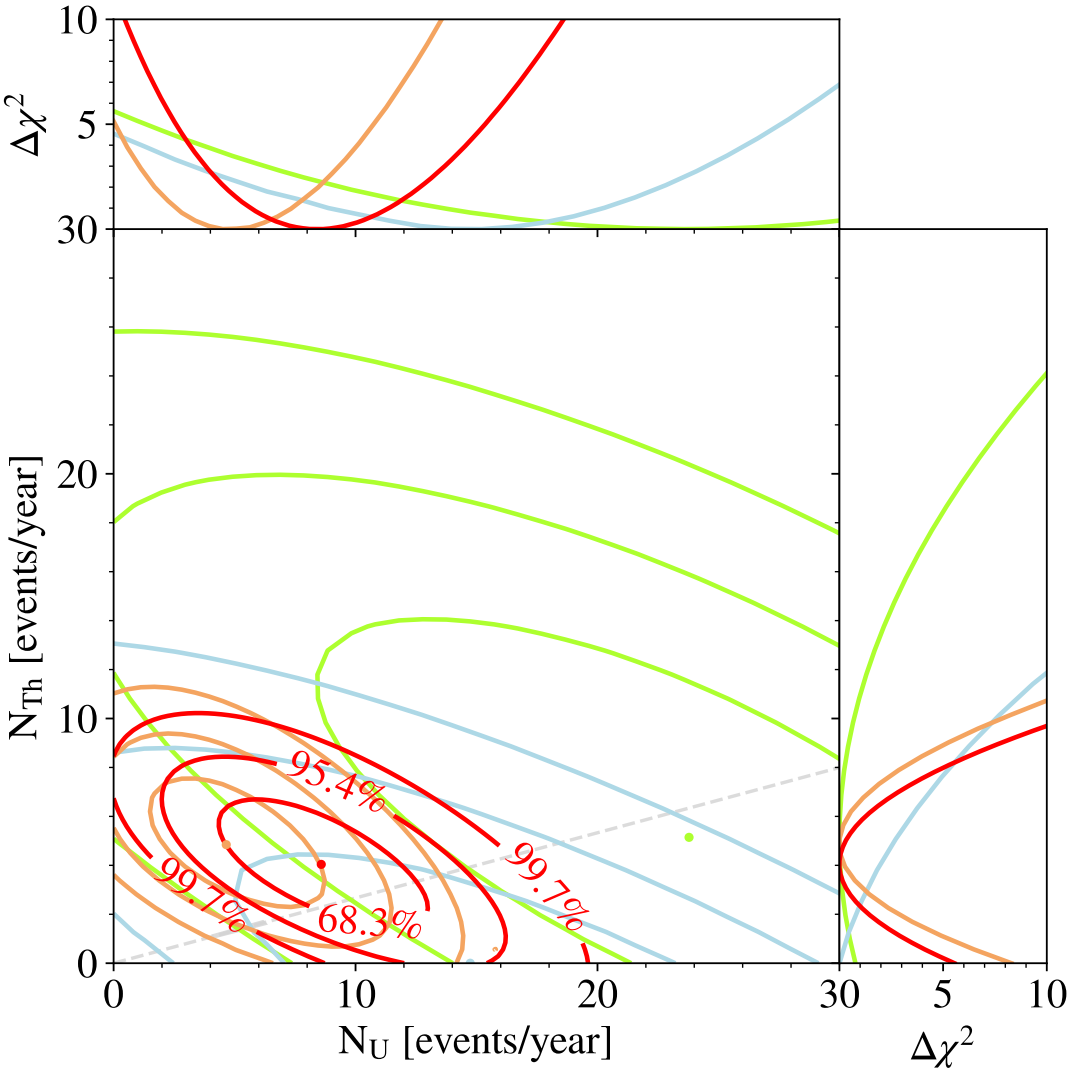

Figure 8.7: Confidence level contours of geoneutrino signals from ^{238}U and ^{232}Th in each period. Green, blue and orange contour correspond to Period1, Period2 and Period3, respectively. Red contour is obtained by the full data set scan. Since the full data set scan benefits from correlations of event rate and systematics across data periods, the red contour is not exactly the same as the summation of the three contours.

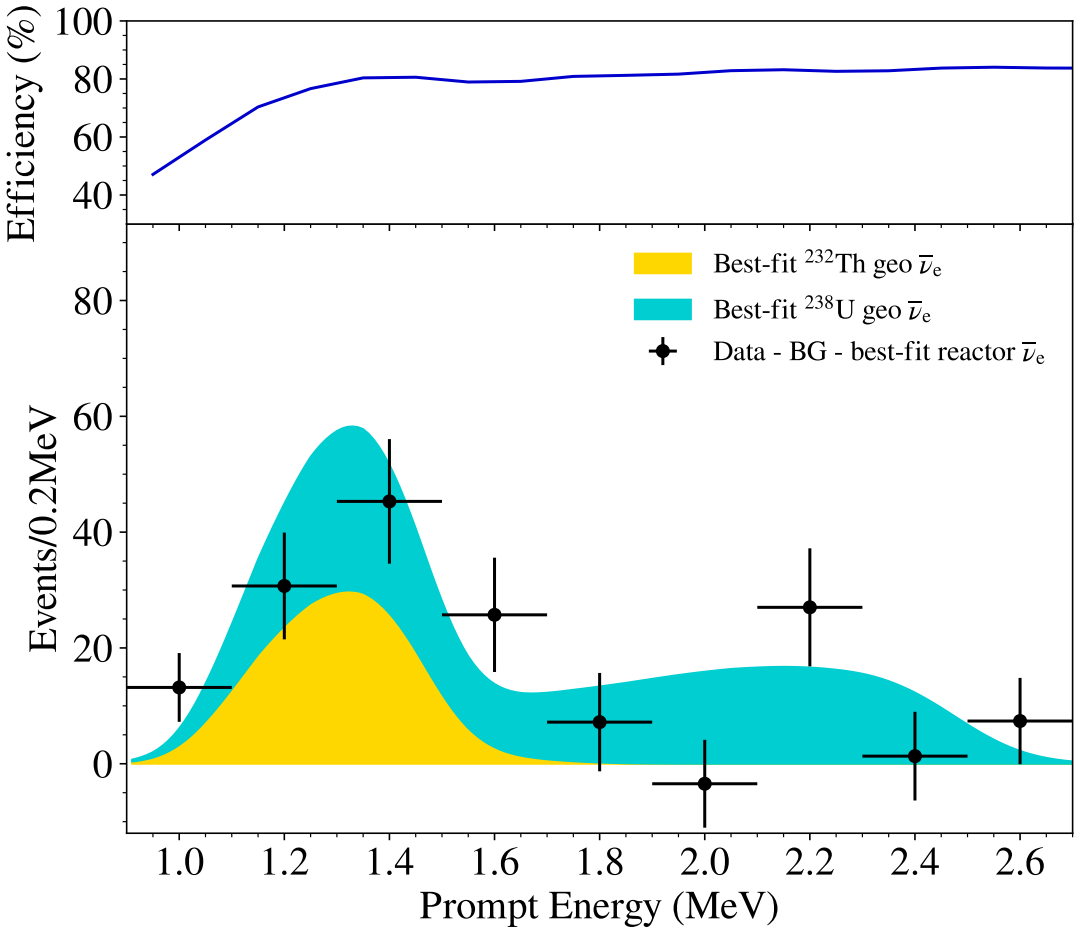

Figure 8.8: Background-subtracted observed energy spectrum and the best fit ^{238}U and ^{232}Th geo $\overline{\nu}_e$. The top pane is the energy-dependent selection efficiency averaged over the whole data set.

where $\Phi^{\mathrm{U,Th}}_{\mathrm{crust}}$ and $Q^{\mathrm{U,Th}}_{\mathrm{crust}}$ are the geoneutrino flux and radiogenic heat estimated in the reference earth model, $\frac{\mathrm{d}Q^{\mathrm{U,Th}}_{\mathrm{mantle}}}{\mathrm{d}\Phi^{\mathrm{U,Th}}_{\mathrm{mantle}}}$ is the conversion coefficient between radiogenic heat and geoneutrino flux from chemically uniform mantle, and $\Phi^{\mathrm{U,Th}}$ represents the measured geoneutrino flux by KamLAND. The crustal estimates are provided from Enomoto et al. (2007) as Table 8.3, after minor corrections of the crustal composition model, which shifted the uranium and thorium concentration in the upper continental crust by -3.6% and -1.9%, respectively, and those for middle continental crust by -19% and $+6.6\%$, respectively (Rudnick and Gao 2014).

Table 8.3: Expected radiogenic heat and geoneutrino flux from Earth model (Enomoto et al. 2007, Rudnick and Gao 2014)

	$Q^{\mathrm{Model}}_{\mathrm{crust}}$ [TW]	$\Phi^{\mathrm{Model}}_{\mathrm{crust}}$ [10^5 cm^{-2}s^{-1}]	$\frac{\mathrm{d}Q_{\mathrm{mantle}}}{\mathrm{d}\Phi_{\mathrm{mantle}}}$ [10^{-5} TW/cm^{-2}s^{-1}]
^{238}U	3.35	17.19	0.73
^{232}Th	3.61	14.51	0.93

The uncertainties of the ^{238}U and ^{232}Th abundances in the upper and middle continental crust are provided by Rudnick and Gao (2014) and in the lower continental crust by Šrámek et al. (2016). Assuming the most conservative full correlation between crustal layers, the total uncertainties are calculated to be 24% and 11% for ^{238}U and ^{232}Th, respectively.

Besides, the ratio of abundances of ^{238}U and ^{232}Th is studied by Wipperfurth et al. (2018) using the time-integrated Pb isotopic ratio in the continental crust to be $3.95^{+0.19}_{-0.13}$ and constrained in the radiogenic heat calculations in this section and mantle model constraint in Sec.8.5.

The best fit value and uncertainties of the total radiogenic heat is determined with a χ^2 defined as

$$\chi^2_{\mathrm{min}}(Q^{\mathrm{U}}, Q^{\mathrm{Th}}) = \min_{Q=Q(\alpha^{\mathrm{U}}_{\mathrm{crust}}, \alpha^{\mathrm{Th}}_{\mathrm{crust}})} \left\{ \chi^2_{\mathrm{KL}}(\Phi^{\mathrm{U}}, \Phi^{\mathrm{Th}}) + \chi^2_{\mathrm{crust}} \right\}$$
$$\chi^2_{\mathrm{crust}} = (\alpha^{\mathrm{U}}_{\mathrm{crust}})^2 + (\alpha^{\mathrm{Th}}_{\mathrm{crust}})^2 + (\alpha^{\mathrm{Th/U}}_{\mathrm{crust}})^2 \tag{8.8}$$

where $\chi^2_{\mathrm{KL}}(\Phi^{\mathrm{U}}, \Phi^{\mathrm{Th}})$ is the χ^2 value for each set of $(\Phi^{\mathrm{U}}, \Phi^{\mathrm{Th}})$ by the KamLAND data, which is drawn in Fig. 8.9, $(\alpha^{\mathrm{U,Th}}_{\mathrm{crust}})^2$ is a penalty term to constraint the abundance of uranium and thorium in the crust given by

$$\alpha^{\mathrm{U}}_{\mathrm{crust}} = \frac{Q^{\mathrm{U}}_{\mathrm{crust}} - Q^{\mathrm{U,Model}}_{\mathrm{crust}}}{Q^{\mathrm{U,Model}}_{\mathrm{crust}} \times (24\%)} = \frac{\Phi^{\mathrm{U}}_{\mathrm{crust}} - \Phi^{\mathrm{U,Model}}_{\mathrm{crust}}}{\Phi^{\mathrm{U,Model}}_{\mathrm{crust}} \times (24\%)} \tag{8.9}$$

$$\alpha^{\mathrm{Th}}_{\mathrm{crust}} = \frac{Q^{\mathrm{Th}}_{\mathrm{crust}} - Q^{\mathrm{Th,Model}}_{\mathrm{crust}}}{Q^{\mathrm{Th,Model}}_{\mathrm{crust}} \times (11\%)} = \frac{\Phi^{\mathrm{Th}}_{\mathrm{crust}} - \Phi^{\mathrm{Th,Model}}_{\mathrm{crust}}}{\Phi^{\mathrm{Th,Model}}_{\mathrm{crust}} \times (11\%)} \tag{8.10}$$

and $(\alpha^{\mathrm{Th/U}}_{\mathrm{crust}})^2$ provides a constraint on the Th/U ratio as

$$\alpha^{\mathrm{Th/U}}_{\mathrm{crust}} = \frac{\alpha^{\mathrm{Th}}_{\mathrm{crust}} - \alpha^{\mathrm{U}}_{\mathrm{crust}}}{\alpha^{\mathrm{U}}_{\mathrm{crust}} \times \left(\frac{4.8\%}{3.5\%}\right)} \tag{8.11}$$

Consequently, the radiogenic heat is calculated to be $Q^{\mathrm{U}} = 3.3^{+3.2}_{-0.8}\,\mathrm{TW}$, $Q^{\mathrm{Th}} = 12.1^{+8.3}_{-8.6}\,\mathrm{TW}$ and $Q^{\mathrm{U}} + Q^{\mathrm{Th}} = 15.4^{+8.3}_{-7.9}\,\mathrm{TW}$, considering the anti-correlation shown in Figure 8.1. If Th/U mass ratio is fixed at 3.9, which is predicted by a geochemical study (McDonough and Sun 1995) based on the analysis of CI carbonaceous chondrites, the estimates are improved to $Q^{\mathrm{U}} = 5.1^{+2.4}_{-2.0}\,\mathrm{TW}$, $Q^{\mathrm{Th}} = 5.9^{+2.7}_{-2.2}\,\mathrm{TW}$ and $Q^{\mathrm{U}} + Q^{\mathrm{Th}} = 10.6^{+5.2}_{-4.2}\,\mathrm{TW}$. The radiogenic heat from ^{40}K and other minor heat producing elements is estimated to be about $\sim 4\,\mathrm{TW}$ by Arevalo et al. (2009). Thus, the Earth's total radiogenic heat is estimated to be $\sim 19.4\,\mathrm{TW}$ with free Th/U ratio and $\sim 14.6\,\mathrm{TW}$ with fixed Th/U ratio.

8.5 Constraint on Earth Composition Models

This section describes constraints on the Earth composition models via geoneutrino spectroscopy by KamLAND. Šrámek et al. (2013) categorized three competing groups of Earth composition models, which lead to different predictions of radiogenic heat abundances, i.e. High-Q, Middle-Q and Low-Q models.

Turcotte and Schubert (2002) advocated the High-Q model based on the assumption that realistic mantle convection is driven by radiogenic heat, which therefore requires a relatively large amount of radiogenic heat, 30–35 TW. The other two groups are based on meteorite composition analysis. The Middle-Q model is proposed by McDonough and Sun (1995) based on the analysis of CI carbonaceous chondrites, terrestrial rock sampling and a consideration on elemental enrichment during the diffusion process of our planet. The radiogenic heat is estimated to be 17–22 TW from the expected abundances of the heat producing elements. On the other hand, Low-Q model is based on the analysis of enstatite chondrites by Javoy et al. (2010), which contains fewer heat producing elements, thus predicting a smaller amount of radiogenic heat, 10–15 TW. Since these two models stand on different reference meteorite, they have different prediction of Th/U mass ratio in the mantle. The Middle-Q model predicts Th/U=3.9, whereas the Low-Q model predicts 2.8.

Not only the abundances of ^{238}U and ^{232}Th in the mantle, their distribution in the mantle is still a open question. This study assumed two hypothesis to test the composition models with geoneutrino spectroscopy, i.e. "homogeneous hypothesis" assuming an uniform distribution of ^{238}U and ^{232}Th in the mantle and "sunken-layer hypothesis" introducing all ^{238}U and ^{232}Th at the boundary of the mantle and the core.

Figure 8.9 shows the $\Delta\chi^2$-profiles for the observed geoneutrino flux from ^{238}U and ^{232}Th (blue contour and point) obtained with KamLAND. The brown ellipse represents the expected geoneutrino flux and its uncertainty from ^{238}U and ^{232}Th in the crust by Enomoto et al. (2007), Rudnick and Gao (2014), Šrámek et al. (2016) with Th/U ratio constraint from Wipperfurth et al. (2018). The Mantle Radiogenic Heat panel shown in red is connected to the center of the crustal ellipse and shows radiogenic heat corresponding to several geoneutrino flux in the homogeneous hypothesis, accompanying red bands indicating the crustal uncertainty. The fully-radiogenic model is an assumption that all the heat flow at earth surface is originated from the

heat producing elements, whose value 36 TW in the Mantle Radiogenic Heat panel is obtained by subtracting the crustal and ^{40}K contribution from the total heat flow at the surface.

On the Mantle Radiogenic Heat panel, Low-Q, Middle-Q and High-Q models are represented by colored bars in blue, green and red, respectively. The length of these model bars correspond to the uncertainties of heat producing element abundances summarized by Šrámek et al. (2013) re-interpreted with the reference crustal model (Enomoto et al. 2007). These models are on the gray dashed lines upward to the right, which imply the expected Th/U mass ratio in the mantle, i.e. Th/U = 3.9 for Middle-Q and High-Q models, and Th/U = 2.8 for Low-Q model. From this figure, it is clear that the KamLAND observation result favor Low-Q or Middle-Q models, and is not consistent with the High-Q nor fully-radiogenic model.

The earth composition models are tested with the KamLAND data on the assumed Th/U mass ratio for each model as shown in Figure 8.10. The upper pane of Figure 8.10 shows the $\Delta\chi^2$-profiles for the geoneutrino flux from ^{238}U and ^{232}Th projected to the gray tilted lines in Figure 8.9 of Th/U = 3.9 (blue line) and 2.8 (blue dashed line). The brown vertical band represents the crustal contribution (Enomoto et al. 2007). The lower pane of Figure 8.10 shows the comparison of the KamLAND data and the models. The Low-Q and Middle-Q models are consistent with the KamLAND data, whereas the High-Q model is incompatible with it.

The tension between the KamLAND data and each BSE composition model is evaluated using χ^2 defined as

$$\chi^2_{\rm min} = \min_{(\alpha^{\rm U}_{\rm crust},\alpha^{\rm Th}_{\rm crust},\alpha_{\rm BSE})} \left\{\chi^2_{\rm KL}(\Phi^{\rm U}_{\rm crust} + \Phi^{\rm Th}_{\rm crust} + \Phi_{\rm mantle}) + \chi^2_{\rm penalty}\right\} \tag{8.12}$$

with

$$\Phi_{\rm mantle} = \left(Q_{\rm BSE} - Q^{\rm U}_{\rm crust} - Q^{\rm Th}_{\rm crust}\right) \frac{{\rm d}\Phi^{\rm U+Th}_{\rm mantle}}{{\rm d}Q^{\rm U+Th}_{\rm mantle}} \tag{8.13}$$

$$\chi^2_{\rm penalty} = (\alpha^{\rm U}_{\rm crust})^2 + (\alpha^{\rm Th}_{\rm crust})^2 + (\alpha^{\rm Th/U}_{\rm crust})^2 + (\alpha_{\rm BSE})^2 \tag{8.14}$$

where $\Phi^{\rm U,Th}_{\rm crust}$, $Q^{\rm U,Th}_{\rm crust}$, $\frac{{\rm d}\Phi^{\rm U+Th}_{\rm mantle}}{{\rm d}Q^{\rm U+Th}_{\rm mantle}}$, $(\alpha^{\rm U,Th}_{\rm crust})^2$, and $(\alpha^{\rm Th/U}_{\rm crust})^2$ are defined in Sec. 8.4. $\chi^2_{\rm KL}(\Phi)$ represents the $\Delta\chi^2$ profiles of geoneutrino flux projected on the assumed Th/U ratio in each Earth model as shown in the upper pane of Fig. 8.10. $Q_{\rm BSE}$ is the radiogenic heat from ^{238}U and ^{232}Th in the crust and mantle, which is constrained by the penalty term $(\alpha_{\rm BSE})^2$ defined for High-Q model as

$$\alpha_{\rm BSE} = \frac{Q_{\rm BSE} - Q^{\rm Model}_{\rm BSE}}{Q^{\rm Model}_{\rm BSE} \times (10\%)} \qquad Q^{\rm Model}_{\rm BSE} = 28.2 \text{ TW} \tag{8.15}$$

Assuming Gaussian error for the crustal contribution and the High-Q model's prediction of the heat producing element abundances on the gray tilted line of Th/U = 3.9, this model is disfavored at 99.76% confidence level with the homogeneous hypothesis, and 97.9% with the sunken-layer hypothesis. This incompatibility indicates that the conventional mantle convection models, e.g. Korenaga (2006), need to be

modified. That is, the elastic properties of the Earth extracted by seismology or the geodynamical modeling of mantle 1-layer convection, which are basis of High-Q model, need to be revised. On the other hand, the KamLAND data is consistent with Low-Q and Middle-Q model, suggesting multi-layer mantle convection as assumed in these models.

In discussing such thermal evolution models, the fraction of radiogenic heat to the global heat production, or "Uray ratio", is an important parameter. As for the mantle, Korenaga (2008) proposed "convective Urey ratio" to refer the Uray ratio of the mantle. Assuming additional radiogenic heat of 3 TW from ^{40}K and ^{235}U in the mantle (Arevalo et al. 2009, Enomoto 2006), the convective Uray ratio measured with KamLAND is $0.13^{+0.15}_{-0.06}$ with the homogeneous hypothesis.

By the same strategy, the fully-radiogenic model is disfavored at 5.2σ with the homogeneous hypothesis, and 4σ with the sunken-layer hypothesis. This result strengthens the indication that the Earth's primordial heat still remains and is responsible for some of the Earth's heat budget.

8.6 Future Prospects

This study observed neutrinos originating from uranium and thorium with the world's highest precision, rejecting the High-Q model and suggesting mantle multi-layer convection. However, with the current observational precision, it is not possible to distinguish between the Low-Q model and the Middle-Q model, and identify Earth's primordial material. Given the presence of various types of meteorites and meteoric iron on Earth today, it is reasonable to assume that the true solution for the Earth's primordial material lies between Low-Q and Middle-Q models. In order to identify the Earth's primordial material by geoneutrino observation, the precision of geoneutrino flux measurement needs to be improved at least by factor, and preferably by orders of magnitude. This requires a further increase in exposure and a further reduction of systematic uncertainties.

Even if the precision of geoneutrino flux measurement be improved by orders of magnitude, it alone would not allow to distinguish between the Low-Q and Middle-Q models. The measurement accuracy of the mantle geoneutrino is limited by the uncertainties of the crustal estimation since the mantle contribution is determined by subtracting the crustal estimation from the measured total geoneutrino flux. Therefore, to improve the measurement accuracy of the mantle contribution, the model-induced uncertainties of the crustal contribution must be reduced. One possible solution is to improve crustal models. Descriptions of near-filed geology might be a key for suppressing the uncertainties. Though various approaches exist, e.g. stochastic modeling method of 3-D compositional distribution (Takeuchi et al. 2019), further development is needed to evaluate and reduce the crustal uncertainties. Another solution is to construct geoneutrino detectors on the ocean floor. Because the oceanic crust is thinner and simpler in composition than the continental crust, a seafloor detector could efficiently reduce the crustal contribution and its uncertainties. However, there are still many technical issues that need to be addressed for construction and operation.

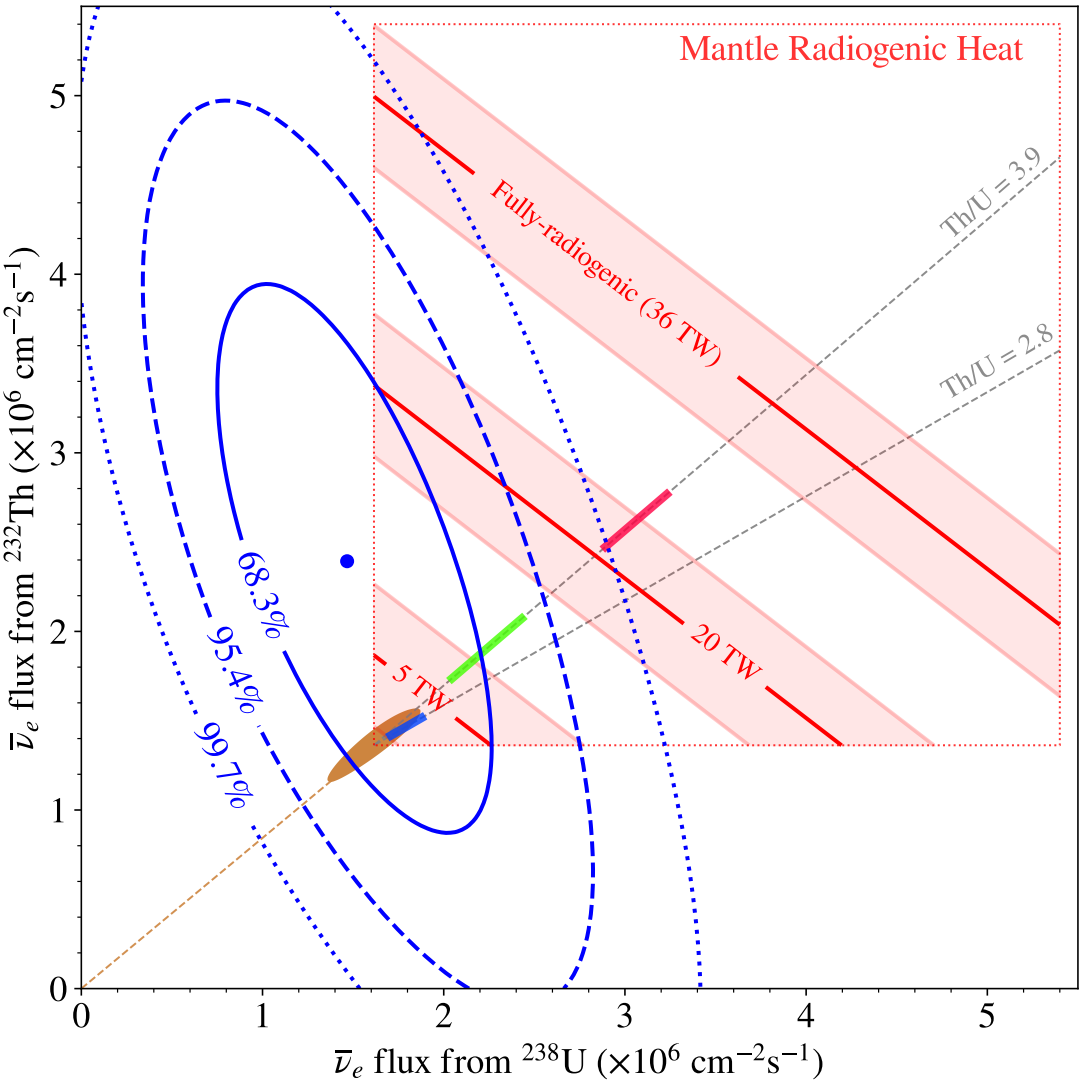

Figure 8.9: Confidence level contour and best fit point of observed geoneutrino flux from ^{238}U and ^{232}Th in the Mantle. Crustal contribution and its uncertainties in the model are described as brown ellipse. The Mantle Radiogenic Heat panel is connected to the crustal ellipse, showing the corresponding radiogenic heat from ^{238}U and ^{232}Th in the Mantle. The red band width implies the conversion uncertainties coming from the crustal uncertainties. The radiogenic heat predictions by some Earth composition models are plotted on the Mantle Radiogenic Heat panel with colored bars. The blue and green bars are Low-Q and Middle-Q models, which are based on compositions of different types of chondrites. The red bar is the High-Q model based on seismology and geodynamical modeling of the mantle convection.

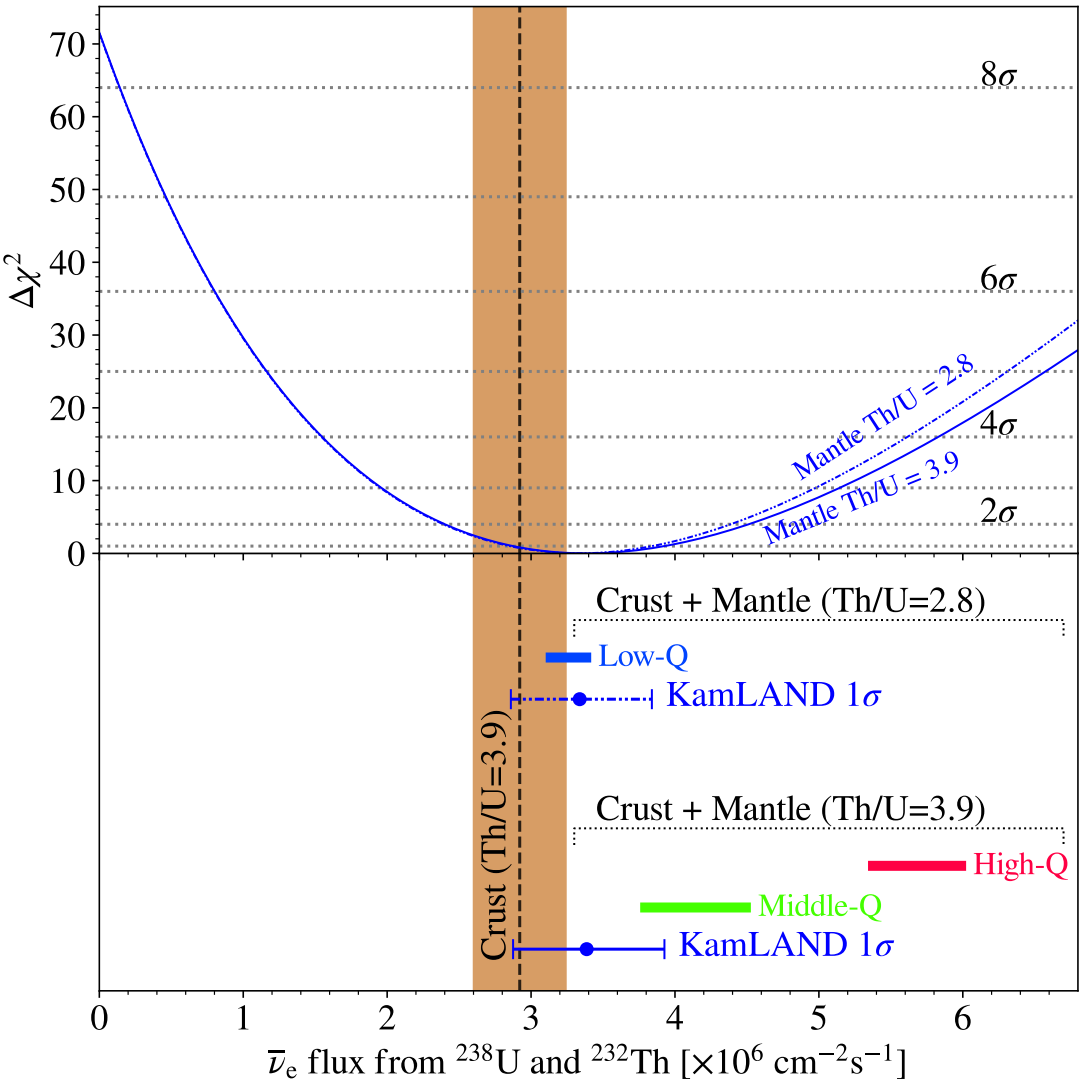

Figure 8.10: Confidence level of observed geoneutrino flux with mantle models. The upper pane shows the $\Delta\chi^2$-profile for the observed geoneutrino flux from ^{238}U and ^{232}Th projected to the brown and gray tilted lines in Fig.8.9 of Mantle Th/U=3.9 for Middle-Q and High-Q models (blue line) and Th/U=2.8 for Low-Q model (blue dash-doted line) starting projection from the center of the crustal contribution. The brown vertical band represents the prediction from the crustal model (Enomoto et al. 2007). The lower pane shows the comparison of the KamLAND data and different mantle models.

Finally, geoneutrino spectroscopy including ^{40}K will provide a very important missing piece of neutrino geoscience. Due to the relatively small Q-value of ^{40}K β-decay, potassium geoneutrinos can not be observed via the inverse-beta decay channel used for ^{238}U and ^{232}Th in this study. Besides, not only its energy, but also the incident direction of potassium geoneutrino is necessary to suppress serious backgrounds from solar neutrinos. However, since ^{40}K can exist in the Earth's core, ^{40}K geoneutrino measurement would allow to test the core's heat budget.

Chapter 9

Conclusions

In this dissertation, the analysis of geoneutrino was performed using KamLAND with a total live time of 5527 days, including 2590 days of low-reactor period.

The low-reactor period significantly reduced the reactor neutrino backgrounds, which is one of the dominant background souce for geoneutrino observation. Besides, lower reactor neutrino flux also contributed to suppressing the accidental coincidence backgrounds by allowing to tighten the likelihood selection criteria with keeping a high signal-to-noise ratio. This enabled us to perform geoneutrino spectroscopy, separating the contribution of geoneutrinos from uranium and thorium. Thus, this study probes the abundances of these major heat producing elements in the Earth.

In the low reactor period, the contribution of global reactors is relatively large. In particular, the contribution of Chinese reactors, which have been increasing rapidly in recent years, could not be ignored. Therefore, based on publicly available data from the IAEA, the monthly power outputs of all the world's nuclear reactors were examined to estimate the reactor neutrino flux reaching KamLAND. The contribution of neutrinos from Taiwanese and Chinese reactors to the total expected reactor neutrino flux in period1, period2, and period3 was estimated to be 0.71%, 1.01%, and 10.45%, respectively. The contributions from outside Japan, Korea, Taiwan and China were similarly estimated to be 0.42%, 0.51%, and 3.51% of the total expected reactor neutrino flux, respectively. Besides, this study employed the reactor neutrino spectra observed by a short-baseline experiment so that latent uncertainties related to the reactor neutrino anomaly were suppressed.

The Rate + Shape + Time analysis is performed within a energy range of 0.9–8.5 MeV for a simultaneous scan of oscillation parameters and geoneutrino signals. The best fit geoneutrino signals are 117^{+41}_{-39}, 58^{+25}_{-24} and 174^{+31}_{-29} from ^{238}U, ^{232}Th and ^{238}U+^{232}Th, respectively. The null-signal hypothesis is disfavored at 8.3σ confidence level. These correspond to geoneutrino flux of $14.7^{+5.2}_{-4.8}$, $23.9^{+10.2}_{-10.0}$ and $32.1^{+5.8}_{-5.3}$ $\times 10^5$ cm^{-2}s^{-1}, respectively. Assuming Th/U mass ratio in the BSE composition at 3.9 recommended by compositional analysis of chondrites McDonough and Sun (1995) and employing our reference earth model Enomoto et al. (2007), the radiogenic heat from ^{238}U and ^{232}Th in the earth is estimated to be $10.6^{+5.2}_{-4.2}$ TW.

The earth compositional models were tested with the KamLAND result via radiogenic heat. The KamLAND data is consistent with Low-Q and Middle-Q models

based on chondrites compositional analysis, whereas the High-Q model is disfavored at 99.76% confidence level with assuming the homogeneous uranium and thorium distribution in the mantle, and at 97.9% with assuming the accumulated heat producing elements at the core-mantle boundary. The incompatibility with the High-Q model indicates that the conventional mantle convection model, which the High-Q model stands on, need to be modified, and implies the multi-layer mantle convection.

The KamLAND result disfavors the fully-radiogenic model at 5.2σ with the homogeneous hypothesis and 4σ with the sunken-layer hypothesis. The indication that the Earth's primordial heat still remains and is responsible for some of the Earth's heat budget was strengthened by the geoneutrino spectroscopy with KamLAND.

References

J. N. Abdurashitov et al. Measurement of the solar neutrino capture rate with gallium metal. III. results for the 2002–2007 data-taking period. *Phys. Rev. C*, 80(1):015807, Jul 2009. doi: 10.1103/PhysRevC.80.015807. URL https://link.aps.org/doi/10.1103/PhysRevC.80.015807.

K. Abe et al. Indication of electron neutrino appearance from an accelerator-produced off-axis muon neutrino beam. *Phys. Rev. Lett.*, 107:041801, Jul 2011a. doi: 10.1103/PhysRevLett.107.041801. URL https://link.aps.org/doi/10.1103/PhysRevLett.107.041801.

S. Abe et al. Production of radioactive isotopes through cosmic muon spallation in KamLAND. *Phys. Rev. C*, 81(2):025807, Feb 2010. doi: 10.1103/PhysRevC.81.025807.

S. Abe et al. Measurement of the ^{8}B solar neutrino flux with the KamLAND liquid scintillator detector. *Phys. Rev. C*, 84:035804, Sep 2011b. doi: 10.1103/PhysRevC.84.035804. URL https://link.aps.org/doi/10.1103/PhysRevC.84.035804.

S. Abe et al. Search for solar flare neutrinos with the KamLAND detector. *The Astrophysical Journal*, 924(2):103, Jan 2022. doi: 10.3847/1538-4357/ac35d1. URL https://doi.org/10.3847/1538-4357/ac35d1.

Y. Abe et al. Reactor $\overline{\nu_e}$ disappearance in the Double Chooz experiment. *Phys. Rev. D*, 86(5):052008, Sep 2012. URL http://link.aps.org/doi/10.1103/PhysRevD.86.052008.

P. Adamson et al. Improved Search for Muon-Neutrino to Electron-Neutrino Oscillations in MINOS. *Phys. Rev. Lett.*, 107(18):181802, Oct 2011. URL http://link.aps.org/doi/10.1103/PhysRevLett.107.181802.

D. Adey et al. Extraction of the ^{235}U and ^{239}Pu Antineutrino Spectra at Daya Bay. *Phys. Rev. Lett.*, 123:111801, Sep 2019. doi: 10.1103/PhysRevLett.123.111801. URL https://link.aps.org/doi/10.1103/PhysRevLett.123.111801.

S. Agostinelli et al. Geant4—a simulation toolkit. *Nuclear Instruments and Methods in Physics Research Section A: Accelerators, Spectrometers, Detectors and Associated Equipment*, 506(3):250–303, 2003. ISSN 0168-9002. doi: https://doi.org/10.1016/S0168-9002(03)01368-8. URL https://www.sciencedirect.com/science/article/pii/S0168900203013688.

B. Aharmim et al. Combined analysis of all three phases of solar neutrino data from the Sudbury Neutrino Observatory. *Phys. Rev. C*, 88:025501, Aug 2013. doi: 10.1103/PhysRevC.88.025501. URL https://link.aps.org/doi/10.1103/PhysRevC.88.025501.

J. K. Ahn et al. Observation of reactor electron antineutrinos disappearance in the RENO experiment. *Phys. Rev. Lett.*, 108:191802, May 2012. doi: 10.1103/PhysRevLett.108.191802. URL https://link.aps.org/doi/10.1103/PhysRevLett.108.191802.

F. P. An et al. Improved measurement of electron antineutrino disappearance at Daya Bay. *Chin. Phys. C*, 37(1), 2013. URL http://stacks.iop.org/1674-1137/37/i=1/a=011001.

F. P. An et al. Improved measurement of the reactor antineutrino flux and spectrum at Daya Bay. *Chin. Phys. C*, 41(1):013002, 2017. URL http://stacks.iop.org/1674-1137/41/i=1/a=013002.

P. Antonioli et al. A three-dimensional code for muon propagation through the rock: MUSIC. *Astroparticle Physics*, 7(4):357–368, 1997. ISSN 0927-6505. doi: https://doi.org/10.1016/S0927-6505(97)00035-2. URL https://www.sciencedirect.com/science/article/pii/S0927650597000352.

R. Arevalo, W. F. McDonough, and M. Luong. The K/U ratio of the silicate Earth: Insights into mantle composition, structure and thermal evolution. *Earth and Planetary Science Letters*, 278(3):361–369, 2009. ISSN 0012-821X. doi: https://doi.org/10.1016/j.epsl.2008.12.023. URL https://www.sciencedirect.com/science/article/pii/S0012821X08007711.

M. D. Ballmer et al. Persistence of strong silica-enriched domains in the earth's lower mantle. *Nature Geosci.*, 10:236–240, 2017. doi: doi.org/10.1038/ngeo2898. URL https://doi.org/10.1038/ngeo2898.

C. Bassin et al. The current limits of resolution for surface wave tomography in North America. *EOS Trans. AGU*, 81:F897, 2000. URL https://cir.nii.ac.jp/crid/1570291225039225344.

G. Bellini et al. Precision measurement of the ^{7}Be solar neutrino interaction rate in Borexino. *Phys. Rev. Lett.*, 107(14):141302, Sep 2011. URL http://link.aps.org/doi/10.1103/PhysRevLett.107.141302.

B. E. Berger et al. The KamLAND full-volume calibration system. *J. Instrum.*, 4 (04):P04017, 2009.

U. C. Bergmann et al. New information on β-delayed neutron emission from ^{12,14}Be. *Nuclear Physics A*, 658(2):129–145, 1999. ISSN 0375-9474. doi: https://doi.org/10.1016/S0375-9474(99)00348-6. URL https://www.sciencedirect.com/science/article/pii/S0375947499003486.

Encyclopedia Britannica. Primary Wave. https://www.britannica.com/science/primary-wave.

A. L. Bull, A. K. McNamara, and J. Ritsema. Synthetic tomography of plume clusters and thermochemical piles. *Earth and Planetary Science Letters*, 278(3):152–162, 2009. ISSN 0012-821X. doi: https://doi.org/10.1016/j.epsl.2008.11.018. URL https://www.sciencedirect.com/science/article/pii/S0012821X08007309.

D. Casper. The nuance neutrino physics simulation, and the future. *Nuclear Physics B - Proceedings Supplements*, 112(1):161–170, 2002. ISSN 0920-5632. doi: https://doi.org/10.1016/S0920-5632(02)01756-5. URL https://www.sciencedirect.com/science/article/pii/S0920563202017565.

B. T. Cleveland et al. Measurement of the Solar Electron Neutrino Flux with the Homestake Chlorine Detector. *Astrophys. J.*, 496:505–526, 1998.

K. C. Condie. Chemical composition and evolution of the upper continental crust: Contrasting results from surface samples and shales. *Chemical Geology*, 104(1):1–37, 1993. ISSN 0009-2541. doi: https://doi.org/10.1016/0009-2541(93)90140-E. URL https://www.sciencedirect.com/science/article/pii/000925419390140E.

C. L. Cowan, F. Reines, F. B. Harrison, H. W. Kruse, and A. D. McGuire. Detection of the Free Neutrino: a Confirmation. *Science*, 124(3212):103–104, 1956. doi: 10.1126/science.124.3212.103. URL https://www.science.org/doi/abs/10.1126/science.124.3212.103.

G. F. Davies. Review of oceanic and global heat flow estimates. *Reviews of Geophysics*, 18(3):718–722, 1980. doi: https://doi.org/10.1029/RG018i003p00718. URL https://agupubs.onlinelibrary.wiley.com/doi/abs/10.1029/RG018i003p00718.

J. H. Davies and D. R. Davies. Earth's surface heat flux. *Solid Earth*, 1(1):5–24, Feb 2010. URL http://www.solid-earth.net/1/5/2010/.

Y. Declais et al. Study of reactor antineutrino interaction with proton at Bugey nuclear power plant. *Phys. Lett. B*, 338(2–3):383–389, Oct 1994. URL http://www.sciencedirect.com/science/article/pii/0370269394913943.

A. M. Dziewonski and D. L. Anderson. Preliminary reference Earth model. *Physics of the Earth and Planetary Interiors*, 25(4):297–356, 1981. ISSN 0031-9201. doi: https://doi.org/10.1016/0031-9201(81)90046-7. URL https://www.sciencedirect.com/science/article/pii/0031920181900467.

S. Enomoto. *Neutrino Geophysics and Observation of Geo-neutrinos at KamLAND*. PhD thesis, Tohoku University, 2005.

S. Enomoto. Experimental study of geoneutrinos with KamLAND. *Earth, Moon, and Planets*, 99(1):131–146, 2006. doi: 10.1007/s11038-006-9120-8.

S. Enomoto, E. Ohtani, K. Inoue, and A. Suzuki. Neutrino geophysics with KamLAND and future prospects. *Earth and Planet. Sci. Lett.*, 258:147–159, 6 2007.

Mitsubishi Nuclear Fuel. Products. https://www.mhi.com/group/mnf/products.

F. Fukao and M. Obayashi. Subducted slabs stagnant above, penetrating through, and trapped below the 660 km discontinuity. *J. Geophys. Res.*, 118:5920–5938, 2013. doi: doi.org/10.1016/j.pepi.2021.106815. URL https://doi.org/10.1016/j.pepi.2021.106815.

M. Fukugita and T. Yanagida. Barygenesis without grand unification. *Physics Letters B*, 174(1):45–47, 1986. ISSN 0370-2693. doi: https://doi.org/10.1016/0370-2693(86)91126-3. URL https://www.sciencedirect.com/science/article/pii/0370269386911263.

A. Gando et al. Reactor on-off antineutrino measurement with KamLAND. *Phys. Rev. D*, 88(3):033001, 08 2013a. URL http://link.aps.org/doi/10.1103/PhysRevD.88.033001.

A. Gando et al. Limit on Neutrinoless $\beta\beta$ Decay of ^{136}Xe from the First Phase of KamLAND-Zen and Comparison with the Positive Claim in ^{76}Ge. *Phys. Rev. Lett.*, 110:062502, Feb 2013b. doi: 10.1103/PhysRevLett.110.062502. URL https://link.aps.org/doi/10.1103/PhysRevLett.110.062502.

A. Gando et al. ^{7}Be solar neutrino measurement with KamLAND. *Phys. Rev. C*, 92:055808, Nov 2015. doi: 10.1103/PhysRevC.92.055808. URL https://link.aps.org/doi/10.1103/PhysRevC.92.055808.

A. Gando et al. Search for majorana neutrinos near the inverted mass hierarchy region with KamLAND-Zen. *Phys. Rev. Lett.*, 117(8):082503, 08 2016. URL https://link.aps.org/doi/10.1103/PhysRevLett.117.082503.

A. Gando et al. The nylon balloon for xenon loaded liquid scintillator in KamLAND-Zen 800 neutrinoless double-beta decay search experiment. *JInst*, 16(08):P08023, Aug 2021. doi: 10.1088/1748-0221/16/08/p08023. URL https://doi.org/10.1088/1748-0221/16/08/p08023.

S. J. Garrett. Chapter 13 - introductory numerical methods. In S. J. Garrett, editor, *Introduction to Actuarial and Financial Mathematical Methods*, pages 411–463. Academic Press, San Diego, 2015. ISBN 978-0-12-800156-1. doi: https://doi.org/10.1016/B978-0-12-800156-1.00013-3. URL https://www.sciencedirect.com/science/article/pii/B9780128001561000133.

M. Goldhaber, L. Grodzins, and A. W. Sunyar. Helicity of neutrinos. *Phys. Rev.*, 109:1015–1017, Feb 1958. doi: 10.1103/PhysRev.109.1015. URL https://link.aps.org/doi/10.1103/PhysRev.109.1015.

M. C. Gonzalez-Garcia, Michele Maltoni, Jordi Salvado, and Thomas Schwetz. Global fit to three neutrino mixing: critical look at present precision. *Journal of High Energy Physics*, 2012(12):123, Dec 2012. ISSN 1029-8479. doi: 10.1007/JHEP12(2012)123. URL https://doi.org/10.1007/JHEP12(2012)123.

S. Goswami and A. Y. Smirnov. Solar neutrinos and 1-3 leptonic mixing. *Phys. Rev. D*, 72:053011, Sep 2005. doi: 10.1103/PhysRevD.72.053011. URL https://link.aps.org/doi/10.1103/PhysRevD.72.053011.

T. Hagner et al. Muon-induced production of radioactive isotopes in scintillation detectors. *Astroparticle Physics*, 14(1):33–47, 2000. ISSN 0927-6505. doi: https://doi.org/10.1016/S0927-6505(00)00103-1. URL https://www.sciencedirect.com/science/article/pii/S0927650500001031.

A. A. Hahn et al. Antineutrino spectra from ^{241}Pu and ^{239}Pu thermal neutron fission products. *Phys. Lett. B*, 218(3):365–368, 2 1989.

S. R. Hart and A. Zindler. In search of a bulk-Earth composition. *Chemical Geology*, 57(3):247–267, 1986. ISSN 0009-2541. doi: https://doi.org/10.1016/0009-2541(86)90053-7. URL https://www.sciencedirect.com/science/article/pii/0009254186900537.

A. W. Hofmann. Chemical differentiation of the Earth: the relationship between mantle, continental crust, and oceanic crust. *Earth and Planetary Science Letters*, 90(3):297–314, 1988. ISSN 0012-821X. doi: https://doi.org/10.1016/0012-821X(88)90132-X. URL https://www.sciencedirect.com/science/article/pii/0012821X8890132X.

A. W. Hofmann. Just add water. *Nature*, 425(6953):24–25, Sep 2003. ISSN 1476-4687. doi: 10.1038/425024a. URL https://doi.org/10.1038/425024a.

A. M. Hofmeister and R. E. Criss. Earth's heat flux revised and linked to chemistry. *Tectonophysics*, 395(3-4):159–177, 1 2005.

M. Honda et al. Comparison of 3-dimensional and 1-dimensional schemes in the calculation of atmospheric neutrinos. *Phys. Rev. D*, 64:053011, Aug 2001. doi: 10.1103/PhysRevD.64.053011. URL https://link.aps.org/doi/10.1103/PhysRevD.64.053011.

J. Hosaka et al. Solar neutrino measurements in Super-Kamiokande-I. *Phys. Rev. D*, 73(11):112001, 06 2006.

P. Huber. Determination of antineutrino spectra from nuclear reactors. *Phys. Rev. C*, 84(2):024617, 08 2011. URL http://link.aps.org/doi/10.1103/PhysRevC.84.024617.

IAEA. Official Website of IAEA, International Atomic Energy Agency, Operating Experience with Nuclear Power Stations in Member States. https://www.iaea.org, 2021.

K. Ichimura. *Precise measurement of neutrino oscillation parameters with KamLAND*. PhD thesis, Tohoku University, 2008.

C. Jaupart et al. *Treatise on Geophysics: Temperatures, Heat and Energy in the Mantle of the Earth Vol. 7*, pages 253–303. Elsevier, Amsterdam, 2007. ISBN 978-0-44-452748-6.

M. Javoy. Chemical earth models. *Comptes Rendus de l'Académie des Sciences - Series IIA - Earth and Planetary Science*, 329(8):537–555, 1999. ISSN 1251-8050. doi: https://doi.org/10.1016/S1251-8050(00)87210-9. URL https://www.sciencedirect.com/science/article/pii/S1251805000872109.

M. Javoy et al. The chemical composition of the Earth: Enstatite chondrite models. *Earth and Planet. Sci. Lett.*, 293(3–4):259–268, May 2010. URL http://www.sciencedirect.com/science/article/pii/S0012821X10001445.

JENDLE. the Japanese Evaluated Nuclear Data Library available at http://wwwndc.jaea.go.jp/jendl/jendl.html, 2005.

N. Kawada. KamLAND-Zen 実験における低ゲイン PMT への信号増幅器導入によるエネルギー分解能向上. Master's thesis, Tohoku University, 2020.

G. W. Kerr, J. M. Morris, and J. R. Risser. Energy levels of ^{17}O from ^{13}C(α,α_0)^{13}C and ^{13}C(α,n)^{16}O. *Nuclear Physics A*, 110(3):637–656, 1968. ISSN 0375-9474. doi: https://doi.org/10.1016/0375-9474(68)90378-3. URL https://www.sciencedirect.com/science/article/pii/0375947468903783.

V. I. Kopeikin, L. A. Mikaelyan, and V. V. Sinev. Inverse beta decay in a nonequilibrium antineutrino flux from a nuclear reactor. *Phys. of At. Nucl.*, 64(5):849–854, 05 2001.

J. Korenaga. Archean Geodynamics and the Thermal Evolution of Earth. *Archean Geodynamics and Environments*, 164:7–32, 2006.

J. Korenaga. Urey ratio and the structure and evolution of Earth's mantle. *Rev. Geophys.*, 46(2):RG2007, Jun 2008.

G. Laske and G. Masters. A global digital map of sediment thickness. *EOS Trans. AGU*, 78:F483, 1997. URL https://cir.nii.ac.jp/crid/1571980075594652800.

G. Laske et al. CRUST 2.0, A New Global Crustal Model at 2x2 Degrees. https://igppweb.ucsd.edu/ gabi/crust2.html, 2001.

G. Laske et al. CRUST 1.0, A New Global Crustal Model at 1x1 Degrees. https://igppweb.ucsd.edu/ gabi/crust1.html, 2011.

T. Lyubetskaya and J. Korenaga. Chemical composition of Earth's primitive mantle and its variance: 2. Implications for global geodynamics. *J. Geophys. Res.*, 112 (B3):B03212, Mar 2007.

W. F. McDonough. *Earth's Core: The Encyclopedia of Geochemistry. 151–156.* Springer, 1999. doi: https://doi.org/10.1007/978-3-319-39312-4.

W. F. McDonough and S. Sun. The composition of the Earth. *Chem. Geol.*, 120: 223–253, 1995.

D. W. McKee, J. K. Busenitz, and I. Ostrovskiy. A $^{13}C(\alpha,n)^{16}O$ calibration source for KamLAND. *Nucl. Instrum. and Meth. A*, 587(2-3):272–276, 2008.

Y. Minekawa. カムランドによる大気ニュートリノ観測のためのバックグランドの研究. Master's thesis, Tohoku University, 2008.

T. A. Mueller et al. Improved predictions of reactor antineutrino spectra. *Phys. Rev. C*, 83(5):054615, May 2011. URL http://link.aps.org/doi/10.1103/PhysRevC.83.054615.

V. R. Murthy, W. van Westrenen, and Y. Fei. Experimental evidence that potassium is a substantial radioactive heat source in planetary cores. *Nature*, 423(6936): 163–165, May 2003. ISSN 1476-4687. doi: 10.1038/nature01560. URL https://doi.org/10.1038/nature01560.

K. Nakajima. *First Results from ^{7}Be Solar Neutrino Observation with KamLAND.* PhD thesis, Tohoku University, 2009.

K. Nakajima et al. A simple model of reactor cores for reactor neutrino flux calculations for the KamLAND experiment. *Nuclear Instruments and Methods in Physics Research Section A: Accelerators, Spectrometers, Detectors and Associated Equipment*, 569(3):837–844, 2006. ISSN 0168-9002. doi: https://doi.org/10.1016/j.nima.2006.09.088. URL https://www.sciencedirect.com/science/article/pii/S0168900206017499.

S. Obara. *A Search for Supernova Relic Neutrinos with KamLAND during Reactor-Off Period.* PhD thesis, Tohoku University, 2018.

K. A. Olive. Review of Particle Physics. *Chinese Physics C*, 38(9):090001, Aug 2014. doi: 10.1088/1674-1137/38/9/090001. URL https://doi.org/10.1088/1674-1137/38/9/090001.

On-Line Q-Value Calculation. Evaluation Group of China Nuclear Data Center, China Institute of Atomic Energy. http://www.nuclear.csdb.cn/qvalue/index.asp.

H. Ozaki. カムランド外水槽チェレンコフ検出器の刷新と性能向上. Master's thesis, Tohoku University, 2016.

H. Ozaki. *High Sensitivity Search for Neutrinoless Double-Beta Decay in KamLAND-Zen with Double Amount of ^{136}Xe.* PhD thesis, Tohoku University, 2020.

H. Ozaki and J. Shirai. Refurbishment of KamLAND outer detector. *Proceedings of Science*, Part F128556, Jan 2016. ISSN 1824-8039. 38th International Conference on High Energy Physics, ICHEP 2016 ; Conference date: 03-08-2016 Through 10-08-2016.

H. Palme and H. St. C. O'Neill. 2.01 - Cosmochemical Estimates of Mantle Composition. In Heinrich D. Holland and Karl K. Turekian, editors, *Treatise on Geochemistry*, pages 1–38. Pergamon, Oxford, 2007. ISBN 978-0-08-043751-4. doi: https://doi.org/10.1016/B0-08-043751-6/02177-0. URL https://www.sciencedirect.com/science/article/pii/B0080437516021770.

T. Plank and C. H. Langmuir. The chemical composition of subducting sediment and its consequences for the crust and mantle. *Chemical Geology*, 145(3):325–394, 1998. ISSN 0009-2541. doi: https://doi.org/10.1016/S0009-2541(97)00150-2. URL https://www.sciencedirect.com/science/article/pii/S0009254197001502.

H. N. Pollack, S. J. Hurter, and J. R. Johnson. Heat flow from the Earth's interior: Analysis of the global data set. *Rev. of Geophys.*, 31:267–280, 1993.

F. Reines and C. L. Cowan Jr. The Neutrino. *Nature*, 178(4531):446–449, Sep 1956. ISSN 1476-4687. doi: 10.1038/178446a0. URL https://doi.org/10.1038/178446a0.

R. L. Rudnick and D. M. Fountain. Nature and composition of the continental crust: A lower crustal perspective. *Reviews of Geophysics*, 33(3):267–309, 1995. doi: https://doi.org/10.1029/95RG01302. URL https://agupubs.onlinelibrary.wiley.com/doi/abs/10.1029/95RG01302.

R. L. Rudnick and S. Gao. *Treatise on Geochemistry: Composition of the Continental Crust Vol. 3*, pages 1–51. Pergamon Press, Oxford, 2014.

M. L. Rudolph, V. Lekić, and C. Lithgow-Bertelloni. Viscosity jump in Earth's mid-mantle. *Science*, 350(6266):1349–1352, 2015. doi: 10.1126/science.aad1929. URL https://www.science.org/doi/abs/10.1126/science.aad1929.

K. Schreckenbach et al. Determination of the antineutrino spectrum from ^{235}U thermal neutron fission products up to 9.5 MeV. *Phys. Lett. B*, 160(4-5):325–330, 10 1985.

J. G. Sclater, C. Jaupart, and D. Galson. The heat flow through oceanic and continental crust and the heat loss of the Earth. *Reviews of Geophysics*, 18(1): 269–311, 1980. doi: https://doi.org/10.1029/RG018i001p00269. URL https://agupubs.onlinelibrary.wiley.com/doi/abs/10.1029/RG018i001p00269.

I. Shimizu. *An Evidence for Spectral Distortion of Reactor Anti-Neutrinos and A Study of Three Flavor Neutrino Oscillation*. PhD thesis, Tohoku University, 2005.

Y. Shimizu. *Observation of Geo-Neutrinos with KamLAND*. PhD thesis, Tohoku University, 2010.

O. Šrámek et al. Geophysical and geochemical constraints on geoneutrino fluxes from Earth's mantle. *Earth and Planet. Sci. Lett.*, 361(0):356–366, Jan 2013. URL http://www.sciencedirect.com/science/article/pii/S0012821X12006097.

O. Šrámek et al. Revealing the earth's mantle from the tallest mountains using the Jinping neutrino experiment. *Scientific Reports*, 6:33034, Sep 2016. doi: doi.org/10.1038/srep33034. URL https://doi.org/10.1038/srep33034.

A. Strumia and F. Vissani. Precise quasielastic neutrino/nucleon cross-section. *Physics Letters B*, 564(1):42–54, 2003. ISSN 0370-2693. doi: https://doi.org/10.1016/S0370-2693(03)00616-6. URL https://www.sciencedirect.com/science/article/pii/S0370269303006166.

K. Tagashira. 高精度17インチ光電子増倍管の性能計測研究. Master's thesis, Tohoku University, 2000.

Y. Takemoto. CNOサイクル太陽ニュートリノ観測のためのデッドタイムフリー電子回路の開発. Master's thesis, Tohoku University, 2009.

A. Takeuchi. *First Search for Majorana Neutrinos in the Inverted Mass Hierarchy Region with KamLAND-Zen*. PhD thesis, Tohoku University, 2022.

N. Takeuchi, K. Ueki, T. Iizuka, J. Nagao, A. Tanaka, S. Enomoto, Y. Shirahata, H. Watanabe, M. Yamano, and H.K.M. Tanaka. Stochastic modeling of 3-d compositional distribution in the crust with bayesian inference and application to geoneutrino observation in japan. *Physics of the Earth and Planetary Interiors*, 288:37–57, 2019. ISSN 0031-9201. doi: https://doi.org/10.1016/j.pepi.2019.01.002. URL https://www.sciencedirect.com/science/article/pii/S0031920118302140.

S. R. Taylor and S. M. McLennan. *The continental crust: Its composition and evolution*. Oxford, Blackwell Scientific, 1985.

S. R. Taylor and S. M. McLennan. The geochemical evolution of the continental crust. *Reviews of Geophysics*, 33(2):241–265, 1995. doi: https://doi.org/10.1029/95RG00262. URL https://agupubs.onlinelibrary.wiley.com/doi/abs/10.1029/95RG00262.

S Togashi et al. Young upper crustal chemical composition of the orogenic Japan Arc. *Geochemistry, Geophysics, Geosystems*, 1(11), 2000. doi: https://doi.org/10.1029/2000GC000083. URL https://agupubs.onlinelibrary.wiley.com/doi/abs/10.1029/2000GC000083.

J. Trčková, R. Živor, and R. Přikryl. Physical and mechanical properties of selected amphibolite core samples from the Kola Superdeep Borehole KSDB-3. *Terra Nova*, 14(5):379–387, 2002. doi: https://doi.org/10.1046/j.1365-3121.2002.00427.x. URL https://onlinelibrary.wiley.com/doi/abs/10.1046/j.1365-3121.2002.00427.x.

D. L. Turcotte and G. Schubert. *Geodynamics, 2nd ed.* Cambridge University Press, 2002.

P. Vogel. Reactor antineutrino spectra and their application to antineutrino-induced reactions. II. *Phys. Rev. C*, 24(4):1543–1553, 1981. doi: 10.1103/PhysRevC.24.1543.

R. B. Walton, J. D. Clement, and F. Boreli. Interaction of Neutrons with Oxygen and a Study of the $C^{13}(\alpha,n)O^{16}$ Reaction. *Phys. Rev.*, 107:1065–1075, Aug 1957. doi: 10.1103/PhysRev.107.1065. URL https://link.aps.org/doi/10.1103/PhysRev.107.1065.

P. H. Warren. Stable-isotopic anomalies and the accretionary assemblage of the Earth and Mars: A subordinate role for carbonaceous chondrites. *Earth and Planetary Science Letters*, 311(1):93–100, 2011. ISSN 0012-821X. doi: https://doi.org/10.1016/j.epsl.2011.08.047. URL https://www.sciencedirect.com/science/article/pii/S0012821X11005115.

H. Watanabe. *Comprehensive Study of Anti-neutrino Signals at KamLAND*. PhD thesis, Tohoku University, 2012.

H. Watanabe. Effect of (α,n) background from position dependent ^{210}Po. presented at KamLAND collaboration meeting, 2021.

K. H. Wedepohl. The composition of the continental crust. *Geochimica et Cosmochimica Acta*, 59(7):1217–1232, 1995. ISSN 0016-7037. doi: https://doi.org/10.1016/0016-7037(95)00038-2. URL https://www.sciencedirect.com/science/article/pii/0016703795000382.

D. L. Williams and R. P. Von Herzen. Heat Loss from the Earth: New Estimate. *Geology*, 2(7):327–328, Jul 1974. ISSN 0091-7613. doi: 10.1130/0091-7613(1974)2⟨327:HLFTEN⟩2.0.CO;2. URL https://pubs.geoscienceworld.org/gsa/geology/article/2/7/327/205562/Heat-Loss-from-the-Earth-New-Estimate.

S. A. Wipperfurth et al. Earth's chondritic Th/U: Negligible fractionation during accretion, core formation, and crust–mantle differentiation. *Earth and Planetary Science Letters*, 498:196–202, 2018. ISSN 0012-821X. doi: https://doi.org/10.1016/j.epsl.2018.06.029. URL https://www.sciencedirect.com/science/article/pii/S0012821X18303807.

S. Yoshida et al. Light output response of KamLAND liquid scintillator for protons and ^{12}C nuclei. *Nuclear Instruments and Methods in Physics Research Section A: Accelerators, Spectrometers, Detectors and Associated Equipment*, 622(3):574–582, 2010. ISSN 0168-9002. doi: https://doi.org/10.1016/j.nima.2010.07.087. URL https://www.sciencedirect.com/science/article/pii/S0168900210017018.

K. Zuber. *NEUTRINO PHYSICS*. IOP Publishing Ltd, 2004.